THE UNIVERSITY of ADELAIDE

Harnessing Hydro-kinetic Energy from Wake-Induced Vibration (WIV) of Bluff bodies

By

Eshodarar Manickam Sureshkumar

School of Mechanical Engineering

Faculty of Engineering, Computer and Mathematical Sciences

This thesis is submitted for the degree of

Doctor of Philosophy

Oct 2018

This page in intentionally left blank

"All that I am
Or ever hope to be,
I owe to my angel mother."

Summary

In this dissertation, the application Wake-Induced Vibration (WIV) of a bluff body for harnessing the kinetic energy of a fluid flow is presented. WIV arises when a body undergoes vibrations in the wake of an upstream body. This project investigates the WIV of a bluff body (circular cylinder), constrained to vibrate in the transverse direction, operating in the wake produced by a stationary and upstream bluff body. The upstream body serves as an energy concentrator and increases the oscillations experienced by the downstream body. An efficient coupling of the spatially and temporally concentrated energy from the upstream body and the downstream and vibrating body will result in WIV being considered as a viable form of renewable energy. The application of induced vibration due to vortices in harnessing hydrokinetic energy of the fluid is relatively immature and this research work, which is written as a compilation of journal articles, attempts to address major scientific and technological gaps in this field.

The wake behind a bluff body augments the hydro-kinetic energy in space as well as time, in the form of a vortex street. Firstly, the kinetic energy distribution of a bluff body (circular cylinder) wake is characterized using numerical modelling, in order to identify the form and density of the available energy. Secondly, the spatial and temporal energy in the wake from different bluff bodies is investigated experimentally to identify a flow energy concentrator that is more suitable for WIV than the circular cylinder. The semicircular, straight-edged triangular, convex-edged triangular and trapezoidal cylinders were chosen for this analysis where the semicircular and convex-edged

triangular cylinders were found to augment more temporal energy compared to the circular cylinder.

Thirdly, experiments were performed in the water channel to investigate the effects of Reynolds number and separation gaps for the different cross-sections of upstream cylinders. The results indicated that an upstream semicircular cylinder produces more efficient WIV in a downstream circular cylinder compared to an upstream circular cylinder. In addition, both numerical and experimental results indicated that a staggered arrangement with $3 \leq x/D \leq 4$ and $1 \leq y/D \leq 2$ (here, D is the diameter of the cylinder, and x and y are the horizontal and vertical offsets, respectively) is the optimum arrangement among all test cases to harness the energy of vortices, resulting in a power coefficient of 33%. This was achieved due to the favourable phase lag between the velocity of the cylinder and force imposed by the fluid.

Finally, the effect of mass and damping ratio of the downstream cylinder is investigated to optimize the vibration efficiency of the staggered semicircular-circular cylinder WIV system. The results of this test showed that a lower damping ratio results in lower impedance of the system and hence a larger vibration response. The vibration response was also inversely proportional to the mass ratio, however, a mass ratio of 2 – 3 proved to be the most efficient for the WIV system resulting in a maximum efficiency of 49%.

Acknowledgements

Apart from my efforts, the success of any project depends mostly on the encouragement and guidelines of many individuals. I take this opportunity to express my sincere gratitude to the people who have been instrumental in the progress of this research.

I would like to show my greatest appreciation to my advisers, **Associate Professor Maziar Arjomandi**, **Professor Benjamin Cazzolato**, **Professor Bassam Dally and Dr Mergen Ghayesh** for supervising my research dedicating both their knowledge and experience.

I thank **Maziar** for his support and guidance through my studies. I have been extremely lucky to have a supervisor, who patiently listened to my personal problems during the ever-challenging PhD research. I am using this opportunity to express my gratitude to Maziar who encouraged me to pursue a PhD and groomed me during the process.

I would also like to express my gratitude to **Benjamin** for his brilliant ideas on scientific issues in particular and effective suggestions in the experiments. Special thanks for his detailed comments, precise attention, and crucial contribution, particularly for the improvement of the written work.

I am highly indebted to **Bassam** for his support and valuable assistances. There is no doubt that this progress would have not been possible without his kind support, attention and encouragement. His advices on both research as well as personal problems have been priceless and ingrained for future endeavours.

I am very thankful to **Mergen** for his support and assistance during the latter part of my project. Special thanks to his detailed comments and suggestions that improved the quality of my work. I would also like to thank him for the kind words of encouragement.

I am thankful my friends in s324b for their valuable assistance and for lending an ear during the hard times. I also wish to thank the many workshop staff members at the school of the Mechanical Engineering who aided in troubleshooting my test rig. A special thank you to **Marc Simpson** for putting up with me during my experiments.

Working away from one's home and family is a burden for many international students. I am very grateful to **Sean Lambert** and **Rohendra Soza** for providing a second home during my Ph.D.

I am particularly thankful for the support of **my family (Avva, Shasi, Dharshi athai, Richu and Naina),** for their continued patience and love. A special thank you goes to my mother, **Logeshwari** for giving me her deep love, encouragement and support during my education. She is my pillar; I am forever in debt to her for supporting me thus far and in future endeavours.

I am also grateful to my uncle **Vijayanathan Loganathan** for his advice and the healthy competition of 'who can get a PhD first?'. Although uncle Vijay passed away in the middle and my research, his personal skills and perseverance gave me a great deal of confidence and motivation to carry out my work and study.

Declaration by Author

I, **Eshodarar Manickam Sureshkumar**, certify that this work contains no material which has been accepted for the award of any other degree or diploma in my name, in any university or other tertiary institution and, to the best of my knowledge and belief, contains no material previously published or written by another person, except where due reference has been made in the text. In addition, I certify that no part of this work will, in the future, be used in a submission in my name, for any other degree or diploma in any university or other tertiary institution without the prior approval of the University of Adelaide and where applicable, any partner institution responsible for the joint-award of this degree.

I acknowledge that copyright of published works contained within this thesis resides with the copyright holder(s) of those works.

I also give permission for the digital version of my thesis to be made available on the web, via the University's digital research repository, the Library Search and also through web search engines, unless permission has been granted by the University to restrict access for a period of time.

I acknowledge the support I have received for my research through the provision of an Australian Government Research Training Program Scholarship.

Eshodarar Manickam Sureshkumar *Date*

26.10.2018

Table of contents

Summary ..... **iv**

Acknowledgement ..... **vi**

List of figures ..... **xi**

List of tables ..... **xxiii**

Chapter 1: Introduction and background **1**

1.1 Motivation 1

1.2 Methods of investigation 10

1.3 Objectives of this research 11

1.4 Structure of the thesis 12

1.5 Publications 13

Chapter 2: Review of literature **19**

2.1 Vortex shedding and flow induced vibrations of bluff bodies. 19

2.2 Flow around a cylinder 22

2.3 Experimental investigations in the wake of a circular cylinder 24

2.4 Energy in the flow: A first principles perspective 26

2.5 Energy concentration in the wake of bluff bodies 31

2.6 Factors that affect VIV and WIV 33

2.7 VIV of a single circular cylinder 36

2.8 Vortex structure in the wake of a vibrating cylinder 42

2.9 Effect of surface roughness 45

2.10 Mass and damping ratio 48

2.11 Effect of Reynolds number on VIV 53
2.12 VIV of a pair of circular cylinders 55
2.13 Wake interference in a WIV system 56
2.14 WIV studies 61
2.15 FIV energy harnessing systems 64
2.16 Virtual mass-spring-damper system 69
2.17 Mathematical modelling for VMSD 72
2.18 Computational fluid dynamics modelling 75
2.19 Summary and gaps 81

Chapter 3: Spatial and temporal concentration of flow energy 97

Chapter 4: Temporal concentration of energy by .....157 different bluff bodies

Chapter 5: Effect of upstream geometry on WIV 209

Chapter 6: Effect of mass and damping ratio on WIV 255

Chapter 7: Summary, conclusions and future work..... 289
7.1 Summary and conclusions 289
7.2 Significance of present work 299
7.3 Recommendations for future work 300

List of figures

Chapter 1:

Figure 1.1 – Breakdown of global energy consumption 2016 (adapted from BP statistical review of world energy 2017).....1

Figure 1.2 - Representation of a WIV system with a stationary upstream cylinder and a downstream cylinder constrained to vibrate transversely (Assi et al. 2010).....4

Figure 1.3 - Large-scale VIVACE convertor concept 5

Figure 1.4 - Volume energy density comparison of the VIVACE convertor and three types of wave convertors (adapted from Bernitsas et al. 2008).....7

Chapter 2:

Figure 2.1 - Dye-based flow visualisation of a vortex street in the wake of a cylinder (Karch et al. 2012).....19

Figure 2.2 – Normalised amplitude response of a circular cylinder undergoing VIV (scatter points) and the upper and lower bounds (red and blue lines, respectively) of WIV of the downstream cylinder in a WIV system (mass ratio = 2.4, damping ratio = 0.01) comprising of cylinders of the same diameter (Derakhshandeh et al. 2015b).....22

Figure 2.3 - Strouhal number vs Reynolds number for a circular cylinder (Blevins 1990).....23

Figure 2.4 - Representative instantaneous streamlines (top row) and instantaneous velocity fields (bottom) at two values of Reynolds number (Lin et al. 1995).....24

Figure 2.5 - Mean streamwise velocity (normalised using freestream velocity) along the wake centreline of a circular cylinder for Re = 1,500 – 14,000 (Norberg 1998). 25
Figure 2.6 - Comparison of normalised turbulent kinetic energy (TKE) distribution in the wake of a cylinder and sphere at Re = 5,000. Minimal and incremental values of TKE for the cylinder and sphere are 0.02 and 0.005, respectively (Ozgoren et al. 2011). 26
Figure 2.7 - Time-averaged normalised streamwise velocity ($\boldsymbol{U/U\infty}$) profiles for a Reynolds number of 92,000 (Goldstein & Kulkarni 2008), where x/D and y/D are the non-dimensionalised streamwise and transverse distances. 32
Figure 2.8 - Time dependant contours of dimensionless energy density (energy in the wake/energy in the freestream) for a circular cylinder (Derakhshandeh et al. 2015c) 33
Figure 2.9 - VIV amplitude response vs reduced velocity (U/Df_0) for a single circular cylinder depicting the three branches of oscillation (Assi 2009). ($m^* = 2.4$; $\zeta = 0.01$) 34
Figure 2.10 - Vortex street behind a circular cylinder (Zdravkovich 1997) 38
Figure 2.11 – Mass-spring-damper schematic of a 1DOF cylinder mounted elastically in a cross flow. 39
Figure 2.12 - Dynamic response of a circular cylinder under VIV mechanism at three different branches of oscillation. Left column: time histories of displacement. Right column: lift coefficient and displacement over one complete cycle, y/D in blue and C_L in red with average cycle in dash black, at a) $U_r = 4.0$, b) $U_r = 5.7$, and c) $U_r = 7.9$, (Assi 2009). 41
Figure 2.13 - Dynamic response of a single circular cylinder under VIV mechanism, including a) amplitude of oscillation, b) normalised PSD of

frequency of oscillation and c) potential and vortex lift phase angles (Assi 2009). 42
Figure 2.14 - Map of vortex synchronization near the fundamental lock-in. A/D is the amplitude ratio and λ/D is the wavelength ratio (λ = freestream velocity/ frequency of oscillation). The ''critical curve'' represents the transition from one mode of vortex formation to another. Curves I and II represent locations where the forces on the body show a sharp jump (Williamson & Roshko 1988).....44
Figure 2.15 - Photographs and sketches showing the two near-wake vortex patterns for a circular cylinder (U = 0.93, Re = 7350) (Brika & Laneville 1993). (a) represents the 2S mode whilst (b) represents the 2P mode of vortex shedding 45
Figure 2.16 – Strouhal number versus Reynolds number for different roughness strips placed at an angle of 50° to the freestream velocity. Curves with triangles are for a smooth surface, squares are for r/D = 9.4 x 10^{-5}, circles are for r/D = 90 x 10^{-5}; where r = diameter of roughness particles and D = diameter of the cylinder (Nakamura & Tomonari 1982). 46
Figure 2.17 – VIV cylinder amplitude versus reduced velocity for different strip locations for P120 roughness. (Chang et al. 2011).....47
Figure 2.18 – VIV cylinder responses for different strip area coverages. (Chang et al. 2011).....48
Figure 2.19 – Two different types of amplitude response for VIV based upon the dependency on mass damping ratio, where high $m^*\zeta$ only shows the initial and lower branches whilst low $m^*\zeta$ has these two branches with the additional upper branch of oscillation (Govardhan and Williamson 2000). 49
Figure 2.20 - Pairs of ampltiude-frequency plots for decreasing mass ratio (m*) plot to the same scale (Govardhan & Williamson 2000). A^* is

the amplitude normalised with the freestream velocity, f^* is the frequency of oscillation normalised with the natural frequency and U^* is the reduced velocity. 50
Figure 2.21 - Transverse cylinder response for four cylinder masses at constant reduced damping, $2m(2\pi\zeta)/\rho D2$ = 1.24 (Blevins & Coughran 2009) 51
Figure 2.22 - Amplitude ratio vs. U* (reduced velocity) , U (freestream velocity), and Re for K = 1800 N/m and various values of damping ratio, ζ_{harn} (Lee & Bernitsas 2011). 53
Figure 2.23 - The different configurations of two identical circular cylinders used in VIV studies; a) in-line, b) side-by-side, c) staggered.56
Figure 2.24 - The different interference regions for the location of a downstream cylinder in the wake of a fixed upstream cylinder (Zdravkovich & Bearman 1988). 57
Figure 2.25 - Wake structure around two stationary cylinders as a function of in-line separation (Derakhshandeh et al. 2015, reproduced from Igarashi 1984). A and B = separation gap less than 1.5D; C and D = separation gap of 1.5D – 3D; E and F separation gap larger than 3D. ..59
Figure 2.26 - Flow visualisation of a pair of circular cylinders; a) - d) are for Re = 3,300, 6,700, 10,000, 12,000 with separation gap = 1.25D, and e) and f) for Re = 10,000 and 12,000 at separation gap = 4D (Ljungkrona and Sunden 1993).....61
Figure 2.27 - Schematic of a typical WIV system consisting of two circular cylinders of the same characteristic diameter. 62
Figure 2.28 - Contours for the Efficiency of VIV response (left – Re = 65000) and WIV response (left – Re = 6000) based on different locations of the downstream cylinder (Derakhshandeh et al. 2014, 2015c).....66

Figure 2.29 - Photograph of the tree inspired piezoelectric flow energy harvester tested by Hobbs and Hu (2012). The device consists of four cylinders placed in series and mounted to a piezoelectric transducer. 68
Figure 2.30 - Schematic of a piezoelectric generator utilising Karman vortex street (Weinstein et al. 2012).....69
Figure 2.31 – Schematic of VMSD system developed by Hover et al. (1997). A computer-controlled servomotor actively positions the test cylinder through a linear slide; this assembly , along with the supporting electronics and sensors, translates along a 25 m towing tank 70
Figure 2.32 - VMSD system developed by Lee et al. 2011 with a horizontally mounted cylinder. 71
Figure 2.33 - Virtual Mass Spring Damper system developed by Derakshandeh et al. (2015a) employing a vertically mounted cylinder (D2).....72
Figure 2.34 – Plot of the normalised centreline velocity in the wake of a circular cylinder using several turbulence models (Altar and Goren 2010). SST = The shear stress transport (SST) $k-\omega$ model; SA = the Spalart-Allmaras model; RKE = realizable $k-\varepsilon$; WKO = Wilcox $k-\omega$ model; and Exp = experimental data.....77
Figure 2.35 - Contours of turbulence length scale/cylinder diameter at Re=10^6; a): URANS model (SST), b): SAS model, (Menter and Egorov 2010). 79
Figure 2.36 – Pressure coefficient around the surface of an upstream stationary cylinder using the SST and SAS models at Re = 65,000 compared against published experimental data by Alam et al. (2003) (Derakhshandeh, Arjomandi, Dally, et al. 2014). 80
Figure 2.37 – Lift coefficient vs the streamwise separation gap between two circular cylinders in a WIV system obtained using the SAS model

and experimental data by Alam et al. (2003) (Derakhshandeh, Arjomandi, Dally, et al. 2014). 81

Chapter 3:

Figure 1 – Structured mesh generated using ANSYS Meshing (Test Case 2 in Table 1). The mesh around the cylinder is finer than the rest of the domain to capture the shear layers accurately. 112
Figure 2 - Pressure coefficient over the top half of the circular cylinder 118
Figure 3 - Lift and Drag coefficients for the circular cylinder at a Reynolds number of 10000 from the SAS model (Grid 2) 120
Figure 4 - Comparison of the mean streamwise velocity at the centreline (y/D = 0) with published experimental data at Re = 10,000. 120
Figure 5 – Contour plot of the mean normalised streamwise energy (Eu) in the wake of the cylinder 123
Figure 6 - Contour plot of the mean normalised transverse energy (Ev) in the wake of the cylinder 123
Figure 7 - Contour plot of the mean normalised spanwise energy (Ew) in the wake of the cylinder 124
Figure 8 - FFT plots of the fluctuating velocity components (u′ and v′) at different x/D and y/D locations in the wake of a circular cylinder. The frequency spectrum was normalised using the vortex shedding frequency (fs) to display the augmentation over harmonics of the shedding frequency. 126
Figure 9 – Normalised streamwise energy fluctuation ($Eufs'$) at the shedding frequency 126
Figure 10 - Normalised transverse energy fluctuations ($Evfs'$) at the shedding frequency 127

Figure 11 - Normalised spanwise energy fluctuations ($Ewfs'$) at the shedding frequency 127
Figure 12 – Comparison of wake energy components obtained via 2D and 3D (a) and b), respectively) numerical simulations. 128
Figure 13 - Energy in the wake due to the mean and fluctuating components at y/D = 0, a); 0.5, b); 1.0, c). 130
Figure 14 - Magnitude of maximum energy (including both the steady and unsteady components) that could be captured by a Wake Energy Extractor (WEE) which can move transversely at fixed x/D locations. The Contour map is the normalised energy distribution due to the total velocity in the wake. 132
Figure 15 - The bluff bodies used to investigate the difference in the wake energy components. The bluff bodies from left to right are circle semi-circle, equilateral triangle and an equilateral triangle with convex sides. 135
Figure 16 - Energy in the wake of a semi-circular cylinder due to the mean and fluctuating components at y/D = 0, a); 0.5, b); 1.0, c). 135
Figure 17 - Energy in the wake of a straight-edged triangle due to the mean and fluctuating components at y/D = 0, a); 0.5, b); 1.0, c). 136
Figure 18 - Energy in the wake of an equilateral triangle with convex sides due to the mean and fluctuating components at y/D = 0, a); 0.5, b); 1.0,c). 137
Figure 19 - Normalised energy magnitude of the mean streamwise component in the wake of different bluff bodies at transverse heights of y/D = 0, a); y/D = 0.5, b); y/D = 1, c); y/D = 1.5, d). 141
Figure 20 - Normalised energy magnitude of the mean transverse component in the wake of different bluff bodies at transverse heights of y/D = 0, a); 0.5, b); 1.0, c); 1.5, d). 142

Figure 21 - Normalised energy magnitude of the fluctuating streamwise component in the wake of different bluff bodies at a transverse height of y/D = 0, a); 0.5, b); 1.0, c); 1.5, d). 143
Figure 22 - Normalised energy magnitude of the fluctuating transverse component in the wake of different bluff bodies at a transverse height of y/D = 0, a); 0.5, b); 1.0, c); 1.5, d); 144

Chapter 4:

Figure 1 - Bluff body cross-sections used in this study (all shapes have a characteristic diameter of 30mm; not to scale); from left to right – circle (a), semicircle (b), c-triangle (c) and trapezoid (d) 172
Figure 2 - Working section of the Thebarton water channel (Birdseye view) with a schematic of the PIV set-up 173
Figure 3 - Power spectrum output for the fluctuating transverse velocity component (v') at x/D = 2 and y/D = 0 for the circular (a) and trapezoidal (b) cylinders. 178
Figure 4 - Power spectrum output for the fluctuating transverse velocity component (v') at x/D = 2 and y/D = 0 for the semi-circular, (a), and convex-edged triangular, (b), cylinders. 179
Figure 5 – Normalised mean streamwise velocity, $u/U0$, of the circular cylinder along the centreline (y/D = 0) compared to the published experimental data by Norberg (1998) 180
Figure 6 - Normalised streamwise velocity, $u/U0$ in the wake of a circular cylinder at Re = 10,000 from PIV (Dong et al. 2006), a), DNS (Dong et al. 2006), b), current research, c) 181
Figure 7 - Mean normalised spanwise vorticity $\overline{\omega_z}D/U_0$ in the wake of the bluff bodies. Top row of images corresponds to *Re* = 5,000 (a – d) and the bottom row (e –h) to *Re* = 10,000. Images from left to right – circle (a

& e), semicircle (b & f), trapezoid (c & g) and c-triangle (d & h). All the contours have the same scale …… 183

Figure 8 - Reynolds stresses in the current research, $\langle u'v' \rangle / U_0^2$. Order of images same as Figure 5 …… 186

Figure 9 - Turbulent kinetic energy $[\overline{u'^2} + \overline{v'^2}] / U_0^2$ (TKE) in the wake of the investigated bluff bodies. Order of images same as Figure 7 … 187

Figure 10 - Normalised energy magnitudes due to the mean streamwise component ($E_{\bar{u}}$). Order of images same as Figure 7 ……... 191

Figure 11 - Normalised energy magnitudes due to the mean transverse component ($E_{\bar{v}}$). Order of images same as Figure 7 ……... 192

Figure 12 - Normalised energy magnitudes due to the fluctuating streamwise component ($E_{u'_{fs}}$). Order of images same as Figure 7 …… 193

Figure 13 - Normalised energy magnitudes due to the fluctuating transverse component ($E_{v'_{fs}}$). Order of images same as Figure 7 …….. 194

Figure 14 - Normalised transverse fluctuating energy magnitudes along the centreline ($y/D = 0$) for all the bluff bodies investigated. The top plot is for $Re = 5{,}000$ and the bottom plot corresponds to $Re = 10{,}000$ …….. 196

Chapter 5:

Figure 1 - Cross-sections used as the first body in the WIV system....220

Figure 2 – Schematic representation of the WIV system consisting of a fixed upstream cylinder of diameter D and a transversely vibrating second bluff body. X and y denote the streamwise and transverse separation gap between the cylinders, respectively; k and c are the spring stiffness and damping coefficient, respectively. 222

Figure 3 - Cross-sections used as the first bluff body in the WIV system. a), circle; b), semicircle; c), convex-edged triangle (c-triangle); d), trapezoid.....222
Figure 4 - Schematic representation of the nine different test cases used for each cross-section in this study, where the shaded circle with the solid outline represents the upstream cylinder, and the dashed circles are the nine locations of the downstream cylinder. 223
Figure 5 - The Virtual-Mass-Spring-Damper (VMSD) system used in this research.....224
Figure 6 - Typical time series of the lift coefficient (dotted line) , cL, and the dimensionless displacement (solid line), y(t) /D, of a single circular cylinder undergoing VIV at a) Re = 6,000 and b) Re = 10,000. (mass ratio = 2.4, damping ratio = 0.01).....230
Figure 7 - Results of the peak dimensionless displacement vs Reynolds number for a single cylinder undergoing VIV using the VMSD system. The results are compared with published experimental results (Assi 2009; Derakhshandeh et al. 2015) with the same structural properties ($m^* = 2.4$ and $\zeta = 0.01$). 230
Figure 8 - Measured time history of displacement for Test Case 3 (x/D = 4, y/D = 0) at Re = 4,000, a), and 8,000, b) for a two-cylinder WIV system. 231
Figure 9 - WIV response of the downstream cylinder as a function of the Reynolds number and a comparison of the data for x_0/D = 4 with previous work (Assi 2009) (Test Case 3).....232
Figure 10 - Amplitude response for the circular cylinder.....234
Figure 11 - Amplitude response for the semi-circular cylinder 234
Figure 12 - Amplitude response for the trapezoidal cylinder 235
Figure 13 - Amplitude response for the c-triangular cylinder 235

Figure 14 - Amplitude comparison for case 9 (x/D = 4, y/D = 2) for all the test cases 236
Figure 15 - Comparison of the average lift coefficient across all tests cases for each Reynolds number and upstream cross-section investigated. The corresponding Reynolds numbers are given in the title of each subplot. The error bars indicate the standard deviation of the lift coefficient across the 9 test cases for each bar on the plots. 238
Figure 16 - Force-displacement phase angle distribution for the circular cylinder 240
Figure 17 - Force-displacement phase angle distribution for the semi-circular cylinder 241
Figure 18 - Correlation of the average force-displacement phase angles and Reynolds number for the different upstream cross-sections used in this project. The standard deviation between the tests cases for each cross-section and Reynolds number is indicated by the error bars.....242
Figure 19 - Power coefficient distribution for the circular cylinder 243
Figure 20 - Power coefficient distribution for the semi-circular cylinder 244
Figure 21 - Power coefficient distribution for the trapezoidal cylinder 245
Figure 22 - Power coefficient distribution for the c-triangular cylinder 246
Figure 23 - Comparison of the maximum WIV power coefficient obtained for the upstream bluff body cross-sections at Re = 6,000. The maximum efficiencies occur for case 9, where x/D = 4 and y/D = 2.....246

Chapter 6:

Figure 1 - Pairs of amplitude-frequency plots of a single cylinder VIV system for decreasing mass ratio (m*) plot to the same scale (Govardhan & Williamson 2000).....263
Figure 2 – Schematic representation of the WIV system consisting of a fixed upstream semicircular cylinder of diameter D and a transversely vibrating downstream circular cylinder of diameter D. k and c are the spring stiffness and damping coefficient, respectively and the downstream cylinder has a separation of 4D and 2D streamwise and transverse from the upstream cylinder, respectively. 267
Figure 3 - The Virtual-Mass-Spring-Damper (VMSD) system used in this research.....268
Figure 4 – Lift coefficient and normalised displacement for the downstream cylinder for a mass ratio of 1 and damping ratio of 0.01 using the VMSD system which exceeds the capabilities of the VMSD rig. 271
Figure 5 - Normalised oscillation peak amplitude vs damping ratio for mass ratios of 2.5 and 5.0 for the vibrating downstream cylinder in a staggered semicircular - circular cylinder WIV system 275
Figure 6 - Lift coefficient vs damping ratio for mass ratios of 2.5 and 5.0 for the vibrating downstream cylinder in a staggered semicircular - circular cylinder WIV system. 275
Figure 7 - Force-velocity phase difference vs damping ratio for mass ratios of 2.5 and 5.0 for the vibrating downstream cylinder in a staggered semicircular - circular cylinder WIV system. 276
Figure 8 - Normalised oscillation peak amplitude (Y*) obtained for the range of damping and mass ratios of the vibrating downstream cylinder in a staggered semicircular - circular cylinder WIV system. 278

Figure 9 – Lift coefficient obtained for the range of damping and mass ratios of the vibrating downstream cylinder in a staggered semicircular - circular cylinder WIV system.....278
Figure 10 – Force-displacement phase angle obtained for the range of damping and mass ratios of the vibrating downstream cylinder in a staggered semicircular - circular cylinder WIV system. 279
Figure 11 – WIV power coefficient (efficiency) obtained for the range of damping and mass ratios of the vibrating downstream cylinder in a staggered semicircular - circular cylinder WIV system. 279
Figure 12 - Plots of normalised displacement amplitude (Y*) versus Reynolds number for combined mass-damping of 0.02, a), 0.03, b), 0.04, c), and 0.05 d). The individual values of mass ratio and damping ratio are given in the legend for each subplot.....282

List of tables

Chapter 2:

Table 1 - Fluidic and Structural parameters that govern VIV 37
Table 2 - Non-dimensional parameters. 73

Chapter 3:

Table 1 - Details of the different meshes used in this study 112
Table 2 - Comparison of physical quantities for a circular cylinder at Re = 10000: Drag coefficient Cd, base pressure coefficient -C_{Pb}, Strouhal number St, r.m.s lift coefficient C_L. Adapted from (Dong et al. 2006) with results from current research 119

Chapter 4:

Table 1 - Strouhal numbers for the circle, semicircle, trapezoid and c-triangle.....184

Chapter 5:

Table 1 - System parameters used in the experiments 226
Table 2 - Non-dimensional parameters. 227

Chapter 6:

Table 1 – Non-dimensional structural and fluidic parameters that govern VIV and WIV 259
Table 2 – Mass and damping ratios used for experiments 270
Table 3 - Non-dimensional parameters. 272

Chapter 1. Introduction and background

1.1 Motivation

A growing energy demand with an increasing consumption rate is a characteristic of present-day living. The exponential growth of the human population is expected to surpass 9.8 billion in 2050 and energy consumption predicted to increase 5% over the next 20 years due to the increase in electricity production by developing countries (Letcher 2013). Fossil fuels such as coal, oil and gas account for majority (86% in 2016) of the global energy production (Figure 1.1) and have benefits of being energy dense, portable and storable. However, fossil fuels produce greenhouse gases, such as carbon dioxide, when they are combusted. Hence, alternative energy sources are needed to cater to the energy demand without contributing to atmospheric pollution. Renewable sustainable and clean energy sources such as wind, solar and hydro are some of the common alternatives to energy from fossil fuels.

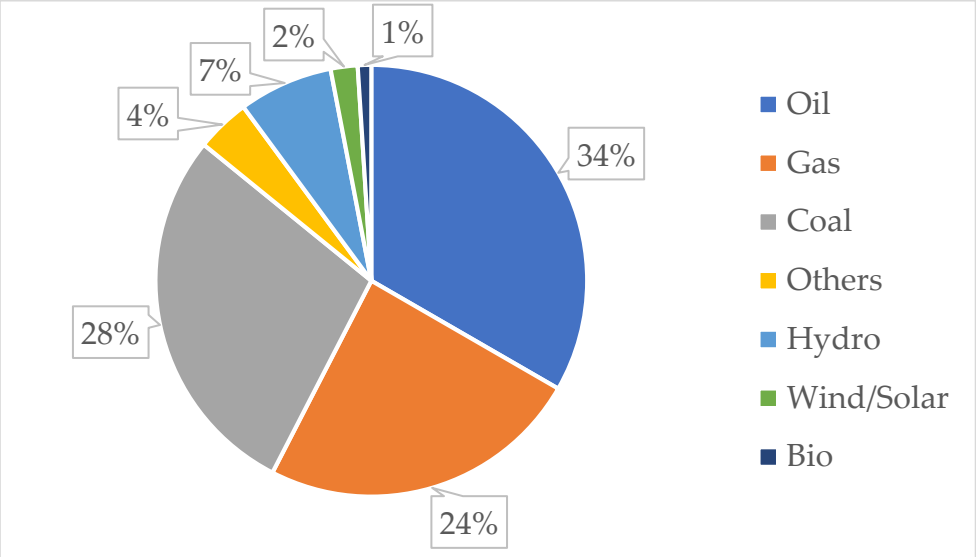

Figure 1.1 – Breakdown of global energy consumption 2016 (adapted from BP statistical review of world energy 2017).

The progression to sustainable sources faces many hurdles. Hydrocarbons used for energy production have many useful by-products that have created thousands of derivative industries. Furthermore, manufacturing of all renewable energy technology also requires significant quantities of fossil fuels and natural resources (Kleijn *et al.* 2011). However, the need for clean energy has sparked research into alternative energy sources like hydroelectricity, wind energy and solar energy which account for about 14% of current global energy production.

Solar, wind and hydro energy are types of renewable energy that are abundantly available and easily accessible, which make them ideal for clean energy production (Yuce & Muratoglu 2015). Hydropower can be a viable replacement for future energy needs since two-thirds of the planet's surface is covered in water with majority of the world's population living near sources of water.

Hydrokinetic energy is a renewable energy source available in moving water bodies, such as oceans and rivers (Oki & Kanae 2006). There are five types of hydrokinetic energy classified as ocean wave, tidal stream, river hydrokinetic, ocean current and ocean thermal (Copping & Geerlofs 2010). Technology to harvest the kinetic energy from currents is in its infancy compared to other forms of renewable energy, but still show promise since they provide an alternative means of renewable energy to population situated near shorelines and rivers (Foufoula-Georgiou *et al.* 2012). Energy convertors for hydrokinetic energy can be classified by the nature of the utilized space in which they operate. Hydrokinetic energy convertors include point absorbers, such as surface buoys (Johnson & Pride 2010), line absorbers, such as the Pelamis attenuator (Lagoun *et al.* 2010), horizontal surface patch

absorbers, such as oscillating water columns (Heath 2012), vertical surface absorbers, such as turbines and open propellers (Batten *et al.* 2006), and three dimensional space absorbers such as devices which operate using Flow Induced Vibrations (FIV), for example the VIVACE Converter (Bernitsas *et al.* 2009).

Mainstream extraction of energy from fluid flows, such as wind and water currents, is usually achieved using turbines which have rotating blades to capture the energy in the flow (Khan *et al.* 2009). Non-turbine systems such as oscillating water columns (using vertical motion of waves) and point convertors (utilising the axial flow of currents) have also been considered lately, since they offer additional benefits when compared to turbine systems. While every system have its strengths and weaknesses the applicability of each technology depends on geographical location and environmental conditions as well as cost. Hydrokinetic energy obtained using dams and water wheels can cause environmental harm due to altering the natural flow of the water source which causes problems with fish migration and blockage of passages (Khan *et al.* 2009; Peng & Zhu 2009; Zhu 2011). Turbine systems experience many structural and centrifugal stresses, which must be overcome with the use of light and strong materials to have high performance capabilities. Horizontal axis water turbines also pose installation issues and pose dangers to the aquatic flora and fauna. Additionally, water turbines usually operate at high flow speeds, which is not always possible. In comparison, VIV and WIV convertors can operate at relatively low flow speeds (> 0.2 m/s) and WIV convertors are operable over a range of flow velocities.

In search for alternative ways to harness the kinetic energy in water currents, researchers have turned to Flow Induced Vibrations

(FIV) such as Vortex Induced Vibration (VIV) and Wake Induced Vibration (WIV). FIV capitalise on the interaction of the fluid forces from the flow with the elastic properties of a structure. VIV, on the other hand, relies on the synchronisation between the frequency of the vortices shed from a bluff body and the natural frequency of the structure supporting the bluff body (Blevins 1997). Finally, WIV occurs when a bluff body undergoes vibrations in the interference region of an upstream bluff body wake.

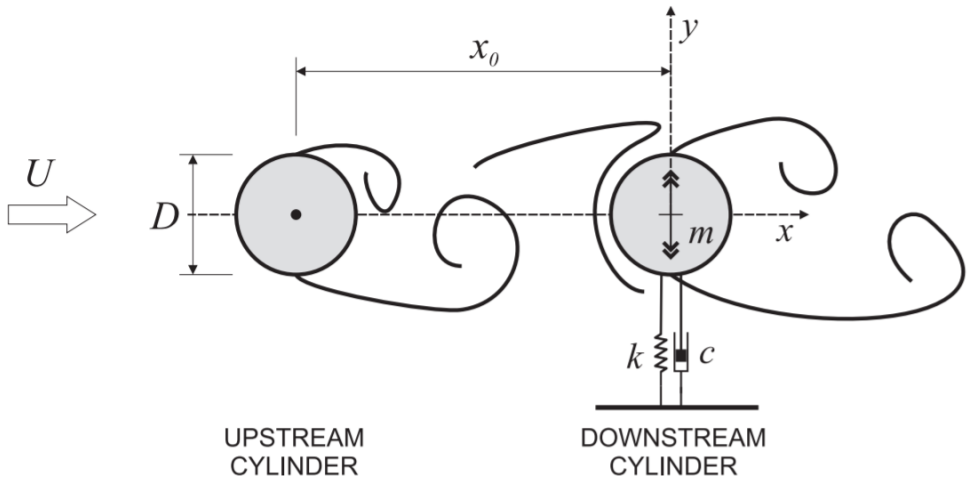

Figure 1.2 - Representation of a WIV system with a stationary upstream cylinder and a downstream cylinder constrained to vibrate transversely (Assi et al. 2010).

The main difference between VIV and WIV is that the latter refers to a body vibrating in the wake produced from an upstream bluff body as depicted in Figure 1.2 (Assi 2009). The wake produced from the stationary upstream bluff body affects the forces on the downstream vibrating body, causing the WIV response. WIV is of interest for energy production, due to the amplitude response not being limited to a lock-in range of velocities as in VIV (Assi 2009; Derakhshandeh *et al.* 2014) and efficiency of WIV systems are higher than VIV systems (Derakhshandeh *et al.* 2014; Derakhshandeh *et al.* 2015a).

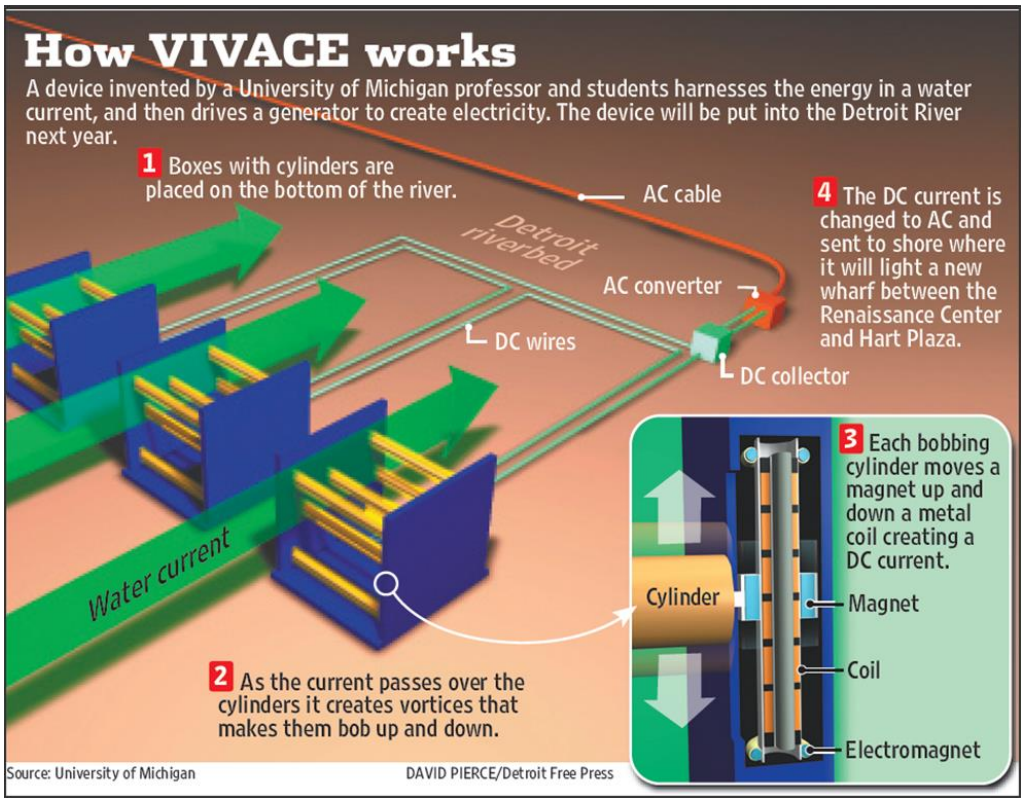

Figure 1.3 - Large-scale VIVACE convertor concept

VIV and WIV have been applied to flow energy technology such as the Vortex Induced Vibration for Aquatic Clean Energy (VIVACE) (Bernitsas *et al.* 2008). Pioneering work by Bernitsas *et al.* (2008), resulted in an early large-scale VIV device, employing a circular cylinder, to produce energy from low speed flows, and this concept is depicted in Figure 1.3. Small-scale devices, such as those used for remote monitoring in ventilation and air conditioning systems, can use WIV to produce the small amounts of energy needed for them to operate and hence make monitoring easier and viable at remote locations (Hobbs & Hu 2012; Wang & Ko 2010; Weinstein *et al.* 2012).

The energy capacity of a VIV or WIV system can range anywhere from milliwatt to megawatt range based upon the dimension and number of cylinders used, the fluid type, as well as the flow speed (Bernitsas *et al.* 2009; Bernitsas & Raghavan 2004; Bernitsas *et al.* 2008).

The scalability and flexibility of the VIV/WIV convertor makes it suitable for a variety of applications from energy for remote monitoring devices to large scale energy production for day-to-day use. Additionally, VIV convertors have been shown to operate at high efficiencies and can be deployed in low velocity currents (Bernitsas *et al.* 2008), unlike their turbine counterparts which usually need high flow speeds to start-up.

In general, the WIV of a downstream cylinder can be thought of as the unsteady vortex-structure interaction that occurs between the cylinder and the wake from the upstream body, as depicted in Figure 1.2 (Assi *et al.* 2010). Hence, the WIV response of a circular cylinder is distinctively different from the VIV response of a circular cylinder in isolation. In the WIV mechanism, when the downstream cylinder is displaced sideways, a lift force acts to move the cylinder towards the centreline (Zdravkovich 1977) and it can occur outside of the resonance frequency (Assi *et al.* 2010).

A bluff body placed in flow produces a vortex street which causes spatial and temporal concentration of the flow energy. Spatial concentration occurs due to the mean velocity flow field, whilst the temporal concentration arises due to the fluctuating velocity components. Unlike spatial concentrators such as diffusers and shrouds, the vortices in the bluff body wake have an added temporal component occurring at the shedding frequency. This added temporal component enhances the vibrations of the second body if the structural resonance coincides with the periodicity of the vortices in the wake. Hence, knowledge of the wake and its features is a significant aspect that needs to be investigated to design WIV technology which can efficiently capture the kinetic energy content of the upstream body's wake.

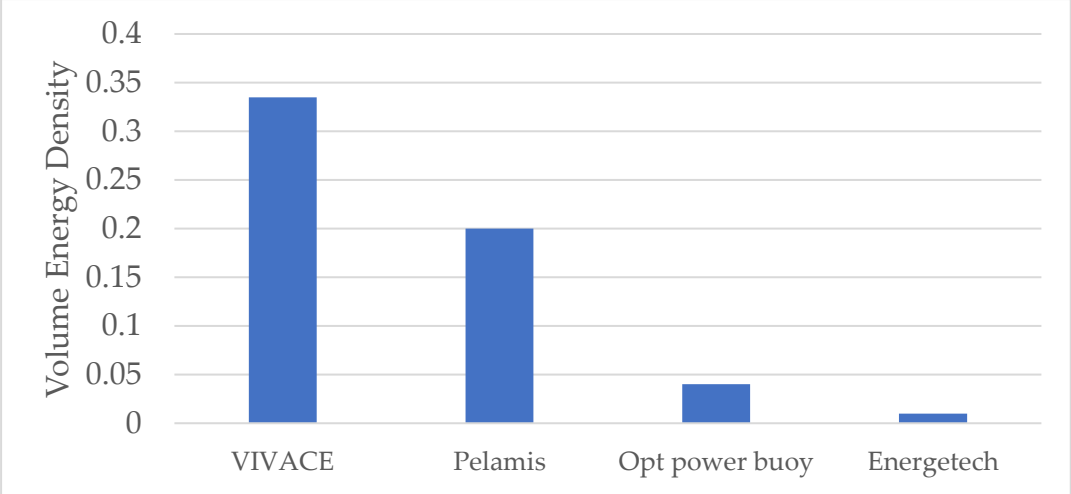

Figure 1.4 - Volume energy density comparison of the VIVACE convertor and three types of wave convertors (adapted from Bernitsas et al. 2008).

Comparing the energy volume densities of some large-scale non-turbine flow energy technology, there is potential to further developing VIV energy. The energy volume density is the ratio of actual energy produced to the physical volume occupied by each technology listed in Figure 1.4; the VIVACE convertor (Bernitsas *et al.* 2008), Pelamis convertor (Henderson 2006), Opt Power Buoy (Edwards & Mekhiche 2014) and Energetech (Thorpe 2002). Pelamis and Energetech are buoy convertors, where Pelamis is a floating buoy and Energetech is moored to the ocean floor. Energetech is a convertor that is either located on the sea bed or moored at a very low depth. As depicted in Figure 1.4, the VIV convertor, has a far higher energy volume density compared to the other energy convertors, making it a formidable energy technology in terms of volumetric power density. Furthermore, power produced from VIV is costed at US $ 0.055/kWh, which is comparable to that from wind and solar at US $ 0.06/kWh and US $ 0.04/kWh, respectively (Bernitsas *et al.* 2008).

The interactions between the vortex street produced by the upstream body and the downstream body gives rise to WIV in a two-

bluff body system. In such WIV systems, the dynamic response of the elastically mounted downstream cylinder is greatly affected by the spacing gap between the cylinders. A thorough study of WIV was performed by Assi (2009); Assi *et al.* (2010); Assi *et al.* (2006) where the effect of fluidic parameters, such as force-displacement phase angle, was studied for cylinders that were separated along the centreline (in-line separation). Derakhshandeh *et al.* (2014, 2015a, 2016) conducted numerous studies on wake induced vibration using two circular cylinders as well as an aerofoil as the downstream body. Their investigations also studied the effect of longitudinal and streamwise spacing, as well as Reynolds number on the efficiency of WIV. Although the effect of fluidic parameters, downstream bluff body shape and position, and Reynolds numbers have been extensively reviewed in these studies, the effect of structural parameters such as mass and damping ratios on WIV have not received much attention in past studies.

Albeit the abundance of extant literature experimentally investigating the VIV phenomenon (Bearman 1984, 2011; Derakhshandeh *et al.* 2015b; Govardhan & Williamson 2000; Govardhan & Williamson 2004; Jauvtis & Williamson 2004; Khalak & Williamson 1997) and WIV (Assi 2009; Carmo *et al.* 2011; Derakhshandeh *et al.* 2014; Derakhshandeh *et al.* 2015a) of elastically mounted cylinders, systematic studies on the improvement of WIV technology for energy generating potential are rare. Notably, the effect of the upstream bluff body cross-section on the WIV system and the distinction of temporal energy concentration caused by the upstream bluff body have not been reported in past studies.

A downstream cylinder in the WIV system is subjected to two distinct types of vortex streets; the oncoming wake vortices of the upstream bluff body and the vortex street shed from the downstream body. The combined effect of both these vortex streets makes WIV distinctly different from VIV. The project gains its primary motivation to improve the efficiency of a WIV energy convertor, in terms of the power transferred from the fluid current to the cylinder. Such an improvement will highlight the potential of WIV as an alternative energy source. Hence, this project aims to employ the WIV mechanism to harness flow energy whilst investigating the effect of structural and fluid parameters of the system.

The WIV response of a downstream elastic circular cylinder is investigated in the current research, to capture the hydrokinetic energy of vortices from a variety of upstream stationary bluff bodies. The analysis was performed for a range of Reynolds numbers and different streamwise and transverse distances between cylinders. The WIV amplitudes and forces were collected for the downstream cylinder and processed to obtain the amplitude of vibration, lift coefficient, force-displacement phase angle and the WIV power coefficient. These results were used to analyse the effect of the chosen cross-sections and is presented in Chapters 3 and 4 of this dissertation.

The concept of temporal energy concentration is introduced first, where many cross-sections are investigated using Numerical methods and water channel experiments with Particle Image Velocimetry (PIV) methods. Next, a WIV system is investigated to ascertain the improvement in power that some upstream bluff-body cross-sections provide. Finally, systematic analysis of the mass and damping ratio is performed for a WIV system with interest on the power generating

potential. Thus, the outcome of this work highlight the most favourable conditions out of the factors tested are reported and explained in this thesis.

1.2 Methods of investigation

The temporal energy concentration of bluff bodies and realisation of a WIV system that surpasses current standards is achieved using laboratory-scale numerical and experimental approaches. Numerical methods were implemented by employing the three-dimensional form of the Navier-Stokes equations in the pressure-based solver of ANSYS FLUENT v17.1. The results were used to analyse the temporal concentration arising from a circular cylinder as well as other cross-sections which are of interest in this project. Experiments were conducted in a closed-loop water channel at the University of Adelaide and the structural parameters (mass and damping ratio) were imposed on the downstream cylinder using a Virtual-Mass-Spring-Damper (VMSD) system. The VMSD system has the advantage of being able to alter the impedance of the system via the control system, rather than use physical springs and dampers. The VMSD system also negates friction and is able to simulate the WIV phenomenon in a controlled environment. The temporal concentration of flow energy as well as the structures in the wake of the cylinders was visualised using Particle Image Velocimetry (PIV) apparatus. These investigations have confirmed the numerical results as well as provided estimates of the power density of WIV technology, in order for meaningful comparisons of the effect of parameters on the power coefficient of WIV.

Further experimental investigations into the mass and damping ratios of the system were performed using the VMSD system to impose virtual mass and damping ratios on the system.

1.3 Objectives of this research

This dissertation emerges at a time of dwindling fossil fuel resources and the threat of their continued use contributing to further degradation of the world climate. Hence, research into alternative energy technology and in particular hydrokinetic energy is at focus in this study. In particular, this study aims to improve VIV and WIV technologies to harness useful, clean and abundant hydrokinetic energy in slow water streams. However, VIV and WIV are not without their own limitations. VIV only generates large amplitude oscillations in the synchronisation range where there is frequency matching between the periodic fluid forces on the cylinder and the natural frequency imposed by the supporting elastic structure. However, this is not present in WIV, which has a characteristically increasing amplitude with increasing free stream velocity, similar to galloping of some bluff bodies. The application of WIV for energy generation is still a relatively novel and new field which has sparked exciting progression over the last decade, with still much improvement possible to increase the energy extraction efficiencies. The focus has been on cross-section and placement of the downstream and vibrating body, as well as the Reynolds number. However, little work has been accomplished on the effect of varying the cross-section of the upstream stationary body and optimisation of the structural properties of the system to improve the WIV response.

Consequently, the aim of this project is to develop an understanding of the parameters affecting the power coefficient of a WIV system, and was achieved by completing the following objectives:

1. Develop an understanding of the spatial and temporal energy distribution in the wake of a circular cylinder using

Computational Fluid Dynamics modelling as well as Particle Image Velocimetry in water channel experiments.

2. Investigate the effect of the cross-section of the stationary upstream bluff body to identify a cross-section which can augment temporal energy concentration better than the current standard circular cylinder bluff body.
3. Develop an understanding of the effect of mass ratios on the power coefficient of a WIV system.
4. Investigate the effect of damping ratios on the system and develop an understanding of how the damping ratio affects the efficiency of a WIV system.

1.4 Structure of the Thesis

This thesis has been divided into 7 chapters. Chapter 1 and 2 present the Background and Introduction, and the Review of Literature, respectively. Chapters 3 to 6 comprise of the manuscripts that have been/are being published from this research project. The Summary, Conclusions and Future Work are given in Chapter 7. The details of the chapters' content are listed here below:

- Chapter 1 – presents the Background and Introduction to this project. A brief review of the background literature pertaining to Flow Induced Vibration is followed by the aim and objectives set out for this work.
- Chapter 2 – contains an exhaustive review of the literature on the topics of Vortex and Wake Induced Vibration, which highlight the gaps pursued in this work.
- Chapter 3 – focuses on the temporal concentration of flow energy by the circular cylinder using numerical methods and a comparison between the circular cylinder and other chosen cross-

sections. The spatial and temporal concentration of flow energy by a circular cylinder was defined and numerical data were generated to analyse the locations and frequencies of temporal energy. Further numerical tests were performed to develop understanding on the effect of the cross-section of the upstream body on the temporally concentrated flow energy.

- Chapter 4 – presents experimental analysis, using PIV, of four cross-sections used to identify the most suitable cross-section for use in a WIV system.
- Chapter 5 – presents an experimental investigation of a WIV system using different upstream cross-sections to explore the effect of downstream cylinder spacing and Reynolds number on the efficiency of the WIV system.
- Chapter 6 – contains the effect of structural properties on the chosen WIV system.
- Chapter 7 – contains a summary of the outputs, the outcomes derived from this work and recommendations for future work.

1.5 Publications

[1.] **Manickam Sureshkumar, E**, Arjomandi, M, Cazzolato, B.S, Dally, B.B, 'Spatial and temporal concentration of hydrokinetic energy in the wake of a bluff body', *Journal of Ocean Engineering*, no. 164, pp. 181-189.

[2.] **Manickam Sureshkumar, E**, Arjomandi, M, Dally, B.B, Cazzolato, B.S, Ghayesh, M.H, 'Energy Concentration by Bluff Bodies - a Particle Image Velocimetry Investigation', *ASME Journal of Fluids Engineering*, accepted

[3.] **Manickam Sureshkumar, E**, Arjomandi, M, Dally, B.B, Cazzolato, B.S, Ghayesh, M.H, 'Effect of the upstream bluff body

shape on the efficiency of a WIV system', *Journal of Applied Energy,* under review

[4.] **Manickam Sureshkumar, E**, Arjomandi, M, Dally, B.B, Cazzolato, B.S, Ghayesh, M.H, 'Effect of mass and damping ratio on a circular cylinder vibrating in the wake of a semi-circular cylinder', *Journal of Fluids and Structures,* under review

References

Assi, GRS 2009, 'Mechanisms for flow-induced vibration of interfering bluff bodies', Ph.D thesis, Imperial College London.

Assi, GRS, Bearman, PW, Kitney, N & Tognarelli, MA 2010, 'Suppression of wake-induced vibration of tandem cylinders with free-to-rotate control plates', *Journal of Fluids and Structures*, vol. 26, no. 7, pp. 1045-57.

Assi, GRS, Meneghini, JR, Aranha, JAP, Bearman, PW & Casaprima, E 2006, 'Experimental investigation of flow-induced vibration interference between two circular cylinders', *Journal of Fluids and Structures*, vol. 22, no. 6, pp. 819-27.

Batten, W, Bahaj, A, Molland, A & Chaplin, J 2006, 'Hydrodynamics of marine current turbines', *Renewable Energy*, vol. 31, no. 2, pp. 249-56.

Bearman, PW 1984, 'Vortex shedding from oscillating bluff bodies', *Annual Review of Fluid Mechanics*, vol. 16, no. 1, pp. 195-222.

Bearman, PW 2011, 'Circular cylinder wakes and vortex-induced vibrations', *Journal of Fluids and Structures*, vol. 27, no. 5, pp. 648-58.

Bernitsas, MM, Ben-Simon, Y, Raghavan, K & Garcia, EM 2009, 'The VIVACE converter: model tests at high damping and Reynolds number around 105', *Journal of Offshore Mechanics and Arctic Engineering*, vol. 131, no. 1, pp. 1 - 15.

Bernitsas, MM & Raghavan, K 2004, 'Converter of current/tide/wave energy', *Provisional Patent Application, US Patent and Trademark Office Serial*, no. 60/628,252.

Bernitsas, MM, Raghavan, K, Ben-Simon, Y & Garcia, EM 2008, 'VIVACE (vortex induced vibration aquatic clean energy): A new concept in generation of clean and renewable energy from fluid flow', *Journal of Offshore Mechanics and Arctic Engineering*, vol. 130, no. 4, pp. 1697–712.

Blevins, RD 1997, *Flow-induced vibration*, Second edn, Van Nostrand Reinhold, New York

Carmo, BS, Sherwin, SJ, Bearman, PW & Willden, RHJ 2011, 'Flow-induced vibration of a circular cylinder subjected to wake interference at low Reynolds number', *Journal of Fluids and Structures*, vol. 27, no. 4, pp. 503-22.

USDE 2010, *Marine and hydrokinetic energy development technical support and general environmental studies*, by Copping, AE & Geerlofs, SH, Pacific Northwest National Laboratory

Derakhshandeh, JF, Arjomandi, M, Cazzolato, B & Dally, B 2014, 'Experimental and computational investigation of wake induced vibration', paper presented to 19th Australasian Fluid Mechanics Conference, Melbourne, Australia, 8 - 11 December 2014.

Derakhshandeh, JF, Arjomandi, M, Dally, B & Cazzolato, B 2015a, 'Harnessing Hydro-Kinetic energy from wake induced vibration using virtual mass spring damper system', *Journal of Ocean Engineering*, vol. 108, pp. 115-28.

Derakhshandeh, JF, Arjomandi, M, Dally, B & Cazzolato, B 2015b, 'A study of the Vortex-Induced Vibration mechanism for harnessing hydrokinetic energy of eddies using a single cylinder', *Journal of Applied Mathematical Modelling*.

Edwards, K & Mekhiche, M 2014, 'Ocean Power Technologies Powerbuoy®: System-Level Design, Development and Validation Methodology'.

Foufoula-Georgiou, E, Guala, M & Sotiropoulos, F 2012, 'Marine-hydrokinetic energy and the environment: Observations, modeling, and basic processes', *Eos, Transactions American Geophysical Union*, vol. 93, no. 10, pp. 111-.

Govardhan, R & Williamson, CHK 2000, 'Modes of vortex formation and frequency response of a freely vibrating cylinder', *Journal of Fluid Mechanics*, vol. 420, pp. 85-130.

Govardhan, R & Williamson, CHK 2004, 'Critical mass in vortex-induced vibration of a cylinder', *European Journal of Mechanics-B/Fluids*, vol. 23, no. 1, pp. 17-27.

Heath, T 2012, 'A review of oscillating water columns', *Philosophical Transactions of the Royal Society of London A: Mathematical, Physical and Engineering Sciences*, vol. 370, no. 1959, pp. 235-45.

Henderson, R 2006, 'Design, simulation, and testing of a novel hydraulic power take-off system for the Pelamis wave energy converter', *Renewable Energy*, vol. 31, no. 2, pp. 271-83.

Hobbs, WB & Hu, DL 2012, 'Tree-inspired piezoelectric energy harvesting', *Journal of Fluids and Structures*, vol. 28, pp. 103-14.

Jauvtis, N & Williamson, C 2004, 'The effect of two degrees of freedom on vortex-induced vibration at low mass and damping', *Journal of Fluid Mechanics*, vol. 509, pp. 23-62.

Johnson, JB & Pride, DJ 2010, *River, tidal, and ocean current hydrokinetic energy technologies: Status and future opportunities in Alaska*, Alaska Center for Energy and Power, viewed 17.11.2015, <http://www.uaf.edu/files/acep/2010_11_1_State_of_the_Art_Hydrokinetic_Final.pdf>.

Khalak, A & Williamson, CHK 1997, 'Investigation of relative effects of mass and damping in vortex-induced vibration of a circular cylinder', *Journal of Wind Engineering and Industrial Aerodynamics*, vol. 69, pp. 341-50.

Khan, M, Bhuyan, G, Iqbal, M & Quaicoe, J 2009, 'Hydrokinetic energy conversion systems and assessment of horizontal and vertical axis turbines for river and tidal applications: A technology status review', *Applied Energy*, vol. 86, no. 10, pp. 1823-35.

Kleijn, R, Van der Voet, E, Kramer, GJ, Van Oers, L & Van der Giesen, C 2011, 'Metal requirements of low-carbon power generation', *Energy*, vol. 36, no. 9, pp. 5640-8.

Lagoun, M, Benalia, A & Benbouzid, M 2010, 'Ocean wave converters: State of the art and current status', in *Energy Conference and Exhibition (EnergyCon), 2010 IEEE International*, pp. 636-41.

Letcher, TM 2013, *Future energy: Improved, sustainable and clean options for our planet*, Elsevier.

Oki, T & Kanae, S 2006, 'Global hydrological cycles and world water resources', *Science*, vol. 313, no. 5790, pp. 1068-72.

Peng, Z & Zhu, Q 2009, 'Energy harvesting through flow-induced oscillations of a foil', *Physics of Fluids*, vol. 21, no. 12, p. 123602.

Thorpe, T 2002, 'Harvesting the waves', *Ingenia, issue13, Royal Academy of Engineering, UK*.

Wang, D-A & Ko, H-H 2010, 'Piezoelectric energy harvesting from flow-induced vibration', *Journal of Micromechanics and Microengineering*, vol. 20, no. 2, p. 025019.

Weinstein, LA, Cacan, MR, So, PM & Wright, PK 2012, 'Vortex shedding induced energy harvesting from piezoelectric materials in heating, ventilation and air conditioning flows', *Smart Materials and Structures*, vol. 21, no. 4, p. 045003.

Yuce, MI & Muratoglu, A 2015, 'Hydrokinetic energy conversion systems: A technology status review', *Renewable and Sustainable Energy Reviews*, vol. 43, pp. 72-82.

Zhu, Q 2011, 'Optimal frequency for flow energy harvesting of a flapping foil', *Journal of Fluid Mechanics*, vol. 675, pp. 495-517.

Chapter 2. Review of literature

A comprehensive review of the literature that is applicable to the research presented in this thesis has been undertaken. First, the background on vortex shedding and resulting fluid structure interactions is first presented, followed by reviews of literature examining Vortex Induced Vibration, VIV and Wake Induced Vibration, WIV, and finally the state-of-art of WIV energy technology is presented.

2.1 Vortex shedding and Flow Induced Vibrations (FIV) of bluff bodies

First documented by Leonardo da Vinci, vortex shedding (Figure 2.1) has been a known phenomenon since the 16th century. However, it was not until the 20th century where the importance of vortex shedding, and associated dynamics were realised and explored. The last century was crucial in understanding the mechanisms behind vortex shedding and fluid structure interactions (Sarpkaya 1979; Tritton 1959; Williamson & Govardhan 2004b; Williamson & Roshko 1988; Zdravkovich 1977). The phenomenon of vortex shedding primarily gained interest to mitigate the fluid structure interactions which leads to vibrations in engineered structures such as buildings, pipelines, power lines and bridges. Whilst a century of research exists on vortex shedding from bluff bodies, deriving useful energy from Flow Induced Vibration, FIV is relatively novel and warrants further investigation.

Figure 2.1 - Dye-based flow visualisation of a vortex street in the wake of a cylinder (Karch et al. 2012).

Fluid structure interactions of a bluff body in an external cross-flow imposes forces on the body and supporting structure (Parkinson & Dicker 1971). This usually results in Flow Induced Vibrations (FIV) which could be Vortex Induced Vibrations (VIV), Wake Induced Vibrations (WIV), galloping or flutter. Galloping is characteristic of non-circular bluff bodies and occurs when the body has one-degree of freedom in a cross-flow. More detailed information about galloping can be found in extant literature (Blevins 1997; Bokaian & Geoola 1984; Parkinson 1989). Vortex and wake induced vibrations are motions induced on the body due to forces emanating from conditions downstream of the body (Assi 2009).

Periodic shedding of vortices from a bluff body induces cyclic forces on the body. When the frequency of these forces are close to the natural frequency of the body, large amplitude vibrations may occur leading to VIV (Williamson & Govardhan 2004b). VIV is mostly associated with the lock-in phenomenon, where the shedding frequency of vortices and the natural frequency are synchronised, leading to resonant behaviour in structures. Hence, undesirable synchronisation has been known to lead to disastrous failures in large engineered structures. The phenomenon becomes more complicated when one or more bodies reside in the wake of an upstream body. The vortices shed from the first (upstream) body can affect or impinge upon the second body (downstream), affecting the vortex shedding of the downstream cylinder (Assi 2009). Wake Induced Vibration (WIV), also sometimes referred to as wake induced galloping, is a phenomenon that occurs when a body lies in the wake interference region of another and hence undergoes oscillations (Assi *et al.* 2010; Derakhshandeh, Arjomandi, Cazzolato, *et al.* 2014). WIV has been referred to as 'galloping' in many

publications due to its similarity with classical galloping of non-circular bluff bodies. WIV is not caused by fluid-dynamic instabilities of the bluff body cross-section, but rather by the unstable flow field caused by the vortices in the wake of the upstream body. VIV of a pair of cylinders is considered WIV, since the dynamic response of the downstream cylinder is affected by the wake of the upstream bluff body. However, WIV has been known to sustain large amplitude vibrations outside the synchronisation range between the natural frequency of the structure and the vortex shedding frequency. Some key differences between VIV and WIV are:

- VIV can occur in either a single bluff body or a pair of bluff bodies, but WIV has to have two or more bodies (Parkinson 1989);
- VIV only occurs for a synchronization range within which the natural frequency of the system is in phase with the vortex shedding. However, WIV does not have a synchronization range. (Assi & Bearman 2015). Figure 2.2 depicts the VIV and WIV response of a circular cylinder, where the VIV response decreases after a Reynolds number (*Re*) of 10,000, but the WIV response is still present at *Re* = 14,000;
- WIV exhibits increasing amplitudes with no known upper limit, while VIV has an upper limit observed within the synchronization range (Figure 2.2);
- The WIV response of a cylinder operating in the wake of another has been shown to be inversely proportional to the mass ratio (Assi 2009), whereas VIV can occur for high and low mass ratios.

There are two categories of VIV; namely fluid oscillators and body oscillators (Naudascher & Rockwell 2012). An oscillator is a system of either a fluidic mass or body which is under the effect of restoring

forces when it is displaced from an equilibrium position. A body oscillator is employed in this study and consists of an elastically mounted circular cylinder constrained to move in the transverse direction.

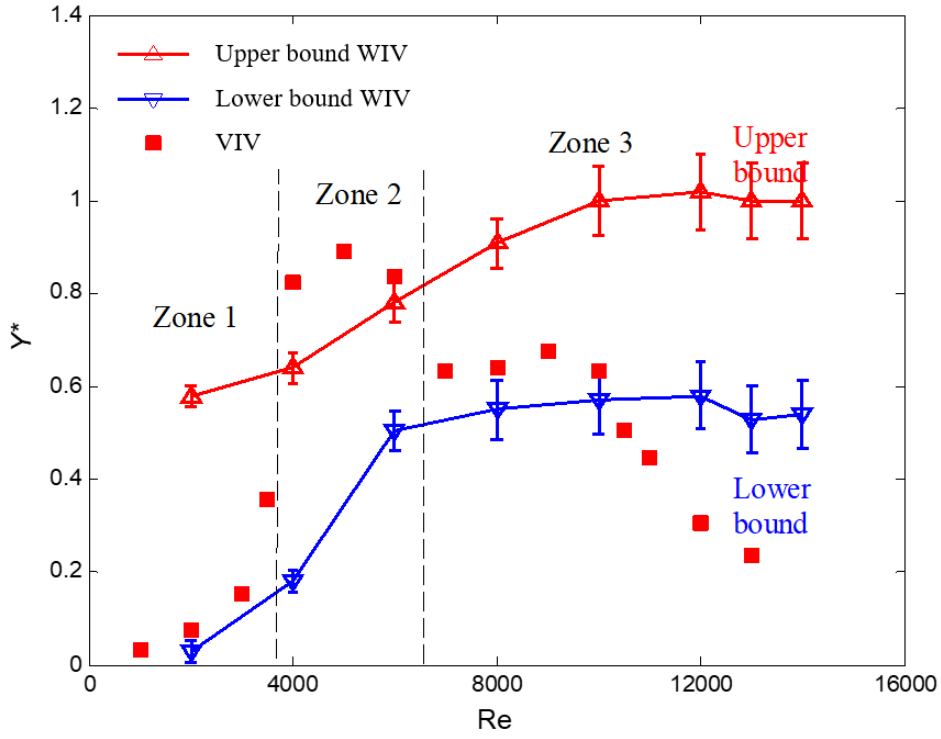

Figure 2.2 – Normalised amplitude response of a circular cylinder undergoing VIV (scatter points) and the upper and lower bounds (red and blue lines, respectively) of WIV of the downstream cylinder in a WIV system (mass ratio = 2.4, damping ratio = 0.01) comprising of cylinders of the same diameter (Derakhshandeh et al. 2015b).

2.2 Flow around a cylinder

The circular cylinder is the most commonly employed bluff body for FIV studies, due to its axisymmetric geometry. Hence a brief explanation of the flow around a circular cylinder is explored in this section.

Flow over a circular cylinder has been classified under many different regimes according to the location in the wake where flow transitions from being laminar to being turbulent. Properties such as the mode of vortex shedding, Strouhal number, and drag coefficient depend

on the flow regime. The Strouhal number is approximately 0.2 within the Transition in Shear Layers regime (TrSL - Reynolds numbers from 350 to 100,000) as depicted in Figure 2.3.

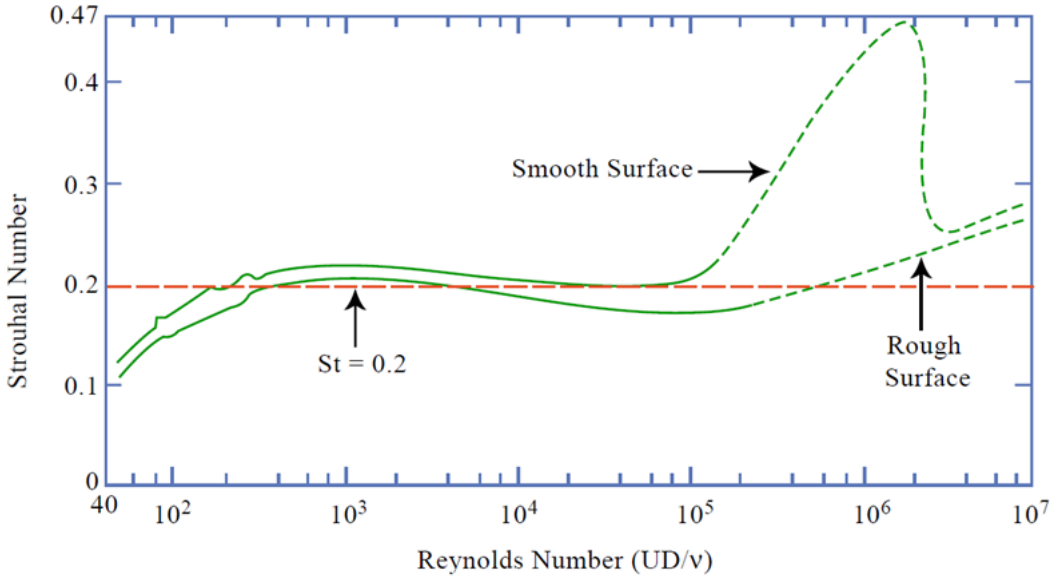

Figure 2.3 - Strouhal number vs Reynolds number for a circular cylinder (Blevins 1990)

The formation of the vortex street arises due to the interaction between the two free shear layers produced on the surface of the cylinder, which contain oppositely signed vorticity. Entrainment of fluid in the formation region is the main cause of the interaction of the shear layers which produces clouds of periodic vorticity (Gerrard 1966). Hence the vorticity in each eddy is only a fraction of that in the shear layers (Roshko 1954). The fraction of circulation that remains in the vortex street of a circular cylinder was numerically estimated to be 43% of the circulation produced in the shear layers by Roshko (1954) for Reynolds numbers between 800 and 15000. Fage and Johansen (1927) estimated that 60% of the produced vorticity remains in the vortices for flat plates (Re = 200000), and a study by Gerrard (1966) estimated a fraction of only 20% - 30% remained in the wakes of circular cylinders (Re = 20000).

2.3 Experimental investigations in the wake of a cylinder

Very few experimental investigations in the wake of a cylinder have hot-wire anemometry measurements at high Reynolds numbers, owing to the recirculation zone and instantaneous flow angles in the near wake of the cylinder. Undeterred by these experimental complexities, velocity and vorticity vectors were measured using a wire probe by Ong and Wallace (1996); and Rajagopalan and Antonia (2005) performed power spectrum analysis using hot wire anemometry measurements.

Probe flow measurements may be overcome using non-invasive techniques such as Particle Image Velocimetry (PIV) or Laser Doppler Velocimetry (LDV). Time-resolved measurements were performed by Lourenco and Shih (1993) at a Reynolds number of 3900, and these data have been used to validate many numerical simulations. A higher Reynolds number range of 1,000 – 10,000 was used by Lin *et al.* (1995) to investigate the velocity and vorticity in the wake of a circular cylinder and the instantaneous streamlines and velocity fields obtained from their study is shown in Figure 2.4.

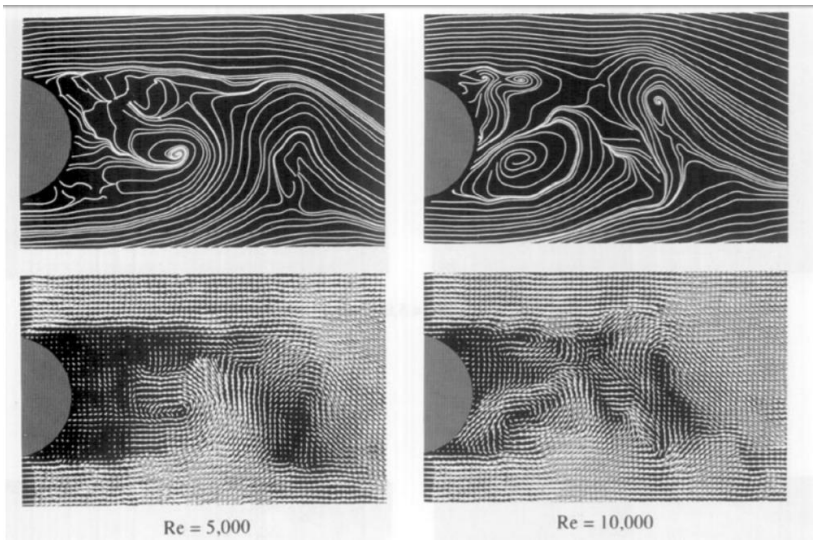

Figure 2.4 - Representative instantaneous streamlines (top row) and instantaneous velocity fields (bottom) at two values of Reynolds number (Lin et al. 1995)

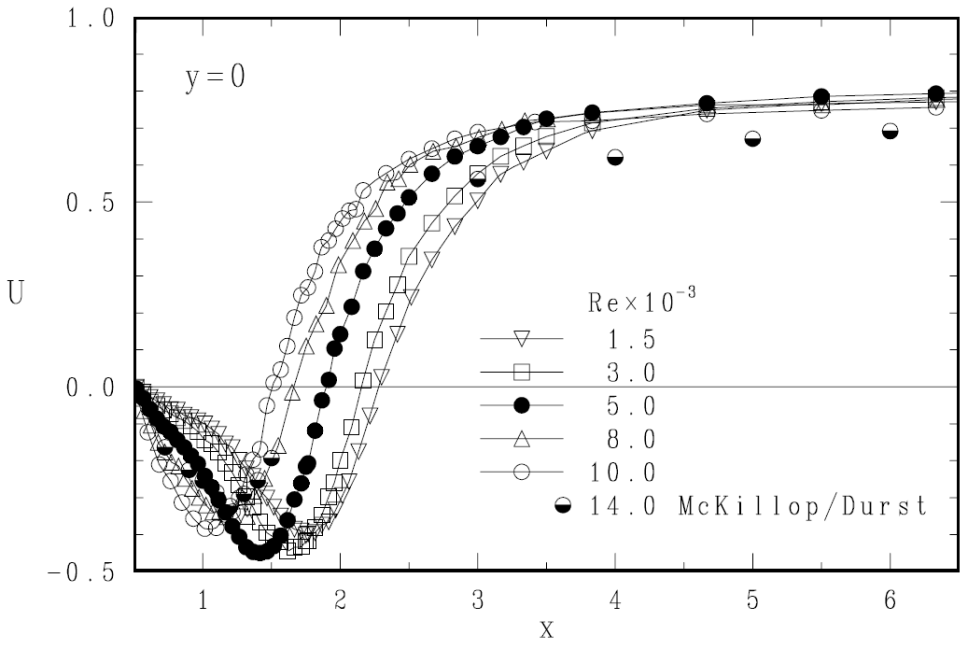

Figure 2.5 - Mean streamwise velocity (normalised using freestream velocity) along the wake centreline of a circular cylinder for Re = 1,500 – 14,000 (Norberg 1998).

Norberg (1998) used LDV to obtain streamwise and transverse turbulence statistics in the near wake of cylinders at a Reynolds number range of 1,500 - 10,000 using a commercial fibre-optic LDV system. The data was then used to identify length scales and location of extrema, as well as the statistical moments for the streamwise and transverse velocity components. The mean streamwise velocity results along the wake centreline of a circular cylinder obtained by Norberg (1998) are depicted in Figure 2.5, where the wake recovery is demonstrated to be faster at higher Reynolds numbers. Ozgoren *et al.* (2011) used PIV techniques, at Re = 5,000 and 10,000, to obtain velocity vectors and compare the flow structures between a sphere and a circular cylinder using a PIV setup with a resolution of 1600 x 1186 pixels and an interrogation window of 32x32 pixels with 50% overlap. Work by Ozgoren *et al.* (2011) resulted in velocity and vorticity vectors as well as the turbulent kinetic energy (Figure 2.6) and other turbulence quantities.

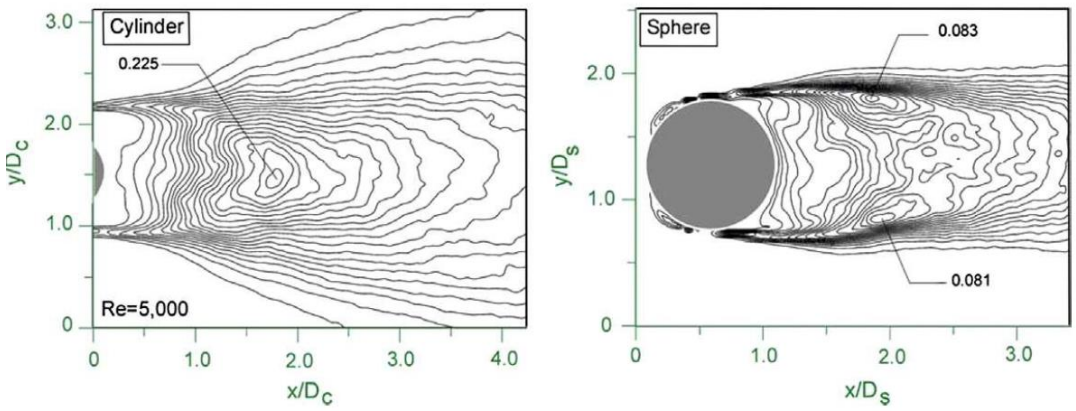

Figure 2.6 - Comparison of normalised turbulent kinetic energy (TKE) distribution in the wake of a cylinder and sphere at Re = 5,000. Minimal and incremental values of TKE for the cylinder and sphere are 0.02 and 0.005, respectively (Ozgoren et al. 2011).

A comparison between PIV and Direct Numerical Simulation in the cylinder wake was published by Dong *et al.* (2006) using a PIV plane measuring 96.8 x 98.8 mm and an interrogation window size of 32 x 32 pixels. They performed investigations at a Reynolds number of 3,900/4,000 as well as at 10,000 to obtain isocontours of the mean and root mean square (r.m.s) streamwise velocity. The flow characteristics behind a circular cylinder have been extensively reviewed in extant literature using PIV and probe techniques to provide results such as Reynolds stresses and Turbulent Kinetic Energy (TKE). However, a comparison of the energy content in the wake between the circle and different bluff bodies has yet to be completed. Knowing the difference in wakes produced by different cross-sections could lead to a better understanding of the flow regimes associated with the vibrating bluff body in a WIV system.

2.4 Energy in the flow: A first principles perspective

A fluid flow can have a combination of kinetic, pressure and thermal energy. The following section contains a fundamental understanding of the energy and mass balance that exists for a control volume.

Consider a control volume with only one steady flow inlet and outlet. Such a system will adhere to the mass balance equation where the time rate of change of mass contained within the control volume at a specific time (t) is the difference between the time rate of flow of mass of fluid entering the control volume at time, t, and the time rate of flow of mass out across the exit at time, t. The mass balance equation is given in equation 2.1.

$$\frac{dm_{cv}}{dt} = \dot{m}_i - \dot{m}_e \tag{2.1}$$

Where m_{cv} is time rate of change of mass contained within the control volume at time t; $\dot{m}_i$ is time rate of flow of mass across inlet at time t; and $\dot{m}_e$ is time rate of flow of mass across the exit at time t

If the control volume has multiple inlets and exits, the mass balance for the control volume can be expressed as in equation 2.2.

$$\frac{dm_{cv}}{dt} = \sum_{inlets} \dot{m}_i - \sum_{exits} \dot{m}_e \tag{2.2}$$

Assuming that the system is at steady state, the flow rate entering a port of area, A, can be defined in equation 2.3.

$$\dot{m} = \int_A \rho \, V_n \, dA \tag{2.3}$$

For a stream with normal uniform velocity passing through the area, A, the mass flow rate can be defined using equation 2.4.

$$\dot{m} = \rho \, \bar{V} \, A \tag{2.4}$$

Hence a multiport system would have the conservation of mass equation defined in 2.5.

$$\frac{dm_{cv}}{dt} = \sum_{inlets} (\rho \bar{V} A)_i - \sum_{exits} (\rho \bar{V} A)_e \quad (2.5)$$

Energy transfer in the system can occur either via heat transfer or work done in the system. Using the first law of thermodynamics, the energy balance for the control volume is given in equation 2.6. The terms in the equation are defined below.

$$\frac{dE_{cv}}{dt} = \dot{Q} - \dot{W} + \dot{m}_i \left(u_i + \frac{V_i^2}{2} + g\, z_i \right) - \dot{m}_e \left(u_e + \frac{V_e^2}{2} + g\, z_e \right) \quad (2.6)$$

$\dot{Q}$ = net rate of energy transferred in as heat transfer at time t

$\dot{W}$ = net rate of energy transferred out as work at time t

u_i = initial internal energy

u_e = final internal energy

g = acceleration due to gravity

z_i = initial elevation

z_e = final elevation

The work term in this equation represents the net work transfer in the system. However, accounting for the work done in more detail provides more insight in to the problem. There is always work done on or by a control volume when there is net mass flow across the inlets or exits. This work can be split in to the work associated with the fluid pressure (flow work) and the work associated with moving components such as rotating shaft or due to boundary displacement. The work due to fluid flow can be expressed as the product of pressure and normal area through which the fluid flows through, or the product of the fluid

force times the velocity. Hence the work term can be defined using equation 2.7.

$$\dot{W} = \dot{W}_{CV} + \sum_{exits} (p\,\bar{V}\,A)_e - \sum_{inlets} (p\,\bar{V}\,A)_i \tag{2.7}$$

Equation 2.7 can also be expressed in terms of the mass flow rate and specific volume as given below in equation 2.8.

$$\dot{W} = \dot{W}_{CV} + \sum_{exits} (p\,v\,\dot{m})_e - \sum_{inlets} (p\,v\,\dot{m})_i \tag{2.8}$$

Equations 2.6 and 2.8 can be combined to give Equations 2.9 and 2.10 below.

$$\frac{d\dot{E}_{cv}}{dt} = \dot{Q}_{CV} - \dot{W}_{CV} + \sum_{inlets} \dot{m}_i \left(u_i + p_i\,v_i + \frac{V_i^2}{2} + g\,z_i \right) - \sum_{exits} \dot{m}_e \left(u_e + p_e\,v_e + \frac{V_e^2}{2} + g\,z_e \right) \tag{2.9}$$

Which can also be expressed using enthalpy in equation 2.10.

$$\frac{d\dot{E}_{cv}}{dt} = \dot{Q}_{CV} - \dot{W}_{CV} + \sum_{inlets} \dot{m}_i \left(h_i + \frac{V_i^2}{2} + g\,z_i \right) - \sum_{exits} \dot{m}_e \left(h_e + \frac{V_e^2}{2} + g\,z_e \right) \tag{2.10}$$

For a steady state system, $\frac{d\dot{E}_{cv}}{dt} = 0$ and for a closed system, the energy in the system s equal to the sum of the kinetic energy, potential energy and enthalpy of the system.

Therefore, for a system with steady flow, equation 2.10 can be reduced to equation 2.11.

$$\dot{Q}_{CV} - \dot{W}_{CV} + \sum_{inlets} \dot{m}_i \left(h_i + \frac{V_i^2}{2} + g\, z_i \right) - \sum_{exits} \dot{m}_e \left(h_e + \frac{V_e^2}{2} + g\, z_e \right) = 0 \tag{2.11}$$

where $h = u + p\, v$ and $v = 1/\rho$.

For isothermal flow, $u_i = u_e$ and for a system with one inlet and one outlet, we obtain equation 2.12, which is commonly known as the Bernoulli's equation.

$$\left(\frac{p_i}{\rho} + \frac{V_i^2}{2} + g\, z_i \right) - \left(\frac{p_e}{\rho} + \frac{V_e^2}{2} + g\, z_e \right) = 0 \tag{2.12}$$

The Bernoulli's equation is a form of mechanical energy balance (forces integrated over distances) and inherently assumes that the flow is incompressible, frictionless, steady and that the flow occurs along a streamline or stream tube. Therefore, for any two points along a streamline, the Bernoulli equation ca also be expressed as equation 2.13 or 2.14.

$$\frac{p_1}{\rho} + \frac{V_1^2}{2} + g\, z_1 = \frac{p_2}{\rho} + \frac{V_2^2}{2} + g\, z_2 \tag{2.13}$$

$$(p_1 - p_2) + \rho \left(\frac{V_1^2}{2} - \frac{V_2^2}{2} \right) + \rho\, g\, (z_1 - z_2) = 0 \tag{2.14}$$

Where the three terms in equation 2.14, from left to right, are commonly known as the pressure head, velocity head and the elevation head. The kinetic energy in the flow is related to the velocity head and any mention of energy in proceeding sections refers to the kinetic energy in the flow, unless otherwise stated.

2.5 Energy concentration in the wake of bluff bodies

Energy in a flow can be concentrated either by flow concentration (e.g. speed up of the flow), or by energy augmentation (e.g. increase the pressure difference) (Dick 1984). Diffusers are a form of mass concentrators which increase the spatial concentration of energy in a flow by reducing the flow area in front of an energy extractor, or increase the flow area behind the extractor (Deshmukh & Deshmukh 2013). Diffusers are most commonly used as flow energy concentrators and can be found in a lot of industries such as in jet engines and in water turbines, in the form of shrouded axial turbines.

Although diffusers can provide an augmentation factor of about 1.3 (Figueiredo *et al.* 2012), there are a number of downfalls to using diffusers as current energy concentrators. The shroud or duct that makes up the diffuser needs to be large and hence adds cost to the system. In comparison, it is cheaper to increase the size of a wind turbine instead of utilising a diffuser to produce the multiplied power output. The shroud also increases the drag experienced by the structure, and hence require stronger tower and components compared to an unshrouded turbine (Hansen 2013). The maximum power coefficient of an energy extractor in an axial flow is known as the Betz limit (59.3%) (Bergey 1979). However, the Betz limit can be exceeded by using diffusers or other energy concentration systems. A universal ideal energy extraction limit of 8/9 was derived using diffuser theory by Jamieson (2009). This limit was shown to be true for any rotor that is influenced by a system that disturbs the flow field without extracting energy (Jamieson 2009).

Separation of freestream thermal energy has been shown to occur in the wakes of cylinders due to the pressure fluctuations in the vortex street, which causes the temperature fluctuations (Goldstein & Kulkarni

2008). Since the cylinder blocks part of the flow, there is a region of low velocity in the centreline of the near wake. The low centreline velocity slowly recovers to the freestream velocity as the flow progresses downstream.

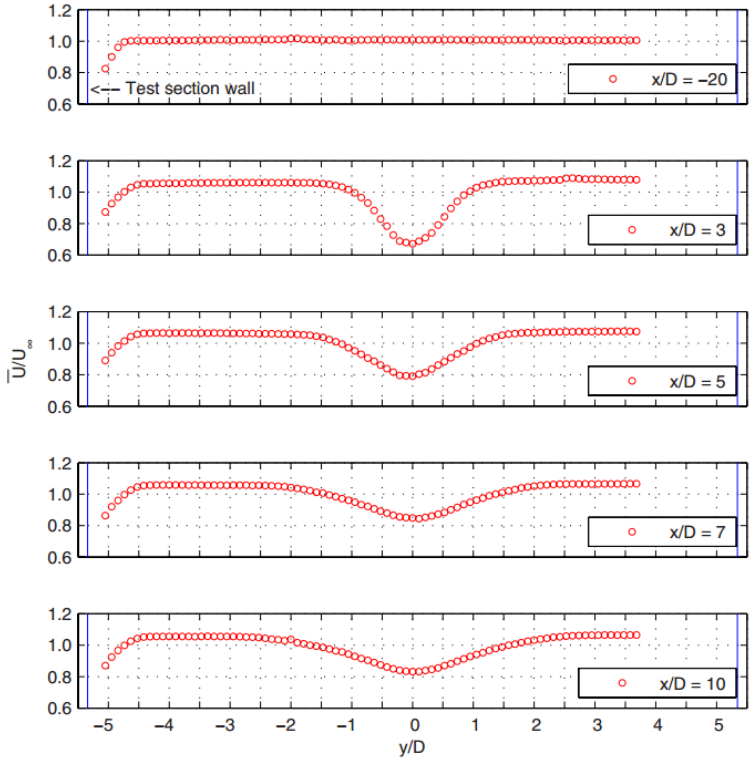

Figure 2.7 - Time-averaged normalised streamwise velocity ($\bar{U}/U_\infty$) profiles for a Reynolds number of 92,000 (Goldstein & Kulkarni 2008), where x/D and y/D are the non-dimensionalised streamwise and transverse distances.

The spatial distribution of dimensionless flow energy (energy in the wake/ energy in the freestream) can be seen in the time-averaged velocity profiles shown in Figure 2.7. Although Figure 2.7 depicts a reduction of freestream energy in the wake of the cylinder, this is a mean result and in practice there would be fluctuations which are dependent on time, leading to a temporal concentration of energy. Depending on the combined spatial and temporal concentrations, there are time dependant peaks of high energy density in the wake as shown in Figure 2.8.

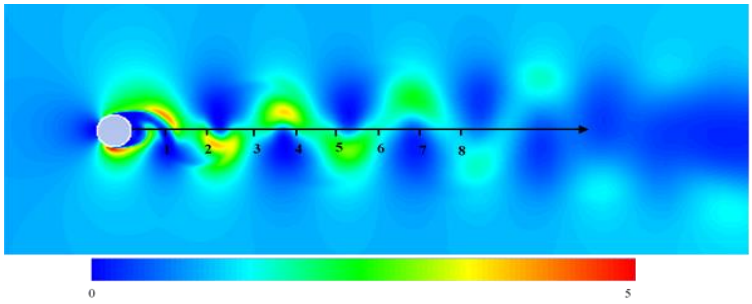

Figure 2.8 - Time dependant contours of dimensionless energy density (energy in the wake/energy in the freestream) for a circular cylinder (Derakhshandeh et al. 2015c)

2.6 Factors that affect VIV and WIV

Flow induced vibrations (FIV) have been investigated for numerous cases such as single, tandem, and staggered cylinders in order to understand and manipulate the phenomenon. Although most studies focused on reducing FIV to increase the life span of engineered structures, their results can be perceived in a manner to increase FIV for energy production purposes. Periodic vortex shedding is associated with corresponding pressure and shear force periodicity on the cylinder, which cause drag and lift forces on the body. The complex interactions between these forces and the structural properties of the elastically mounted rigid body govern the VIV phenomenon (Khalak & Williamson 1997a).

Maximum amplitude vibrations from an oscillating bluff body occur when the reduced velocity is close to but not equal to the inverse of the Strouhal number (i.e., the shedding frequency is almost equal to the natural frequency of the body) (Bearman 1984). Equations that define the reduced velocity and Strouhal number are given in Appendix B. The relationship between the reduced velocity and transverse amplitude of vibration has been characterized in previous studies, where three distinct branches existed for cylinders with low mass and damping (Govardhan & Williamson 2006; Khalak & Williamson 1997a;

Williamson & Govardhan 2004b). The three different response branches within the lock-in range are listed below and are depicted in Figure 2.9 (Assi 2009):

- Initial branch – amplitude of oscillation starts to increase;
- Upper branch – oscillation of maximum amplitude occurring at the resonance peak;
- Lower branch – amplitude of oscillation tends to slowly reduce until the end of the synchronization range where the vibrations cease to exist.

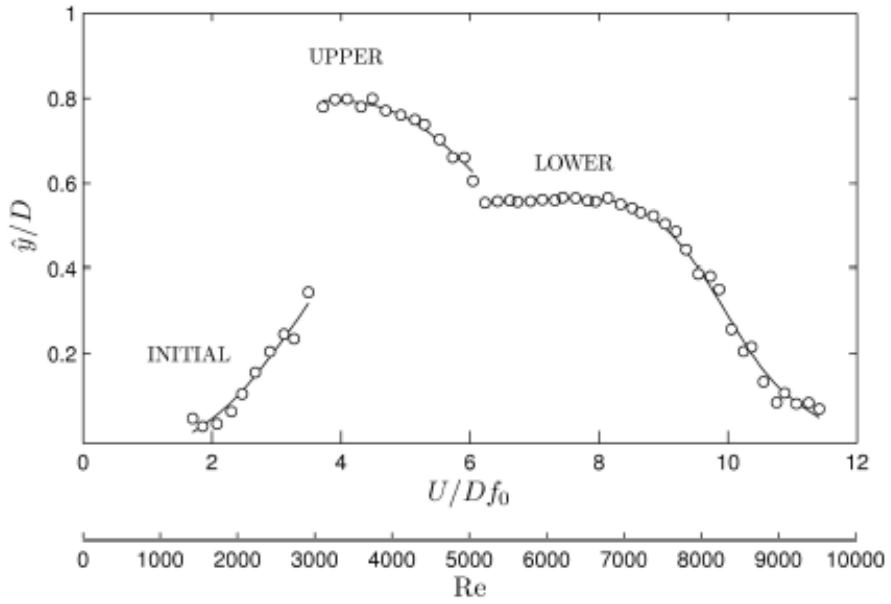

Figure 2.9 - VIV amplitude response vs reduced velocity (U/Df_0) for a single circular cylinder depicting the three branches of oscillation (Assi 2009). ($m^* = 2.4$; $\zeta = 0.01$)

The flow generated around a single oscillating cylinder can exhibit significant differences compared to a fixed cylinder case due to coupling of the flow along the span of the body, which increases the correlation length of the streamwise vortices (Bearman 1984). Hence the frequency of force fluctuations is more uniform along the span of the vibrating cylinder compared to the fixed case.

The effect of separation distance between two tandem cylinders is necessary when trying to optimise FIV configurations for flow energy harnessing. A cylinder in the wake of a fixed rigid cylinder can undergo both VIV and WIV either at separate instances or at the same time, dependant on the separation gap (Bokaian & Geoola 1984). Assi *et al.* (2006) investigated the effect of separation distance between two circular cylinders for Reynolds numbers ranging between 3,000 and 13,000. A continuous increase in the vibration amplitude was observed, instead of distinct branches as in the single cylinder case, due to WIV occurring in conjunction with VIV. Their results indicated that the peak amplitude of transverse oscillations for the downstream cylinder (diameter = D) occurred for a separation gap of $3D$ (Assi *et al.* 2006). An optimum separation gap of $3.5 < x/D < 4.5$, $1 < y/D < 2$ was identified by Derakhshandeh, Arjomandi, Dally, *et al.* (2014). The difference in streamwise gap maybe attributed to the staggered arrangement rather than the in-line arrangement investigated by Assi *et al.* (2006).

Periodic vortex shedding from a circular cylinder does not occur for three ranges of Reynolds numbers in subsonic flow. Bernitsas *et al.* (2008) experimentally identified these Reynolds numbers as $Re < 40$, $150 < Re < 400$, and $30{,}000 < Re < 50{,}000$ where VIV would not occur. These results were obtained for smooth circular cylinders and are also affected by various fluid factors such as the temperature, salinity and viscosity. However, the obtained Reynolds numbers can be generally assumed to hold for most cases. The mass ratio is an influencing parameter on whether the downstream cylinder undergoes a combination of WIV and VIV, or just one of the two. Monotonically increasing amplitudes, a characteristic of WIV "galloping", were not observed for tests carried

out in air tunnels for a high mass ratio (Brika & Laneville 1999), but were observed in the low mass ratio tests performed by Assi *et al.* (2006).

Objects attached to the downstream surface of the cylinder can also affect the VIV response. Drag reduction studies have investigated the use of splitter plates in order to mitigate WIV in structures (Assi *et al.* 2009). Although free-to-rotate plates were shown to supress WIV in circular cylinders (Assi *et al.* 2010), fixed splitter plates of length between 0.5D and 1D resulting in vibration amplitudes of more than 1D. Additionally, the vibrations of a single circular cylinder with fixed splitter plates increased monotonically for the range of Reynolds numbers tested by Assi and Bearman (2015). A study by Ozono (1999) highlighted the dependency of the base pressure coefficient and the Strouhal number, on the transverse separation gap between the wake centreline of a bluff body and a downstream splitter plate. When the plate nears the wake centreline, there is a critical fall in the base suction coefficient causing a reduction in the drag force.

2.7 VIV of a single circular cylinder

The VIV response of cylinders is governed by a multitude of structural and fluidic parameters. The fluidic parameters have been identified in published literature as the Reynolds number, Strouhal number and reduced velocity, whilst the structural parameters include the mass and damping ratio of the system (Hover *et al.* 1997; Huera-Huarte & Bearman 2009; Jauvtis & Williamson 2003, 2004; Sarpkaya 2004; Williamson & Govardhan 2004b). The fluidic and structural parameters are defined in Table 1 with the individual terms described following the table.

Table 1 - Fluidic and Structural parameters that govern VIV

Reynolds number	Re	$\rho UD/\mu$
Strouhal number	St	$f_s D/U$
Reduced velocity	U_r	$U/f_{osc}D$
Mass ratio	m^*	$4M/\rho\pi D^2 L$
Damping ratio	ζ	$c/2\sqrt{kM}$

In Table 1, ρ (kg/m^3) is the density of the fluid, D (m) is the characteristic diameter of the cylinder, U (m/s) is the freestream velocity, f_s (Hz) is the shedding frequency of the vortices, f_{osc} (Hz) is the oscillation frequency of the cylinder, M (kg) is the mass of the oscillating structure, c (Ns/m) is the damping coefficient of the system, and k (N/m) is the spring stiffness in the system.

Understanding and studying the concept of vortex induced vibration necessitates examining the phenomenological aspects of VIV and understanding the effective governing parameters of a single circular cylinder mounted elastically under the influence of a cross-flow. A circular cylinder in cross-flow forces the approaching flow to divert around its cross-section. This causes a stagnation point on the upstream surface and an area of negative back-pressure on the downstream surface of the cylinder. Hence a pressure difference exists between the upstream and downstream faces of the body. The diverting flow also causes shear layers to form on either side of the body. These shear layers progress downstream of the body, where they interact together to form the characteristic vortex street found in the wakes of bluff bodies (Figure 2.10). This process of the vortices being shed periodically from alternate sides of the body causes the pressure field to be cyclical. Integration of the pressure field around the surface of the cylinder calculates the periodic forces acting on the body, which can be derived in to orthogonal

forces of lift and drag, that act on the body in the transverse and streamwise directions, respectively.

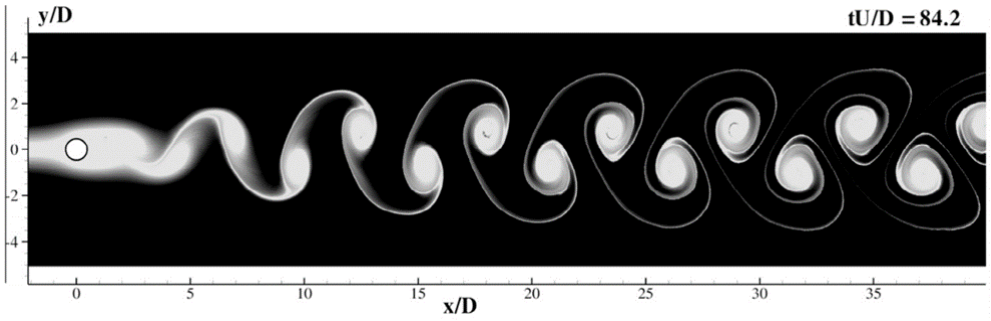

Figure 2.10 - Vortex street behind a circular cylinder (Zdravkovich 1997)

Vortices shed in the wake of a bluff body adhere to a shedding frequency which is mostly dependant on the Reynolds number. The shedding frequency is usually presented in its non-dimensional form as the Strouhal number defined in Table 1. Each cycle of vortex shedding includes a positive and a negative vortex to be shed from respective sides of the cylinder. Hence, the fluctuating lift and drag forces arising from the shed vortices also adhere to the shedding frequency, f_s , where the lift force occurs at f_s and the drag force occurs at $2f_s$ (Bishop & Hassan 1964). On a single cylinder, these forces are harmonic in nature and the vibration response is governed by the degrees-of-freedom that the cylinder can vibrate.

A cylinder that has two degrees of freedom (DOF) can experience the lock-in phenomenon in both the transverse (lift force) or streamwise (drag force) directions. Consequently, the oscillation of the cylinder can vary from small amplitude vibrations at a high frequency to large amplitude vibrations at a lower frequency, depending on the structural parameters (Sarpkaya 2004; Sumer & Fredsøe 2006; Williamson & Govardhan 2004a; Williamson & Roshko 1988). Hence, it is a crucial factor to note for any analysis of the lift force frequency. Although a

cylinder can vibrate in the streamwise and transverse directions with respect to the flow, transverse amplitudes have been shown to be about three times greater than streamwise amplitudes (Bearman 2011). Hence energy production utilising VIV has been mainly focused on cylinders with a single degree of freedom in the transverse direction (Bernitsas *et al.* 2008; Hobbs & Hu 2012; Wang & Ko 2010).

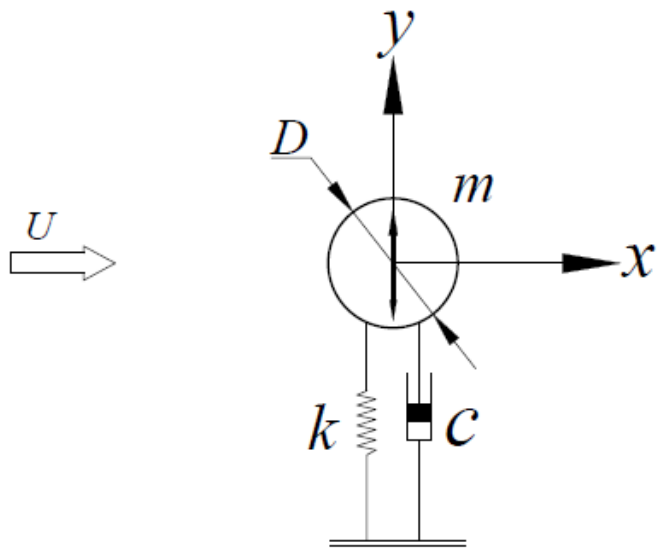

Figure 2.11 – Mass-spring-damper schematic of a 1DOF cylinder mounted elastically in a cross flow.

The harmonic vibration response observed in 1DOF VIV can be approximated as a Mass-Spring-Damper (MSD) system as depicted in Figure 2.11. Such a system was first modelled by Bearman (1984) using the following equation:

$$\ddot{y}(t) + 2\zeta\omega_n\dot{y}(t) + {\omega_n}^2 y(t) = F_y(t)/M, \qquad (2.15)$$

where, y (m), $\dot{y}$ (m/s) and $\ddot{y}$ (m/s^2) are the transverse displacement, velocity and acceleration of the cylinder, respectively. The term ζ represents the damping ratio of the second order system, and $\omega_n = 2\pi f_n$, where f_n (Hz) represents the natural frequency. On the right-hand side of Equation (2.1), F_y (N) and M (kg) are the fluid force

exerted on the cylinder perpendicular to the flow direction, and the effective mass of the system, respectively.

The time dependent transverse displacement and the lift coefficient can be obtained from the following equations by assuming a harmonic response of the cylinder:

$$y(t) = y_{\max}\sin(2\pi f_s t), \tag{2.16}$$

$$c_L(t) = C_L\sin(2\pi f_s\, t + \Phi), \tag{2.17}$$

Note that here $y_{\max}$ is the peak displacement amplitude, c_L and C_L are the time dependent lift coefficient and the peak lift coefficient amplitude, respectively, and Φ (rad) is the force-displacement phase angle, which is vital in the understanding the VIV response of the cylinder, particularly for energy conversion (Bernitsas *et al.* 2009; Bernitsas & Raghavan 2004; Bernitsas *et al.* 2008; Khalak & Williamson 1997a).

Figure 2.12 and Figure 2.13 highlight the differences in force-displacement phase for a circular cylinder undergoing VIV. The vibration amplitude response and the curves of normalised amplitude (y/D) and lift coefficient (C_L) are displayed in Figure 2.12**.** The curves are plotted for reduced velocities of 4.0, 5.7 and 7.9, which correspond to the cylinder undergoing VIV in the upper branch, upper-to-lower branch transition and the lower branch, respectively. As depicted in Figure 2.12, y/D and C_y are approximately in phase (angle close to 0 degrees) in the upper branch ($U_r = 0$), whilst higher reduced velocities result in the phase difference being close to 180 degrees. In addition, the highest lift coefficient and non-dimensional amplitude are observed for the upper branch, with increasing reduced velocity degrading both parameters.

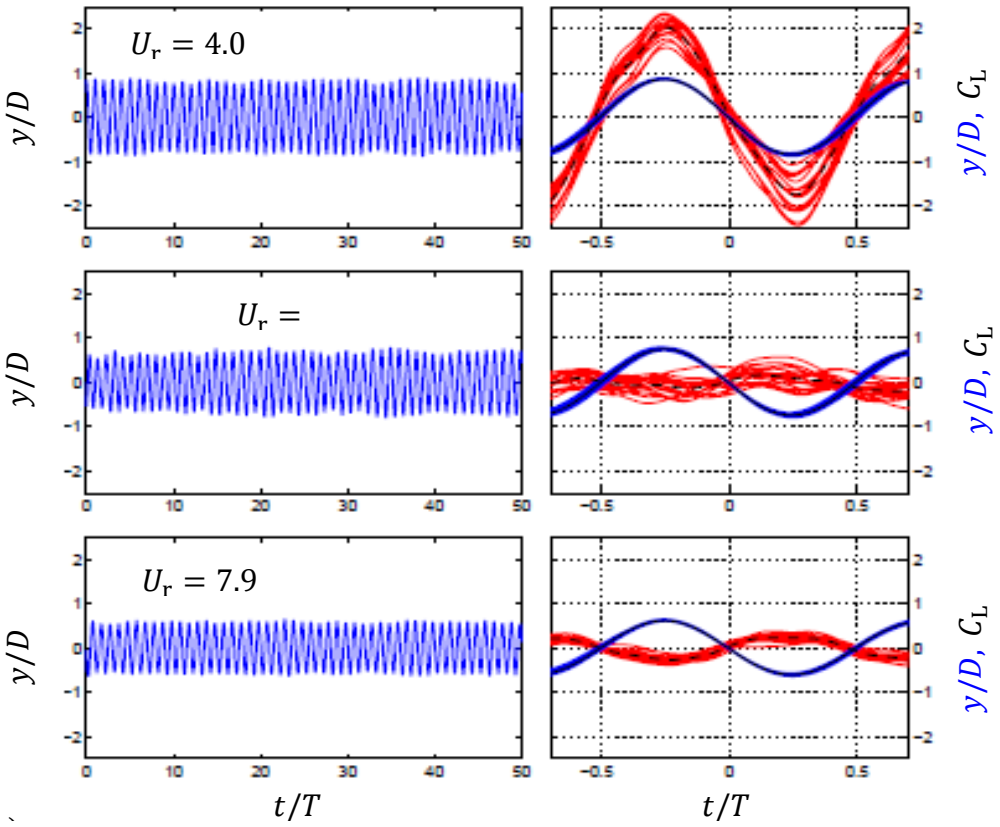

Figure 2.12 - Dynamic response of a circular cylinder under VIV mechanism at three different branches of oscillation. Left column: time histories of displacement. Right column: lift coefficient and displacement over one complete cycle, y/D in blue and C_L in red with average cycle in dash black, at a) $U_r = 4.0$, b) $U_r = 5.7$, and c) $U_r = 7.9$, (Assi 2009).

Figure 2.13 depicts the non-dimensional amplitude response, Power Spectral Density (PSD) of oscillation frequency normalised against the natural frequency of the structure and the force-displacement angles obtained by Assi (2009). The three branches of VIV are clearly depicted in Figure 2.13 a) and associated phase angles in Figure 2.13 c). The upper branch of oscillation occurs at a frequency very close to the natural frequency of the cylinder. Additionally, in-phase and out-of-phase force-displacement phase angles for the upper and lower branch, respectively, are evidenced in this figure.

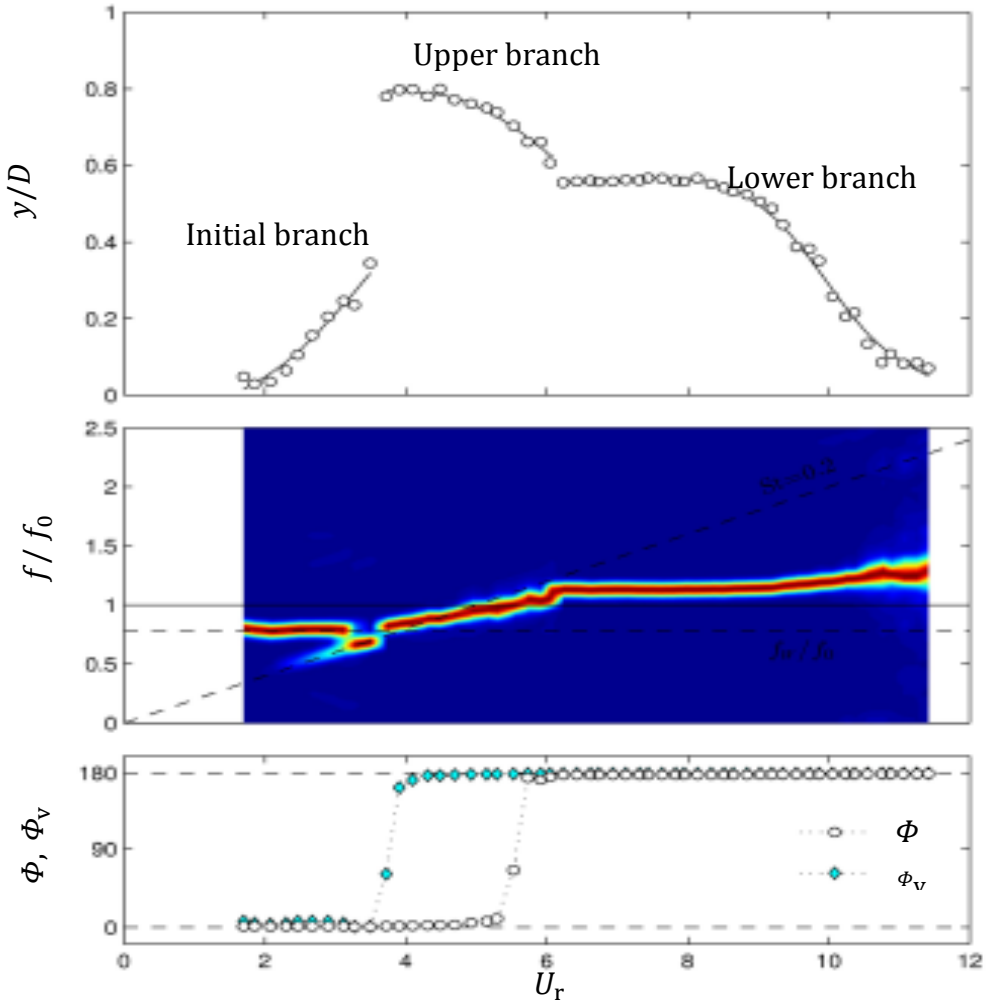

Figure 2.13 - Dynamic response of a single circular cylinder under VIV mechanism, including a) amplitude of oscillation, b) normalised PSD of frequency of oscillation and c) potential and vortex lift phase angles (Assi 2009).

2.8 Vortex structure in the wake of a vibrating cylinder

A fundamental understanding of the vortex dynamics in the wake of a cylinder is necessary for extraction of energy from oncoming vortices in a VIV or WIV system. The vortices from the upstream body concentrate the flow energy spatially and temporally for the downstream body, whilst vortices shed from the downstream body induce forces on the downstream body. This section examines the shear layers and corresponding vortex structure in bluff body wakes, as well as the governing parameters.

Pioneering work that deduced the relationship between vortex shedding and displacement of a self-excited cylinder was performed by Angrilli *et al.* (1972). The experiments in water were conducted for Reynolds numbers ranging from 2,000 to 7,000. It was established that small amplitude vibrations resulted in vortex dynamics very much like vortices shed from a stationary cylinder. In contrast, large amplitude VIV was found to have a pair of discrete vortex paths which must cross each other twice to establish a stable wake configuration.

An investigation in to the force-displacement phase angle was performed using flow visualisation by Zdravkovich (1997). A discontinuous jump of almost 180 degrees was observed at the upper branch of oscillation which coincides with maximum amplitude vibrations in VIV. This phase change in the vortex shedding frequencies near synchronisation is caused by a switch in the timing of vortex shedding (Gu *et al.* 1993; Lu & Dalton 1996).

Investigations into the modes of vortex shedding within the synchronisation range has resulted in identifying two distinct modes of shedding for a single circular cylinder (Angrilli *et al.* 1972; Griffin & Ramberg 1974; Zdravkovich 1982, 1996). When lock-in is first established, vortices are shed from either side of the cylinder as the cylinders is displaced to its maximum endpoint from the equilibrium position. Contrarily, another vortex is formed again on the same side when the cylinder is near its maximum displacement, towards the end of the lock-in range. Additionally, it is argued that these two modes are the limitations of the reduced velocities at which the maximum amplitude of oscillation of the cylinder occurs (Zdravkovich 1982).

A deeper investigation into the regimes of vortex shedding was performed by Williamson and Roshko (1988) via water channel

experiments of a vibrating circular cylinder. The tests were conducted for a range of Reynolds numbers between 300 and 1,000 and resulted in the identification of several vortex shedding regimes being mapped out which were dependant on the non-dimensional amplitude of vibration (y/D) and wavelength ratio ($\lambda/D = U/f\,D$). Williamson and Roshko (1988) found that vortices can be shed in patterns involving single vortices (S mode), or a pair of vortices (P mode) and are dependent on the wave length ratio and the reduced velocity (Figure 2.14). Resultant patterns such as 2S (2 single vortices), 2P (2 pairs of vortices) and 2S+P (a combination of singular and pairs of vortices) were defined by the patterns emerging during a single cycle of vortex shedding.

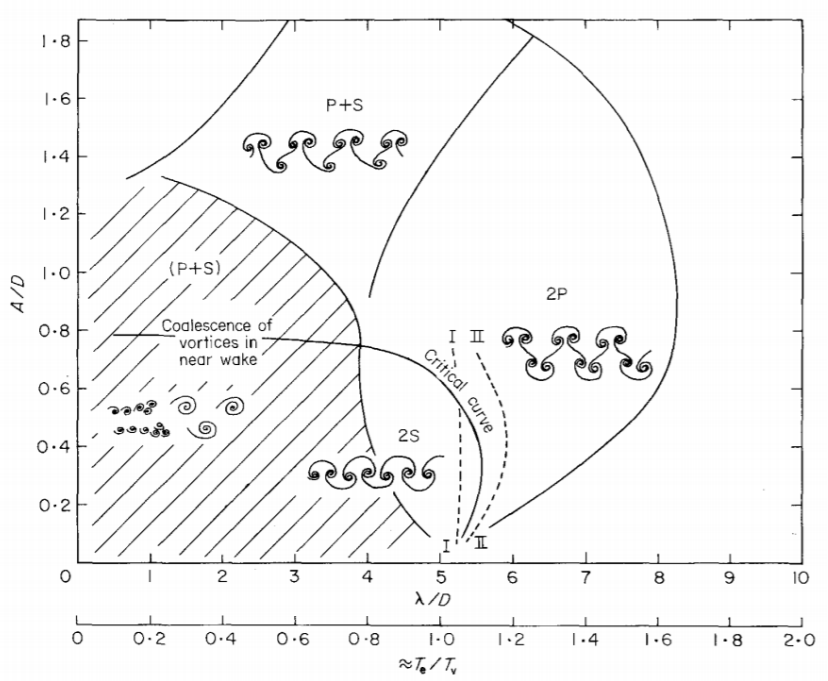

Figure 2.14 - Map of vortex synchronization near the fundamental lock-in. A/D is the amplitude ratio and λ/D is the wavelength ratio (λ = freestream velocity/ frequency of oscillation). The ''critical curve'' represents the transition from one mode of vortex formation to another. Curves I and II represent locations where the forces on the body show a sharp jump (Williamson & Roshko 1988)

Photographs and sketches of the 2S and 2P modes of vortex shedding for a circular cylinder are shown in Figure 2.15 (Brika & Laneville 1993). The 2S mode of vortex shedding is usually generated in the initial branch of oscillation for a limited range of amplitudes

(Bearman *et al.* 1981; Williamson 1985). Contrastingly, the 2P mode, characterized by the two pairs of vortices shed during a cycle of oscillation, appears at the lower branch. The 2P mode also appears in the upper branch, but the second vortex shed from each pair is much weaker than the first one (Pan *et al.* 2007).

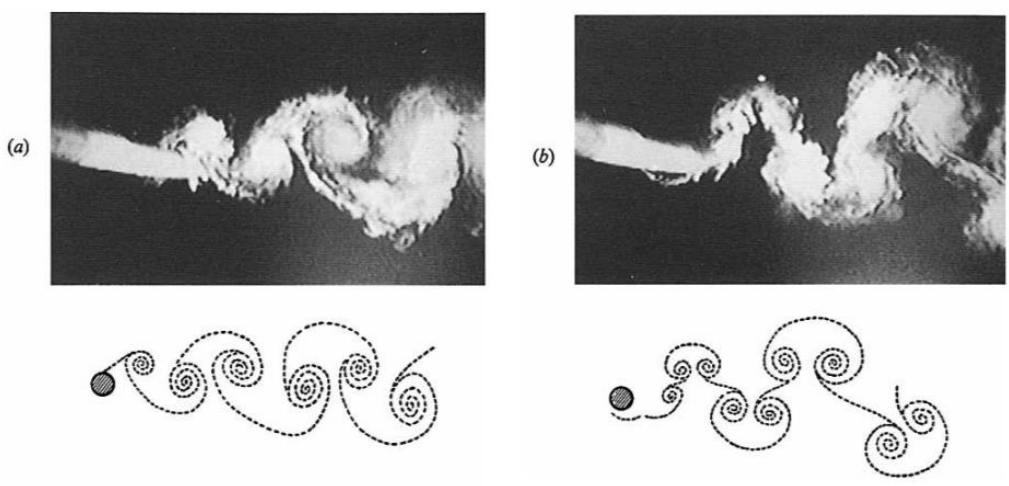

Figure 2.15 - Photographs and sketches showing the two near-wake vortex patterns for a circular cylinder (U = 0.93, Re = 7350) (Brika & Laneville 1993). (a) represents the 2S mode whilst (b) represents the 2P mode of vortex shedding

2.9 Effect of surface roughness

Surface roughness is one of the parameters governing VIV due to its effect on the dynamics of the shear layer formed on the surface of the cylinder. The effect of surface roughness on the flow separation, cylinder surface pressure distribution and Strouhal number was investigated by Nakamura and Tomonari (1982) using wind tunnel tests of a circular cylinder. Surface roughness was varied using strips of different roughness placed on the cylinder, and the effects were investigated between a Reynolds number of 40,000 and 1,700,000. At Reynolds numbers less than 200,000, there is negligible variations in the pressure coefficient and Strouhal number. Contrastingly, increasing Reynolds numbers above 200,000 displays a significant effect on the parameters being considered. This relationship is shown in Figure 2.16 where the

effect of roughness on the Strouhal number is displayed. The data was plotted for normalised roughness of $r/D_p = 0$ (smooth), 9.4 x 10^{-5} and 90 x 10^{-5}, where D_p is the diameter of the roughness particles. Although the results of the authors agreed with previously reported results by Roshko (1961) and Achenbach (1971), Nakamura and Tomonari (1982) limited their experiments to roughness strips placed on the cylinder at an angle of 50° relative to the freestream velocity.

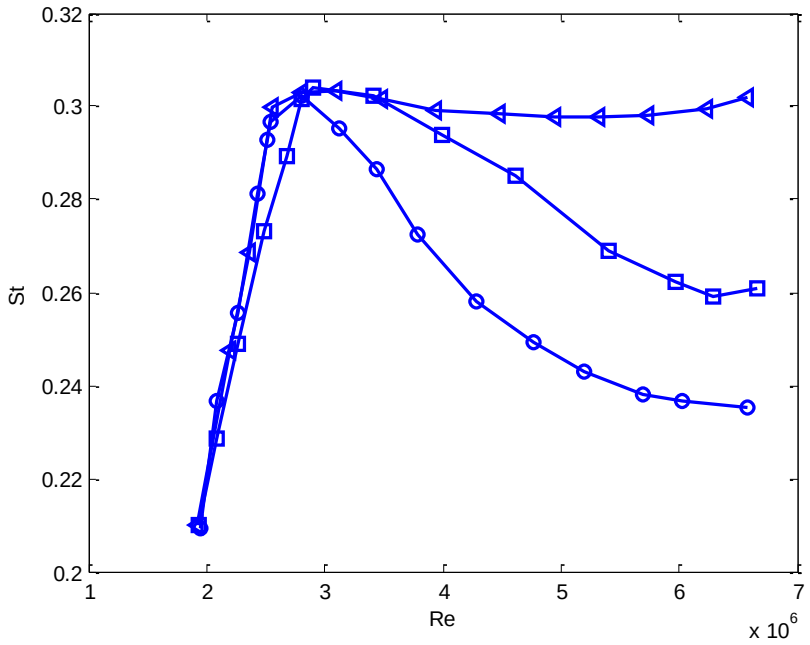

Figure 2.16 – Strouhal number versus Reynolds number for different roughness strips placed at an angle of 50° to the freestream velocity. Curves with triangles are for a smooth surface, squares are for r/D = 9.4 x 10^{-5}, circles are for r/D = 90 x 10^{-5}; where r = diameter of roughness particles and D = diameter of the cylinder (Nakamura & Tomonari 1982).

The position of roughness strips has also shown to affect VIV (Achenbach 1971; Roshko 1961). Chang *et al.* (2011) reported that VIV is supressed when roughness strips are placed at an angle of 64° to the freestream velocity, where the frequency of oscillation also reduces greatly for reduced velocities greater than 7 (Figure 2.17). This effect was due to the dynamics of the shear layer, which separates around 70° for a cylinder. The roughness strips energize the shear layers earlier, which affects their interaction and hence the dynamics of the formed vortices,

since a higher level of diffusion in the shear layer results in weaker vorticity. Chang *et al.* (2011) performed the investigations between a Reynolds number of 30,000 and 120,000, and investigated the surface coverage, roughness height and circumferential location of roughness strips on the cylinder. Additionally, the authors also reported that increasing roughness height resulted in an earlier manifestation of galloping, although the effect on amplitude and frequency of vibration was negligible. The effect of changing the coverage of the strip from 8° to 24° at starting at a location of 40° significantly increases the amplitude response of the cylinder (Figure 2.18). However, a further increase of strip coverage to 32° results in reduction of vibration amplitude. The lower area of coverage caused the shear layers to re-join the surface of the cylinder after separating at the start of the strip, whilst a higher area of coverage caused the shear layers to separate earlier with reduced vorticity. This explains the suppression of VIV at higher coverages.

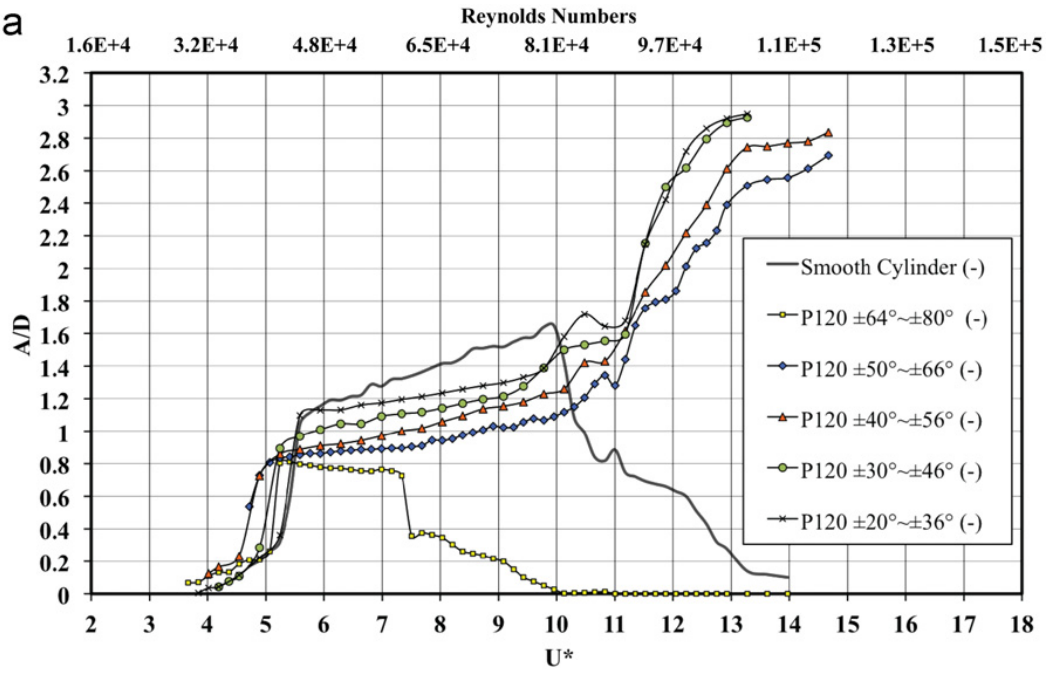

Figure 2.17 – VIV cylinder amplitude versus reduced velocity for different strip locations for P120 roughness. (Chang et al. 2011)

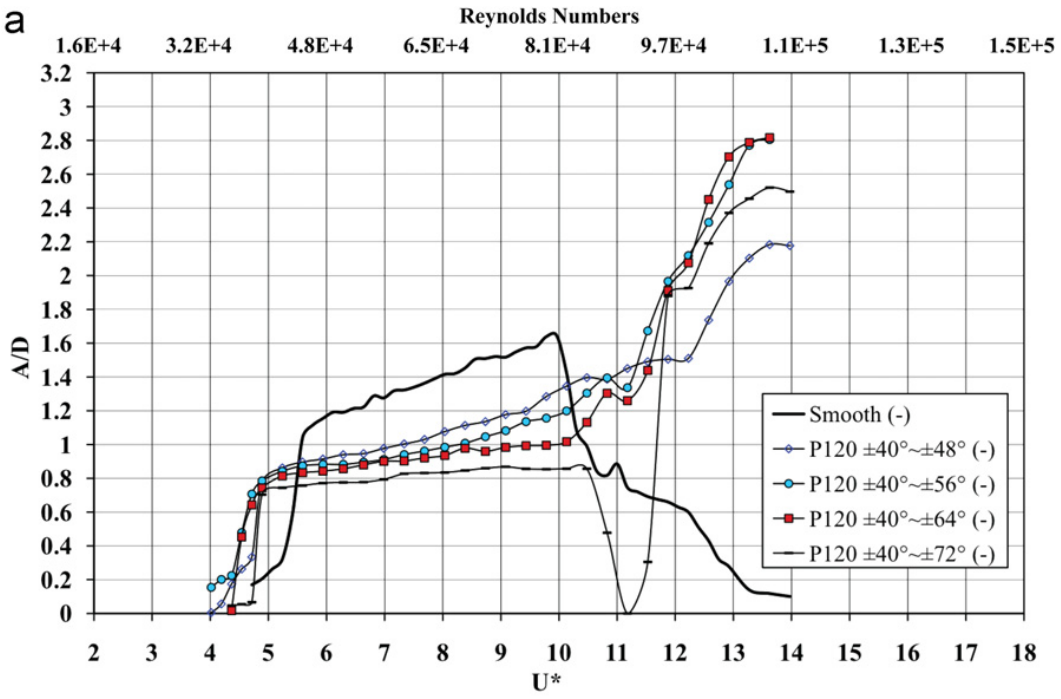

Figure 2.18 – VIV cylinder responses for different strip area coverages. (Chang et al. 2011).

2.10 Mass and Damping ratio

The product of the mass and damping ratio ($m^*\zeta$) is inversely proportional to the amplitude response of a cylinder undergoing VIV (Bearman 1984). The acceleration of the cylinder in the fluid is governed by the mass of the cylinder and mass of the fluid which is displaced. Hence the mass ratio (defined in Table 1) affects the frequency of oscillation of the cylinder, as evidenced by the differences in oscillation frequencies for a cylinder vibrating in air and water, due to the different densities of the fluids.

Investigations by Govardhan and Williamson (2000) regarding VIV of a circular cylinder confirmed the inversely proportional relationship between $m^*\zeta$ and the vibration amplitude of the cylinder. Accompanying this finding, Govardhan and Williamson (2000) also concluded that the synchronisation band of Reynolds numbers or reduced velocity was primarily dependent on the mass ratio, where lower m^* results in a larger band of synchronisation when the product

$m^*\zeta$ was constant. They also reported the existence of the 'upper branch' of VIV with high amplitude vibrations existing for low $m^*\zeta$ (order of 1), whilst higher mass damping ratios only had the 'initial' branch and 'lower' branch of VIV Figure 2.19.

Feng (1968) also showed that only the initial and lower branches of oscillation existed for high mass damping ratios. The existence of the upper branch of VIV was later confirmed by Govardhan and Williamson (2004) in another investigation of mass and damping ratio on VIV of a single circular cylinder. This research also helped establish a critical mass ratio in water (m^* = 0.54), below which the VIV response has high amplitude vibrations at very high frequencies Figure 2.20.

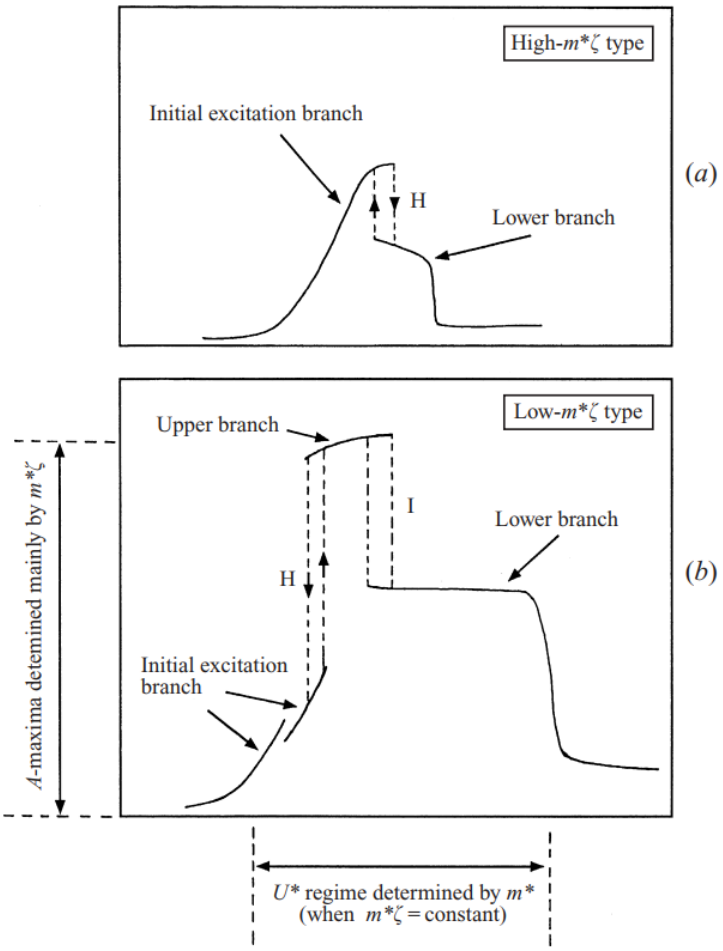

*Figure 2.19 – Two different types of amplitude response for VIV based upon the dependency on mass damping ratio, where high m*ζ only shows the initial and lower branches whilst low m*ζ has these two branches with the additional upper branch of oscillation (Govardhan and Williamson 2000).*

The oscillation frequency for VIV is primarily dependant on the mass ratio. At large mass ratios (order of 100), the vibration frequency for synchronisation lies close to the natural frequency, whilst lower mass ratios (order of 1) can result in vibration frequencies that are higher harmonics of the natural frequency. The highest mass ratio at which this high frequency vibration occurs is defined as the critical mass ratio. Williamson and Govardhan (2004a) performed a study on the mass ratio for VIV to identify the critical mass ratio. The authors reported a critical mass ratio of 0.54, below which large amplitude vibrations occur at high frequencies. Amplitudes of 0.8D were reported at mass ratios (0.45) below the critical mass ratio when no springs were attached to the cylinder (i.e., no structurally restoring force).

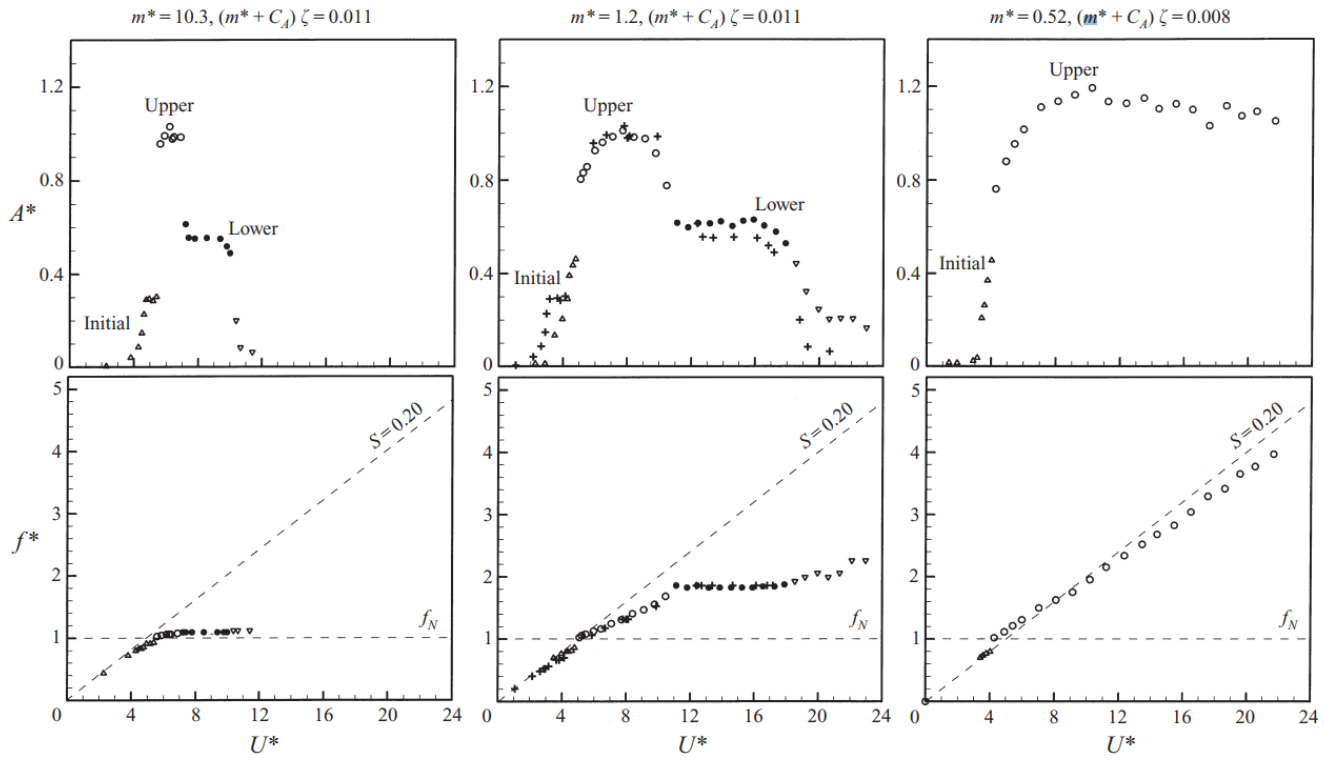

Figure 2.20 - Pairs of ampltiude-frequency plots for decreasing mass ratio (m) plot to the same scale (Govardhan & Williamson 2000). A^* is the amplitude normalised with the freestream velocity, f^* is the frequency of oscillation normalised with the natural frequency and U^* is the reduced velocity.*

Blevins and Coughran (2009) reported a precise relationship between the VIV response and changes of parameters such as mass ratio, damping coefficient and Reynolds number. Their tests were performed for mass ratios of 0.18 – 1.57, damping ratios of 0.002 – 0.4, and Reynolds numbers of 170 – 15,000 which corresponds to a reduced velocity of 2 – 12. The tests were conducted for 1-DOF and 2-DOF vibration and the three different diameters of cylinders were used to attain the mass and damping ratios as well as the reduced velocities reported. For transversely limited vibration, increasing the damping ratio from 0.002 – 0.02 decreased the amplitude of vibration by 15%, whereas further increasing damping ratio by a factor of 10 (0.02 – 0.2) decreases the amplitude by 90%. The maximum vibration amplitude was nearly identical when the mass and damping ratios were individually varied, but the product of mass and damping was maintained constant (Figure 2.21). Hence the authors proposed a reduced damping factor ($2m(2\pi\zeta)/\rho D^2$) which is the only factor influencing transversely limited amplitudes when the Reynolds number is kept constant.

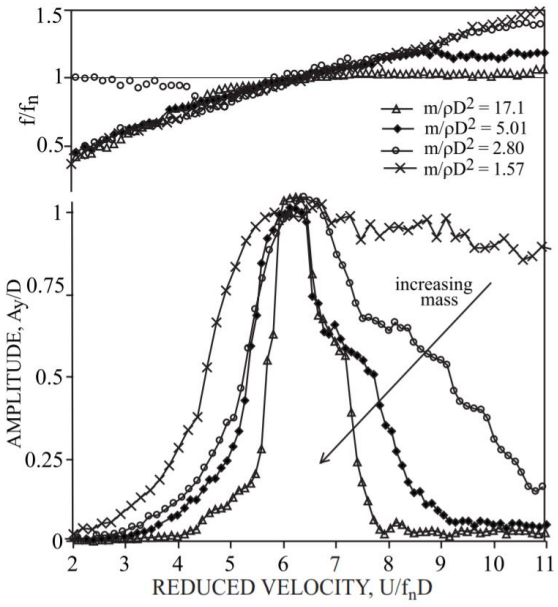

Figure 2.21 - Transverse cylinder response for four cylinder masses at constant reduced damping, $2m(2\pi\zeta)/\rho D^2 = 1.24$ (Blevins & Coughran 2009)

A water channel investigation of both the mass (m^*) and damping ratio (ζ) for VIV was conducted by Khalak and Williamson (1997b). The product of mass and damping ratios ($m^*\zeta$) was varied from 0.006 – 0.030, whilst individual mass ratios used were m^* = 2.4, 10.3 and 20.6. The amplitude of vibration was reported to increase with reducing mass ratios. A numerical investigation by Bahmani and Akbari (2010) at low Reynolds numbers (80 – 160) in the laminar flow regime further confirmed an increase in oscillation amplitude, as well as the synchronisation range for the upper and lower branches of VIV, when either the mass or the damping ratio of the system was reduced. However, the authors reported that the mass ratio had a more profound effect on the vibration response compared to the damping ratio.

A damping ratio investigation was performed by Lee and Bernitsas (2011) for the VIVACE convertor. Water channel tests were performed at high Reynolds numbers between 40,000 and 120,000 where the damping ratio was varied between 0 – 0.16. The authors found that increasing damping ratio reduced the amplitude response of the cylinder as well as the synchronisation range for VIV. However, the authors' primary focus was on sustaining high amplitude vibration at high damping ratios, since a Power-Take-Off (PTO) unit in real world scenarios is likely to have high damping. The authors performed the tests at high spring stiffness' of 400 – 1,800 and found that at a high damping ratio, high amplitude vibrations can be sustained as long as the system has a high spring stiffness, as depicted in Figure 2.22.

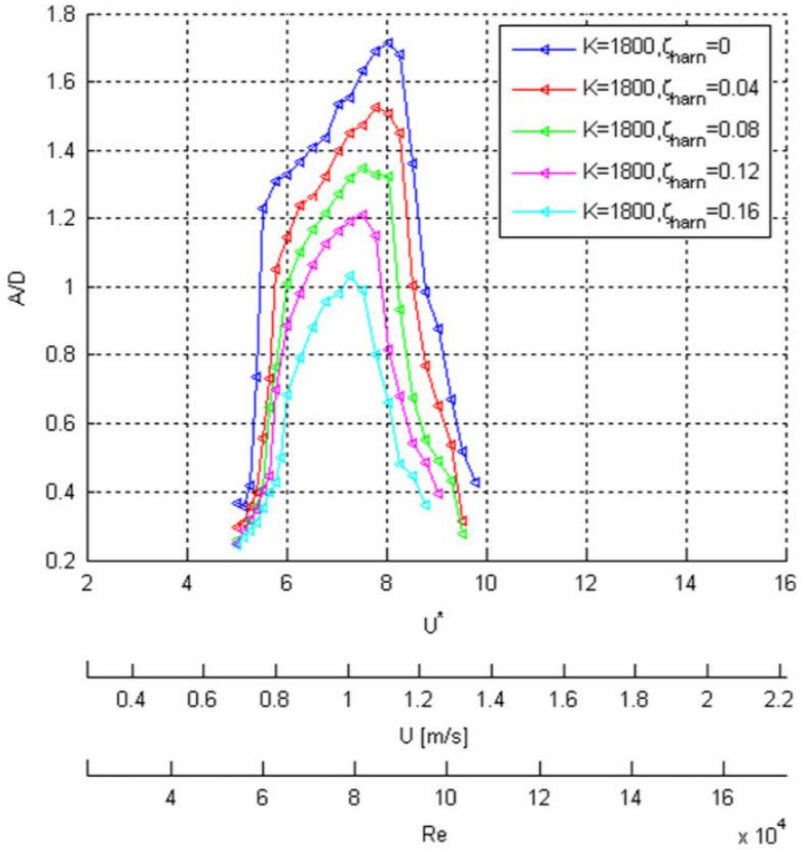

Figure 2.22 - Amplitude ratio vs. U (reduced velocity) , U (freestream velocity), and Re for K = 1800 N/m and various values of damping ratio, ζ_{harn} (Lee & Bernitsas 2011).*

Although the dependency of vibration response on the mass and damping ratio for VIV has been established in previous studies, the effect has been proven to be secondary; where the primary governor for the VIV phenomenon is the Reynolds number (Raghavan & Bernitsas 2011). However, the mass and damping ratio have to be investigated for WIV energy technology to attain an efficient system.

2.11 Effect of Reynolds number on VIV

The Reynolds number is the most influential parameter of VIV in a circular cylinder. As such, extant literature includes extensive investigations of the effect of Reynolds number on the VIV of a circular cylinder spanning across the laminar flow regime (Anagnostopoulos & Bearman 1992; Koopmann 1967) to transient and turbulent flows

(Bernitsas *et al.* 2009; Derakhshandeh *et al.* 2015c; Ding *et al.* 2004; Moe *et al.* 1994; Vikestad 1998).

Pioneering research to study the velocity measurements and frequency in the wake of a circular cylinder was performed by Koopmann (1967) who established that displacement of the cylinder increased with Reynolds number from 100 – 300.

A higher amplitude of vibration was observed in the lower branch, than the initial branch of lock-in range for VIV in experiments performed by Anagnostopoulos and Bearman (1992) between Re = 90 – 150. In such low Reynolds number situations, the lower branch of oscillation would be desirable for energy harvesting purposes.

Due to velocity restrictions in most experimental facilities, where conditions of VIV experiments can be controlled, most VIV experiments are limited to Reynolds numbers in the order of 10^6. Some high Reynolds single cylinder VIV investigations are as follows; Moe *et al.* (1994) at Re = 8,400, Khalak and Williamson (1996) at Re = 12,000, Vikestad (1998) at Re = 10,000, Ding *et al.* (2004) at Re = 250,000, Bernitsas *et al.* (2009) at Re = 100,000 and (Raghavan & Bernitsas 2011).

Raghavan and Bernitsas (2011) compared the effect of Reynolds number and the product of mass and damping ratio on a single cylinder VIV system. They found that the amplitude response shows more dependency on the Reynolds number than the product of the mass and damping. The tests were performed for Reynolds numbers from 20,000 to 600,000, and the authors reported that the amplitude of vibration increases within the transition-in-shear-layers regime (TrSL) which is usually between Re = 1,000 and 100,000 (Zdravkovich 1997). A maximum non-dimensional amplitude of 1.9D was achieved for a rigid circular

cylinder, which was almost twice larger than previously reported maximum amplitudes by (Govardhan & Williamson 2000; Khalak & Williamson 1997a). The amplification observed in the study by Raghavan and Bernitsas (2011) was attributed to a high fluctuating lift caused in the higher end of the TrSL regime. The authors concluded that even though they utilised a m^* 20 times higher than experiments by Govardhan & Williamson (2000), they were able to achieve high amplitude vibrations in the upper branch of VIV oscillation. Hence the effect of Reynolds number was observed to surpass the effect of mass ratio, and the TrSL regime identified as an optimal regime for harnessing energy using VIV.

Singh and Mittal (2005) simulated numerically VIV of a circular cylinder at low Reynolds numbers by utilising two sets of computations. They investigated the effects of *Re* and reduced natural frequency ($f_N = 1/U^*$) and found that the effect of *Re* on VIV was very significant.

2.12 VIV of a pair of circular cylinders

A pair of circular cylinders have been studied in extant literature to examine the effect of a cylinder working downstream of another cylinder in a flow. The research was mostly driven by the need to better understand and mitigate VIV in engineered structures, and lately to enhance vibrations for energy capture. VIV with a pair of cylinders is more enigmatic compared to the single cylinder case due to the interactions between the vortices from the upstream and downstream bodies. VIV studies of a pair of cylinders may have cylinders placed in the in-line, side-by-side and staggered configurations as shown in Figure 2.23. VIV of a pair of staggered or in-line cylinders, where the downstream cylinder is in the wake interference region is considered a

WIV response. The WIV phenomenon is the primary focus of this research and will be further elaborated on, in the proceeding sections.

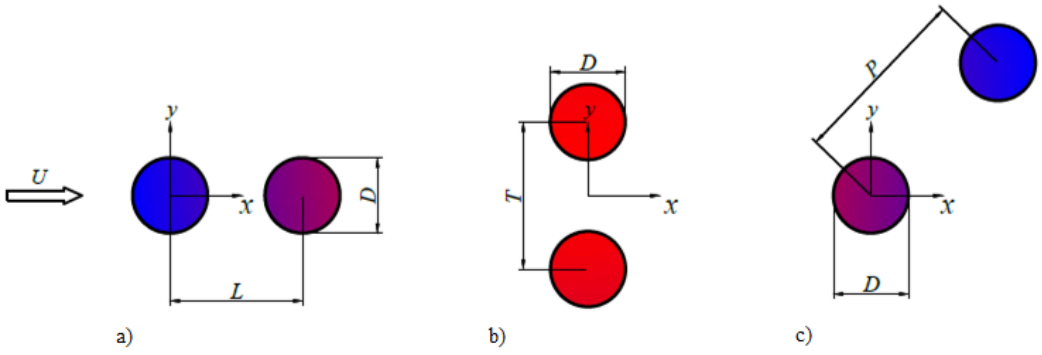

Figure 2.23 - The different configurations of two identical circular cylinders used in VIV studies; a) in-line, b) side-by-side, c) staggered.

2.13 Wake interference in a WIV system

The transverse and streamwise spacing between the upstream and downstream bluff bodies is one of the governing parameters in the WIV mechanism. Figure 2.24 maps out the three distinct interference regions for a downstream cylinder based on a fixed upstream cylinder; namely the proximity interference region, wake interference region and a region with no interference (Zdravkovich & Bearman 1998). The proximity interference region is defined as the region where the two cylinders are in close vicinity to each other and the shear layers produced by the two cylinders interact with each other. The side-by-side arrangement presented earlier is the most popular example of a cylinder operating in the proximity interference region. The wake interference region is a region where the downstream cylinder is under the influence of the wake, and hence vortices, produced by the upstream cylinder. Given a sufficient transverse and streamwise spacing in a staggered arrangement, the downstream cylinder can also be in the no interference region, where it is not affected by the upstream cylinder.

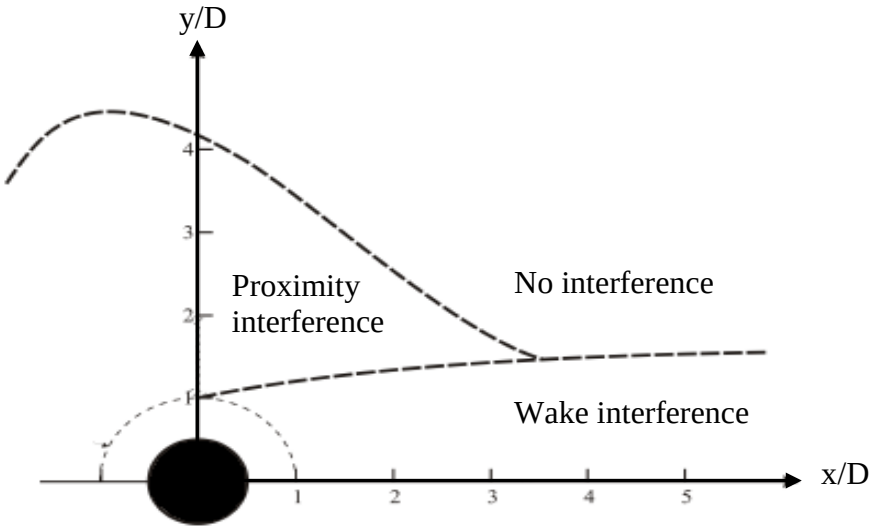

Figure 2.24 - The different interference regions for the location of a downstream cylinder in the wake of a fixed upstream cylinder (Zdravkovich & Bearman 1988).

For a cylinder to undergo WIV, the downstream cylinder needs to be in the wake interference region, and hence this region is the only focus of research on WIV for energy. Wake regimes have been interpreted and categorised in previous investigations based upon experimental measurements such as Strouhal number, base pressure coefficient and forces on the cylinder.

The Strouhal number of a pair of staggered fixed cylinders in a wind tunnel was investigated by Kiya *et al.* (1980) at Re = 15,800. The staggered spacing between the centres of the cylinders was investigated, and it was observed that the pair of cylinders behaved as a single cylinder if the staggered spacing was less than 1.4D. This spacing also drastically reduced the Strouhal number of the downstream cylinder to 0.12 (compared to 0.2 for a single circular cylinder). The proximity region causes the shear layers to merge together and only be shed from the downstream cylinder. Since this causes more interaction within the shear layers and diffuses the vortices, a wider wake is formed for the downstream cylinder compared to the upstream cylinder. This wider

wake and reduced intensity of circulation was attributed to the lower Strouhal number observed (Kiya *et al.* 1980).

The pressure coefficient around the surface of the cylinder is another parameter that has been extensively reviewed in early extant literature (Hiwada *et al.* 1982; Igarashi 1984; Ljungkrona 1992; Ljungkrona *et al.* 1991). Igarashi (1984) studied the pressure distribution around a cylinder for different Reynolds numbers and streamwise separations (1.1*D* and 1.2*D*). The study concluded that the effect of Reynolds number was greater than the effect of streamwise spacing, and that the effect of the gap between the cylinder was more prominent at the separation point (70° from the stagnation point).

The observed wake structure of an upstream cylinder in a pair of in-line separated circular cylinders was investigated in a study by Igarashi (1984). The upstream cylinder wake is highly dependent on the position of the downstream cylinder (when in the near wake, < 5*D*), and the wake can be categorised into six different patterns as displayed in Figure 2.25. Patterns A and B in Figure 2.25 represent cases where the in-line gap is less than 1.5*D*, where there is a single joined shear layer from both cylinders, and no vortex production by the upstream cylinder. Increasing the gap from 1.5*D* to 3*D* produces a wake structure like C and D, where two recirculation regions are formed in the gap between the cylinders. For a smaller gap, the recirculation regions are almost identical in size, however, increasing the gap causes an alternating region of large circulation. This alternating behaviour is caused due to the separation and re-attachment of shear layers from either side of the cylinders. Hence, the mean value of lift is equal to zero, as for the the single cylinder case (Assi 2009). Any further increase in the gap allows the rolling up of the shear layers in the gap, resulting in a wake structure

shown in patterns E and F. Pattern E is similar to D, where there is alternate merging of the upstream and downstream shear layers on either side, whereas in pattern F, the shear layers from the upstream body interact with each other to produce vortices in the gap. Similar observations have been reported via experimental investigation by Zdravkovich and Bearman (1998) and through numerical modelling by Carmo *et al.* (2008).

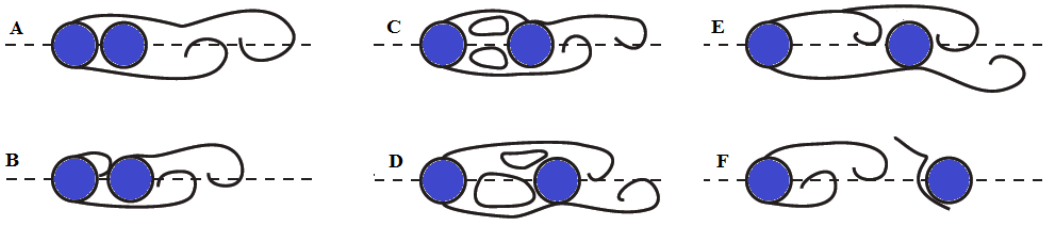

Figure 2.25 - Wake structure around two stationary cylinders as a function of in-line separation (Derakhshandeh et al. 2015, reproduced from Igarashi 1984). A and B = separation gap less than 1.5D; C and D = separation gap of 1.5D – 3D; E and F separation gap larger than 3D.

Figure 2.26 displays some of the wind tunnel flow visualisation results performed by Ljungkrona and Sundén (1993) using smoke wire techniques for in-line separated cylinders at a Reynolds number range of 3,000 – 40,000. The investigation varied the streamwise separation between the cylinders as well as the Reynolds number simultaneously. This study was important in realising that the wake structure is dependent on both the Reynolds number and the spacing, and for a Reynolds number of 42,000, the critical wake spacing was identified as 3.0*D*. The critical wake spacing is the minimum separation gap for vortices to form between the cylinders. As shown in Figure 2.26 e) and f), the critical spacing increases when the Reynolds number decreases as there is vortex shedding from the upstream cylinder when *Re* = 12,000 and not when *Re* = 10,000 when the gap is constant (4*D*). Lower freestream velocities delay the formation of the wake behind a bluff body by causing the shear layers to travel further downstream before

mutually interacting with each other. A prolonged wake development is caused by the location of transition in the shear layers, which moves further upstream with increasing Reynolds number. Hence, the critical wake spacing is dependent on the Reynolds number and this is evidenced by other studies by Igarashi (1981), who reported a critical spacing between 3.53*D* and 1.5*D* corresponding *Re* = 8,700 – 52,000 whilst Kuo *et al.* (2008) reported a critical wake spacing of 6*D* for *Re* = 1,000.

The wake structure between two cylinders is also affected by the relative sizes of the upstream and downstream cylinders. Alam and Zhou (2008) investigated the effect of changing the diameter of the upstream cylinder from 6 – 25 mm whilst the downstream cylinder was kept constant at 25 mm. The separation gap between the cylinders was 5.5 times the diameter of the downstream cylinder. The authors concluded that a smaller dimeter of the upstream cylinder caused a narrower wake to impinge on the downstream cylinder, due to which in turn increased the Strouhal number of the second cylinder.

The separation gap between cylinders determines the shear layer interaction, and hence the strength of the vortices produced. A larger gap allows fully formed coherent vortices to form, however, too large a gap would mean the circulation would dissipate before reaching the downstream cylinder. Vortices carrying higher levels of circulation are desirable to transfer more energy to the shear layers in the downstream cylinder. As such, the separation gap is a principal factor to consider when extracting energy using WIV.

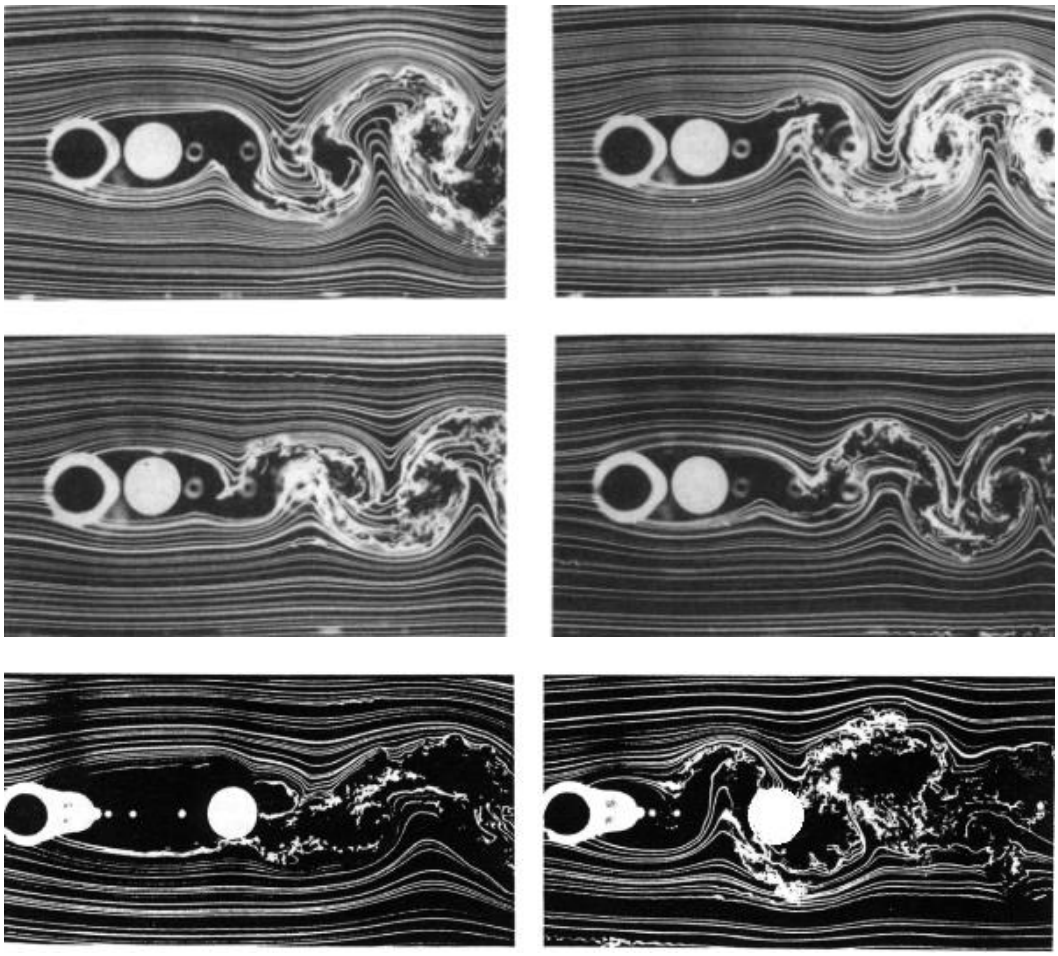

Figure 2.26 - Flow visualisation of a pair of circular cylinders; a) - d) are for Re = 3,300, 6,700, 10,000, 12,000 with separation gap = 1.25D, and e) and f) for Re = 10,000 and 12,000 at separation gap = 4D (Ljungkrona and Sunden 1993).

2.14 WIV Studies

WIV research is in its infancy stage when compared with VIV research due to the confusion regarding differences between WIV and galloping, the latter which is vibration caused in non-circular cylinders. Contrastingly, WIV is the unsteady-vortex interaction that occurs in a cylinder due to the wake from an upstream cylinder (Assi *et al.* 2010), which is considerably different to the VIV phenomenon of a single cylinder. A cylinder displaced from its equilibrium position experiences a lift force to restore the cylinder to its initial position in the WIV response (Zdravkovich 1977). This lift force can occur outside the

resonant frequency unlike the VIV mechanism. A 1DOF WIV system consisting of two circular cylinders in a staggered arrangement is shown in Figure 2.27, where the upstream cylinder is fixed whilst the downstream cylinder can vibrate in the transverse direction.

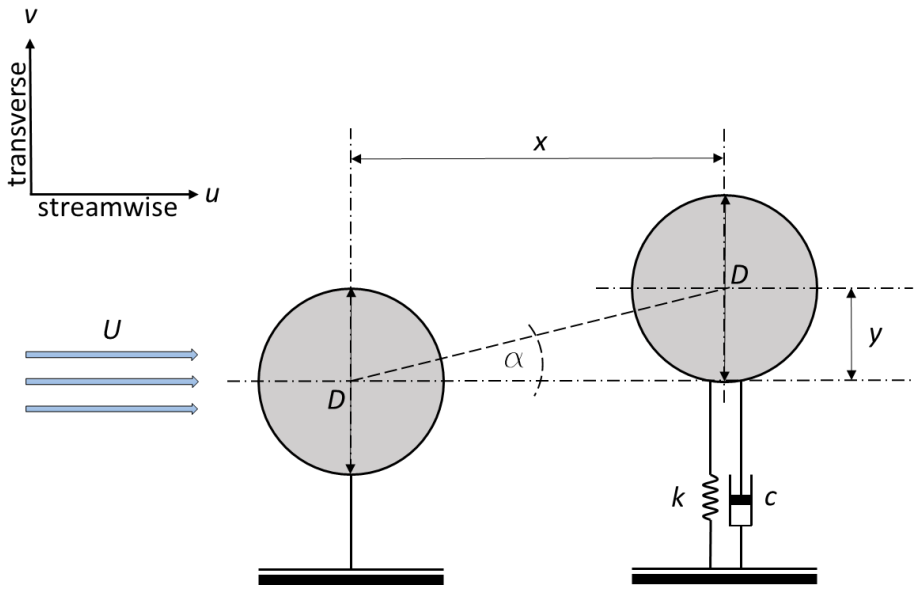

Figure 2.27 - Schematic of a typical WIV system consisting of two circular cylinders of the same characteristic diameter.

WIV of a pair of identical cylinders was investigated by Assi (2009) for a wide range of Reynolds numbers (1,000 – 30,000) corresponding to reduced velocities of 2 – 17. The WIV set-up included a fixed upstream cylinder and a transversely vibrating downstream cylinder. The in-line separation gap between the cylinders was varied from 4*D* – 20*D*, and the author observed a separation gap of 4*D* to have higher amplitudes than the other spacings. Unlike the limited response range displayed in VIV, Assi (2009) demonstrated that high amplitudes of vibration were possible even at a reduced velocity of 17. The amplitudes observed were also much higher than for a single cylinder undergoing VIV.

Derakhshandeh *et al.* showed that a WIV system, consisting of two circular cylinders, had an efficiency of 48.6% (*Re* = 9,000) whereas a VIV system only had a maximum efficiency (η) of 22.2% at *Re* = 65,000 and η = 10% at *Re* = 6,000 (Derakhshandeh *et al.* 2015b, 2015c). Work by these authors led to the realization that staggered separations of cylinders in a WIV system are more efficient compared to inline separations for energy harvesting.

For a pair of cylinders under the WIV mechanism, it is worthwhile noting that the total measured lift force acting on the surface of the cylinder might be divided into two separate components (Govardhan and Williamson 2000). The total lift force on the cylinder includes a *potential-force* component ($F_{potential}$) due to the ideal flow inertia and a *vortex-force* (F_{vortex}), which is only produced by the dynamics of the vorticity field around the downstream cylinder. Therefore:

$$\vec{F}_{\text{total}} = \vec{F}_{\text{potential}} + \vec{F}_{\text{vortex}} \tag{2.18}$$

Here, the *potential-force* is a function of the cylinder acceleration and its magnitude is proportional to the product of the displaced fluid mass and the acceleration of the cylinder. On the other hand, the *vortex-force* is dependent on the dynamics of the generated vortices and can be expressed in terms of another phase angle such as (Φ_{v}) in relation to the displacement of the cylinders (Assi 2009). Assuming Φ is the phase angle between displacement and total lift force and that the lift force is sinusoidal; the total lift can be formulated in terms of the lift coefficient as given in equation 2.19.

$$c_{\text{total}} \sin(2\pi f t + \Phi) = c_{\text{potential}} \sin(2\pi f t + 180°) + c_{\text{vortex}} \sin(2\pi f t + \Phi_{\text{v}}). \quad (2.19)$$

Consequently, the maximum lift coefficient acting on the cylinder is accessible when both potential lift coefficient and vortex lift coefficient become maximum and the phase angle between total lift force and displacement (Φ) remains close to zero. This concept has been also verified by Assi (2009) through a series of water channel tests where the force, displacement and frequency of oscillation were measured.

Equation (2.5) is important to analyse and evaluate the lift force and later in the experimental tests will be applied to analyse the efficiency of harnessing hydropower of a fluid using the WIV mechanism

2.15 FIV harnessing energy systems

A prototype known as the Vortex Induced Vibration Aquatic Clean Energy (VIVACE) generator was developed by Bernitsas *et al.* (2008), who were pioneers in realising the energy harnessing potential of VIV. The hydrokinetic energy convertor utilised circular cylinders to strengthen vortex shedding and hence enhanced VIV. Assuming that the cylinder exhibits a sinusoidal response, and thus allowing the use of a linear oscillator model, the theoretical efficiency of power conversion for VIV of a single cylinder unit was calculated to be 37% at a Reynolds number of 93,662. In comparison, the maximum power experimentally obtainable from a single cylinder system was 22%. As a result of their research, Bernitsas *et al.* (2008) identified the need for further work in optimising the hydrodynamics of VIV as well as the power take off system that would be used to capture the hydrokinetic energy. The

motivation for their work was based on mimicking movement in schools of fish, where the fish achieve high speeds using their streamlined flexible bodies to propagate vortices while swimming. Hence Bernitsas *et al.* (2008) also planned to test flexible splitter plates attached to cylinders to achieve larger lift forces and displacement amplitudes in the system.

A similar study was performed at the University of Adelaide to assess the applicability of harnessing hydrokinetic energy using VIV and WIV. The project employed numerical simulations using CFD, as well as a Virtual Mass-Spring-Damper (VMSD) testing rig employed in a water channel. This study demonstrated a maximum theoretical efficiency of 22.4% utilising a single cylinder undergoing 1DOF VIV at a Reynolds number of 65,000 (using SAS CFD simulations). The efficiency of power conversion was investigated for placement of the downstream cylinder at different positions in the wake of the upstream cylinder. The simulation of a pair of tandem circular cylinders revealed a maximum efficiency of 48.4% which was achieved at a separation of $3.5D < x/D < 4.5D$ and $1D < y/D < 2D$ between the cylinders (Figure 2.28). This study was crucial in identifying that staggered cylinder arrangements are favourable compared to centreline separated cylinders (Derakhshandeh, Arjomandi, Dally, *et al.* 2014). Furthermore, another numerical study by the same authors revealed an efficiency of 10% for a single cylinder and 28% for staggered cylinders at a Reynolds number of 8000 (Derakhshandeh *et al.* 2015c).

WIV was also investigated using both experimental and numerical methods by Derakhshandeh *et al.* (2015b). The results showed that a staggered arrangement rather than a centre aligned arrangement resulted in a maximum efficiency of 28% at a Reynolds number of 6,000

(Figure 2.28). The spacing between staggered cylinders for WIV was similar to the VIV experiments (Derakhshandeh *et al.* 2015b). A WIV response instead of a VIV response was achieved by choosing mass and damping ratios which were shown to result in a significant WIV response (Assi 2009).

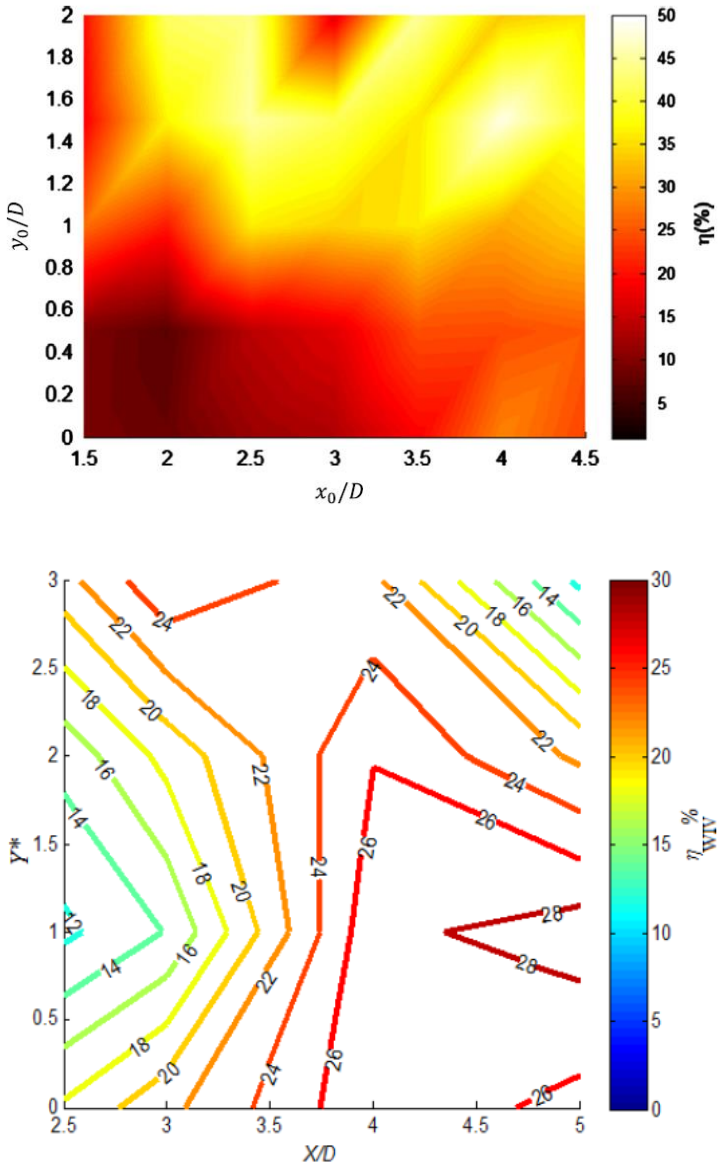

Figure 2.28 - Contours for the Efficiency of VIV response (left – Re = 65000) and WIV response (left – Re = 6000) based on different locations of the downstream cylinder (Derakhshandeh et al. 2014, 2015c).

Derakhshandeh *et al.* (2015a) then studied the effect of using a NACA 0012 symmetric aerofoil as the transversely vibrating downstream body in the system. Water channel experiments were performed at a Reynolds number of 10,000. The position of the aerofoil was varied as per previous studies done by the authors. The angle of attack was varied to different fixed angles to identify the angle that provided the highest efficiency of harnessing energy. A maximum efficiency of 30% was observed for FIV of the aerofoil at a fixed angle of attack of 10^{o} and a separation gap of $3.5 \leq x/D \leq 4.5$ and $1 \leq y/D \leq 1.5$. The authors suggested that coupling the angle of attack to the oncoming flow could increase the energy harnessing potential of the WEE system. The authors developed a Virtual-Mass-Spring-Damper (VMSD) system which was used to control the mass and damping ratios as well as the angle of attack in the system.

Energy generation using vortex induced vibrations have been investigated and employed by many researchers in order to produce small amounts of power for wireless sensing devices. Although these devices may differ in terms of arrangement and configuration, they all operate on the same principle of piezoelectric transduction. A miniature pneumatic generator, measuring 50mm x 30mm x 7mm, was developed by Wang and Ko (2010) to produce electricity from flow induced vibration. The authors demonstrated that 200 nW of energy could be produced with a voltage output of 2.2V. However, such a device is only useful when a small amount of energy is needed like in the case of wireless sensing devices for pipelines (Wang & Ko 2010). Another conceptual energy harvester was investigated by Hobbs and Hu (2012). A linear array of four cylinders connected to piezoelectric transducers were tested based on different conditions to get the optimal inter-

cylinder spacing and shedding frequency (Figure 2.29). Their results indicate maximum power production occurs at a cylinder spacing of 3.3*D* and when the shedding frequency is about 1.6 times the natural frequency of the system (Re = 10,000). They also noted that an array like this would function more efficiently when there are three or more cylinders as the latter few cylinders generate most of the energy in the system (Hobbs & Hu 2012).

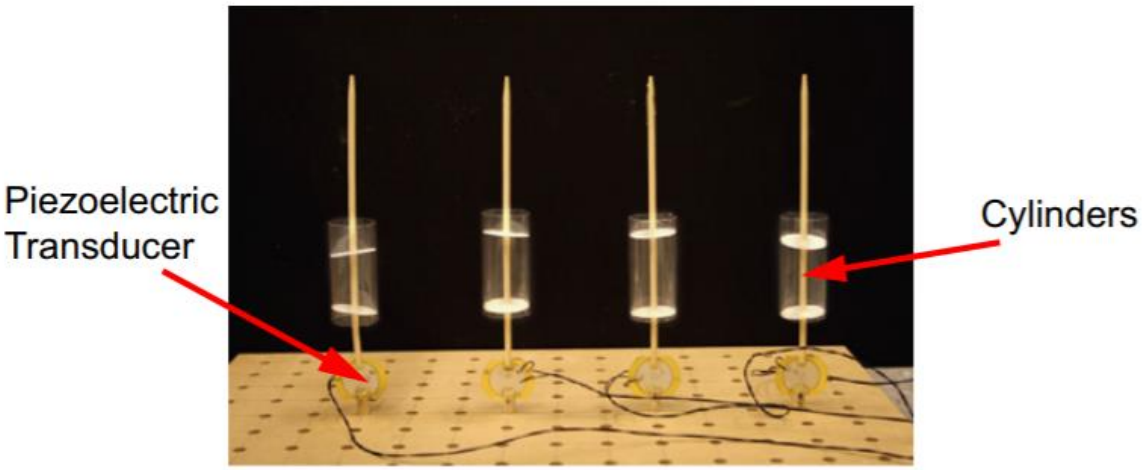

Figure 2.29 - Photograph of the tree inspired piezoelectric flow energy harvester tested by Hobbs and Hu (2012). The device consists of four cylinders placed in series and mounted to a piezoelectric transducer.

A similar piezoelectric generator was developed by Weinstein *et al.* (2012), intended to be used in heat and ventilation air conditioning systems (Figure 2.30). A power generation of 200 μW and 3 mW were produced for flow speeds of 2.5 and 5 m/s from a device measuring 22.5cm x 11cm. Interactions between the vortices produced by an upstream bluff body and a fin connected to the cantilevered piezoelectric beam enable power generation by the beam (Weinstein *et al.* 2012). The maximum efficiency obtained in this study was 2%.

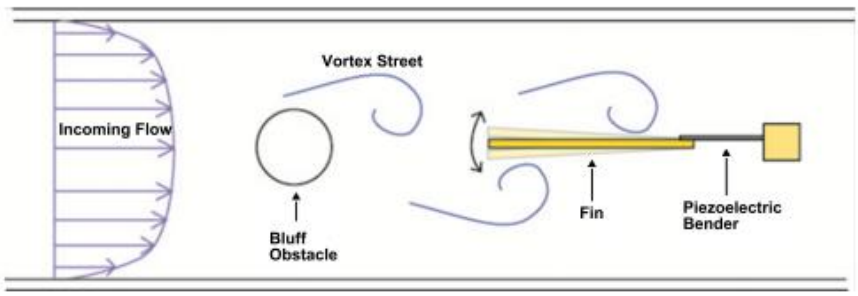

Figure 2.30 - Schematic of a piezoelectric generator utilising Karman vortex street (Weinstein et al. 2012)

2.16 Virtual mass spring damper system

Emulating fluidic parameters is accomplished in experimental studies using wind or water tunnels. However, imposing the structural parameters has more complexity due to the physical springs and dampers needed. To overcome this, a few studies have developed Virtual Mass-Spring-Damper (VMSD) systems to impose structural parameters such as the stiffness and damping on to the cylinder. As mentioned earlier, Bearman (1984) was the first to postulate that the response of an elastically mounted circular cylinder can be modelled as a Mass Spring Damper system (MSD). Following the proposed model by Bearman (1984), Hover *et al.* (1997), a pioneer of the computer model of Virtual Mass Spring Damper (VMSD), designed and employed a force-feedback controller in real time. The schematic of the VMSD system is depicted in Figure 2.31. The VMSD system allowed the operator to electronically set the desired impedance of the MSD. The advantage of VMSD is that it allows a wider range of tests to be conducted rapidly compared to the real physical MSD which requires changes in the physical elements of the system in order to change the impedance. The ease of application of the VMSD allowed Hover *et al.* (1997) to conduct a wide range of air channel tests to analyse the effects of damping ratio and the Reynolds number on the VIV response of a cylinder. They observed that the maximum amplitude of oscillation can

be obtained when the damping ratio is zero. Although, it was shown that the VMSD is able to record reliable results, such as lift coefficients and the amplitude of oscillation, the system was observed to produce an additional phase lag of 12 degrees. The phase lag between lift and displacement was due to the Chebyshev third-order digital filter (Hover *et al.* 1997), which can cause a reduction in energy conversion.

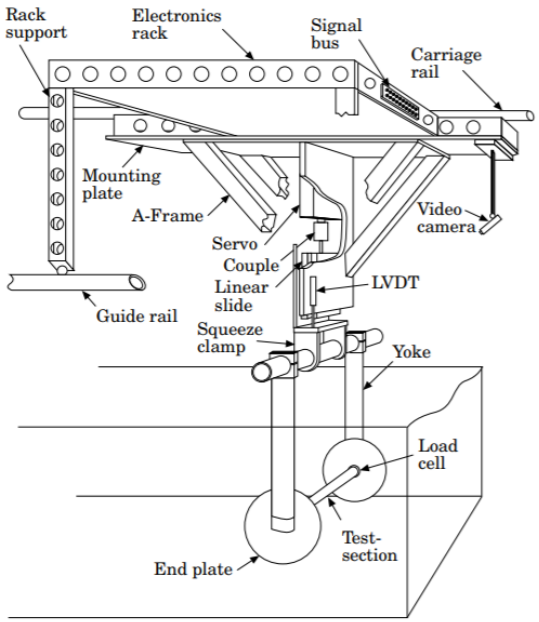

Figure 2.31 – Schematic of VMSD system developed by Hover et al. (1997). A computer-controlled servomotor actively positions the test cylinder through a linear slide; this assembly , along with the supporting electronics and sensors, translates along a 25 m towing tank

The use of VMSD models opened the way for optimisation and further development of energy extraction from VIV. In particular, it was used to explore many unresolved issues including the force-displacement phase lag, the power coefficient of energy harnessing, etc. For example, Lee *et al.* 2011 developed a VMSD of a VIV converter including a circular cylinder, a timing belt-pulley, a motor, and a controller. The VMSD allowed them to perform a wide range of experiments in which the spring stiffness was kept constant and the viscous damping was varied. In this model, there was no artificial phase lag between the force and displacement which could bias the energy

conversion. In addition, to eliminate the vibration of the timing belt, an idler was utilized to remove the non-linearity of the oscillations. Furthermore, in order to protect the motor, a coupling was employed between the pulley and the motor shaft.

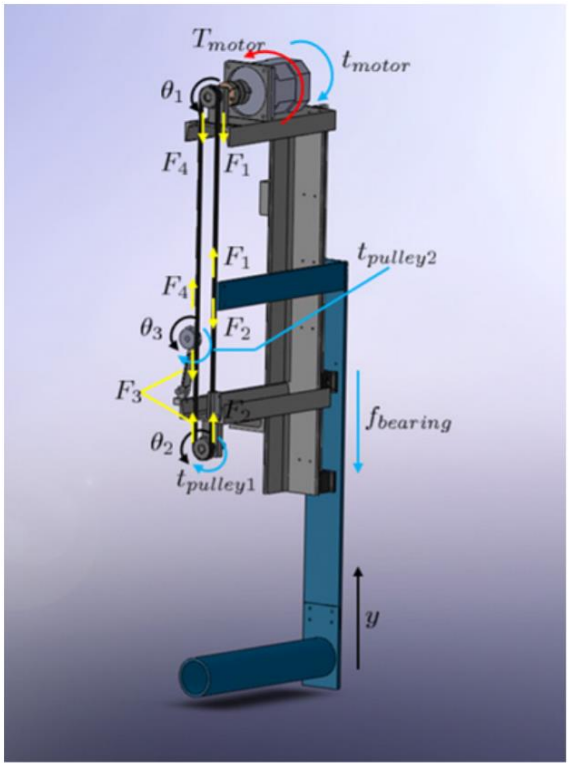

Figure 2.32 - VMSD system developed by Lee et al. 2011 with a horizontally mounted cylinder.

Although significant improvements were made in this model, the mass of the cylinder was imposed on the motor and generated significant frictional force due to the static weight of the cylinder. This caused a nonlinear behaviour for the response of the cylinder at low velocities.

A VMSD system was also developed by Derakshandeh *et al.* (2015a) and is depicted in Figure 2.33 with the control apparatus and testing section of a water channel. In this approach, a vertically mounted cylinder in a cross-flow was utilized, as opposed to previous designs, which employed horizontally mounted cylinders. The advantage of this

approach was that the static weight (minus the buoyancy force) was no longer applied to the motor. In addition, the gravitational force was not in the same direction as the lift force acting on the cylinder and, therefore, it did not affect the dynamic response of the cylinder. Hence, it was not necessary to compensate for the gravitational force, as was done in the previous study (Lee *et al.* 2011).

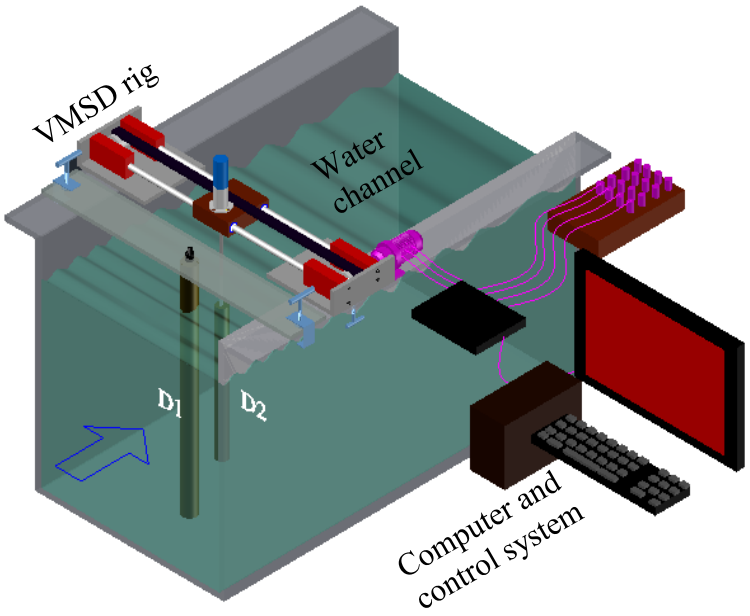

Figure 2.33 - Virtual Mass Spring Damper system developed by Derakshandeh et al. (2015a) employing a vertically mounted cylinder (D2).

2.17 Mathematical modelling for the VMSD

An overview of the mathematical modelling is presented in this section. A detailed description of the model can be found in Derakhshandeh *et al.* (2015).

The vibration of the cylinder mounted to a simple spring-mass-damper system has been modelled by Bearman (1984) as:

$$m\ddot{y}(t) + c\dot{y}(t) + ky(t) = F_y(t), \qquad (2.20)$$

where, y, $\dot{y}$ and $\ddot{y}$ are the transverse displacement, velocity and acceleration of the cylinder, respectively, c is the damping coefficient, k is the spring stiffness and m is the mass of the cylinder. On the right-

hand side of Equation (1), F_y is the fluid force exerted on the cylinder perpendicular to the flow direction and can be defined as the sum of viscous and pressure forces on the cylinder:

$$F_y(t) = F_{viscous} + F_{pressure} \tag{2.21}$$

The structural parameters and the response of the cylinder due to the flow can be set by the non-dimensional parameters defined in Table 2. Here, ρ is the fluid density, U is the freestream velocity and μ is the dynamic viscosity of water.

Table 2 - Non-dimensional parameters.

Mass ratio	m^*	$4m/\rho\pi {D_2}^2 L$
Damping ratio	ζ	$c/2\sqrt{km}$
Lift coefficient	C_L	$F_y/0.5\,\rho U^2 D_2 L$
Amplitude ratio	Y^*	y_{max}/D_2
Frequency ratio	f^*	f/f_n
Reynolds number	Re	$\rho U D_1/\mu$

The time dependent displacement and the lift coefficient can be obtained from equations (2.22) and (2.23), respectively, by assuming linear behaviour and sinusoidal response of the cylinder;

$$y(t) = y_{max}\sin(2\pi f_{osc} t), \tag{2.22}$$

$$c_L(t) = C_L\sin(2\pi f_{osc}\, t + \Phi), \tag{2.23}$$

In Equation (2.22), y_{max} is the harmonic displacement amplitude and f_{osc} represents the oscillation frequency. In Equation (2.23), c_L is the time dependent lift coefficient, C_L is the lift coefficient amplitude and Φ is the force-displacement phase angle, which is vitally important in the WIV response of the cylinder (Sarpkaya 1978, Khalak and Williamson 1999),

particularly for energy conversion (Bernitsas and Raghavan 2004 and Bernitsas *et al.* 2008).

Consequently, the damped natural frequency can be approximated as:

$$\omega_{\mathrm{d}} = \frac{2\pi}{T_{\mathrm{d}}} = \omega_{\mathrm{n}}\sqrt{1-\zeta^2} \approx \omega_{\mathrm{n}} = \sqrt{\frac{k}{m_{\mathrm{eff}}}}\,. \tag{2.24}$$

where, T_{d} represents the damped period of oscillation. The servo-motor produces a virtual spring and damping torque utilising the angle and angular velocity measurements, and hence the rotation of the shaft is converted into the vibration of the cylinder. The acting torque from the motor affects the angle and angular velocity, while the shear forces due to vortices are exerted on the surface of the cylinder. The rotary movement of the shaft is then converted to a linear displacement via the pulleys, the timing belt, the carriage and finally the cylinder, which is connected to the carriage.

Thus, integrating the inner product of the force and the instantaneous velocity, the total generated work can be calculated over a complete cycle of oscillation (T),

$$W_{\mathrm{WIV}} = \int_0^T F_y \dot{y} dt. \tag{2.25}$$

The average power is given by

$$P_{\mathrm{WIV}} = \frac{W_{\mathrm{WIV}}}{T}. \tag{2.26}$$

The fluid power given by $P_{\mathrm{fluid}} = (½)\rho U^3 D_2 L$ (Bernitsas and Raghavan 2004), was used to calculate the power coefficient

$$\eta_{\mathrm{WIV}} = \frac{P_{\mathrm{WIV}}}{P_{\mathrm{fluid}}}. \tag{2.27}$$

Utilising the equations above the power coefficient for WIV of the cylinder can be represented by

$$\eta_{\mathrm{WIV}} = \frac{\pi C_{\mathrm{L}} f_{\mathrm{osc}} y_{\max} \sin(\Phi)}{U}. \tag{2.28}$$

Further details of the mathematical derivation can be found in in Derakhshandeh *et al.* (2015a).

2.18 Computational Fluid Dynamics modelling

In addition to experimental investigations, numerical modelling has been utilised to investigate stationary cylinders as well as cylinders undergoing VIV and WIV. The complexity of numerical modelling the flow around a cylinder arises due to the adverse pressure gradient around the cylinder surface and the uncertainty of the separation point and reattachment length of the shear layers. Turbulence models such as large eddy simulation (LES) and Reynolds-averaged Navier-Stokes (RANS), as well as direct numerical simulation (DNS) models have been used in the published literature to model the flow around a cylinder. LES models are computationally expensive but provide accurate and detailed results. RANS models require less computational power and model the turbulence instead of resolving it and include models such as $k-\omega$ and $k-\varepsilon$. DNS is the most computationally expensive and is impractical at high Reynolds numbers. For high Reynolds number investigations LES and RANS models such as $k-\varepsilon$ and $k-\omega$ have received a lot of attention in literature (Atlar & Gören 2010; Celik & Shaffer 1995; Derakhshandeh, Arjomandi, Dally, *et al.* 2014; Franke & Rodi 1993; Khan *et al.* 2016; Tutar & Holdo 2000).

High Reynolds number (10^4 – 10^7) flow tests using the $k-\varepsilon$ model were performed by Celik and Shaffer (1995), where the authors observed the importance of grid distribution in the boundary layer on

attained results. Best predictions were achieved when the first grid point was within the viscous sublayer. Franke and Rodi (1993) reported that the Reynolds stress equation turbulence model performed better than the $k-\varepsilon$ model for the flow around a square cylinder at Re = 22,000. However, the Reynolds stress equation model over-predicted the fluctuation motion in the wake. Both models were incapable of providing a detailed flow prediction unlike simulations which used LES.

Transient simulations using Large Eddy Simulation (LES) and Detached Eddy Simulation (DES) were performed on a stationary cylinder by Liaw (2005). Large-scale turbulence is directly computed while solving the Navier-Stokes equations, whilst small-scale eddies are modelled (Sagaut 2006). Although the flow structure in the wake of the cylinder was accurately resolved in this study with little dissipation, the LES model requires significantly higher computation requirements compared to Reynolds Averaged Navier-Stokes (RANS) turbulence models.

The Shear Stress Transport (SST) model, developed by Menter (1994), combines the $k-\omega$ and $k-\varepsilon$ turbulence models to overcome the problems associated with the prediction of length scales close to the walls for the $k-\omega$ and free stream dependency of the $k-\varepsilon$ model. The SST model can be utilized to compute the transport of the turbulence shear stress inside the boundary layers for flow over cylinders. SST aimed to increase the accuracy of flow predictions with strong adverse pressure gradients. It has been shown that SST can better predict flow separation compared with either the $k-\omega$ or $k-\varepsilon$ models (Liaw 2005). Despite the advantages of the SST model compared with $k-\omega$ and $k-\varepsilon$, it behaves similarly to the $k-\varepsilon$ model away from the wall (Fletcher & Langrish 2009). When the SST model is utilised in transient simulations,

it generates large length-scales and consequently turbulence viscosities are too high. Hence, this does not allow a spectrum of length scales to be determined appropriately (Menter & Egorov 2005). Hence, seeking a solution to investigate the flow behaviour around a pair of cylinders can provide both computational efficiency and accurate flow predictions.

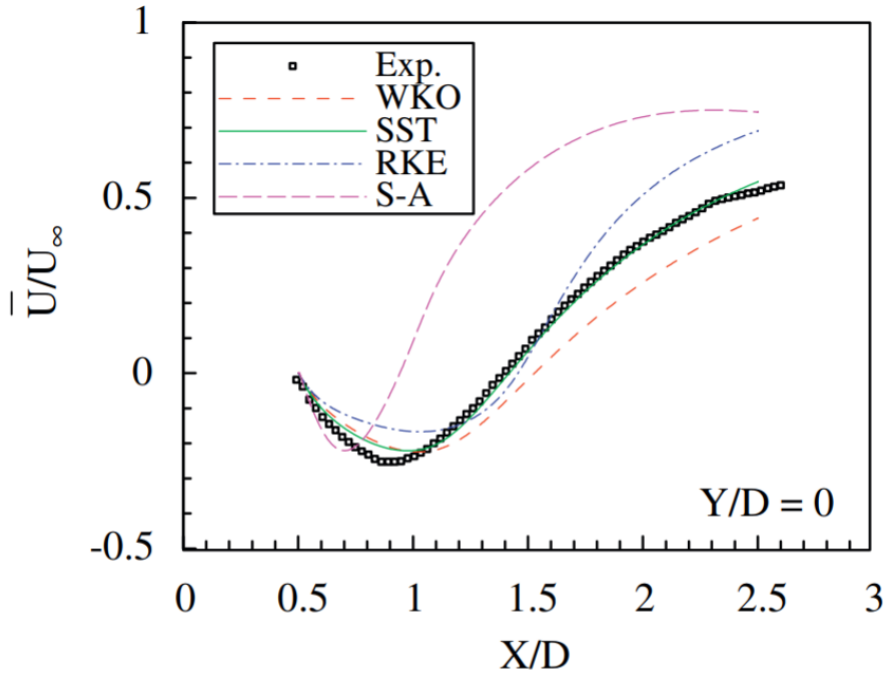

Figure 2.34 – Plot of the normalised centreline velocity in the wake of a circular cylinder using several turbulence models (Altar and Goren 2010). SST = The shear stress transport (SST) $k-\omega$ model; SA = the Spalart-Allmaras model; RKE = realizable $k-\varepsilon$; WKO = Wilcox $k-\omega$ model; and Exp = experimental data.

Atlar and Gören (2010) published a comparison of the near wake of a cylinder modelled by four RANS models at a Reynolds number of 43,000. The shear stress transport (SST) $k-\omega$ model provided better predictions of the flow structure compared to the Spalart-Allmaras (S-A), realizable $k-\varepsilon$ (RKE) and Wilcox $k-\omega$ models (WKO). Figure 2.34 compares the mean normalised (using freestream velocity) for the centreline in the wake of the cylinder obtained using the four RANS models, where the SST model is closer to the experimental data compared to the other RANS models.

Guilmineau and Queutey (2004) also used the SST $k-\omega$ model to investigate the VIV response of the cylinder at three branches of oscillation. The numerical results showed that although SST *k-ω* predicted the dynamic response of the cylinder at the initial and lower branches, the model could not predict the upper branch of vibration.

Forced oscillation utilising the LES model in 2D and 3D models of a cylinder was investigated by (Tutar & Holdo 2000) at a Reynolds number of 24,000. The 3D LES simulations gave a more realistic flow field compared to the 2D model and were in better agreement with experimental data. Another LES study by Khan *et al.* (2016) successfully modelled the cylinder wake at *Re* = 3,900. Khan *et al.* (2016) suggested that a 3D mesh and fine resolution in the spanwise direction are necessary to perform LES simulations over the cylinder.

Within a transient flow, hybrid models have drawn less attention and no simulations have been yet conducted utilizing a combined formulation of RANS and LES, known as the scale adaptive simulation (SAS) model. In the SAS turbulence model, the turbulence length-scale is resolved by considering the definition of von Karman length scale. In contrast to previous turbulence models, the SAS overcomes the deficiency of SST in resolving the turbulence length-scale by considering the definition of von Karman length scale. This assists in more accurately capturing the vortex structure in the wake of the structure. The von Karman length scale is given by:

$$L_{vk} = k \left| \frac{\partial U/\partial y}{\partial^2 U/\partial y^2} \right|. \tag{2.7}$$

Using the von Karman length scale, the model can adapt its behaviour to Scale Resolving Simulation (SRS) according to the stability parameters of the flow (Egorov *et al.* 2010). This allows the model to

provide a balance between the contributions of the simulated and resolved parts of the turbulence stresses. Hence, the model can effectively and automatically switch from the Large Eddy Simulation (LES) mode to the Reynolds Averaged-Navier Stokes (RANS) mode (Menter & Egorov 2010).

Furthermore, the mesh resolution requirements for the SAS model are significantly lower compared to LES models. SAS can also capture the turbulence length scales more accurately compared to the simple SST model. This fact is highlighted in Figure 2.35, which compares contours of non-dimensional turbulence length scales at high Reynolds number, Re = 10^6. These capabilities make SAS as an attractive model for unsteady flow with lower computational cost than current alternatives whilst still maintaining reasonable accuracy.

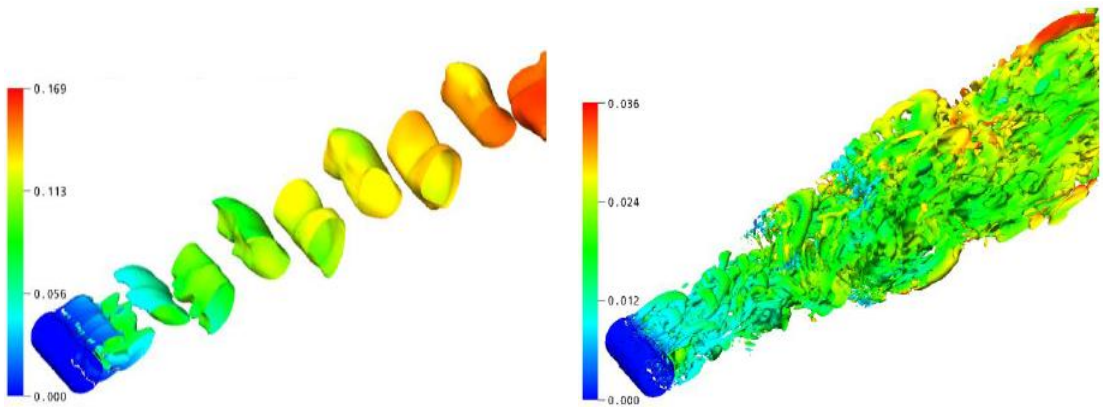

Figure 2.35 - Contours of turbulence length scale/cylinder diameter at Re=10^6; a): URANS model (SST), b): SAS model, (Menter and Egorov 2010).

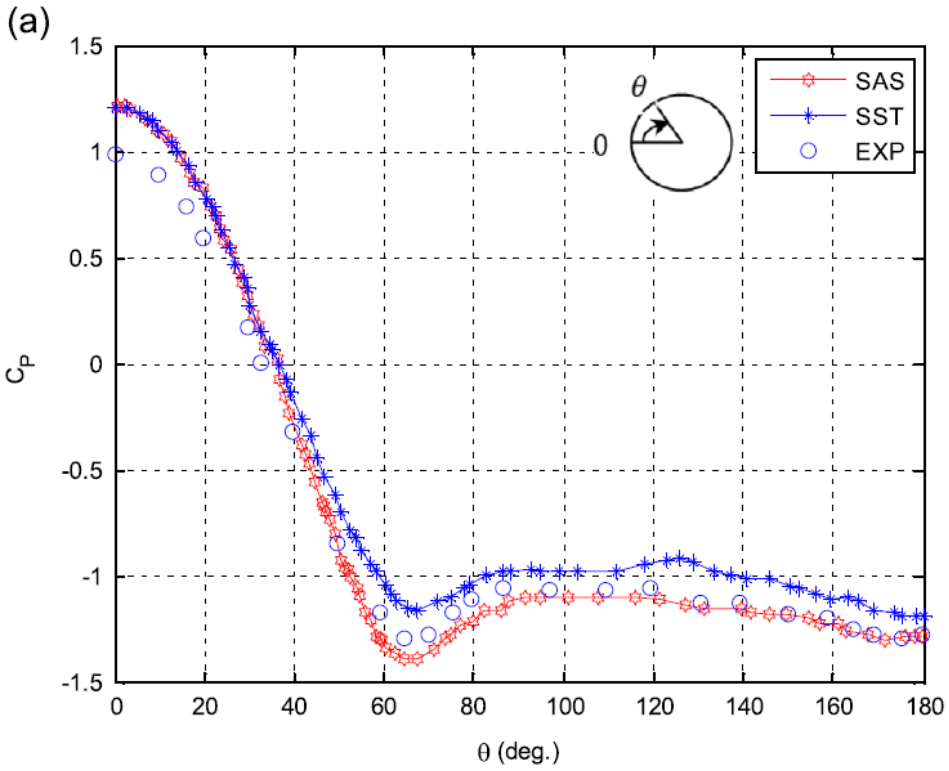

Figure 2.36 – Pressure coefficient around the surface of an upstream stationary cylinder using the SST and SAS models at Re = 65,000 compared against published experimental data by Alam et al. (2003) (Derakhshandeh, Arjomandi, Dally, et al. 2014).

Derakhshandeh, Arjomandi, Dally, *et al.* (2014) performed a CFD study on the WIV of a pair of cylinders using the SAS turbulence model for a Reynolds number of 65,000. The CFD models also compared the results between the SAS and SST models to analyse the validity of the SAS models. Although, both models agreed with the experimental data within experimental uncertainty standards (10%), the SAS model was more accurate than the SST model. Figure 2.36 depicts the comparison of the pressure coefficient around the upstream stationary cylinder for the two turbulence models as well as published experimental data, where the SAS model is in better agreement with the experimental data. Additionally, Figure 2.37 depicts the results for lift coefficients of the two cylinders obtained using the SAS model as well as experiments, where the results deviate by less than 10%.

Keeping these considerations in mind, the SAS model was used for the work undertaken in this thesis as it is computationally less expensive than the LES model and provides better predictions of the flow field for the WIV case.

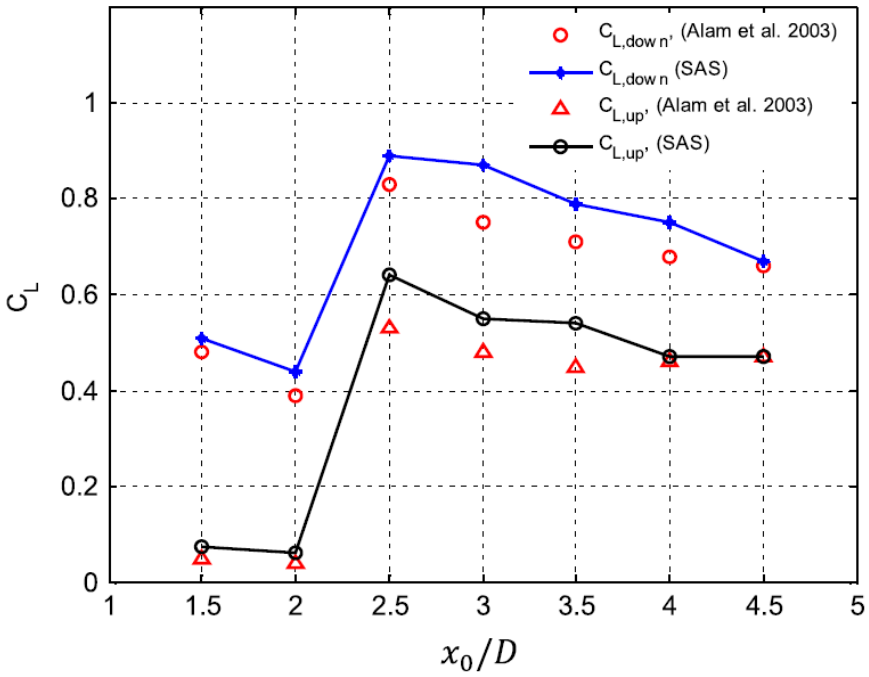

Figure 2.37 – Lift coefficient vs the streamwise separation gap between two circular cylinders in a WIV system obtained using the SAS model and experimental data by Alam et al. (2003) (Derakhshandeh, Arjomandi, Dally, et al. 2014).

2.19 Summary and gaps

Regions of time-averaged maximum energy density in the wake of a bluff body were determined in previous studies (Assi 2009; Derakhshandeh *et al.* 2015a, 2015b; Goldstein & Kulkarni 2008). However, this is a spatial energy concentration comparable to diffusers, which are known to have large energy losses and pose limitations due to their large size. Considering bluff body wakes, there is an element of temporal energy concentration in addition to the spatial concentration in the form of coherent structures. Hence, the combined effect leads to

high temporal energy density zones in the wake. The scientific understanding of spatial and temporal concentration of energy by the circular cylinder wake has not been established, with regards to the frequency and energy density of the wake energy field.

In most WIV studies, the upstream cylinder has been a circular cylinder. Although there have been investigations with different downstream cylinder cross-sections (Derakhshandeh *et al.* 2015a; Wang & Ko 2010), different cross-sections of the upstream stationary cylinder have yet to be investigated for their applicability in WIV energy technology.

WIV depends on a variety of factors such as the Reynolds number, mass of the body, stiffness and damping of the system, aspect ratio of the cylinder, surface roughness, shear forces and the turbulence intensity. The circular cylinder has been widely investigated to identify how these factors affect its vibrations. However, if other cross sections were used, there is little known about how the system will react to changes in parameters that govern the WIV/VIV phenomenon and how the parameters can be optimised to make the system more efficient.

Consequently, the main objectives identified for this research are listed as follows:

1. Investigating and providing understanding on the concept of temporal energy concentration in the wake of a circular cylinder.
2. Investigating the wakes of different bluff body geometries to identify cross-sections that can provide greater temporal energy to a downstream body in a WIV system.
3. Studying the effectiveness of employing a cross-section other than the circular cylinder as the upstream cylinder on the power

coefficient for a WIV system for different downstream locations of the downstream cylinder.

4. Investigating the effect of system parameters such as the mass and damping ratio on the efficiency of a WIV system for a fixed downstream cylinder location.

References

Achenbach, E 1971, 'Influence of surface roughness on the cross-flow around a circular cylinder', *Journal of Fluid Mechanics*, vol. 46, no. 2, pp. 321-35.

Alam, MM & Zhou, Y 2008, 'Strouhal numbers, forces and flow structures around two tandem cylinders of different diameters', *Journal of Fluids and Structures*, vol. 24, no. 4, pp. 505-26.

Anagnostopoulos, P & Bearman, P 1992, 'Response characteristics of a vortex-excited cylinder at low Reynolds numbers', *Journal of Fluids and Structures*, vol. 6, no. 1, pp. 39-50.

Angrilli, F, Di Silvio, G & Zanardo, A 1972, 'Hydroelasticity study of a circular cylinder in a water stream', in *Flow-Induced Structural Vibrations IUTAM–IAHR Symposium, Karlsruhe (ed. E. Naudascher)*, pp. 504-12.

Assi, GRS 2009, 'Mechanisms for flow-induced vibration of interfering bluff bodies', Ph.D thesis, Imperial College London.

Assi, GRS, Bearman, P & Kitney, N 2009, 'Low drag solutions for suppressing vortex-induced vibration of circular cylinders', *Journal of Fluids and Structures*, vol. 25, no. 4, pp. 666-75.

Assi, GRS & Bearman, PW 2015, 'Transverse galloping of circular cylinders fitted with solid and slotted splitter plates', *Journal of Fluids and Structures*.

Assi, GRS, Bearman, PW, Kitney, N & Tognarelli, MA 2010, 'Suppression of wake-induced vibration of tandem cylinders with free-to-rotate control plates', *Journal of Fluids and Structures*, vol. 26, no. 7, pp. 1045-57.

Assi, GRS, Meneghini, JR, Aranha, JAP, Bearman, PW & Casaprima, E 2006, 'Experimental investigation of flow-induced vibration interference between two circular cylinders', *Journal of Fluids and Structures*, vol. 22, no. 6, pp. 819-27.

Atlar, M & Gören, Ö 2010, 'Effect of turbulence modelling on the computation of the near-wake flow of a circular cylinder', *Ocean Engineering*, vol. 37, no. 4, pp. 387-99.

Bahmani, M & Akbari, M 2010, 'Effects of mass and damping ratios on VIV of a circular cylinder', *Ocean Engineering*, vol. 37, no. 5, pp. 511-9.

Bearman, PW 1984, 'Vortex shedding from oscillating bluff bodies', *Annual Review of Fluid Mechanics*, vol. 16, no. 1, pp. 195-222.

Bearman, PW 2011, 'Circular cylinder wakes and vortex-induced vibrations', *Journal of Fluids and Structures*, vol. 27, no. 5, pp. 648-58.

Bearman, PW, Graham, J, Naylor, P & Obasaju, E 1981, 'The role of vortices in oscillatory flow about bluff cylinders', in *International Symposium on Hydrodynamics in Ocean Engineering*, pp. 621-35.

Bergey, KH 1979, 'The Lanchester-Betz limit (energy conversion efficiency factor for windmills)', *Journal of Energy*, vol. 3, no. 6, pp. 382-4.

Bernitsas, MM, Ben-Simon, Y, Raghavan, K & Garcia, EM 2009, 'The VIVACE converter: model tests at high damping and Reynolds number around 105', *Journal of Offshore Mechanics and Arctic Engineering*, vol. 131, no. 1, pp. 1 - 15.

Bernitsas, MM & Raghavan, K 2004, 'Converter of current/tide/wave energy', *Provisional Patent Application, US Patent and Trademark Office Serial*, no. 60/628,252.

Bernitsas, MM, Raghavan, K, Ben-Simon, Y & Garcia, EM 2008, 'VIVACE (vortex induced vibration aquatic clean energy): A new concept in generation of clean and renewable energy from fluid flow', *Journal of Offshore Mechanics and Arctic Engineering*, vol. 130, no. 4, pp. 1697–712.

Bishop, R & Hassan, A 1964, 'The lift and drag forces on a circular cylinder oscillating in a flowing fluid', in *Proceedings of the Royal Society of London A: Mathematical, Physical and Engineering Sciences*, vol. 277, pp. 51-75.

Blevins, RD 1997, *Flow-induced vibration*, Second edn, Van Nostrand Reinhold, New York

Blevins, RD & Coughran, CS 2009, 'Experimental investigation of vortex-induced vibration in one and two dimensions with variable mass, damping, and Reynolds number', *ASME J. Fluids Eng.*, vol. 131, no. 10, p. 101202.

Bokaian, A & Geoola, F 1984, 'Wake-induced galloping of two interfering circular cylinders', *Journal of Fluid Mechanics*, vol. 146, pp. 383-415.

Brika, D & Laneville, A 1993, 'Vortex-induced vibrations of a long flexible circular cylinder', *Journal of Fluid Mechanics*, vol. 250, pp. 481-508.

Brika, D & Laneville, A 1999, 'The flow interaction between a stationary cylinder and a downstream flexible cylinder', *Journal of Fluids and Structures*, vol. 13, no. 5, pp. 579-606.

Carmo, BS, Sherwin, SJ, Bearman, PW & Willden, RH 2008, 'Wake transition in the flow around two circular cylinders in staggered arrangements', *Journal of Fluid Mechanics*, vol. 597, pp. 1-29.

Celik, I & Shaffer, FD 1995, 'Long time-averaged solutions of turbulent flow past a circular cylinder', *Journal of Wind Engineering and Industrial Aerodynamics*, vol. 56, no. 2-3, pp. 185-212.

Chang, C-CJ, Kumar, RA & Bernitsas, MM 2011, 'VIV and galloping of single circular cylinder with surface roughness at 3.0× 10 4≤ Re≤ 1.2× 10 5', *Ocean Engineering*, vol. 38, no. 16, pp. 1713-32.

Derakhshandeh, JF, Arjomandi, M, Cazzolato, B & Dally, B 2014, 'Experimental and computational investigation of wake induced vibration', paper presented to 19th Australasian Fluid Mechanics Conference, Melbourne, Australia, 8 - 11 December 2014.

Derakhshandeh, JF, Arjomandi, M, Dally, B & Cazzolato, B 2014, 'The effect of arrangements of two circular cylinders on the maximum efficiency of vortex-induced vibration power using a scale-adaptive simulation model', *Journal of Fluids and Structures*, vol. 49, pp. 654-66.

Derakhshandeh, JF, Arjomandi, M, Dally, B & Cazzolato, B 2015a, 'Flow induced vibration of an elastically mounted aerofoil under the influence of oncoming vortices', *Journal of Physics of Fluids*, no. (under review).

Derakhshandeh, JF, Arjomandi, M, Dally, B & Cazzolato, B 2015b, 'Harnessing Hydro-Kinetic energy from wake induced vibration using virtual mass spring damper system', *Journal of Ocean Engineering*, vol. 108, pp. 115-28.

Derakhshandeh, JF, Arjomandi, M, Dally, B & Cazzolato, B 2015c, 'A study of the Vortex-Induced Vibration mechanism for harnessing hydrokinetic energy of eddies using a single cylinder', *Journal of Applied Mathematical Modelling*.

Deshmukh, NR & Deshmukh, SJ 2013, 'Development of modified wind turbine: A past review', *International Journal of Mechanical Engineering and Robotics Research*, vol. 2, no. 3, pp. 61-6.

Dick, E 1984, 'Momentum analysis of wind energy concentrator systems', *Energy Conversion and Management*, vol. 24, no. 1, pp. 19-25.

Ding, Z, Balasubramanian, S, Lokken, R & Yung, T 2004, 'Lift and damping characteristics of bare and straked cylinders at riser scale Reynolds numbers', in *Offshore Technology Conference*.

Dong, S, Karniadakis, G, Ekmekci, A & Rockwell, D 2006, 'A combined direct numerical simulation–particle image velocimetry study of the turbulent near wake', *Journal of Fluid Mechanics*, vol. 569, pp. 185-207.

Egorov, Y, Menter, F, Lechner, R & Cokljat, D 2010, 'The scale-adaptive simulation method for unsteady turbulent flow predictions. Part 2: Application to complex flows', *Flow, Turbulence and Combustion*, vol. 85, no. 1, pp. 139-65.

Fage, A & Johansen, FC 1927, 'On the flow of air behind an inclined flat plate of infinite span', *Proceedings of the Royal Society of London. Series A, Containing Papers of a Mathematical and Physical Character*, pp. 170-97.

Feng, C 1968, 'The measurement of vortex induced effects in flow past stationary and oscillating circular and d-section cylinders', University of British Columbia.

Figueiredo, SWO, Pereira, AA, Lins, EF, de Oliveira Silva, M & Vaz, JRP 2012, 'Experimental and numerical study of the velocity profile in a conical diffuser aiming the efficient design of a horizontal axis wind turbine', in *14th Brazilian Congress of Thermal Sciences and Engineering*, Rio de Janeiro, Brazil.

Fletcher, D & Langrish, T 2009, 'Scale-adaptive simulation (SAS) modelling of a pilot-scale spray dryer', *Chemical Engineering Research and Design*, vol. 87, no. 10, pp. 1371-8.

Franke, R & Rodi, W 1993, 'Calculation of vortex shedding past a square cylinder with various turbulence models', in *Turbulent Shear Flows 8*, Springer, pp. 189-204.

Gerrard, JH 1966, 'The mechanics of the formation region of vortices behind bluff bodies', *Journal of Fluid Mechanics*, vol. 25, no. 2, pp. 401-13.

Goldstein, RJ & Kulkarni, KS 2008, 'Energy Separation in the Wake of a Cylinder', *Journal of Heat Transfer*, vol. 130, no. 6, p. 061703.

Govardhan, R & Williamson, CHK 2000, 'Modes of vortex formation and frequency response of a freely vibrating cylinder', *Journal of Fluid Mechanics*, vol. 420, pp. 85-130.

Govardhan, R & Williamson, CHK 2004, 'Critical mass in vortex-induced vibration of a cylinder', *European Journal of Mechanics-B/Fluids*, vol. 23, no. 1, pp. 17-27.

Govardhan, R & Williamson, CHK 2006, 'Defining the modified Griffin plot in vortex-induced vibration: revealing the effect of Reynolds number using controlled damping', *Journal of Fluid Mechanics*, vol. 561, pp. 147-80.

Griffin, OM & Ramberg, SE 1974, 'The vortex-street wakes of vibrating cylinders', *Journal of Fluid Mechanics*, vol. 66, no. 3, pp. 553-76.

Gu, Z, Sun, T, He, D & Zhang, L 1993, 'Two circular cylinders in high-turbulence flow at supercritical Reynolds number', *Journal of Wind Engineering and Industrial Aerodynamics*, vol. 49, no. 1-3, pp. 379-88.

Guilmineau, E & Queutey, P 2004, 'Numerical simulation of vortex-induced vibration of a circular cylinder with low mass-damping in a turbulent flow', *Journal of Fluids and Structures*, vol. 19, no. 4, pp. 449-66.

Hansen, MOL 2013, *Aerodynamics of wind turbines*, Routledge.

Hiwada, M, Mabuchi, I & Yanagihara, H 1982, 'Fluid flow and heat transfer around two circular cylinders', *Bulletin of JSME*, vol. 25, no. 209, pp. 1737-45.

Hobbs, WB & Hu, DL 2012, 'Tree-inspired piezoelectric energy harvesting', *Journal of Fluids and Structures*, vol. 28, pp. 103-14.

Hover, F, Miller, S & Triantafyllou, M 1997, 'Vortex-induced vibration of marine cables: experiments using force feedback', *Journal of Fluids and Structures*, vol. 11, no. 3, pp. 307-26.

Huera-Huarte, F & Bearman, P 2009, 'Wake structures and vortex-induced vibrations of a long flexible cylinder—part 1: dynamic response', *Journal of Fluids and Structures*, vol. 25, no. 6, pp. 969-90.

Igarashi, T 1984, 'Characteristics of the flow around two circular cylinders arranged in tandem: 2nd report, unique phenomenon at small spacing', *Bulletin of JSME*, vol. 27, no. 233, pp. 2380-7.

Jamieson, PM 2009, 'Beating Betz: Energy Extraction Limits in a Constrained Flow Field', *Journal of Solar Energy Engineering*, vol. 131, no. 3, p. 031008.

Jauvtis, N & Williamson, C 2003, 'Vortex-induced vibration of a cylinder with two degrees of freedom', *Journal of Fluids and Structures*, vol. 17, no. 7, pp. 1035-42.

Jauvtis, N & Williamson, C 2004, 'The effect of two degrees of freedom on vortex-induced vibration at low mass and damping', *Journal of Fluid Mechanics*, vol. 509, pp. 23-62.

Karch, GK, Sadlo, F, Weiskopf, D, Hansen, CD, Li, G-S & Ertl, T 2012, 'Dye-based flow visualization', *Computing in Science & Engineering*, vol. 14, no. 6, pp. 80-6.

Khalak, A & Williamson, CHK 1996, 'Dynamics of a hydroelastic cylinder with very low mass and damping', *Journal of Fluids and Structures*, vol. 10, no. 5, pp. 455-72.

Khalak, A & Williamson, CHK 1997a, 'Fluid forces and dynamics of a hydroelastic structure with very low mass and damping', *Journal of Fluids and Structures*, vol. 11, no. 8, pp. 973-82.

Khalak, A & Williamson, CHK 1997b, 'Investigation of relative effects of mass and damping in vortex-induced vibration of a circular cylinder', *Journal of Wind Engineering and Industrial Aerodynamics*, vol. 69, pp. 341-50.

Khan, NB, Jameel, M, Badry, ABBM & Ibrahim, ZB 2016, 'Numerical study of flow around a smooth circular cylinder at Reynold number= 3900 with large eddy simulation using CFD code', in *ASME 2016 35th International Conference on Ocean, Offshore and Arctic Engineering*, pp. V002T08A16-VT08A16.

Kiya, M, Arie, M, Tamura, H & Mori, H 1980, 'Vortex shedding from two circular cylinders in staggered arrangement', *ASME J. Fluids Eng.*, vol. 102, no. 2, pp. 166-71.

Koopmann, G 1967, 'The vortex wakes of vibrating cylinders at low Reynolds numbers', *Journal of Fluid Mechanics*, vol. 28, no. 3, pp. 501-12.

Kuo, C, Chein, S & Hsieh, H 2008, 'Self-sustained oscillations between two tandem cylinders at Reynolds number 1,000', *Experiments in fluids*, vol. 44, no. 4, pp. 503-17.

Lee, J & Bernitsas, M 2011, 'High-damping, high-Reynolds VIV tests for energy harnessing using the VIVACE converter', *Ocean Engineering*, vol. 38, no. 16, pp. 1697-712.

Liaw, K 2005, 'Simulation of flow around bluff bodies and bridge deck sections using CFD', University of Nottingham.

Lin, J-C, Towfighi, J & Rockwell, D 1995, 'Instantaneous structure of the near-wake of a circular cylinder: on the effect of Reynolds number', *Journal of Fluids and Structures*, vol. 9, no. 4, pp. 409-18.

Ljungkrona, L 1992, *Characteristics of mean and fluctuating surface pressure distributions on tubes in tandem arrangement and in-line tube bundles*, Chalmers University of Technology.

Ljungkrona, L, Norberg, C & Sunden, B 1991, 'Free-stream turbulence and tube spacing effects on surface pressure fluctuations for two tubes in an in-line arrangement', *Journal of Fluids and Structures*, vol. 5, no. 6, pp. 701-27.

Ljungkrona, L & Sundén, B 1993, 'Flow visualization and surface pressure measurement on two tubes in an inline arrangement', *Experimental thermal and fluid science*, vol. 6, no. 1, pp. 15-27.

Lourenco, L & Shih, C 1993, 'Characteristics of the plane turbulent near wake of a circular cylinder', *A particle image velocimetry study.(data taken from Beaudan, Moin*.

Lu, X-Y & Dalton, C 1996, 'Calculation of the timing of vortex formation from an oscillating cylinder', *Journal of Fluids and Structures*, vol. 10, no. 5, pp. 527-41.

Menter, FR 1994, 'Two-equation eddy-viscosity turbulence models for engineering applications', *AIAA journal*, vol. 32, no. 8, pp. 1598-605.

Menter, FR & Egorov, Y 2005, 'A scale adaptive simulation model using two-equation models', in *43rd AIAA aerospace sciences meeting and exhibit*, p. 1095.

Menter, FR & Egorov, Y 2010, 'The scale-adaptive simulation method for unsteady turbulent flow predictions. Part 1: Theory and model description', *Flow, Turbulence and Combustion*, vol. 85, no. 1, pp. 113-38.

Moe, G, Holden, K & Yttervoll, P 1994, 'Motion of spring supported cylinders in subcritical and critical water flows', in *The Fourth International Offshore and Polar Engineering Conference*.

Nakamura, Y & Tomonari, Y 1982, 'The effects of surface roughness on the flow past circular cylinders at high Reynolds numbers', *Journal of Fluid Mechanics*, vol. 123, pp. 363-78.

Naudascher, E & Rockwell, D 2012, *Flow-induced vibrations: an engineering guide*, Courier Corporation.

Norberg, C 1998, 'LDV-measurements in the near wake of a circular cylinder', *ASME Paper No. FEDSM98-521*.

Ong, L & Wallace, J 1996, 'The velocity field of the turbulent very near wake of a circular cylinder', *Experiments in fluids*, vol. 20, no. 6, pp. 441-53.

Ozgoren, M, Pinar, E, Sahin, B & Akilli, H 2011, 'Comparison of flow structures in the downstream region of a cylinder and sphere', *International Journal of Heat and Fluid Flow*, vol. 32, no. 6, pp. 1138-46.

Ozono, S 1999, 'Flow control of vortex shedding by a short splitter plate asymmetrically arranged downstream of a cylinder', *Physics of Fluids*, vol. 11, pp. 2928-34.

Pan, Z, Cui, W & Miao, Q 2007, 'Numerical simulation of vortex-induced vibration of a circular cylinder at low mass-damping using RANS code', *Journal of Fluids and Structures*, vol. 23, no. 1, pp. 23-37.

Parkinson, GV 1989, 'Phenomena and modelling of flow-induced vibrations of bluff bodies', *Progress in Aerospace Sciences*, vol. 26, no. 2, pp. 169-224.

Parkinson, GV & Dicker, D 1971, 'Wind-induced instability of structures', *Philosophical Transactions of the Royal Society of London A: Mathematical, Physical and Engineering Sciences*, vol. 269, no. 1199, pp. 395-413.

Raghavan, K & Bernitsas, M 2011, 'Experimental investigation of Reynolds number effect on vortex induced vibration of rigid circular cylinder on elastic supports', *Ocean Engineering*, vol. 38, no. 5, pp. 719-31.

Rajagopalan, S & Antonia, R 2005, 'Flow around a circular cylinder—structure of the near wake shear layer', *Experiments in fluids*, vol. 38, no. 4, pp. 393-402.

Roshko, A 1954, *On the drag and shedding frequency of two-dimensional bluff bodies*, DTIC Document.

Roshko, A 1961, 'Experiments on the flow past a circular cylinder at very high Reynolds number', *Journal of Fluid Mechanics*, vol. 10, no. 3, pp. 345-56.

Sagaut, P 2006, *Large eddy simulation for incompressible flows: an introduction*, Springer Science & Business Media.

Sarpkaya, T 1979, 'Vortex-induced oscillations: A selective review', *Journal of applied mechanics*, vol. 46, no. 2, pp. 241-58.

Sarpkaya, T 2004, 'A critical review of the intrinsic nature of vortex-induced vibrations', *Journal of Fluids and Structures*, vol. 19, no. 4, pp. 389-447.

Singh, S & Mittal, S 2005, 'Vortex-induced oscillations at low Reynolds numbers: hysteresis and vortex-shedding modes', *Journal of Fluids and Structures*, vol. 20, no. 8, pp. 1085-104.

Sumer, BM & Fredsøe, J 2006, *Hydrodynamics around cylindrical structures*, World Scientific.

Tritton, D 1959, 'Experiments on the flow past a circular cylinder at low Reynolds numbers', *Journal of Fluid Mechanics*, vol. 6, no. 4, pp. 547-67.

Tutar, M & Holdo, AE 2000, 'Large eddy simulation of a smooth circular cylinder oscillating normal to a uniform flow', *ASME J. Fluids Eng.*, vol. 122, no. 4, pp. 694-702.

Vikestad, K 1998, 'Multi-frequency response of a cylinder subjected to vortex shedding and support motions. Dr. Ing', thesis. Department of Marine Structures, Norwegian University of Science and Technology.

Wang, D-A & Ko, H-H 2010, 'Piezoelectric energy harvesting from flow-induced vibration', *Journal of Micromechanics and Microengineering*, vol. 20, no. 2, p. 025019.

Weinstein, LA, Cacan, MR, So, PM & Wright, PK 2012, 'Vortex shedding induced energy harvesting from piezoelectric materials in heating, ventilation and air conditioning flows', *Smart Materials and Structures*, vol. 21, no. 4, p. 045003.

Williamson, CHK 1985, 'Sinusoidal flow relative to circular cylinders', *Journal of Fluid Mechanics*, vol. 155, pp. 141-74.

Williamson, CHK & Govardhan, R 2004a, 'Critical mass in vortex-induced vibrations of a cylinder', *European Journal of Mechanics-B/Fluids*, vol. 23, pp. 17-27.

Williamson, CHK & Govardhan, R 2004b, 'Vortex-induced vibrations', *Annual Review of Fluid Mechanics*, vol. 36, pp. 413-55.

Williamson, CHK & Roshko, A 1988, 'Vortex formation in the wake of an oscillating cylinder', *Journal of Fluids and Structures*, vol. 2, no. 4, pp. 355-81.

Zdravkovich, MM 1977, 'Review of flow interference between two circular cylinders in various arrangements', *ASME J. Fluids Eng.*, vol. 99, no. 4, pp. 618-33.

Zdravkovich, MM 1982, 'Modification of vortex shedding in the synchronization range', *ASME J. Fluids Eng.*, vol. 104, no. 4, pp. 513-7.

Zdravkovich, MM 1996, 'Different modes of vortex shedding: an overview', *Journal of Fluids and Structures*, vol. 10, no. 5, pp. 427-37.

Zdravkovich, MM 1997, 'Flow around circular cylinders, vol. 1. Fundamentals', *Journal of Fluid Mechanics*, vol. 350, pp. 377-8.

Zdravkovich, MM & Bearman, PW 1998, *Flow Around Circular Cylinders—Volume 1: Fundamentals*, American Society of Mechanical Engineers, 0098-2202.

This page is intentionally left blank

Chapter 3. Spatial and temporal concentration of flow energy

Published numerical and experimental investigations have explored the phenomenon of VIV in detail. Leading on from research on VIV, WIV has also gained popularity in research for the applicability to harnessing energy from flows. The circular cylinder has been the most common candidate for VIV and WIV of bluff bodies and published literature contains detailed information about the vibration and wake characteristics of a circular cylinder. However, the concept of spatial and temporal energy concentration by the circular cylinder has not been investigated and reported in published literature.

Regions of time-averaged maximum energy density in the wake of a bluff body were determined in previous studies. However, this is a spatial energy concentration comparable to diffusers, which are known to have large energy losses and pose problems due to their large size. Considering bluff body wakes, there is an element of temporal energy concentration in addition to the spatial concentration. Hence the combined effect may lead to high energy density zones in the wake. If a Power-Take-Off (PTO) device had the correct impedance and properties to harness these energy regions, a significant amount of energy can be extracted from the flow. Thus there is a gap regarding the scientific concept of spatial and temporal concentration of energy by bluff bodies such as cylinders, as well as its use in extracting energy from currents.

This chapter investigated and established the concept of temporal and spatial concentration of flow energy by the circular cylinder. The energy available in the wake of the circular cylinder is analysed using three-dimensional computational modelling to model the cylinders

numerically utilizing the Scale Adaptive Simulation (SAS) model, which is a turbulence model that utilizes both Large Eddy Simulation (LES) and Reynolds-Averaged Navier-Stokes (RANS) concepts to resolve turbulence. The zones of peak temporal energy in the wake of the cylinder are identified and the maximum extractable energy by an ideal PTO are examined in the first part of this paper. Additionally, several bluff body cross-sections are also examined, using similar numerical analysis, to provide comparisons among the different energy components in the wakes of the bodies. The transverse wake energy component is a potential contributor to WIV of the downstream body; and the semi-circular and convex-edged triangular cylinders were shown to provide zones with higher temporal energy in the transverse direction compared to the circular cylinder. These results can be used to design efficient WIV energy systems with an upstream body that can provide more temporally concentrated energy than the industry standard (circular cylinder).

This chapter has been submitted for publication as:

Manickam Sureshkumar, E, Arjomandi, A, Cazzolato, B & Dally, B, 2018 'Spatial and temporal concentration of hydrokinetic energy in the wake of a bluff body', *Journal of Ocean Engineering*, no. 164, pp. 181-198.

Statement of Authorship

Title of Paper	Spatial and temporal concentration of hydrokinetic energy in the wake of a bluff body
Publication Status	☐ Published ☑ Accepted for Publication ☐ Submitted for Publication ☐ Unpublished and Unsubmitted w ork w ritten in manuscript style
Publication Details	Manickam Sureshkumar, E, Arjomandi, M, Cazzolato, B, Dally, B, 'Spatial and temporal concentration of hydrokinetic energy in the wake of a bluff body', *Journal of Ocean Engineering*, (in press)

Principal Author

Name of Principal Author (Candidate)	Eshodarar Manickam Sureshkumar		
Contribution to the Paper	Three-dimensional numerical modelling of a circular cylinder and other cross-sections using ANSYS FLUENT. Validated simulations and post processing of wake data to obtain the spatial and temporal concentration of flow energy.		
Overall percentage (%)	85		
Certification:	This paper reports on original research I conducted during the period of my Higher Degree by Research candidature and is not subject to any obligations or contractual agreements with a third party that would constrain its inclusion in this thesis. I am the primary author of this paper.		
Signature		Date	22/06/2018

Co-Author Contributions

By signing the Statement of Authorship, each author certifies that:

i. the candidate's stated contribution to the publication is accurate (as detailed above);
ii. permission is granted for the candidate in include the publication in the thesis; and
iii. the sum of all co-author contributions is equal to 100% less the candidate's stated contribution.

Name of Co-Author	Maziar Arjomandi		
Contribution to the Paper	Supervised the work, assisted in developing ideas and manuscript evaluation		
Signature		Date	22/06/2018
Name of Co-Author	Benjamin S. Cazzolato		
Contribution to the Paper	Supervised the work, assisted in developing ideas and manuscript evaluation		
Signature		Date	22/6/18
Name of Co-Author	Bassam B. Dally		
Contribution to the Paper	Supervised the work, assisted in developing ideas and manuscript evaluation		
Signature		Date	25/06/2018
Name of Co-Author			
Contribution to the Paper			
Signature		Date	

This page is intentionally left blank

Article

Title - Spatial and temporal concentration of hydrokinetic energy in the wake of a bluff body

Authors – Eshodarar Manickam Sureshkumar (Corresponding Author), Maziar Arjomandi, Benjamin S. Cazzolato, Bassam B. Dally

Affiliation – The University of Adelaide

Address – School of Mechanical Engineering, The University of Adelaide, North Terrace, Adelaide, SA, 5005

Abstract:

Numerical simulations of a rigid, stationary, bluff body were performed using three-dimensional Computational Fluid Dynamics (CFD) and validated against published data. Bluff body cross sections such as the circle, semi-circle, straight-edged triangle, concave-edged triangle and convex-edged triangle were modelled at a Reynolds number of 10,000 in ANSYS FLUENT (v17.1). The streamwise and transverse wake energy components were investigated using Fourier analysis to analyse the spatial and temporal concentration of bluff bodies. The simulation results of the circular cylinder are compared against known experimental values and there was good agreement for the flow characteristics. The time-averaged energy in the wake, for all the shapes, does not present significant augmentation in the wake, except for a 60% increase in the streamwise kinetic energy near the surface of the cylinder due to a jetting effect (spatial concentration). Maxima for the temporal fluctuations in kinetic energy components (u' and v') occur between a streamwise distance of $1 < x/D < 3$ and a transverse distance of $0 < |y/D| < 1$ and occur mostly at the shedding frequency. Since WIV is vibration that is enhanced by fluctuations in the wake, a cross-section which increases temporal energy can lead to more energy captured by such a system. Changing the cross-section of the cylinder changes the distribution of the wake energy, where the convex-edged triangle and semi-circular cylinders demonstrated the greatest concentration of energy in transverse velocity fluctuations compared to others (1.5 times the freestream energy).

Key words: Bluff body; Spatial and Temporal; Wake Induced Vibration; Energy concentration; Wake Energy; CFD.

Nomenclature:

x	streamwise direction
y	transverse direction
z	spanwise direction
u	streamwise velocity (m/s)
v	transverse velocity (m/s)
w	spanwise velocity (m/s)
u'	fluctuating component of the streamwise velocity
v'	fluctuating component of the transverse velocity
w'	fluctuating component of the spanwise velocity
fs	vortex shedding frequency of the cylinder
ρ	density of the fluid
P	static pressure
k	turbulent kinetic energy
P_0	static pressure in the freestream, free from any disturbance
ρ_0	density of water in the freestream (998.2 kg/m^3 at 20^{o}C)
U_0	velocity of fluid in the freestream
$\bar{C}_{\mathrm{D}}$	mean drag coefficient
C_p	pressure coefficient
$\bar{C}_{\mathrm{pb}}$	mean back pressure coefficient
C_{L}	root mean square (r.m.s) lift coefficient
St	Strouhal number

Re Reynolds number

$E_{\overline{u}}$ mean normalised streamwise energy

$E_{\overline{v}}$ mean normalised transverse energy

$E_{\overline{w}}$ mean normalised spanwise energy

$E_{u'_{fs}}$ normalised energy due to fluctuating streamwise component at *fs*

$E_{v'_{fs}}$ normalised energy due to fluctuating transverse component at *fs*

$E_{w'_{fs}}$ normalised energy due to fluctuating spanwise component at *fs*

$u_{mag\ ps}$ power spectrum magnitude obtained for the streamwise velocity at the primary shedding frequency

$v_{mag\ ps}$ power spectrum magnitude obtained for the transverse velocity at the primary shedding frequency

$w_{mag\ ps}$ power spectrum magnitude obtained for the spanwise velocity at the primary shedding frequency

1 Introduction

There is a growing worldwide demand for energy due to the ever-increasing population, increased energy consumption and desire for improved quality of life (Bilgen et al. 2008). Future energy needs and its sources are a popular topic among environmentalists, governments and scientists around the world. A large proportion of energy is produced via combustion of non-renewable fossil fuels which are dwindling due to their limited quantities (Kaltschmitt, Streicher & Wiese 2007). The desire to transition to more sustainable energy and low carbon intensity are major drivers of new environmental policies and technology development. Renewable energy sources are expected to play a key role in this transition. However, it is predicted that by the year 2035, global energy demand will increase by 53% over the level in 2008, while renewable energy sources are predicted to increase to only 16% over the same period (USEIA 2011). Hence there is an interest in exploring other avenues to find viable, clean and abundant energy sources. Besides wind, solar, geothermal and hydro-electric (based on hydrostatic head pressure) energy sources, hydrokinetic energy (based on the kinetic energy in flows and waves) is a widely untapped resource of renewable energy.

Energy convertors for hydrokinetic energy can be classified by the nature of the utilized space in which they operate. Hydrokinetic energy convertors include point absorbers, such as surface buoys (Johnson & Pride 2010); line absorbers, such as the Pelamis attenuator (Lagoun, Benalia & Benbouzid 2010); horizontal surface patch absorbers, such as oscillating water columns (Heath 2012); vertical surface absorbers, such as turbines and open propellers (Batten et al. 2006); and three dimensional space absorbers such as devices which operate using

Vortex Induced Vibrations (VIV), for example the Vortex Induced Vibration for Aquatic Clean Energy (VIVACE) Converter (Bernitsas et al. 2009). Turbines, which are the most popular hydrokinetic energy convertor, operate at efficiencies of about 20% to 55% (Hansen, MO 2015; Vries 1983), and usually need high start-up flow speeds (Khan et al. 2009).

Flow energy can be split up in to spatial and temporal energy. The definition arises from the steady component and the unsteady, fluctuating component in the flow. The steady component is defined as the mean component of the flow which gives a steady value over time, whereas the unsteady component arises from fluctuations in the flow. Hence, spatial flow energy concentrators would perform better in situations with steady flow conditions (i.e. upstream of turbines), whilst temporal flow concentrators are needed for devices which operate utilising the temporal flow energy.

Spatial flow energy concentrators, such as diffusers, have been analysed ever since the Betz limit was established for turbines and other vertical surface absorbers (Dick 1984). In theory diffusers can result in a combined system efficiency of 89% (Hansen, MOL, Sørensen & Flay 2000; Jamieson 2008), however, in practice duct augmented turbines have not been able to reach such a high power coefficient (Khan et al. 2009). Diffusers fall under the class of spatial energy concentrators, where energy is augmented at specific locations in the flow field.

There are many different types of diffusers, and each has their own merits and limitations (Gaden & Bibeau 2006; Ohya et al. 2001; Ponta, Fernando & Dutt 2000; Ponta, FL & Jacovkis 2008; Setoguchi, Shiomi & Kaneko 2004). In addition to spatial concentration, temporal concentration can further increase power densities that can be obtained

from a hydrokinetic energy convertor system. A combination of spatial and time-dependant energy concentration (i.e. temporal concentration) can be achieved using bluff bodies as shown in previous studies (Assi 2009; Bernitsas et al. 2008; Derakhshandeh et al. 2014). The concentration is time specific due to the characteristic von-Karman vortex street that forms in the wakes of bluff bodies.

Circular cylinders have received the most attention amongst bluff bodies in a cross-flow. There are numerous review papers on the vibration response of single circular cylinders and the factors that affect it due to early research being focused on mitigating the phenomenon to reduce failure in engineered structures (King 1977; Sarpkaya, Turgot 1979; Sarpkaya, T 2004; Williamson, C & Govardhan 2004, 2008). The current state of art has shifted focus to harness the vibrations in bluff bodies exposed to cross-flow, to produce useful, clean and renewable energy (Bernitsas et al. 2008; Derakhshandeh et al. 2014, 2015a, 2016; Hansen, MOL, Sørensen & Flay 2000). In VIV energy harnessing systems, it has been identified that tandem bodies result in higher power efficiencies when compared to the single bluff body case because they can generate a larger temporal component. A stationary upstream bluff body in a flow produces a vortex street, and hence the downstream body operates in a wake containing spatially and temporally concentrated hydrokinetic energy. Transverse vibration amplitudes, of cylinders undergoing VIV, are about 3 times greater than the streamwise amplitudes, and hence been of more interest for energy generating potential (Bernitsas et al. 2008; Hobbs & Hu 2012; Wang & Ko 2010).

There exist two different classes of devices which utilise VIV for energy generation and this is based on the energy output of the device. Many small-scale devices using a combination of VIV and piezoelectric

transduction have been investigated to provide power for wireless sensing devices. Although these devices can vary in configuration, most of them use a circular or triangular cross section bluff body to produce vortices which impinge on to a beam containing piezoelectric materials. These devices usually provide power in the order of milli-watts and have very low efficiencies (Hobbs & Hu 2012; Wang & Ko 2010; Weinstein et al. 2012).

Larger scale devices which operate using VIV are aimed at providing useful energy to the grid from low speed currents in oceans and rivers. A prototype known as the Vortex Induced Vibration Aquatic Clean Energy (VIVACE) generator was developed by Bernitsas et al. (2008), who pioneered the energy harnessing potential of VIV and have continued to research the field (Bernitsas 2011; Bernitsas et al. 2009; Bernitsas & Raghavan 2004; Bernitsas et al. 2008; Chang, Kumar & Bernitsas 2011; Lee & Bernitsas 2011). The theoretical efficiency of power conversion for VIV of a single cylinder unit was calculated to be 37% at a Reynolds number of 100,000. However, the maximum power obtained via experiments conducted on a single cylinder system was 22%. This sparked more interest in the field to improve the energy harnessing efficiency from VIV. Very recent experimental work by Ding et al. (2016) demonstrated that higher efficiencies (η = 37%) can be obtained at lower Reynolds numbers (Re = 60,000) using passive turbulence control by attaching roughness strips to the cylinder. Most research on VIV for energy has been performed on circular cylinders due to the abundant research available on the flow features of a circular cylinder (Braza, Chassaing & Minh 1986; Cantwell & Coles 1983; Ong & Wallace 1996; Williamson, CHK 1996).

Derakhshandeh et al. (2014) have shown the feasibility of Vortex and Wake Induced Vibrations (VIV and WIV respectively) to harness hydrokinetic energy. A transverse spacing of $0 < y/D < 1$ and streamwise spacing of $3 < x/D < 4$, between tandem staggered cylinders provided maximum energy harnessing efficiency ($\eta = 48.4\%$) for a cylinder with diameter equal to D at a Reynolds number of 65,000 (Derakhshandeh et al. 2014). The power generating potential of VIV has been confirmed by these studies and further work, in particular on the flow field in between the cylinders, is required to identify an efficient and realisable system.

Other bluff bodies have also been tested for the purpose of Flow Induced Motion (FIM). Although the vibration responses of single bluff bodies such as square cylinders (Amandolèse & Hémon 2010; Barrero-Gil & Fernandez-Arroyo 2013; Nemes et al. 2012), triangular prisms (Alonso & Meseguer 2006; Alonso, Meseguer & Pérez-Grande 2005), and a comparison between various bodies (Ding et al. 2015) have been studied in extant literature, analysis of the energy concentration in their wake has not been investigated. Additionally, these investigations analysed the vibration responses of the bodies, but there has been no mention of the energy in the wake produced by bodies of different cross-sections.

Past studies have established that a bluff body placed with proper spacing in front of a vibrating bluff body enhances the VIV response of the downstream body (Derakhshandeh et al 2016b). The spacing has been varied to find the optimum spacing that results in high power efficiency for the system for various shapes and sizes of cylinders. The attributing cause to the response is due to impedance matching which occurs when the velocity of the vibrating body and the forces acting on it are in phase. However, extant literature has not yet identified the

contribution of the frequency and magnitude of the velocity components that attribute to a higher energy harnessing potential. It is clear from previous studies that the concentration in the wake of a bluff body is not only spatial in nature, but has a temporal attribute as well, due to the unsteady components which occur at different frequencies and velocities. There exists a gap in the understanding of the contribution of the different wake velocity components to the energy in the wake and how these components result in the temporal and spatial concentration of the upstream energy in the flow. Understanding the factors which contribute to the observed responses, can lead to knowledge on how these components can be manipulated to result in a high efficiency system. Based on the above, this work aims to start this investigation by developing a validated Computational Fluid Dynamics (CFD) and Fourier analysis on the wake of different bluff bodies to characterise the spatial and temporal variation of the streamwise and transverse velocity components (u and v respectively). Although there are many different bluff bodies, the circular cylinder was considered in this paper as a starting point of investigation since there are numerous experimental data available for the validation of the circular cross-section. Following the circular cylinder, several other cross-sections such as the semi-circular cylinder and equilateral triangles with curved sides were analysed. The proceeding section details the methodology utilised in this paper, which is followed by the results and their discussion, and finally the main findings are summarised in the conclusion.

2 Method

Transient velocity data in the wake of the cylinder are needed to analyse the contribution of the streamwise and crosswise components. To gather these data, three-dimensional (3D) CFD simulations were performed using ANSYS FLUENT (v 17.1). A 3D model was simulated in order to resolve the turbulent spectrum using the SAS model rather than compute the isotropic turbulence that is characteristic of Reynolds Averaged Navier Stokes (RANS) models. Even though the CFD model was performed in 3D, only the velocities in the transverse and streamwise directions were collected and used for analysis as the primary focus was on the distribution of the transverse fluctuations which contribute to the transverse vibrations that are desired in WIV systems. A validated CFD model was deemed appropriate for the purpose of this research, due to the existence of experimental data available at high Reynolds numbers for circular cylinders. A circular cylinder was used as the bluff body since it is the most investigated bluff body for VIV, and serves as a good starting point for the wake analysis. A Reynolds number of 10,000 was used since it is still in the transition-in-the-shear layer regime (Zdravkovich 1997), as well as being high enough to cover real world applications. Existing experimental and computational work were available to validate the CFD model. A detailed account of the methods and validation used for the circular cylinder case are presented in this section.

2.1 Grid Definition

The mesh for the flow domain was created using the ANSYS meshing software and the resulting mesh is shown in Figure 1.

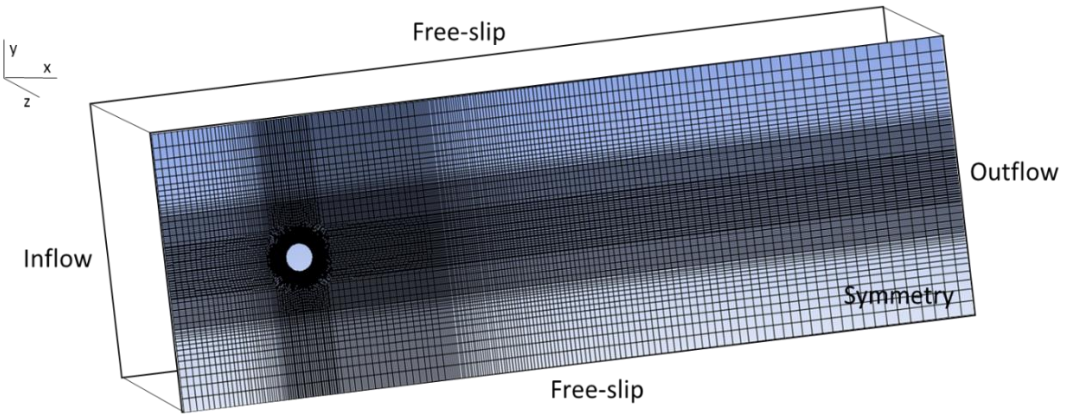

Figure 1 – Structured mesh generated using ANSYS Meshing (Test Case 2 in Table 1). The mesh around the cylinder is finer than the rest of the domain to capture the shear layers accurately.

The first layer height of 0.0017D was chosen to maintain a non-dimensional wall distance, y-plus of 1 near the cylinder wall region. Sensitivity of the mesh size was also tested by using three different sizes for each type of mesh. The details of the different meshes used are given in Table 1 and grid 2 proved to be sufficient for this analysis.

Table 1 - Details of the different meshes used in this study

Grid No	Grid	Nodes on cylinder	Nodes in Boundary layer	Nodes in the wake (*)	Spanwise nodes	Max wake element size (*)	Total meshing nodes (x10^6)
1	Coarse	50	20	250	15	0.020D	1.95
2	Slightly refined	100	30	500	30	0.015D	4.20
3	Highly refined	200	40	750	50	0.010D	7.95

(*) the max wake element size was computed for the elements in the near wake (< 5D) and there was no biasing in this area to maintain isotropic cells for efficient resolution of turbulence length scales.

2.2 Numerical method and mathematical modelling

The 3D form of the incompressible Navier-Stokes equations was solved using a finite-volume scheme with second order spatial and temporal discretization. The pressure-based solver was used and solved with double precision. The domain used for this study is presented in Figure 1. The rectangular fluid domain extends 25D downstream of the cylinder and 5D on either side, where the diameter (D) of the cylinder is 30mm. The cylinder is placed 5D from the velocity inlet and has a span wise depth of 3D, which is similar to that used in other published CFD work (Cao & Xiang 2001; Derakhshandeh et al. 2014, 2015b; Wei, Sekine & Shimura 1995). The large boundary distances were chosen to negate blockage effects and to prevent reversed flow from the pressure-outlet. The transverse boundary spacing results in a blockage ratio of about 4% which can be considered negligible as shown in previous studies (Derakhshandeh et al. 2014; Wanderley et al. 2008).

The top and bottom boundaries, and the span wise boundaries were defined as free slip walls to negate blockage effects and to prevent boundary layers developing on these surfaces. A no-slip wall condition was applied to the cylinder wall and the mesh was concentrated around the cylinder to accurately resolve the boundary layer. The streamwise (x), transverse (y) and spanwise (z) distances are measured from the centre of the cylinder.

The Navier-Stokes equations for the conservation of mass (Equation 2.1) and momentum (Equation 2.2) for three-dimensional, viscous, incompressible flow with constant density are solved in the CFD model and are as follows:

$$\frac{\partial u_i}{\partial x_i} = 0, \tag{2.1}$$

$$\frac{\partial u_i}{\partial t} + u_j \frac{\partial u_i}{\partial x_j} = -\frac{1}{\rho}\left(\frac{\partial P}{\partial x_i}\right) + \vartheta \frac{\partial^2 u_i}{\partial x_j^2} - \frac{\overline{u'_i u'_j}}{\partial x_j}\,, \tag{2.2}$$

where,

x represents the direction

u is the mean velocity component in x, y and z directions

u' is the fluctuating component of the velocity

ρ is the density of the fluid

P denotes the pressure.

The term $\overline{u'_i u'_j}$ presents the Reynolds stress component which is defined in terms of a turbulent viscosity ϑ_t as

$$-\frac{\overline{u'_i u'_j}}{\partial x_j} = \vartheta_t \left(\frac{\partial u_i}{\partial x_j} + \frac{\partial u_j}{\partial x_i}\right) - \frac{2}{3}\, k\delta_{ij}\,, \tag{2.3}$$

where, k is the turbulent kinetic energy and δ_{ij} is the Kronecker delta function.

The Scale-Adaptive Simulation (SAS) model, which is a form of Scale Resolving Simulations (SRS), was used to model the turbulence in the CFD simulation. The SAS model is an improved form of the Unsteady Reynolds-Averaged Navier-Stokes (URANS) formulation, and differs from classic URANS models in its ability to resolve the turbulence spectrum. The URANS models such as SST are only able to model large-scale unsteadiness whereas the SAS model can resolve spectral content in the detached regions.

Turbulence length-scale in the SAS model is resolved by considering the definition of Von Karman length scale. SAS overcomes the deficiency of other URANS models in resolving the turbulence

length-scale by considering the definition of Von Karman length scale. This assists in more accurately to capturing the vortex structure in the wake of the structure. The Von Karman length scale is given by:

$$L_{vk} = k \left| \frac{\partial U/\partial y}{\partial^2 U/\partial y^2} \right|. \qquad (2.4)$$

The SAS model uses the von Karman length scale to adapt its behaviour to SRS according to the stability parameters of the flow (Egorov *et al.* 2010) and provides a balance between the contributions of the simulated and resolved parts of the turbulence stresses. Hence, the model can effectively and automatically switch from the Large Eddy Simulation (LES) mode to the Reynolds Averaged-Navier Stokes (RANS) mode (Menter & Egorov 2010). Further derivation and information on this model can be found in Menter and Egorov (2010) and in ANSYS help version 17.1.0.

Compared to Reynolds-Averaged Navier-Stokes (RANS) models such as the k-ω Shear Stress Transport (SST) model, SAS is able to capture vortical structures effectively as shown by previous studies (Derakhshandeh et al. 2014, 2016).

Identical initial and boundary conditions were used for all the cases. A time step size of 0.5 milliseconds was needed to satisfy the Courant-Friedrichs-Lewy condition (CFL < 1), which is essential for convergence of the CFD simulation. However, the simulations for test cases 2 and 3 were run at both 0.1 ms and 1 ms and there was no difference observed in the results for the drag coefficient, lift coefficient and Strouhal number. Hence, a time step of 1ms was chosen for the rest of the simulations. The chosen time step was also sufficient to resolve the time scales in the fluid flow, as there are approximately 416 time steps per vortex shedding cycle (shedding frequency = 2.2 Hz). A

streamwise velocity of 0.335 m/s was defined at the inlet boundary and the outlet had a gauge pressure of 0 Pa. This inlet velocity resulted in a Reynolds number of 10,000 computed using properties of water at 25°C (density, ρ = 997.1 and dynamic viscosity, μ = 0.001003).

Results showed that the shear layers first form on either side of the cylinder and start to interact to produce the vortex street as the simulation time progresses. Hence, the solution needs to be allowed to establish in order for the vortex street to fully develop and regular vortex shedding is observed. The model was initialised with a steady state solution in order to reduce the time for established flow. The CFD model was deemed to be established when steady-state sinusoidal behaviour is observed for the lift and drag coefficients of the cylinder, which occurred within 10 seconds of flow time from the start of the simulation. A convergence criterion of 10^{-5} was used for all the residuals, and this resulted in a maximum of 12 iterations for each time step.

2.3 Post processing methods

Transient velocity data were gathered in the cylinder wake along the spanwise centre (1.5D away from the symmetry walls) of the domain during the simulation. The wake velocity data were time-averaged to analyse the mean components and decomposed using Fast Fourier Transforms (FFT) to identify the contribution of the fluctuating velocity components (u' and v'). Utilising this information, the kinetic energy due to these components was computed. Velocity data from 10,000 time steps were used as the input for the FFT analysis of the wake. The FFT analysis was used to identify the dominant frequencies of the fluctuating components as well as the magnitude at which they appear in the wake.

The *pwelch* function in MATLAB was used to perform a Welch's power spectrum estimate of the fluctuating streamwise and transverse velocity components. The transient velocity data were de-trended and the DC mean was removed from the signal. The data were then normalised using the freestream velocity (0.335 m/s). A flat top window was used with 50% overlap to get the magnitude of the power at different frequencies in the power spectrum. The FFT used 10000 points to have sufficient resolution for the frequencies considered, whilst still managing to capture the peak from the power spectrum.

The output from the velocity power spectrum has units of m^2/s^2 and hence represents the normalised energy contained in the fluctuating component at the frequency of interest. The energy obtained from the spectrum was a ratio compared to the available free stream energy since the input to the Welch power spectrum was the velocity data normalised by the free stream velocity.

These data were used to analyse the temporal and spatial distribution of the wake augmented energy, which can then be correlated to identify optimum locations for known Wake Energy Extractors (WEEs). This was accomplished by identifying the shedding frequency and its harmonics occurring in the wake, and then finding the magnitude of energy contribution from the power spectrum.

2.4 Validation of the CFD model

The CFD model was validated using experimental data from previous publications to demonstrate the accuracy of the model. The pressure coefficient on the surface of the cylinder was compared to the experimental data at similar Reynolds numbers (Dong et al. 2006). The

equation used to calculate the pressure coefficient is given below, with a description of the variables used.

$$C_p = \frac{P - P_0}{\frac{1}{2}\rho_0 U_0^2}$$

P - Static pressure at the location where the pressure coefficient is being evaluated

P_0 - Static pressure in the freestream, free from any disturbance

ρ_0 - Density of water in the freestream (998.2 kg/m^3 at 20°C)

U_0 - Velocity of fluid in the freestream

The time-averaged pressure coefficient around the top half of the cylinder surface is plotted in Figure 2. The pressure coefficient distribution obtained from the CFD simulation showed a similar trend to experimental values and had a minimum around 70 degrees which agrees well with extant literature (Dong et al. 2006; Norberg 1992).

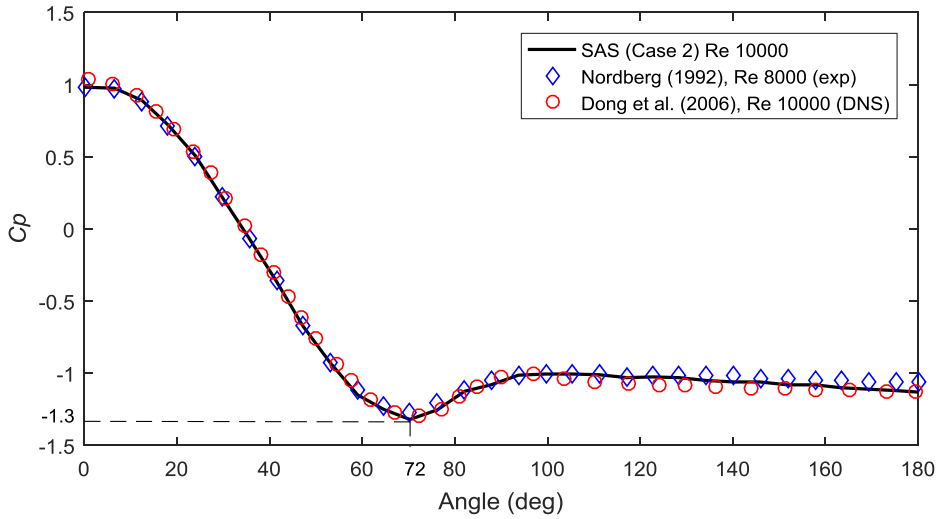

Figure 2 - Pressure coefficient over the top half of the circular cylinder

Table 2 - Comparison of physical quantities for a circular cylinder at Re = 10000: Drag coefficient Cd, base pressure coefficient -C_{Pb}, Strouhal number St, r.m.s lift coefficient C_L. Adapted from (Dong et al. 2006) with results from current research

	$\bar{C}_{\mathrm{D}}$	$\bar{C}_{\mathrm{pb}}$	St	C_{L}
Current research SAS (Grid 1)	1.32	1.38	0.212	0.57
Current research SAS (Grid 2)	1.21	1.31	0.205	0.52
Current research SAS (Grid 3)	1.20	1.31	0.205	0.52
Wieselsberger (1921)	1.104	-	-	-
Bishop & Hassan (1964)	-	-	0.201	0.463
Nordberg (1987)	-	1.21	0.201	-
Moeller & Leehey (1984)	-	-	-	0.532
Gopalkrishnan (1993)	1.186	-	0.193	0.384
West & Apelt (1993)	-	-	-	0.461
Nordberg (2003)	-	-	0.202	0.394

The independence of the solution from the grid was analysed by testing the three different mesh configurations. The mesh sizes were varied and integral parameters such as the mean drag coefficient ($\bar{C}_{\mathrm{D}}$), the back pressure ($\bar{C}_{\mathrm{pb}}$), root mean square (r.m.s) lift coefficient (C_{L}) and Strouhal number (St) were monitored in the current work and are presented in Table 2 along with values from experiments. Based on these results, grid 2 and 3 had a difference of less than 5% for the parameters considered and hence case 2 was used for this paper and the drag and lift coefficients are plotted in Figure 3.

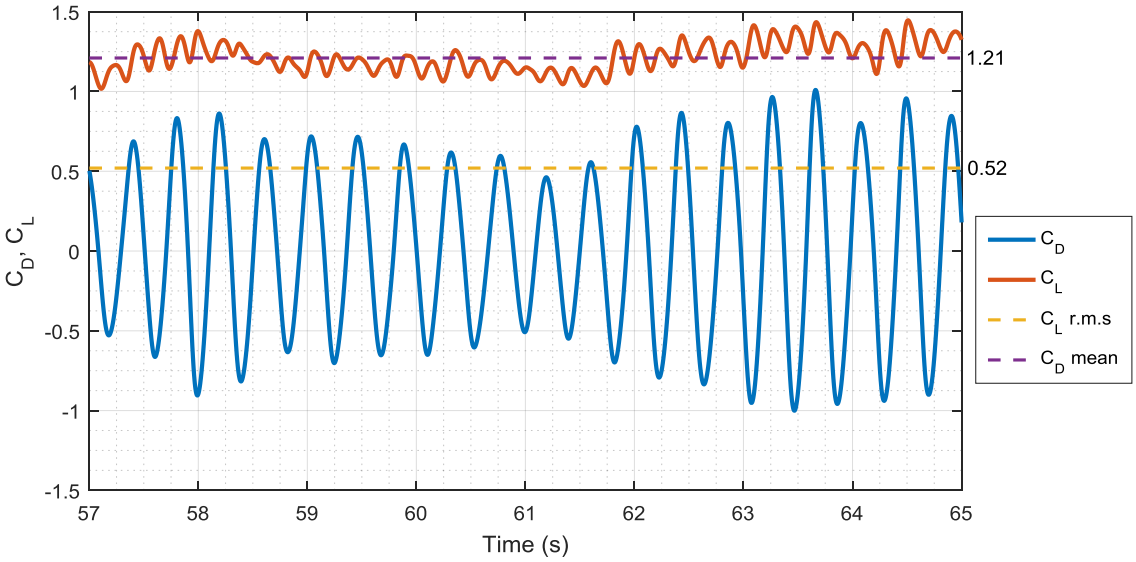

Figure 3 - Lift and Drag coefficients for the circular cylinder at a Reynolds number of 10000 from the SAS model (Grid 2)

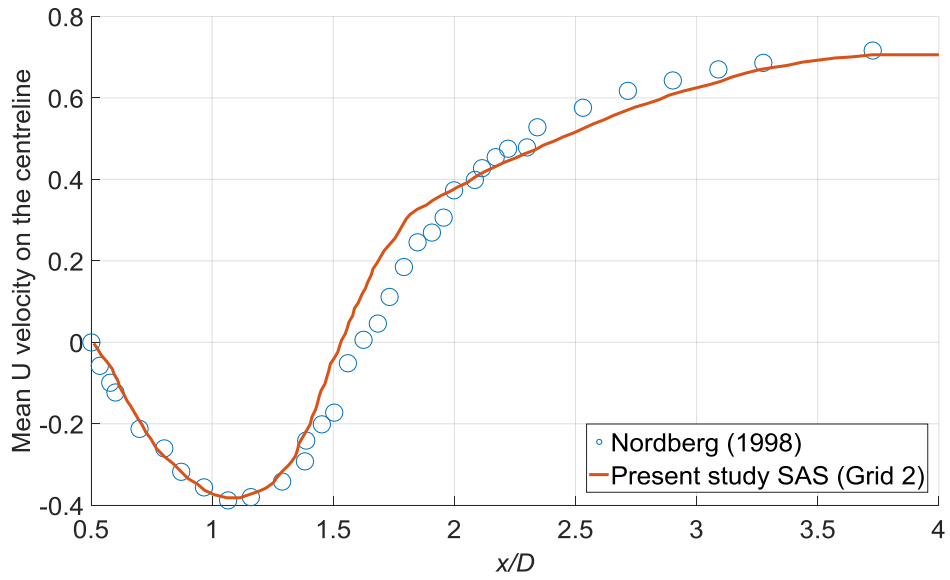

Figure 4 - Comparison of the mean streamwise velocity at the centreline (y/D = 0) with published experimental data at Re = 10,000.

Further validation of the model was done by comparing the mean streamwise velocity at the centreline to data published by Norberg (1998). The comparison is displayed in Figure 4, and a reasonable agreement (less than 10% difference) was observed.

3 Results

This section contains the post processed results of the unsteady wake velocity data which were exported from the CFD simulation. Considering the two-dimensional wake behind a circular cylinder, the wake has streamwise and transverse linear velocity components, in addition to a rotational component due to the vorticity. The velocity field can be split up in to the mean ($\bar{u}$ and $\bar{v}$) and fluctuating (u' and v') components of the transverse and streamwise velocity. Thus, the energy in the wake arises from the mean and fluctuating parts of the streamwise and transverse components. Due to the temporal nature of the vortex street, the instantaneous energy density will also fluctuate with time. This is the concept of temporal energy concentration and is observed when the time-dependant data are analysed. In this section, the frequencies at which the fluctuating components occur are presented as multiples of the shedding frequency, since the dominant frequencies observed were all harmonics of the shedding frequency. All the energy magnitudes inferred to in this paper are normalised using the available freestream energy in the flow upstream of the cylinder, and hence are an indication of the ratio of energy concentration by the cylinder.

The definition of the energy terms derived for the temporal wake analysis is given in Equations (3a) – (3f). The primary shedding frequency was identified for each shape and the corresponding magnitude for that frequency was taken from the power spectrum. Since most of the temporal energy is found at the vortex shedding frequency, the temporal investigation only includes the normalised energy found at the primary shedding frequency for each bluff body. Contour maps of the resulting magnitudes at their respective locations, were used to observe the trends in temporal wake energy.

Mean Normalised streamwise energy	$E_{\bar{u}} = \bar{u}^2/U_0^2$	(3a)
Mean Normalised transverse energy	$E_{\bar{v}} = \bar{v}^2/U_0^2$	(3b)
Mean Normalised spanwise energy	$E_{\bar{w}} = \bar{w}^2/U_0^2$	(3c)
Normalised energy due to fluctuating streamwise component at *fs*	$E_{u'_{fs}} = u_{mag\ ps}/U_0^2$	(3d)
Normalised energy due to fluctuating transverse component at *fs*	$E_{v'_{fs}} = v_{mag\ ps}/U_0^2$	(3e)
Normalised energy due to fluctuating transverse component at *fs*	$E_{w'_{fs}} = w_{mag\ ps}/U_0^2$	(3f)

where u = streamwise velocity; v = transverse velocity; w = spanwise velocity; $u_{mag\ ps}$ = power spectrum magnitude obtained for the streamwise velocity at the primary shedding frequency, *fs*; $v_{mag\ ps}$ = power spectrum magnitude obtained for the transverse velocity at the primary shedding frequency; $w_{mag\ ps}$ = power spectrum magnitude obtained for the spanwise velocity at the primary shedding frequency; U_0 = freestream velocity; and the overbar indicates the mean of the variable.

3.1 Time-averaged spatial energy distribution in the wake

The time-averaged values of the streamwise, transverse and spanwise velocities were used to plot the non-dimensional mean energy due to each of these components ($\bar{u}, \bar{v}, \bar{w}$), as depicted in Figures 5, 6 and 7 respectively. The energy is normalised using the energy available in the flow upstream of the cylinder.

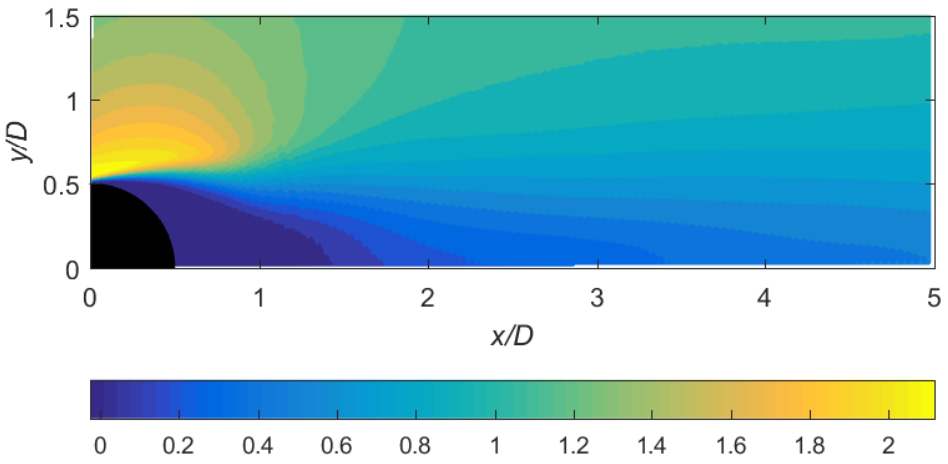

Figure 5 – Contour plot of the mean normalised streamwise energy ($E_{\bar{u}}$) in the wake of the cylinder

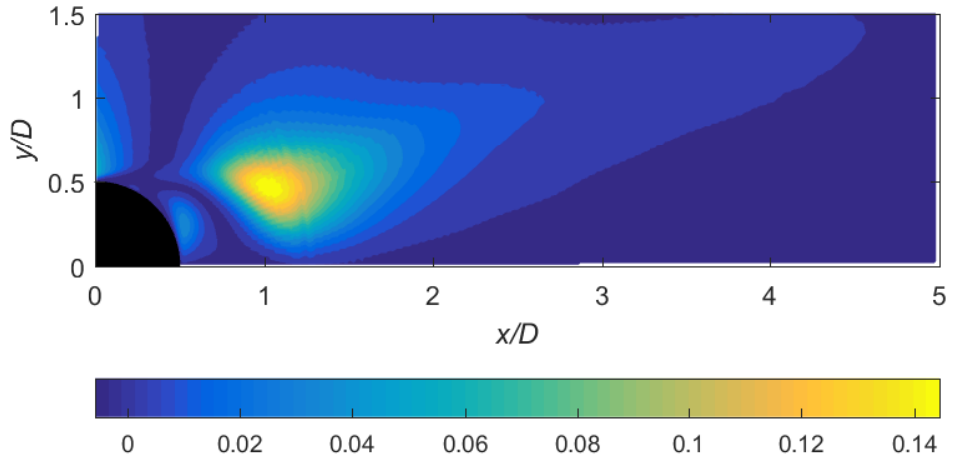

Figure 6 - Contour plot of the mean normalised transverse energy ($E_{\bar{v}}$) in the wake of the cylinder

As the flow approaches the cylinder, there is a reduction in the $\bar{u}$ energy, followed by an increase near the surface of the cylinder. The wake has a lower energy than the freestream as the flow is recovers to the freestream condition. The highest value for the mean streamwise energy is close to the surface of the cylinder and is attributed to flow accelerating up around the cylinder, due to the blockage to the flow caused by the cylinder. The aft part of the cylinder has the minimum point for energy from $\bar{u}$, due to the low velocity region caused by the recirculating flow.

The mean transverse energy ($\bar{v}$) is much lower in general when compared to the mean streamwise energy ($\bar{u}$) which was to be expected. The normalised energy due to $\bar{v}$ plotted in Figure 6 shows a single peak of energy at about one diameter downstream of the cylinder due to the interaction between the shear layers from the top and bottom surfaces of the cylinder, which is where the large scale vortices are formed.

The time-averaged energy of the transverse component does not display a significant augmentation effect in the wake because the time dependency of the energy peaks is not taken in to effect, and hence the fluctuations cancel each other out. The streamwise component, on the other hand, has almost double the energy compared to the upstream flow near the surface of the cylinder. This is due to the high velocity shear layer which forms around the surface of the cylinder.

The time-averaged spanwise energy component has a very low magnitude and is almost 10^4 times less than the other time-averaged energy components (Figure 7). Hence, $E_{\bar{w}}$ is not very useful for harvesting energy from WIV.

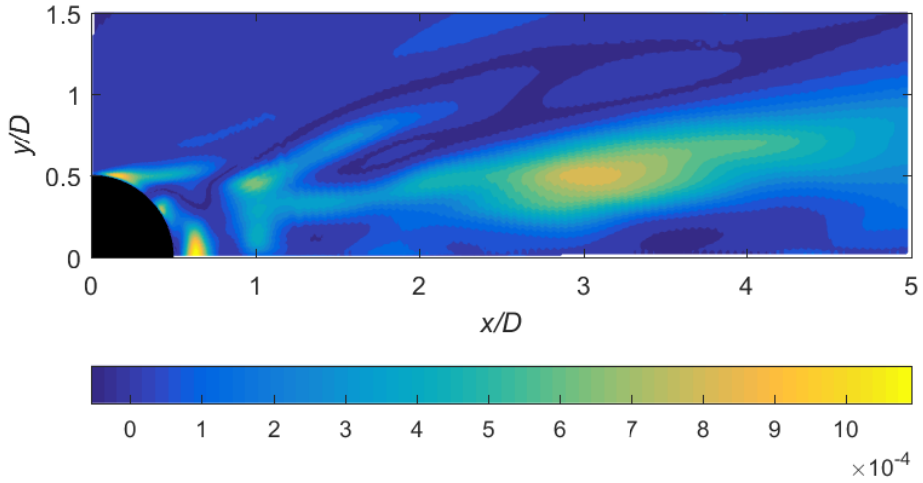

Figure 7 - Contour plot of the mean normalised spanwise energy ($E_{\bar{w}}$) in the wake of the cylinder

3.2 Fluctuating temporal energy distribution in the cylinder wake

Fourier analyses were performed on the transient velocity data field in MATLAB to identify the frequency of the fluctuations and the magnitude at which the unsteady components appear in the wake of the cylinder. Fourier analysis was performed on the normalised velocity data and the harmonic frequencies that appear in the wake were identified. A power spectrum of the data utilising a flat top window was used to extract the magnitude of energy due to u' and v' at the harmonic frequencies. The frequencies at which maxima appeared on the FFT plots were all harmonics of the primary shedding frequency of the cylinder.

This section only contains contours of the fluctuating components at the shedding frequency (*fs*) and not the other frequencies, as the magnitude of the normalised energy at the other frequencies was at least an order of magnitude less than the primary shedding frequency. Figure 8 displays the FFT plots for u' and v' at different x/D and y/D locations in the wake of the circular cylinder and highlights the difference in magnitude. The frequencies were normalised using the shedding frequency to display the magnitudes at consecutive harmonics of the vortex shedding frequency. Figure 9, 10 and 11 depict the contour maps of the normalised streamwise, transverse and spanwise energy fluctuations at the shedding frequency.

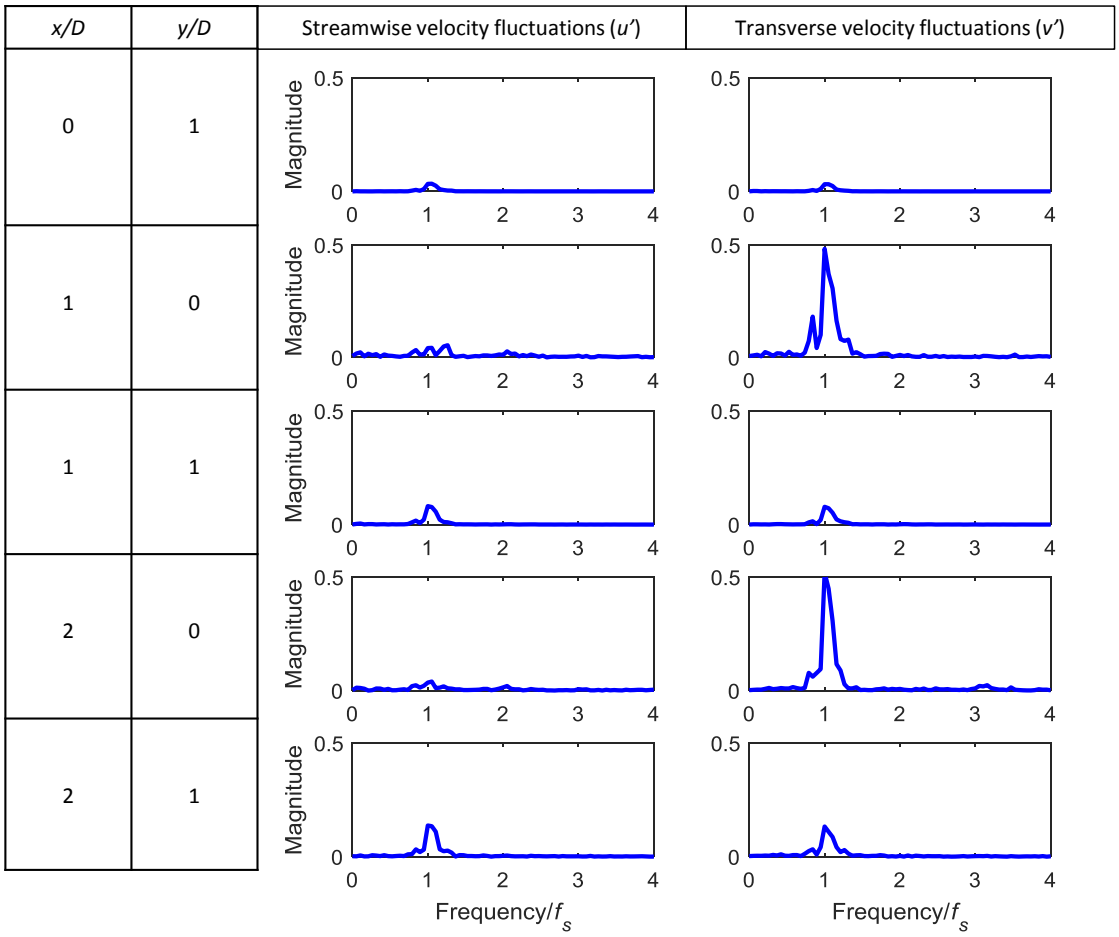

Figure 8 - FFT plots of the fluctuating velocity components (u′ and v′) at different x/D and y/D locations in the wake of a circular cylinder. The frequency spectrum was normalised using the vortex shedding frequency (fs) to display the augmentation over harmonics of the shedding frequency.

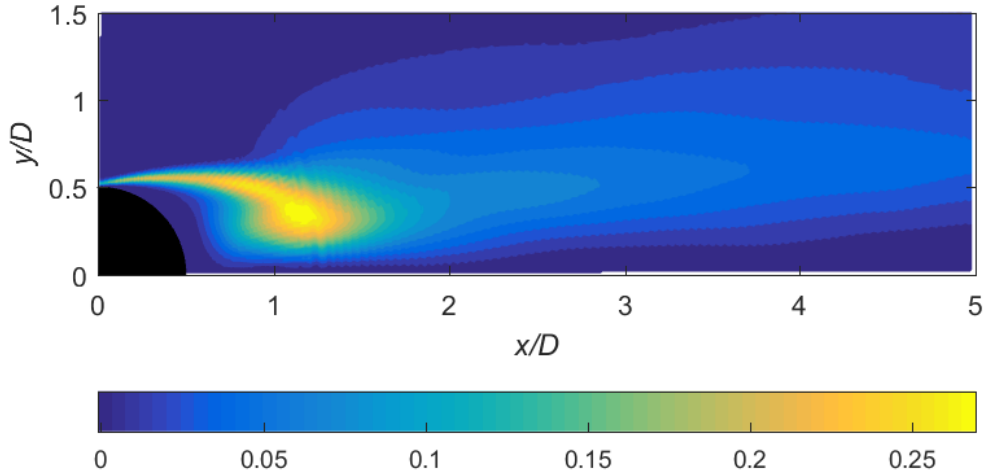

Figure 9 – Normalised streamwise energy fluctuation ($E_{u'_{fs}}$) at the shedding frequency

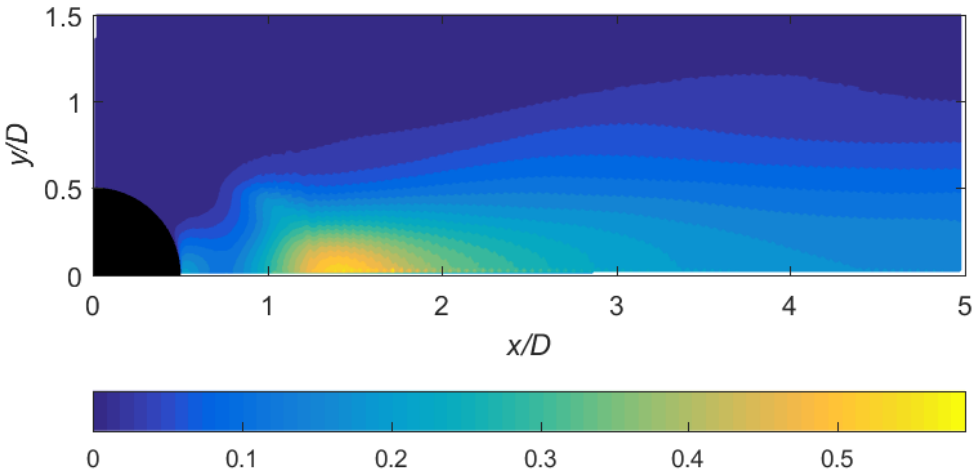

Figure 10 - Normalised transverse energy fluctuations ($E_{v'_{fs}}$) at the shedding frequency

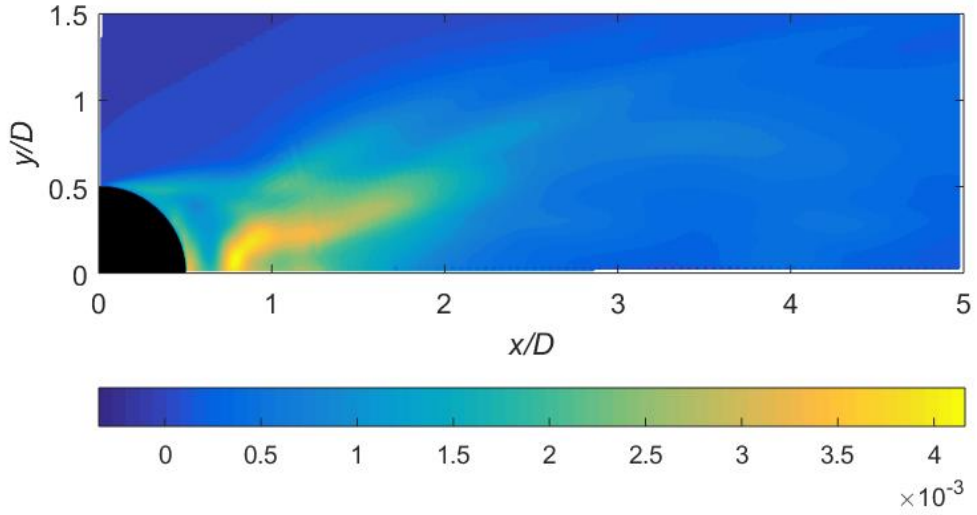

Figure 11 - Normalised spanwise energy fluctuations ($E_{w'_{fs}}$) at the shedding frequency

As shown in Figure 11, the energy contained in w' is negligible (10^3 times lower in magnitude) when compared to the other fluctuating velocity components (u' and v'). The spanwise velocity component has negligible energy content compared to the other components and hence, will not be investigated further in this study. To further prove the 2-dimensionality of the energy content in the wake of the cylinder in this study, 2D CFD simulations were performed using the surface mesh from the 3D analysis. The energy contour maps of the 2D and 3D simulation

for $E_{\bar{u}}$, $E_{\bar{v}}$, $E_{u'_{fs}}$ and $E_{v'_{fs}}$ are presented side-by-side in Figure 12 where the maximum energy zones are similar in magnitude and location between the 2D and 3D simulations.

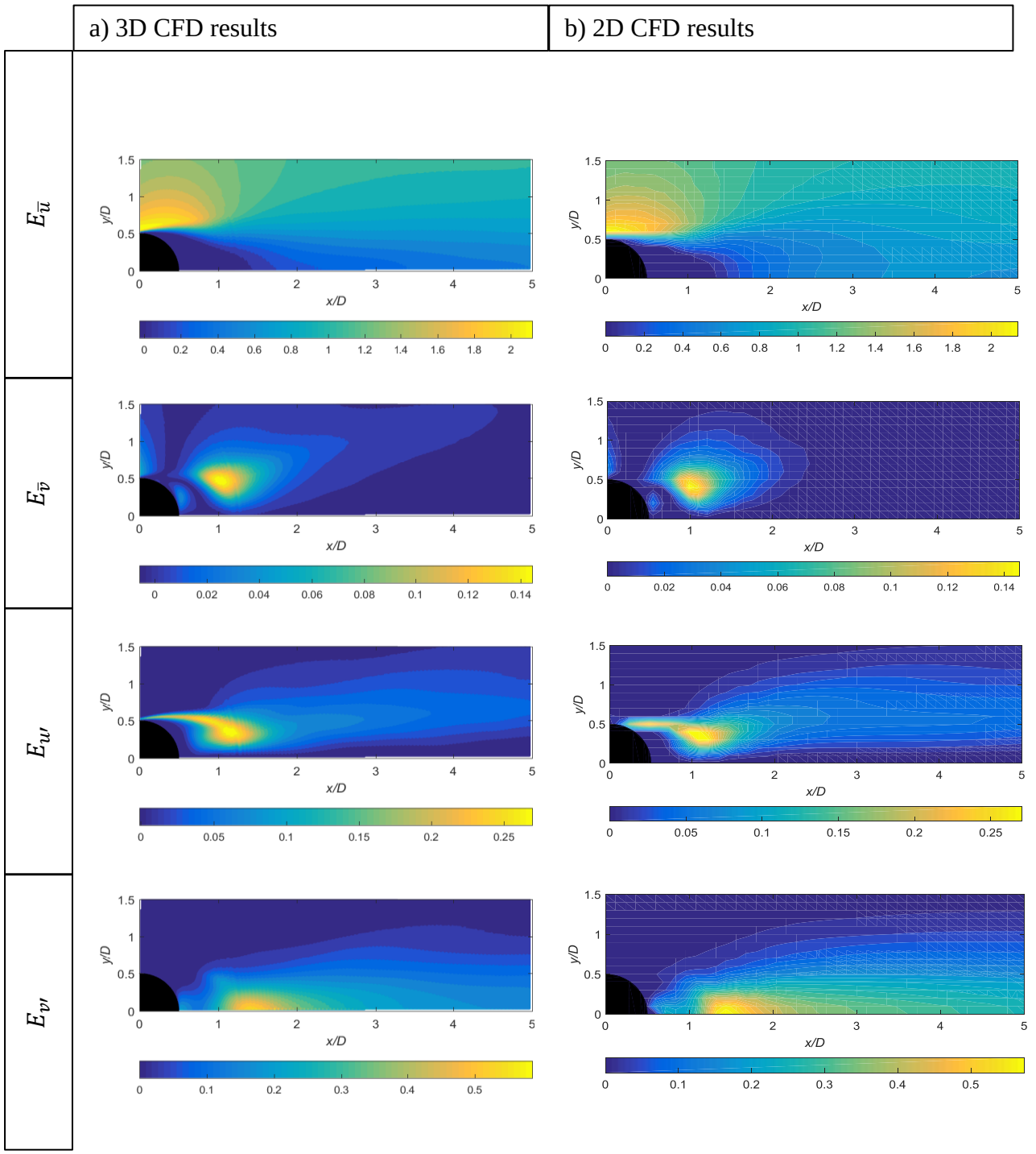

Figure 12 – Comparison of wake energy components obtained via 2D and 3D (a) and b), respectively) numerical simulations.

Analysis of energy in the harmonic frequencies showed that the zones containing the maximum energy due to u' and v' alternate between y/D = 0 and 0.5 between the different harmonic frequencies. However, at any given frequency, the maxima for the streamwise and transverse fluctuations never occur in the same location. The location of the maximum transverse energy fluctuation is between $1 < x/D < 2$, whilst the maximum streamwise fluctuation is located between $0 < x/D < 2$ for all the harmonic frequencies.

Another interesting observation was that there is a higher maximum magnitude of the fluctuating transverse energy at the third harmonic (6Hz) compared to the second harmonic (4Hz). This correlates to the secondary peak that is usually seen at the third harmonic of the shedding frequency for a cylinder undergoing VIV at high Reynolds numbers (Branković & Bearman 2006) and odd harmonics are common in harmonic distortions arising from non-linear processes.

3.3 Variation of the energy components at different transverse locations

Variation of the normalised fluctuating energy components with the streamwise distance from the cylinder, at a given transverse location (y/D = 0, 0.5 or 1), is displayed in Figure 13. These results were used to compare the magnitudes of the fluctuating energy components in relation to the mean components. Only y/D = 0, 0.5 and 1 are included to exhibit the observed trends, since at greater transverse distances from the cylinder, only small magnitudes for the $\bar{u}$ component were observed near x/D = 0.5 and all the other components exhibited no significant augmentation. At all y/D locations, the highest energy component is due to the $\bar{u}$ velocity. This is due to the streamwise direction of the flow. The $\bar{u}$ energy does not recover to unity by the end of the domain in the plots

presented since these y/D locations are still within the wake of the cylinder and hence experience the effects of reduced velocity flow. Energy from fluctuating components occurring at higher harmonics of the shedding frequency is not included to maintain clarity, as they are of negligible magnitude.

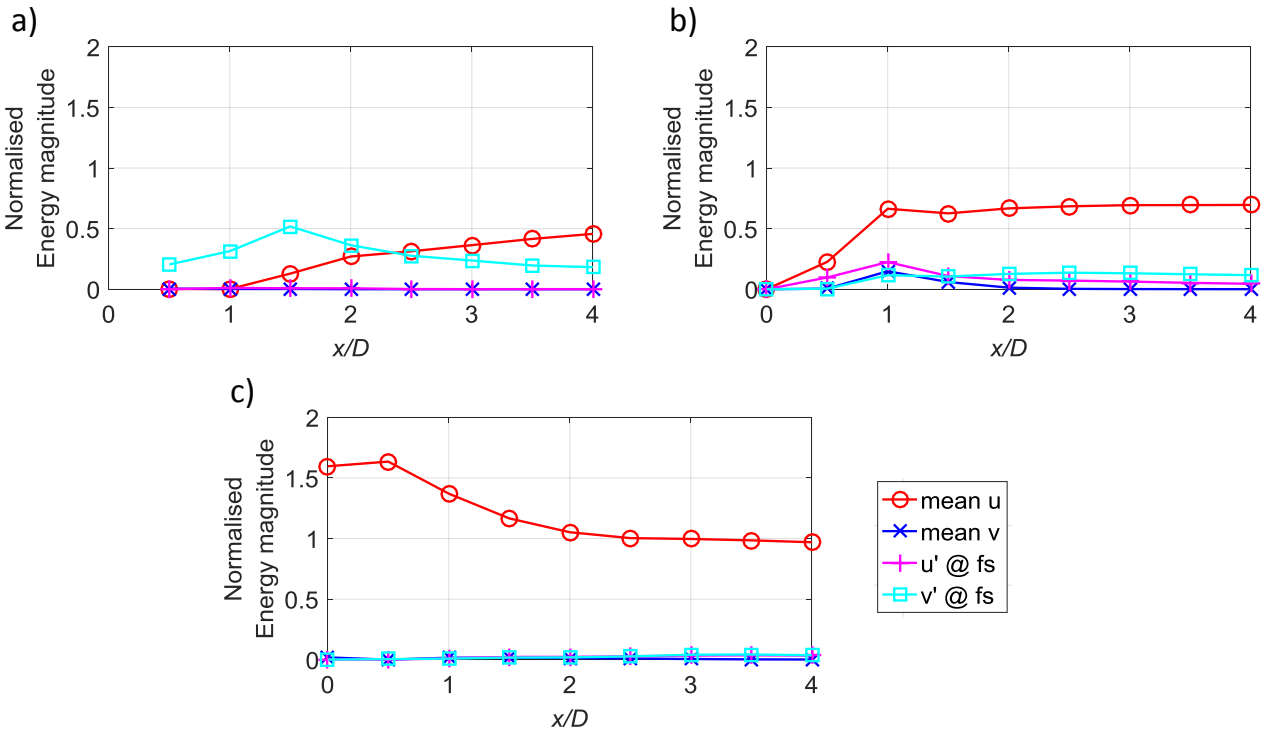

Figure 13 - Energy in the wake due to the mean and fluctuating components at y/D = 0, a); 0.5, b); 1.0, c).

The normalised energy due to $\bar{u}$ and u' at the shedding frequency show maxima at $x/D = 1$ and $y/D = 0.5$. This is due to the shear layers that are moving towards the centreline of the cylinder. The energy due to v' at the primary shedding frequency, also exhibits a peak at $x/D = 1$ due to the propagation of eddies formed in the shear layer. The normalised energy magnitude due to v' at the primary harmonic exhibited a lower magnitude at $y/D = 0.5$ compared to the $y/D = 0$ location due to the rapid dissipation of vorticity when the shear layers interact with each other.

When y/D = 0 and 0.5, the mean streamwise energy goes to zero at x/D = 0 since the cylinder is blocking the flow at these locations. At y/D = 1, there is a maximum of 1.58 (Figure 13 c)) for the $\bar{u}$ energy as this is the region where the flow accelerates around the cylinder. Although not included in these plots, the fluctuating components exhibit small peaks at the second and third harmonics, but these peaks are still very low in magnitude and not suitable for energy capture.

3.4 Energy that can be captured by an energy extractor over one cycle of vortex shedding

The Betz limit was developed for turbines and rotors in a flow. The Betz limit also has been applied to shrouded turbines since the concentration by diffusers is internal. However, the Betz limit is not applicable to the cylinder case as no area could be defined to calculate the limit, due to the external concentration of the flow.

The maximum energy that can be captured as a ratio of the upstream energy can be derived if a Wake Energy Extractor (WEE) can move transversely, at a fixed streamwise distance. To examine the limit of energy extraction, it was assumed that a WEE can move to the zones of maximum energy at a specific streamwise distance from the cylinder, and can absorb all the energy available at that region. Hence, this analysis was pointwise and not spatially averaged as in the preceding section. Streamwise distances in increments of 0.5D from 0 to 4D from the cylinder were chosen, as this range encompassed all the maximum energy points discovered in the previous section. It was also assumed that no energy is wasted in the movement. These assumptions were necessary to examine the order of magnitude of the energy limit for the external flow concentration by a cylinder. The lift data from the CFD simulation were used to identify the vortex shedding cycles in the data

gathered. Once the start and end of a cycle were known, the data were split to have 8 frames of analysis for a single cycle. The time-dependant streamwise and transverse energies were investigated for every 1/8th of a single cycle, as a ratio compared to the available freestream energy.

Utilizing the maximum streamwise and transverse energy available at each stage of the cycle, the maximum energy extractable by a WEE was calculated for each streamwise distance from the cylinder. The results for the maximum energy extractable are depicted in Figure 14, where a contour of the average normalised energy is used as the background for the line plots which show the trend for the streamwise and transverse energy components.

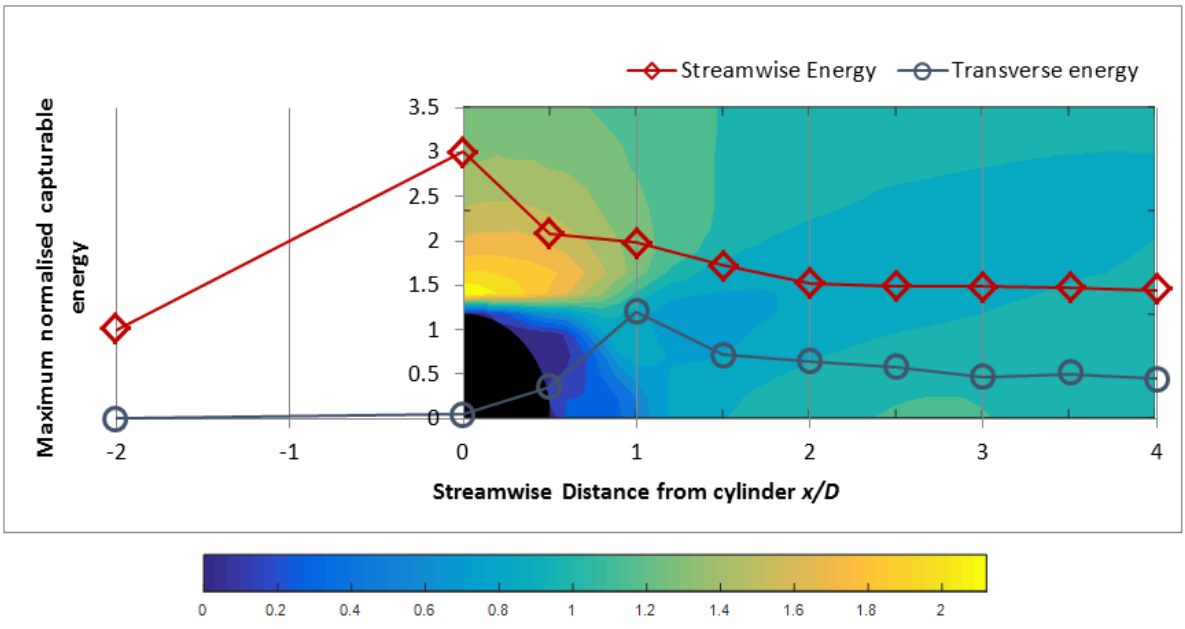

Figure 14 - Magnitude of maximum energy (including both the steady and unsteady components) that could be captured by a Wake Energy Extractor (WEE) which can move transversely at fixed x/D locations. The Contour map is the normalised energy distribution due to the total velocity in the wake.

The maximum obtainable pointwise energy density was at $x/D = 0$ from to the streamwise energy. This occurred due to the jet that formed on the surface of the cylinder, and was almost three times the magnitude

of the available upstream flow energy. The maximum obtainable transverse energy occurred at $x/D = 1$ and had a magnitude of about 1.25 times the oncoming energy. If a WEE was able to capture both the transverse and the streamwise energies, a combined maximum of 3.25 times the free stream energy is available at $x/D = 1$. The transverse energy ratio is comparatively lower than the streamwise component, due to the streamwise propagation of the flow from the inlet. Beyond $x/D = 3$, the magnitudes of transverse and streamwise energy reduced at a lower rate compared to the near wake, as the turbulence dissipated in the far wake.

3.5 Effect of bluff body cross-section

The circular cylinder has been extensively reviewed and many experiments exist on VIV of the cylinder. There has not been any systematic study to investigate the performance of other bluff body cross-sections with similar length characteristics, operating under the same flow conditions.

Particularly, there has been no focus given to the wake characteristics and the differences in downstream flow conditions from the standard circular cylinder configuration. Varying the bluff body cross section will change the amount of energy in the streamwise and transverse components. By investigating these differences, it is possible to identify a cross section that will concentrate most of the energy in a carrier that is ideal for energy harnessing (e.g. transverse fluctuations). A number of selected cross-sections were investigated to identify the differences in wake energy carriers for different bluff bodies and realise a cross-section that resulted in increasing the energy concentrated in transverse fluctuations. The shapes chosen were a semi-circular cylinder, an equilateral triangle and a midway shape between the semicircle and the triangle; a triangle with convex sides as shown in

Figure 15. The semi-circular cylinder was chosen to investigate the effect of halving the cross-section of the circular cylinder such that there is a flat aft edge, which would lead to a larger back pressure and hence a larger pressure difference between the fore and aft faces of the cylinder. The equilateral triangle was chosen due to its widespread use in piezoelectric systems as the upstream energy concentrator. The transition from the semi-circular cylinder to the equilateral cylinder resulted in the triangle with convex-edged sides and a flat aft face.

The shapes were simulated such that the aft part of the cylinders was the flat end and hence was downstream of the body and all the cylinders had a characteristic diameter of 30 mm and a length of 90 mm. The 3D CFD models for the different cross-sections used the same mesh configuration, turbulence model and method of analysis as that of the circular cylinder.

The differences in energy magnitude of the different velocity components were investigated and particular attention was on whether an increase in the transverse fluctuations could be observed. As the CFD techniques used were identical to the circular cylinder, it is expected that the numerical data are valid for analysis. The results of the variation of the components are given in the proceeding subsections. Results were analysed at increments of $0.1D$ in the transverse direction and the results for y/D = 0, 0.5 and 1 are presented here and a detailed comparison is given in Section 4.

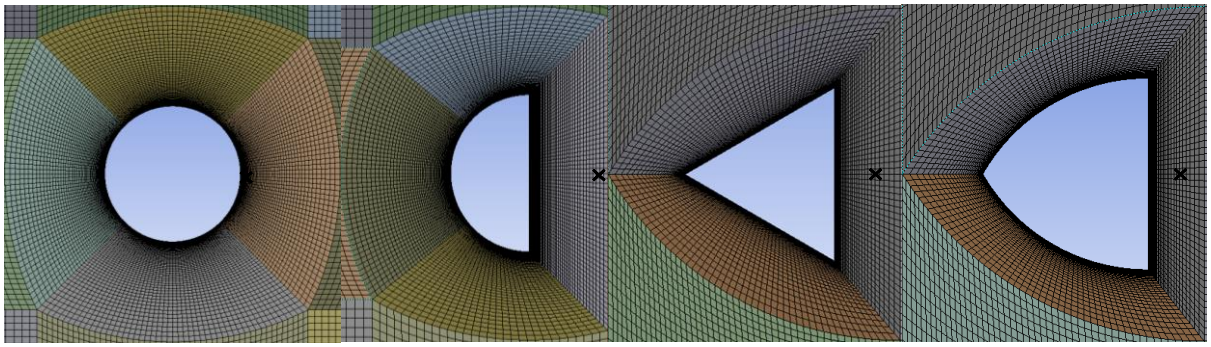

Figure 15 - The bluff bodies used to investigate the difference in the wake energy components. The bluff bodies from left to right are circle semi-circle, equilateral triangle and an equilateral triangle with convex sides.

3.5.1 Semi-circular cylinder

The magnitudes of the energy components for the semi-circular cylinder are plotted in Figure 16. The shedding frequency was almost equal to the shedding frequency observed in the full cylinder case since the separation point was approximately the same for both the cases. The maximum normalised magnitude of the transverse fluctuations at the shedding frequency was 0.92 and occurs at y/D = 0 and x/D = 1. Other harmonics have very low energy magnitudes for both the transverse and streamwise energy fluctuations.

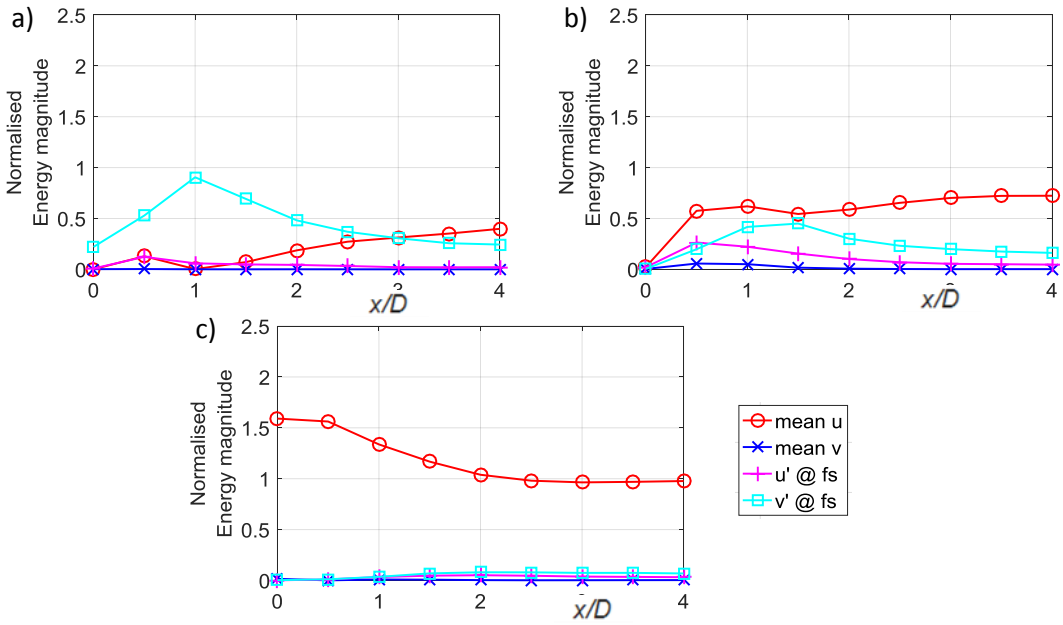

Figure 16 - Energy in the wake of a semi-circular cylinder due to the mean and fluctuating components at y/D = 0, a); 0.5, b); 1.0, c).

3.5.2 Straight-edged equilateral triangle

Results of the normalised energy magnitudes for the different energy components in the wake of an equilateral triangle are displayed in Figure 17. Apart from the energy concentration of the mean streamwise component, there is no significant concentration of energy observed in the wake by the other velocity components. The mean streamwise energy component was similar to the circular cylinder.

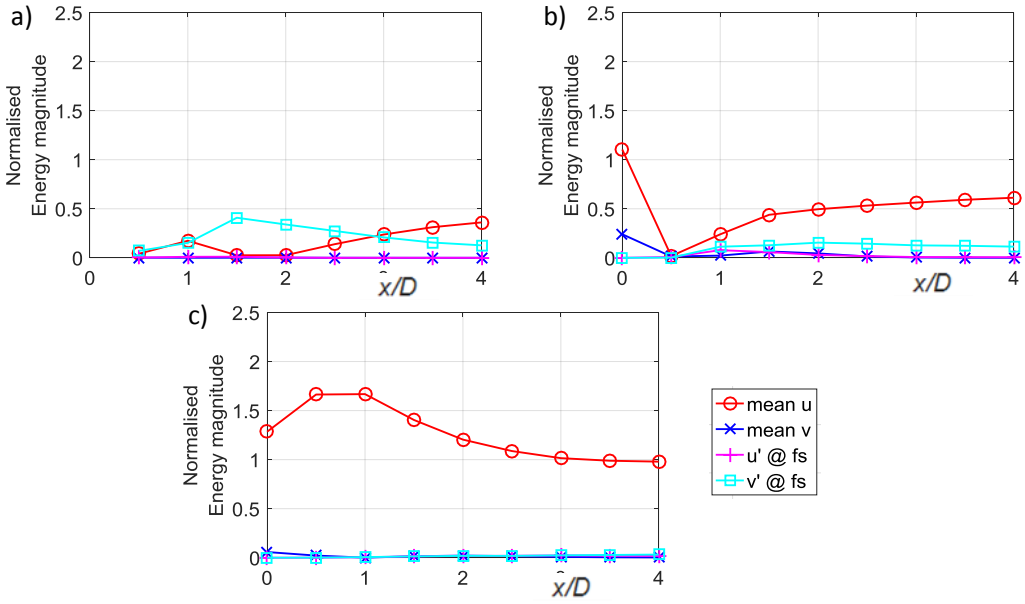

Figure 17 - Energy in the wake of a straight-edged triangle due to the mean and fluctuating components at y/D = 0, a); 0.5, b); 1.0, c).

3.5.3 Equilateral triangle with convex sides

The magnitudes of the energy components for the equilateral triangle with convex sides are plotted in Figure 18. The shedding frequency was higher (2.8 Hz) than that observed in the circular and semi-circular cylinder cases. The maximum for the mean streamwise energy is also higher in this case.

The maximum normalised magnitude of streamwise energy fluctuations at the shedding frequency was around 0.2 and occurred at y/D = 0.5 and x/D = 1. The transverse fluctuations of energy, at the shedding frequency, occur at a higher magnitude than the circular

cylinder, but occur at the same location of about $y/D = 0$ and $x/D = 1 – 1.5$. At transverse distances higher than $0.5D$, the only significant component observed is the mean streamwise component.

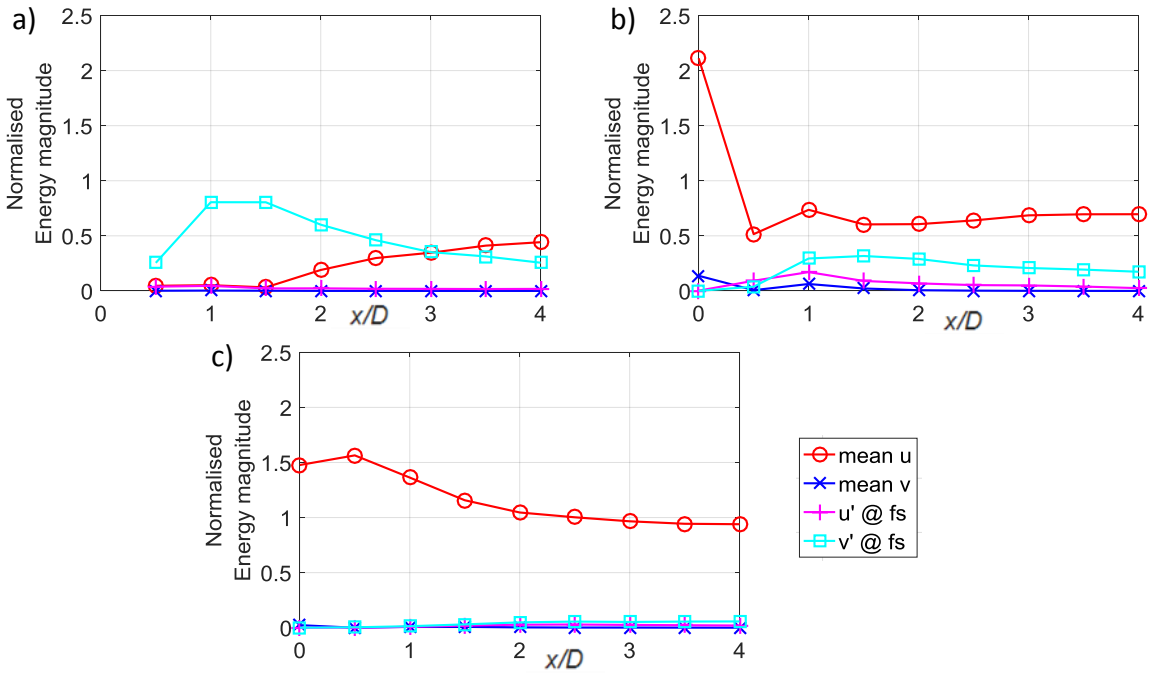

Figure 18 - Energy in the wake of an equilateral triangle with convex sides due to the mean and fluctuating components at y/D = 0, a); 0.5, b); 1.0,c).

4 Discussion

The results demonstrate the temporal and spatial concentration of energy in a flow using different bluff bodies. For the circular cylinder, the temporal energy concentration due to the fluctuating components is lower in magnitude compared to the concentration observed in the mean streamwise component. The mean streamwise energy component exhibits a large magnitude due to the accelerating shear layer near the surface of the cylinder, but this concentrated energy cannot be captured as it is too close to the cylinder's surface and occurs only over a small region.

It is known that a circular cylinder can be used to convert the mean streamwise energy in to the transverse fluctuations, which in turn can contribute to transverse vibrations in a downstream body. Tuning a system to either the mean or unsteady component will affect the response observed and hence the efficiency of the system. There is a possibility of designing smarter Wake Energy Extractors (WEEs) which are able to operate at high energy extraction efficiencies by utilising the information known about the locations of maximum magnitude of the components.

Utilising the results gathered about the circular cylinder wake, a suitable WEE would have to be placed between $1 < x/D < 3$ and $0 < y/D < 1$ to harness the maxima of the temporal energy (u' and v'), and near the boundary of the cylinder to capture the maximum mean streamwise energy due to the jetting effect. However, if a WEE is placed too close to the first body, the flow is blocked, and hence regions further downstream which have high energy densities are best for energy capturing. The energy due to the $\bar{v}$ component is not very useful as it is lower in magnitude compared to the others (Figure 9). The oscillating transverse component of the energy in the wake is significant compared to the other temporal fluctuations. The unsteady components (u' and v') are maximum near the wake of the cylinder since eddies are produced in the boundary layer of the cylinder and start to dissipate when they form in to the vortex clouds. The third harmonic of the transverse velocity oscillations also seem to be a significant contributor to the temporal concentration of energy and corresponds to the secondary peak found in the Power Spectral Density of the oscillation amplitude reported by Branković and Bearman (2006). An effective WEE needs to

be able to capture both the mean streamwise energy as well as the transverse fluctuations to maximise the energy extraction efficiency.

The total temporally-averaged energy in the wake of the cylinder would be lower than the energy in a comparable upstream area. This is due to energy losses in the flow due to friction and the effects of viscosity. However, peaks of augmented energy, which occur during a vortex shedding cycle and exceed upstream energy densities, could be captured to result in a large amount of energy being harnessed. Energy analysis of the wake showed that if a WEE were able to capture the maximum energy regions in a vortex shedding cycle, a maximum of 3.25 times the available upstream energy can be harnessed at a streamwise distance of $x = 1D$. A WEE working further downstream (beyond $x = 3D$), will be able to harness approximately 1.8 times the available upstream energy. These results indicate that there is significant external concentration of energy in the wake due to the cylinder. Compared to the augmentation factor of about 1.6 for diffusers, cylinders can be used to spatially and temporally concentrate energy to achieve higher ratios. Assuming a WEE that is capable of actively harnessing the high energy density regions, a significant portion of the augmented energy can be captured and converted to useful energy. However, this limit was calculated assuming the WEE can move to the high energy density regions without losing any energy, and is non-impacting on the flow field. The efficiency of power conversion from the available energy to useful energy also has not been considered. A complete system configuration will need to be realised to obtain the actual efficiencies, and to investigate whether augmenting and harvesting temporally concentrated energy will achieve a higher efficiency compared to the Betz limit.

It is possible to identify the characteristic diameter of a second cylinder, and the operating region where it will be able to harness a maximum amount of energy. The vortex shedding of the second cylinder needs to be known to achieve the maximum efficiency from the system configuration. When considering bluff bodies, a second body that is much smaller in size compared to the first body would benefit in being able to capture the augmented energy. A smaller second body has a smaller effect on the flow structure from the upstream body, and can capture higher magnitudes of the fluctuating components, as demonstrated by the planar averaging results presented in section 3.4. The positions of maximum efficiency found in previous studies with a tandem circular cylinder (Derakhshandeh et al. 2014) and aerofoil (Derakhshandeh et al. 2016) do not match up with the results seen in this study, as that position would also depend on the wake of the downstream body and the phase difference between the forces on the body due to its own vortex shedding, as well the fluctuations in velocity caused by the upstream body. The maximum regions for the spatial and temporal concentration cannot be captured by WEE due to the flow field differing significantly when a second body is placed downstream. If the streamwise gap is smaller than 1.5D, the flow does not separate between the bodies and hence there is no vortex shedding in the gap for rigid bluff bodies (Igarashi 1981). Both bodies behave as one and the shear layer connects the bodies. This may be a reason for the smaller gaps not being the place of high power efficiency as reported by others (Derakhshandeh et al. 2014, 2015a, 2016).

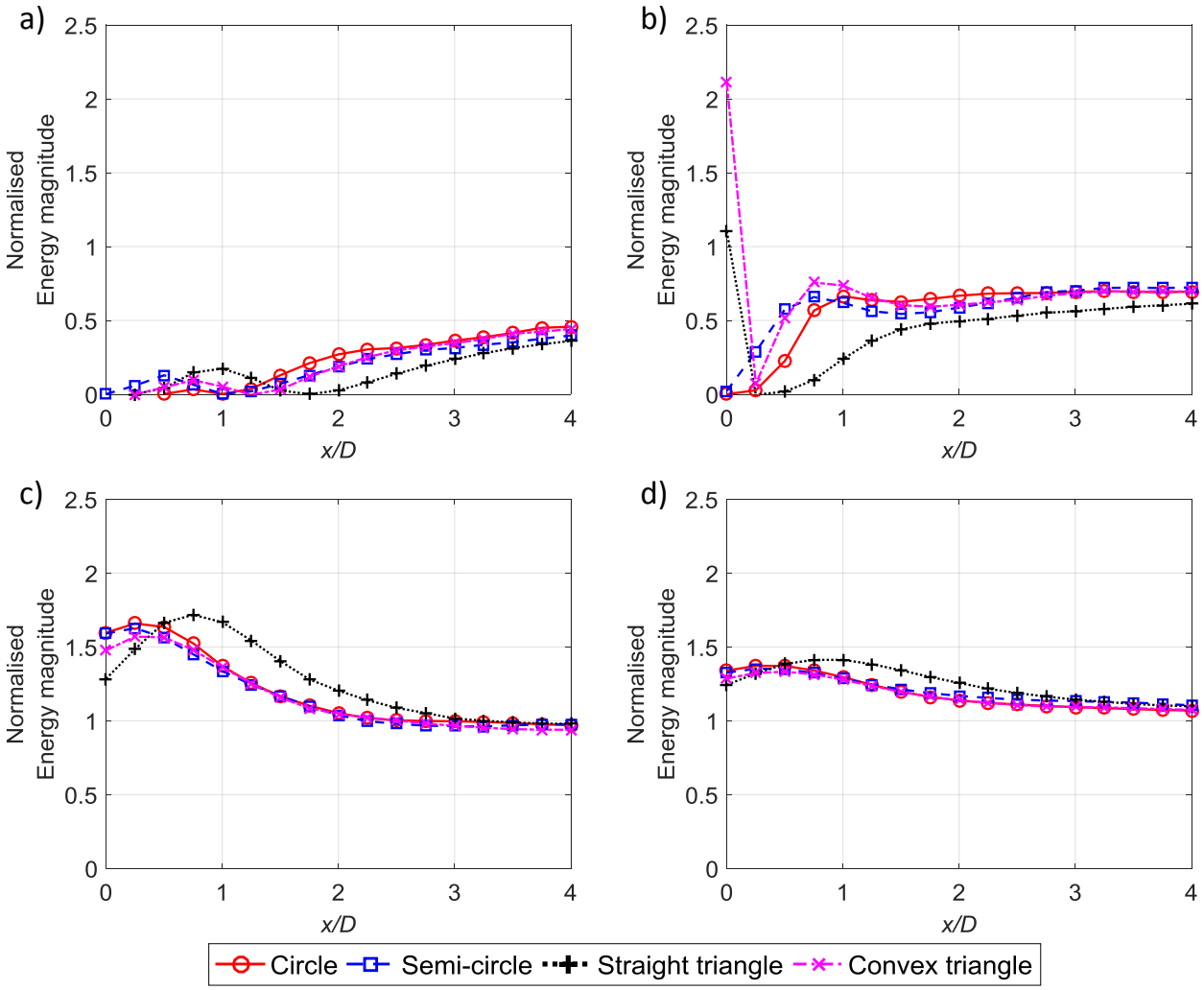

Figure 19 - Normalised energy magnitude of the mean streamwise component in the wake of different bluff bodies at transverse heights of y/D = 0, a); y/D = 0.5, b); y/D = 1, c); y/D = 1.5, d).

The effect of different bluff body cross-sections was also briefly investigated in this paper. For comparison, the results of energy concentration by the different bluff bodies, including the circular cylinder, are shown in Figures 19 - 22. The mean streamwise component, shown in Figure 19, exhibits a similar trend along all bluff bodies which has been discussed in the preceding section. There is similarity in the recovery of the mean streamwise component for all shapes and at y/D = 1.5, all the bluff bodies have approximately the same magnitude along x

and have a normalised magnitude slightly higher than 1. The mean transverse component some augmentation of energy for both the convex-edged and straight-edged triangle, since the flow gets diverted up by the leading edges. As expected, the straight triangle has a higher magnitude (0.24) than that of the convex edge (0.14). Figure 20 shows this trend, and the maximum mean transverse component occurs for the straight-edged triangular cylinder at $y/D = 0.5$ and $x/D = 0$.

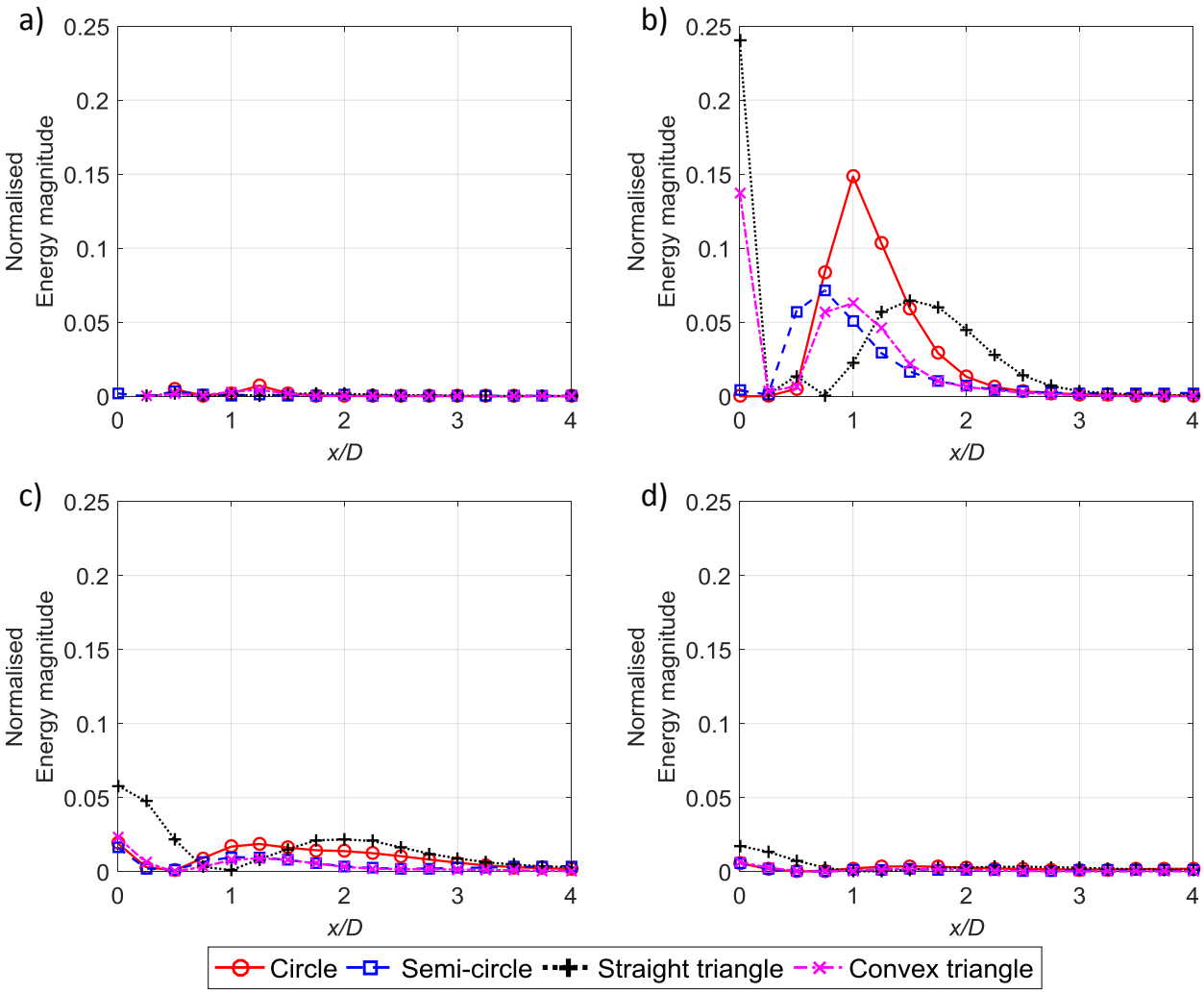

Figure 20 - Normalised energy magnitude of the mean transverse component in the wake of different bluff bodies at transverse heights of y/D = 0, a); 0.5, b); 1.0, c); 1.5, d).

The fluctuating streamwise component is not a significant carrier of the wake energy downstream from the bluff bodies. However, the near wake (x/D = 0.2, y/D = 0.5) of bluff bodies such as the semicircular and convex triangle bodies have at least a quarter of the upstream available energy as shown in Figure 21. The minimal energy trend observed in the fluctuating streamwise component maybe due to the high energy mean streamwise component, which dissipates the fluctuations.

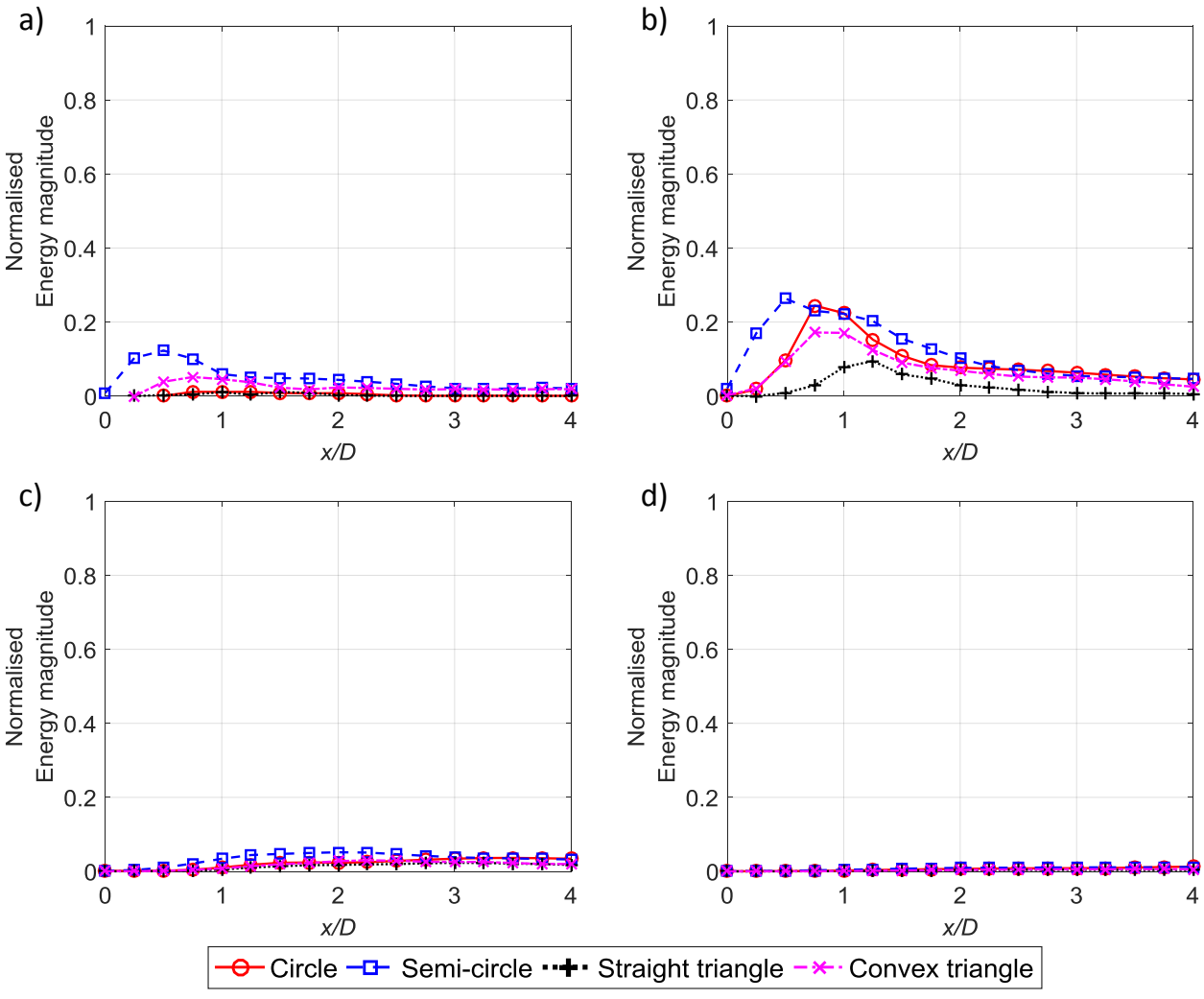

Figure 21 - Normalised energy magnitude of the fluctuating streamwise component in the wake of different bluff bodies at a transverse height of y/D = 0, a); 0.5, b); 1.0, c); 1.5, d).

The fluctuating transverse component has very small magnitudes of energy at transverse distances greater than $y/D = 1$. At $y/D = 0$ and $x/D = 0.5$, the semi-circle and convex triangle have magnitudes greater than 1.5, which is much greater than the other bluff bodies (Figure 22). The semi-circle and convex triangle also have larger magnitudes of normalised energy compared to the other bodies at $y/D = 0.5$. Hence the semi-circle and the convex triangle are bluff bodies which are most suited to obtain a wake with more transverse fluctuations.

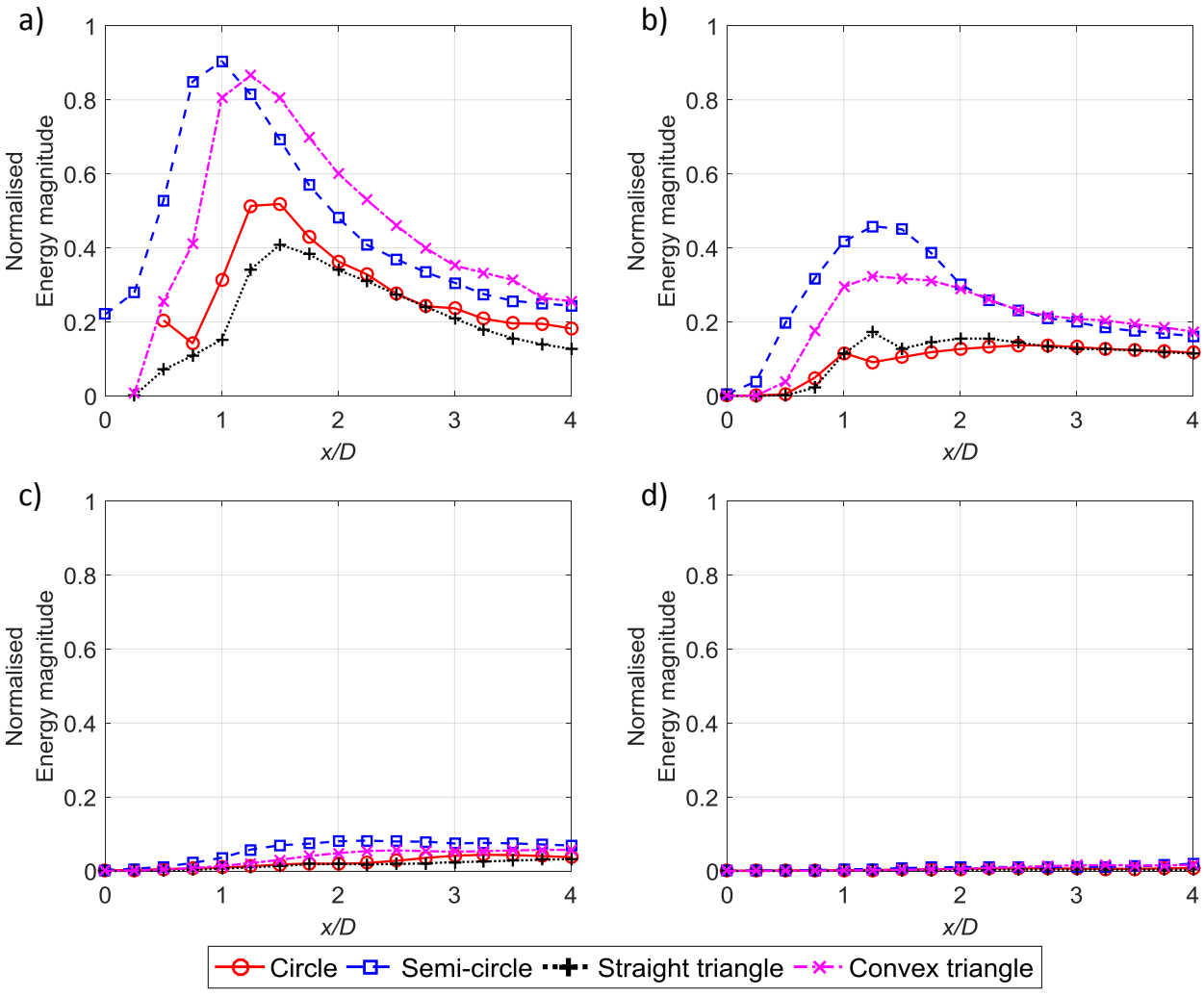

Figure 22 - Normalised energy magnitude of the fluctuating transverse component in the wake of different bluff bodies at a transverse height of y/D = 0, a); 0.5, b); 1.0, c); 1.5, d);

The results presented here were obtained for a single Reynolds number, and a change in Reynolds number will result in different values for the energy. However, the general trend will be the same and this paper has used only one Reynolds number to verify that a cylinder can be used as an external flow energy concentrator. The concentration will also differ significantly based upon the second downstream body. Factors such as the surface roughness, Reynolds number, characteristic diameter, turbulence in the flow, and spacing between the bodies will significantly change the flow field and hence will need to be considered when investigating a specific WIV system. Hence, further analysis of the wake with a second body present would be necessary in the future.

5 Conclusions

Three-dimensional CFD simulation of a rigid, stationary cylinder was performed to identify the variation of the streamwise and transverse velocity components in the wake. Spatial and temporal velocity concentration of the flow caused by the cylinder was investigated using Fourier analysis of the wake velocity data. The fluctuating components of the streamwise and transverse energy components (u' and v') were separated from the mean components ($\overline{u}$ and $\overline{v}$).

There was significant spatial energy concentration due to the mean streamwise velocity component which occurred near the top and bottom surfaces of the circular cylinder, due to the blockage by the cylinder. The mean transverse component does not display any significant augmentation of energy in the wake. The temporal components of velocity contribute to the temporal concentration of energy at different harmonics of the vortex shedding frequency. Most of the temporal

concentration occurs at the shedding frequency due to the large scale von Karman vortices shed from the body and the maxima occur at $1< x/D < 3$ and $0 < |y/D| < 1$. The maximum amount of energy that could be captured by an ideal WEE, assuming that the WEE could capture high energy density regions in a single cycle of vortex shedding was also computed. A maximum of 3.25 times the available upstream energy can be harnessed at a streamwise distance of $x = 1D$ if both the temporally and spatially concentrated energy is harnessed.

Considering an ideal case where the WEE can move between high energy density locations at different time steps of the vortex shedding cycle, a high amount of energy can be captured by a device. Most of the augmentation from the different energy components occurred in the very near wake of the cylinder. A suitable WEE which operates using the temporal concentration will operate in the very near wake of the cylinder without changing the flow structure. However, extant literature suggests a critical spacing of at least $1.5D$ (Carmo et al. 2008; Igarashi 1984; Zdravkovich & Bearman 1998), between in-line separated circular cylinders of equal diameter, for the vortices to form in the gap between the cylinders. Current VIV systems seem to be utilising a combination of the temporal and spatial concentration, where the location of maximum efficiency is when the contribution from the unsteady components is in phase to the contribution from the steady components.

The effect of varying the cross-section of the cylinder was investigated using shapes such as the semi-circle, straight-edged triangle, concave-edged triangle and convex-edged triangle. The spatial concentration of the bodies varied very little from that of the circular cylinder. However, there was a significant increase in the temporal concentration of wake energy by the convex-edged triangle and the

semi-circular cylinder. Hence, these bodies would be ideal for use as primary bodies in WIV systems, where they can provide a large amount of energy in the form of transverse fluctuations in the wake.

The influence of the second body significantly changes the flow field and hence future work should investigate the spatial and temporal analysis of tandem bodies, to identify how the flow field is different. However, this paper has identified the concept of spatial and temporal concentration in the wake of cylinder and the methods which can be used to analyse the flow field and identify crucial factors that can be used to improve the design of VIV energy harnessing systems.

References

Alonso, G & Meseguer, J 2006, 'A parametric study of the galloping stability of two-dimensional triangular cross-section bodies', *Journal of Wind Engineering and Industrial Aerodynamics*, vol. 94, no. 4, pp. 241-53.

Alonso, G, Meseguer, J & Pérez-Grande, I 2005, 'Galloping instabilities of two-dimensional triangular cross-section bodies', *Experiments in fluids*, vol. 38, no. 6, pp. 789-95.

Amandolèse, X & Hémon, P 2010, 'Vortex-induced vibration of a square cylinder in wind tunnel', *Comptes Rendus Mécanique*, vol. 338, no. 1, pp. 12-7.

Assi, GRS 2009, 'Mechanisms for flow-induced vibration of interfering bluff bodies', Ph.D thesis, Imperial College London.

Barrero-Gil, A & Fernandez-Arroyo, P 2013, 'Maximum vortex-induced vibrations of a square prism', *Wind and Structures*, vol. 16, no. 4, pp. 341-54.

Batten, W, Bahaj, A, Molland, A & Chaplin, J 2006, 'Hydrodynamics of marine current turbines', *Renewable Energy*, vol. 31, no. 2, pp. 249-56.

NREL 2011, *The VIVACE Convertor - Enhancing Flow Induced Motions to Harness Hydrokinetic Energy in an Environmentally Compatible Way*, by Bernitsas, MM, viewed 29.06.2015, <http://www.nrel.gov/docs/fy12osti/51421-09.pdf>.

Bernitsas, MM, Ben-Simon, Y, Raghavan, K & Garcia, EM 2009, 'The VIVACE converter: model tests at high damping and Reynolds number around 105', *Journal of Offshore Mechanics and Arctic Engineering*, vol. 131, no. 1, pp. 1 - 15.

Bernitsas, MM & Raghavan, K 2004, 'Converter of current/tide/wave energy', *Provisional Patent Application, US Patent and Trademark Office Serial*, no. 60/628,252.

Bernitsas, MM, Raghavan, K, Ben-Simon, Y & Garcia, EM 2008, 'VIVACE (vortex induced vibration aquatic clean energy): A new concept in generation of clean and renewable energy from fluid flow', *Journal of Offshore Mechanics and Arctic Engineering*, vol. 130, no. 4, pp. 1697–712.

Bilgen, S, Keleş, S, Kaygusuz, A, Sari, A & Kaygusuz, K 2008, 'Global warming and renewable energy sources for sustainable development: A case study in Turkey', *Renewable and Sustainable Energy Reviews*, vol. 12, no. 2, pp. 372-96.

Branković, M & Bearman, P 2006, 'Measurements of transverse forces on circular cylinders undergoing vortex-induced vibration', *Journal of Fluids and Structures*, vol. 22, no. 6, pp. 829-36.

Braza, M, Chassaing, P & Minh, HH 1986, 'Numerical study and physical analysis of the pressure and velocity fields in the near wake of a circular cylinder', *Journal of Fluid Mechanics*, vol. 165, pp. 79-130.

Cantwell, B & Coles, D 1983, 'An experimental study of entrainment and transport in the turbulent near wake of a circular cylinder', *Journal of Fluid Mechanics*, vol. 136, pp. 321-74.

Cao, F-C & Xiang, H-F 2001, 'Calculation of unsteady flow around circular cylinder and vortex-induced vibration [J]', *Journal of Hydrodynamics*, vol. 1, p. 014.

Carmo, BS, Sherwin, SJ, Bearman, PW & Willden, RH 2008, 'Wake transition in the flow around two circular cylinders in staggered arrangements', *Journal of Fluid Mechanics*, vol. 597, pp. 1-29.

Chang, C-CJ, Kumar, RA & Bernitsas, MM 2011, 'VIV and galloping of single circular cylinder with surface roughness at $3.0\times 10^4 \leq Re \leq 1.2\times 10^5$', *Ocean Engineering*, vol. 38, no. 16, pp. 1713-32.

Derakhshandeh, JF, Arjomandi, M, Dally, B & Cazzolato, B 2014, 'The effect of arrangements of two circular cylinders on the maximum efficiency of vortex-induced vibration power using a scale-adaptive simulation model', *Journal of Fluids and Structures*, vol. 49, pp. 654-66.

—— 2015a, 'Harnessing Hydro-Kinetic energy from wake induced vibration using virtual mass spring damper system', *Journal of Ocean Engineering*, vol. 108, pp. 115-28.

—— 2015b, 'A study of the Vortex-Induced Vibration mechanism for harnessing hydrokinetic energy of eddies using a single cylinder', *Journal of Applied Mathematical Modelling*.

—— 2016, 'Flow-induced vibration of an elastically mounted airfoil under the influence of the wake of a circular cylinder', *Experimental Thermal and Fluid Science*, vol. 74, pp. 58-72.

Dick, E 1984, 'Momentum analysis of wind energy concentrator systems', *Energy Conversion and Management*, vol. 24, no. 1, pp. 19-25.

Ding, L, Zhang, L, Bernitsas, MM & Chang, C-C 2016, 'Numerical simulation and experimental validation for energy harvesting of single-cylinder VIVACE converter with passive turbulence control', *Renewable Energy*, vol. 85, pp. 1246-59.

Ding, L, Zhang, L, Wu, C, Mao, X & Jiang, D 2015, 'Flow induced motion and energy harvesting of bluff bodies with different cross sections', *Energy Conversion and Management*, vol. 91, pp. 416-26.

Dong, S, Karniadakis, G, Ekmekci, A & Rockwell, D 2006, 'A combined direct numerical simulation–particle image velocimetry study of the turbulent near wake', *Journal of Fluid Mechanics*, vol. 569, pp. 185-207.

Gaden, DL & Bibeau, EL 2006, 'Increasing power density of kinetic turbines for cost-effective distributed power generation', *Power-gen, April*, pp. 10-2.

Hansen, MO 2015, *Aerodynamics of wind turbines*, Routledge.

Hansen, MOL, Sørensen, NN & Flay, R 2000, 'Effect of placing a diffuser around a wind turbine', *Wind Energy*, vol. 3, no. 4, pp. 207-13.

Heath, T 2012, 'A review of oscillating water columns', *Philosophical Transactions of the Royal Society of London A: Mathematical, Physical and Engineering Sciences*, vol. 370, no. 1959, pp. 235-45.

Hobbs, WB & Hu, DL 2012, 'Tree-inspired piezoelectric energy harvesting', *Journal of Fluids and Structures*, vol. 28, pp. 103-14.

Igarashi, T 1981, 'Characteristics of the flow around two circular cylinders arranged in tandem: 1st report', *Bulletin of JSME*, vol. 24, no. 188, pp. 323-31.

—— 1984, 'Characteristics of the flow around two circular cylinders arranged in tandem: 2nd report, unique phenomenon at small spacing', *Bulletin of JSME*, vol. 27, no. 233, pp. 2380-7.

Jamieson, P 2008, 'Beating Betz-energy extraction limits in a uniform flow field', in *European Wind Energy Conference, European Wind Energy Association Paper CS3. 2Apr*.

Johnson, JB & Pride, DJ 2010, *River, tidal, and ocean current hydrokinetic energy technologies: Status and future opportunities in Alaska*, Alaska Center for Energy and Power, viewed 17.11.2015, <http://www.uaf.edu/files/acep/2010_11_1_State_of_the_Art_Hydrokinetic_Final.pdf>.

Kaltschmitt, M, Streicher, W & Wiese, A 2007, *Renewable energy: technology, economics and environment*, vol. 3, Springer, Berlin.

Khan, M, Bhuyan, G, Iqbal, M & Quaicoe, J 2009, 'Hydrokinetic energy conversion systems and assessment of horizontal and vertical axis turbines for river and tidal applications: A technology status review', *Applied Energy*, vol. 86, no. 10, pp. 1823-35.

King, R 1977, 'A review of vortex shedding research and its application', *Ocean Engineering*, vol. 4, no. 3, pp. 141-71.

Lagoun, M, Benalia, A & Benbouzid, M 2010, 'Ocean wave converters: State of the art and current status', in *Energy Conference and Exhibition (EnergyCon), 2010 IEEE International*, pp. 636-41.

Lee, J & Bernitsas, M 2011, 'High-damping, high-Reynolds VIV tests for energy harnessing using the VIVACE converter', *Ocean Engineering*, vol. 38, no. 16, pp. 1697-712.

Menter, F & Egorov, Y 2010, 'The scale-adaptive simulation method for unsteady turbulent flow predictions. Part 1: theory and model description', *Flow, Turbulence and Combustion*, vol. 85, no. 1, pp. 113-38.

Nemes, A, Zhao, J, Lo Jacono, D & Sheridan, J 2012, 'The interaction between flow-induced vibration mechanisms of a square cylinder with varying angles of attack', *Journal of Fluid Mechanics*, vol. 710, pp. 102-30.

Norberg, C 1992, 'Pressure forces on a circular cylinder in cross flow', in *IUTAM Symposium on Bluff Body Wakes, Dynamics and Instabilities, eds H Eckelmann, JMR Graham, P Hierre, PA Monkewitz*, pp. 275-8.

—— 1998, 'LDV-measurements in the near wake of a circular cylinder', *ASME Paper No. FEDSM98-521*.

Ohya, Y, Karasudani, T, Sakurai, A & Inoue, M 2001, 'Development of high-performance wind turbine system by wind-lens effect (locally concentrated wind energy)', in *JWEA Proc. of the 23 rd Wind Energy Utilization Symposium, Tokyo, Japan*, vol. 79.

Ong, L & Wallace, J 1996, 'The velocity field of the turbulent very near wake of a circular cylinder', *Experiments in fluids*, vol. 20, no. 6, pp. 441-53.

Ponta, F & Dutt, GS 2000, 'An improved vertical-axis water-current turbine incorporating a channelling device', *Renewable Energy*, vol. 20, no. 2, pp. 223-41.

Ponta, F & Jacovkis, P 2008, 'Marine-current power generation by diffuser-augmented floating hydro-turbines', *Renewable Energy*, vol. 33, no. 4, pp. 665-73.

Sarpkaya, T 1979, 'Vortex-induced oscillations: A selective review', *Journal of Applied Mechanics*, vol. 46, no. 2, pp. 241-58.

Sarpkaya, T 2004, 'A critical review of the intrinsic nature of vortex-induced vibrations', *Journal of Fluids and Structures*, vol. 19, no. 4, pp. 389-447.

Setoguchi, T, Shiomi, N & Kaneko, K 2004, 'Development of two-way diffuser for fluid energy conversion system', *Renewable Energy*, vol. 29, no. 10, pp. 1757-71.

2011, *International energy outlook 2011* by USEIA, viewed 17.11.2015, <http://205.254.135.7/forecasts/ieo/>.

Vries, O 1983, 'On the theory of the horizontal-axis wind turbine', *Annual Review of Fluid Mechanics*, vol. 15, no. 1, pp. 77-96.

Wanderley, JB, Souza, GH, Sphaier, SH & Levi, C 2008, 'Vortex-induced vibration of an elastically mounted circular cylinder using an upwind TVD two-dimensional numerical scheme', *Ocean Engineering*, vol. 35, no. 14, pp. 1533-44.

Wang, D-A & Ko, H-H 2010, 'Piezoelectric energy harvesting from flow-induced vibration', *Journal of Micromechanics and Microengineering*, vol. 20, no. 2, p. 025019.

Wei, R, Sekine, A & Shimura, M 1995, 'Numerical analysis of 2D vortex-induced oscillations of a circular cylinder', *International Journal for Numerical Methods in Fluids*, vol. 21, no. 10, pp. 993-1005.

Weinstein, LA, Cacan, MR, So, PM & Wright, PK 2012, 'Vortex shedding induced energy harvesting from piezoelectric materials in heating, ventilation and air conditioning flows', *Smart Materials and Structures*, vol. 21, no. 4, p. 045003.

Williamson, C & Govardhan, R 2004, 'Vortex-induced vibrations', *Annual Review of Fluid Mechanics*, vol. 36, pp. 413-55.

—— 2008, 'A brief review of recent results in vortex-induced vibrations', *Journal of Wind Engineering and Industrial Aerodynamics*, vol. 96, no. 6, pp. 713-35.

Williamson, CHK 1996, 'Vortex dynamics in the cylinder wake', *Annual Review of Fluid Mechanics*, vol. 28, no. 1, pp. 477-539.

Zdravkovich, MM 1997, 'Flow around circular cylinders, vol. 1. Fundamentals', *Journal of Fluid Mechanics*, vol. 350, pp. 377-8.

Zdravkovich, MM & Bearman, PW 1998, *Flow Around Circular Cylinders—Volume 1: Fundamentals*, American Society of Mechanical Engineers, 0098-2202.

This page has been left blank intentionally

Chapter 4. Energy concentration in the wake of bluff bodies

Various geometries such as aerofoils, circles, squares and triangles have been used to capture the energy in the wake of an upstream bluff body. However, the upstream cylinder has been the circular cylinder in most WIV investigations. The circular cylinder has a multitude of research on its behaviour in a cross flow and the vibration characteristics that ensue from VIV and WIV. However, there has been less emphasis on the wake characteristics of different cross-sections of cylinders in regards to the temporal concentration of flow energy. This chapter is focused on identifying a suitable replacement for the upstream circular cylinder in a WIV system, which can generate higher levels of temporally concentrated wake energy. Higher levels of temporally concentrated transverse energy in the wake of an upstream body can aid in the transverse 1 degree-of-freedom vibrations of the downstream body, and hence are useful for energy harnessing in a WIV system.

The upstream bluff body was shown to spatially and temporally concentrate flow energy in a WIV system. Following on from the numerical analysis performed in Chapter 3, this chapter focuses on the experimental verification of the temporal wake energy concentration using Particle Image Velocimetry (PIV). The differences in form and frequency of the energy concentrated by different bluff body cross-sections is investigated for Reynolds numbers of 5,000 and 10,000. The cross-sections were chosen based on past literature and as a by-product of the numerical investigation in the previous chapter. Experiments in a water channel with PIV analysis were used to record and process data to analyse the turbulence and velocity statistics in the wake of the

cylinders. The turbulent kinetic energy, spanwise vorticity patterns and the spatial and temporal wake energy components are compared between the different cross-sections investigated. This chapter identified two cross-sections of the cylinder (semi-circular and convex-edged triangular) that provide zones of higher temporal energy in the wake when compared to the circular cylinder. Hence, these cross-sections were identified as possible upstream bodies for a WIV energy system.

This chapter has been submitted for publication as:

Manickam Sureshkumar, E, Arjomandi, M, Dally, B, Cazzolato, B, Ghayesh, M, 'Energy Concentration by Bluff Bodies - a Particle Image Velocimetry Investigation', *ASME Journal of Fluids Engineering* (under review).

Statement of Authorship

Title of Paper	Energy Concentration by Bluff Bodies - a Particle Image Velocimetry Investigation
Publication Status	☐ Published ☐ Accepted for Publication ☑ Submitted for Publication ☐ Unpublished and Unsubmitted w ork w ritten in manuscript style
Publication Details	Manickam Sureshkumar, E, Arjomandi, M, Dally, B, Cazzolato, B, Ghayesh, M, 'Energy Concentration by Bluff Bodies - a Particle Image Velocimetry Investigation', *ASME Journal of Fluids Engineering*, (under review)

Principal Author

Name of Principal Author (Candidate)	Eshodarar Manickam Sureshkumar		
Contribution to the Paper	Water channel experiments and particle image velocimetry to obtain the velocity fields in the wake of a circular cylinder and cylinders with different cross-sections. Temporal and spatial energy analysis of the wake velocity fields to identify an efficient upstream energy concentrator.		
Overall percentage (%)	85		
Certification:	This paper reports on original research I conducted during the period of my Higher Degree by Research candidature and is not subject to any obligations or contractual agreements with a third party that would constrain its inclusion in this thesis. I am the primary author of this paper.		
Signature		Date	22/06/2018

Co-Author Contributions

By signing the Statement of Authorship, each author certifies that:

i. the candidate's stated contribution to the publication is accurate (as detailed above);
ii. permission is granted for the candidate in include the publication in the thesis; and
iii. the sum of all co-author contributions is equal to 100% less the candidate's stated contribution.

Name of Co-Author	Maziar Arjomandi		
Contribution to the Paper	Supervised the work, assisted in developing ideas and manuscript evaluation		
Signature		Date	22/06/2018
Name of Co-Author	Bassam B. Dally		
Contribution to the Paper	Supervised the work, assisted in developing ideas and manuscript evaluation		
Signature		Date	25/06/2018
Name of Co-Author	Benjamin S. Cazzolato		
Contribution to the Paper	Supervised the work, assisted in developing ideas and manuscript evaluation		
Signature		Date	22/6/18
Name of Co-Author	Mergen H. Ghayesh		
Contribution to the Paper	Supervised the work, assisted in developing ideas and manuscript evaluation		
Signature		Date	22/06/2018

This page is intentionally left blank

Article

Title - Spatial and temporal concentration of hydrokinetic energy in the wake of a bluff body

Authors – Eshodarar Manickam Sureshkumar (Corresponding Author), Maziar Arjomandi, Benjamin S. Cazzolato, Bassam B. Dally

Affiliation – The University of Adelaide

Address – School of Mechanical Engineering, The University of Adelaide, North Terrace, Adelaide, SA, 5005

Chapter 4: Temporal concentration of flow energy by different bluff bodies

Abstract

Particle Image Velocimetry (PIV) of four cylinders with different cross-sections were performed in a recirculating water channel at Reynolds numbers of 5,000 and 10,000. The cylinders were split into two distinct categories; semi-circular and convex-edged triangular (c-triangular) prisms which have a smooth diverging fore-face and a flat, backward facing step aft-face, and a trapezoid which has a flat fore face and a backward-facing step aft-face. The resulting streamwise and transverse velocity vectors (u and v respectively) were analyzed to provide a qualitative comparison of the bluff body wakes to the circular cylinder, which is the standard upstream stationary body in Wake Induced Vibration (WIV) energy technology. The Reynolds stresses, Turbulent Kinetic Energy (TKE), mean spanwise vorticity, and the energy in the fluctuating component of the wake were compared. The main findings are: i) a convex fore-face and a backward-facing step aft face are more effective at converting the flow energy to temporal wake energy (+ 20%) compared to a circular cylinder, ii) a trapezoid type shape is less effective at converting flow energy to temporal wake energy (- 40%) compared to a circular cylinder, iii) increasing Reynolds number reduces the efficiency of conversion of upstream flow energy to downstream transverse temporal energy. Utilizing stationary upstream bodies such as the semi-circle and the c-triangle can result in concentrating more energy in the fluctuating components for the downstream transversely vibrating bluff body in a WIV system, and hence can realize in more efficient WIV technology.

1 Introduction

Wake-Induced Vibration (WIV) is a form of flow induced vibration of bluff bodies (Zdravkovich 1997), and can be used in extracting energy from low-speed flows (Bernitsas *et al.* 2008; Derakhshandeh *et al.* 2014b). Previous research indicates that more energy can be extracted by using a tandem system, where an upstream stationary bluff body concentrates the flow energy and a second downstream bluff body vibrates in the transverse direction (Assi 2009; Bernitsas 2011; Derakhshandeh *et al.* 2014a).

Although mitigation of Flow-Induced Vibration (FIV) such as Vortex-Induced Vibration (VIV) and WIV sparked research on the phenomena, recent evidence suggests that FIV could be applied to flow energy technology such as the Vortex Induced Vibration for Aquatic Clean Energy (VIVACE) (Bernitsas *et al.* 2008). Pioneering work by Bernitsas *et al.* (2008), resulted in an early large-scale VIV device, employing a circular cylinder, to produce energy from low speed flows. Further research by the aforementioned group has led to significant advancements in VIV and WIV energy technology (Ding *et al.* 2015a; Ji *et al.* 2018; Kinaci *et al.* 2016; Lan *et al.* 2018; Ma *et al.* 2018; Xu *et al.* 2017). Small-scale devices, such as those used for remote monitoring in ventilation and air conditioning systems, can use WIV to produce the minuscule amounts of energy needed for them to operate and hence making monitoring easier and viable at remote locations (Hobbs & Hu 2012; Wang & Ko 2010; Weinstein *et al.* 2012). WIV has also been proven to enhance vibrations of flapping aerofoils and hence aid in flow energy harvesting (Derakhshandeh *et al.* 2016; Wei & Zheng 2018).

The main difference between VIV and WIV is that the latter needs a body vibrating in the wake produced from an upstream and stationary bluff body (Assi 2009). The fluctuating wake produced from the stationary bluff body affects both the mean and fluctuating forces on the downstream and vibrating body, causing the WIV response. WIV is of interest for energy production, due to the amplitude response not being limited to a lock-in range of velocities, as in VIV (Assi 2009; Derakhshandeh *et al.* 2014b) as well as the fact that efficiency of WIV systems are higher than VIV systems (Derakhshandeh *et al.* 2014b, 2015a). Although FIV can be a 2 degree-of-freedom (2DOF) system, WIV energy technology is usually constrained to transverse resonance (1DOF), since the vibration amplitudes are at least 3 times greater than the streamwise amplitudes (Bernitsas *et al.* 2008; Blevins & Coughran 2009; Hobbs & Hu 2012; Wang & Ko 2010).

Derakhshandeh and others showed that a WIV system, consisting of two circular cylinders, had an efficiency of 48.6% (Reynolds number (Re) = 9000) whereas a VIV system only had a max efficiency $\eta = 22.2\%$ at Re = 65,000 based on CFD modelling and obtained $\eta = 10\%$ at Re = 6,000 based on experiments (Derakhshandeh *et al.* 2015a, 2015b). Work by these authors suggested that a staggered separation of cylinders in a WIV system are more efficient compared to inline separations for the purpose of energy harvesting, and this was demonstrated using both a circular cylinder as well as an aerofoil as the downstream vibrating body. Bernitsas *et al.* (2009) worked out a theoretical efficiency of 37% for a single circular cylinder VIV system, but only obtained $\eta = 22\%$ at $Re = 1x10^5$. Recent research on single cylinder VIV responses for different bluff body cross-sections yielded a max efficiency of 45.7% for a trapezoid operating in a Reynolds number range of 10,000 – 130,000

(Ding *et al.* 2015b). The application of WIV for energy production is still a relatively novel and new field which has sparked exciting progress over the last decade, however further understanding is still required to increase the energy extraction efficiencies. Previous focus has been on cross-section and placement of the downstream vibrating body, as well as system parameters such as mass and damping ratio. However, there is a gap in knowledge of the impact of flow features on energy concentration for upstream cross-sections apart from the circular cylinder.

A bluff body placed in flow produces a vortex street which causes spatial and temporal concentrations of the flow energy. Energy in a flow field can be subdivided into spatial and temporal energy because of the steady and the unsteady (fluctuating) velocity components in the flow, respectively (Manickam Sureshkumar *et al.* 2018). Equations (1) – (4) in Section 2.4 are used to define the spatial (Equations (1) and (2)) and temporal (Equations (3) and (4)) energy components of the flow in this study. The steady component is defined as the mean velocity component of the flow which is constant over time. On the other hand, the temporal concentration is time-dependant and hence is caused by the fluctuating and periodic components of the velocity in the wake of the body, which arise due to the periodicity of the vortex street shed by the body. Hence, spatial flow energy concentrators would perform better in situations with steady flow conditions (i.e. upstream of turbines), whilst temporal flow concentrators are needed for devices which operate utilising the temporal flow energy.

Unlike spatial concentrators such as diffusers and shrouds, the vortices in the bluff body wake have an added temporal component occurring at the shedding frequency. This added temporal component enhances the vibrations of the second body through resonance due to the periodicity of the vortices in the wake. Hence, knowledge of the wake and its temporal features is a significant aspect that can aid efficient WIV technology.

Bluff bodies of various cross-sections have been investigated for FIV in many past studies. These include the vibration responses of bluff bodies such as square cylinders, triangular prisms (Alonso & Meseguer 2006; Alonso *et al.* 2005), and a comparison between various bodies (Ding *et al.* 2015b). These investigations reported the flow-induced vibration responses of the bodies, but there has been no analysis of the energy concentrated in the wake of different bluff bodies.

The observed wake structure of an upstream cylinder in a pair of in-line separated circular cylinders was investigated in a study by Igarashi (1984). Similar observations have been reported via experimental investigation by Zdravkovich and Bearman (1998) and through numerical modelling by Carmo *et al.* (2008). The upstream circular cylinder wake is highly dependent on the position of the downstream circular cylinder (when in the near wake, $< 5D$), and the wake was categorised into six different patterns dependant on the separation gap and the flow field in-between the cylinders. However, this classification was for cylinders separated at the centreline, and recent studies have shown that a staggered arrangement of cylinders is favourable for efficient WIV. Although the downstream body will influence the flow structure of the upstream body, characterization of the energy density

produced in the wake of bluff bodies is necessary knowledge for efficient design of WIV systems.

The turbulence properties in the near wake of a cylinder has been investigated using hot-wire anemometry measurements as well as flow visualisation in numerous experimental works in the last century. Experiments involving hot-wire measurements in the near wake of a cylinder (<5*D*) are relatively complex at high Reynolds numbers due to the recirculation zone and instantaneous flow angles in the near wake of the cylinder. Undeterred by these experimental complexities, many experimental works have tackled the near wake of a cylinder at high Reynolds numbers. Velocity and vorticity vectors have been measured using a wire probe by Ong and Wallace (1996) and Rajagopalan and Antonia (2005) performed power spectrum analysis using hot wire anemometry measurements. Mean streamwise velocity and turbulent intensity profiles were obtained by Bloor and Gerrard (Bloor & Gerrard 1966) for Reynolds numbers between 1,000 and 10,000 using a single-sensor hot-wire probe. Notable works by Cantwell (Cantwell, BJ 1975) and Cantwell and Coles (Cantwell, Brian & Coles 1983) utilised phase-averaging and flying-hot wire anemometry to measure the near field wake of a cylinder. Gaudin and others (Gaudin *et al.* 1998) quantitatively analysed the spatial properties of the near wake velocities of a cylinder at Re = 6,000 – 12,000 and presented evidence of scaling laws for velocity structure functions. A combined hot-wire probe and flow visualisation study by Kourta and others (Kourta *et al.* 1987) found evidence of strong interaction between the small-scale vorticial structures, arising because of the transition from laminar to turbulence in the cylinder wake, and vortices shed from the body; this interaction occurs for a Re = 2,000 – 16,000 due to the similar frequencies in both phenomena. However, the

rather intrusive nature of probe measurement techniques may affect the order of magnitude of the systematic errors in a general way.

Non-invasive techniques such as Particle Image Velocimetry (PIV) or Laser Doppler Velocimetry (LDV) have been used to overcome limitations of intrusive flow measurement methods. Time-resolved PIV measurements in the wake of a circular cylinder were performed by Lourenco and Shih (1993) at a Reynolds number of 3900, and these data have been used to validate many numerical simulations. PIV at higher Reynolds numbers ranging between 1,000 – 10,000 were used by Lin *et al.* (1995) to investigate the velocity and vorticity in the wake of a circular cylinder. Norberg (1998) used LDV to obtain streamwise and transverse turbulence statistics in the near wake of cylinders at Reynolds numbers 1,500 - 10,000 using a commercial fibre-optic LDV system. The data was then used to identify length scales and location of extrema, as well as the statistical moments for the streamwise and transverse velocity components.

Ozgoren *et al.* (2011) used PIV techniques, at Re = 5,000 and 10,000, to obtain velocity vectors and compare the flow structures between a sphere and a circular cylinder using PIV with a resolution of 1600 x 1186 pixels and an interrogation window of 32x32 pixels with 50% overlap; the authors' work resulted in velocity and vorticity vectors as well as the turbulent kinetic energy and other turbulence quantities. A comparison between PIV and Direct Numerical Simulation in the cylinder wake was published by Dong *et al.* (2006) using a PIV plane measuring 96.8 x 98.8 mm and an interrogation window size of 32 x 32 pixels. They performed investigations at the Reynolds number of 3,900/4,000 as well as at 10,000 to obtain isocontours of the mean and root mean square (r.m.s) streamwise velocity. The flow characteristics behind a circular cylinder

have been extensively reviewed in extant literature using PIV and probe techniques to provide results such as Reynolds stresses and Turbulent Kinetic Energy (TKE). However, the temporal concentration of flow energy for energy harvesting has not been experimentally investigated to increase the energy available in the fluctuating velocity components.

Variation of gap spacing between two cylinders has shown that proper gap spacing between two cylinders results in an amplified VIV response of a downstream cylinder (Derakhshandeh *et al.* 2015a). The highly efficient vibrations are attributed to favourable impedance matching which occurs when the velocity of the vibrating body is in phase with the forces acting on the body. However, the contribution of the frequency and magnitude of the velocity components to the energy harnessing potential has not been reported in literature. It is clear that the wake produced by bluff bodies provide not only a spatial concentration of flow energy, but also a temporal concentration due to the periodic vortex street. Hence, there is a gap in the understanding of the contribution of different velocity components in the wake to the concentration of the upstream flow energy. Understanding the magnitude and frequency of the energy concentration in the wake can lead to knowledge on how this energy can be manipulated to result in a high efficiency system. Previous work by the current authors (Manickam Sureshkumar *et al.* 2018) identified the maximum energy that can be captured from the wake of a circular cylinder. The maximum energy that can be extracted was calculated assuming that a Wake Energy Extractor (WEE) can move transversely to points of high energy density, at a fixed streamwise distance; and that all the concentrated energy could be captured. Time-dependant streamwise and transverse energy available at every 1/8th of a single vortex shedding cycle were

analysed to identify the zones of maximum energy density. Based on this analysis, the highest streamwise energy density was at $x/D = 0$ due to the jet that formed on the surface of the cylinder and was almost three times the magnitude of the available upstream flow energy. The maximum for obtainable transverse energy in the wake occurred at $x/D = 1$ and had a magnitude of about 1.25 times the oncoming flow energy. A combined maximum of 3.25 times the free stream energy is available at $x/D = 1$ for a WEE that is able to capture both the streamwise and transverse concentration of energy in the wake of the cylinder. Hence, the concentration of energy in the wake of the cylinder was shown to be significant and can result in efficient vibrations of a WIV system. The work in (Manickam Sureshkumar *et al.* 2018) also identified that the energy in the wake due to the vortex street occurred at harmonics of the shedding frequency where most of the temporal energy in the wake occurred at the primary shedding frequency, whilst negligible energy concentration occurred in the second and third harmonics.

Efficient utilisation of the WIV concept strongly depends on the temporal concentration of wake energy behind the stationary upstream bluff body. While a plethora of research studies have been reported on circular cylinders, other cross-sections have not been systematically explored for this purpose. Knowing the difference in wakes will lead to a better understanding of the flow regimes available to the Power Take-Off (PTO) unit in a WIV system. Hence, this study aims at investigating the impact of different shapes on the resulting wake flows and the effectiveness of concentrating the upstream kinetic energy into temporal wake energy at flow conditions relevant to the subcritical flow regime. In this paper, four bluff body cross-sections are investigated in a circulating water channel utilising Particle Image Velocimetry (PIV) at

two Reynolds numbers (5,000 and 10,000). The Reynolds numbers lie within the shear layer transition regime, where the laminar-turbulent transition occurs in the shear layers and moves upstream with increasing Reynolds number (Rosetti *et al.* 2012). The flow structure, shedding frequency, temporal concentration of energy in the wake and turbulent kinetic energy are reported and analysed. The effect of the wake energy concentration depends on the cross-section, Reynolds number, characteristic diameter and roughness of the bluff body (Blevins 1997). Hence all conditions, other than the cross-sectional shape, were similar for all cases. Experimental methodology and comparison with existing circular cylinder data is presented in Section 2, followed by the results and discussion in Section 3, and finally the paper is summarised in the conclusion in Section 4.

2 Methodology

A circular cylinder was used as the first control body since it is the most widely used profile for VIV and WIV. Its axisymmetric profile does not have orientation constraints compared to shapes with vertices. The numerical investigation conducted in Manickam Sureshkumar *et al.* (2018) has shown that semi-circular (Figure 1 b) and convex-edged triangular prisms (Figure 1 c) (midway shape between a semi-circle and an equilateral triangle) provided greater concentrations of temporally occurring energy in their wake compared to circular, straight-edged triangular and concave-edged triangular prisms. The convex-edged triangle (c-triangle henceforth) was used to provide a transition shape between the semi-circular and straight-edged triangles. Hence, they were chosen for the current investigation, along with a trapezoid shape (Figure 1 d) previously reported by Ding *et al.* (2015b). The trapezoid is

a shape that is between a square and a triangle, and hence has a short edge and long edge which are parallel to each other. Although a trapezoidal shape with the blunt leading-edge (larger of the two parallel side as the upstream face) was shown to be an efficient vortex generator by Venugopal *et al.* (2017), the Strouhal number varies greatly between *Re* = 2,500 and 20,000. Thus, the blunt leading-edged trapezoidal cylinder is not very suitable for WIV in the Reynolds number range tested in this study, and hence the trapezoid was tested with the short edge set as the leading edge (Figure 1 (d)). The straight-edged triangle and concave-edged triangle investigated in the authors' previous CFD investigation were not used in this study, as they did not display any significant augmentation of temporal wake energy. This was attributed to the shear layers being diverted up/down from the body, reducing the magnitude of fluctuations when they interact together downstream of the body. Cross-sections other than the circle were also categorized into two groups – shapes with curved fore surfaces (semi-circle and c-triangle) and a shape with a flat fore surface (trapezoid) (Figure 1).

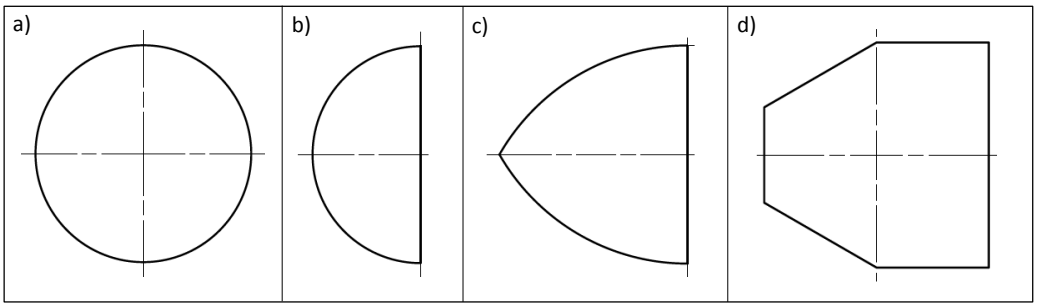

Figure 1 - Bluff body cross-sections used in this study (all shapes have a characteristic diameter of 30mm; not to scale); from left to right – circle (a), semicircle (b), c-triangle (c) and trapezoid (d)

The cylinders of varying cross-section were placed in an open water channel and the wake velocities was measured using PIV. The resulting mean and fluctuating energy components as well as some turbulence statistics were investigated at Reynolds numbers of 5,000 and 10,000. Experiments were conducted in the recirculating water channel located

at the Thebarton campus of the University of Adelaide. The experimental details and the data reduction methods including Fourier analysis are detailed in the following section.

2.1 Setup

The working section of the low-speed, recirculating and open water channel measures 500mm^{W} x 500mm^{H} x 2000mm^{L} as shown in Figure 2. The water channel has a maximum velocity of 0.335 m/s. Cylinders with a characteristic diameter of 30mm were mounted vertically in the water channel with a wetted length of 400mm. The cylinders did not have end plates; the top-end was connected to a supporting frame with the top-end of the cylinder being 10mm from the water surface; and the bottom-end was suspended freely in the water channel (110mm from the bottom of the tunnel).

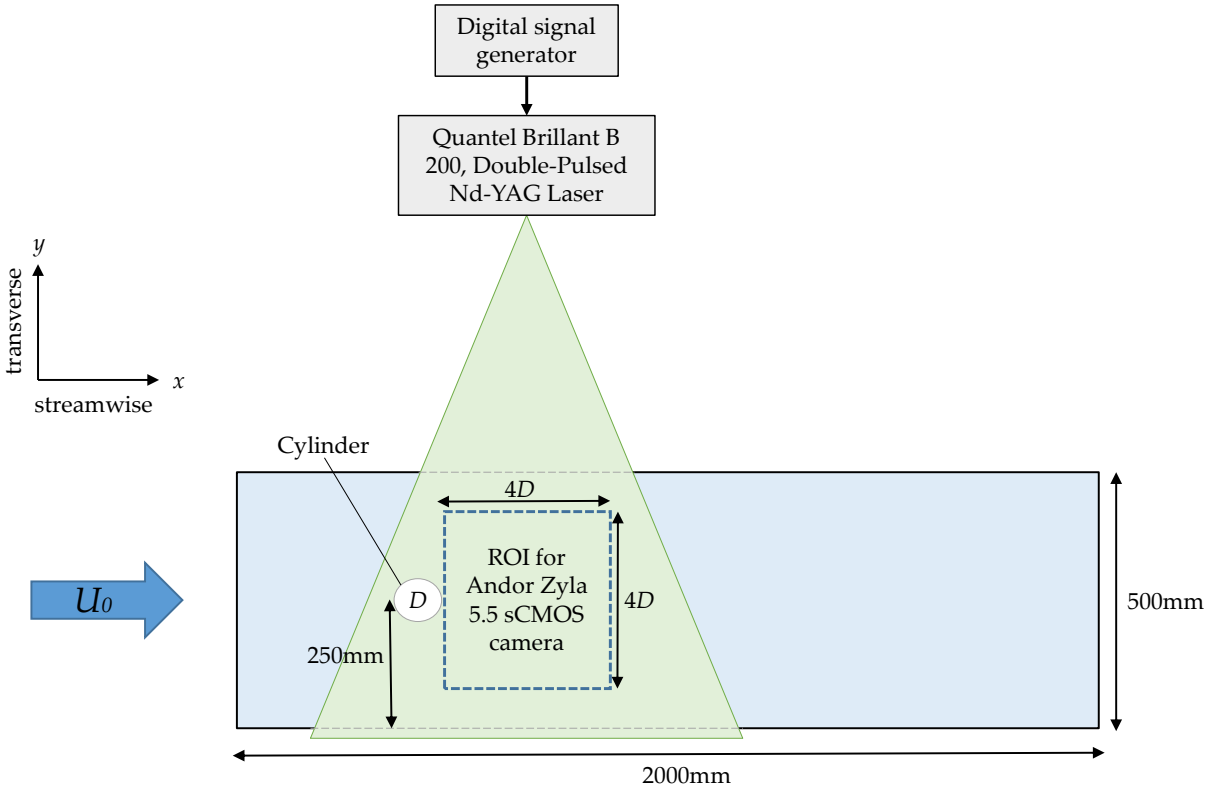

Figure 2 - Working section of the Thebarton water channel (Birdseye view) with a schematic of the PIV set-up

The smooth cylinders were fabricated out of aluminium and painted matte black to reduce reflection of the laser sheet. Data was collected at Reynolds numbers of 5,000 and 10,000 which corresponds to a freestream flow velocity of 0.168 ms^{-1} and 0.335 ms^{-1}, respectively.

2.2 Single frame double-exposure Particle Image Velocimetry (PIV)

A Quantel Evergreen 200 (200 mJ) Nd-YAG, double-pulsed laser with an articulated mirror arm was used to produce a horizontal laser sheet, at 532 nm, with <1mm thickness. The sheet passed through the middle of the channel downstream of the bluff body. A mirror angled at 45° was placed under the tunnel to reflect the elastic scatter from the seeded particle in the water into a camera, situated near the side wall of the tunnel. The recirculating water channel was seeded with 50-micron Polyamide PSP particles from Dantec Dynamics and the concentration was kept constant ~15 parts per million. An Andor ZYLA sCMOS 5.5 camera, with a resolution of 5.5 megapixels, was used to capture the region of interest (2000 x 2000 pixels) utilising the Andor SOLIS image capturing software. Each interrogation window had a minimum of 15 particles as suggested by Keane and Adrian (1990a). The region of interest was x/D = 0.5 to 4.5 (length-wise) and y/D = -2.0 to 2.0 (width-wise). The laser and camera were connected to a digital timing box to capture 3000 pairs of illuminated images at a frequency of 15 Hz, which is sufficient to analyse turbulent statistics (Ozkan *et al.* 2017). A time difference of 1.6 ms was used for the Re = 10,000 case and 3.2 ms for the Re = 5,000 case in order to have sufficient movement of particles in each interrogation window. The setup of the PIV system is shown in Figure 1.

2.3 Post-processing of PIV image pairs

The pairs of images captured were post processed by the PIVlab toolbox available for Matlab (Westerweel & Scarano 2005). PIVlab uses the images to generate instantaneous velocity vectors, which were saved and used for the temporal analysis. The image pairs were processed using double pass interrogation with a window size of 64 x 64 pixels and a second pass of 32 x 32 pixels with an overlap of 50% for both passes. Spurious vectors resulting from post-processing of data (< 2%) were detected using the normalized median test (Westerweel & Scarano 2005) (local median filter in PIVlab (Thielicke & Stamhuis 2014)). The 3 x 3 neighbourhood of velocity vectors around a central vector is used to compute the velocity fluctuation with respect to the median; and is used as normalisation for a more classical median test. This is one of the most used methods for universal outlier detection in PIV and works by normalizing a residual of measured velocities, such that data vectors in high-gradient zones are not discarded as outliers simply due to the variability of their neighbours (Duncan *et al.* 2010). Once spurious vectors had been detected, they were replaced by vectors resulting from a linear interpolation in each direction from the surrounding 3 × 3 set of vectors.

The u and v (streamwise and transverse components, respectively) velocities obtained from PIVlab were further processed for the mean and temporal analysis of energy in the wake of the cylinders. The mean energies were calculated by taking the squares of the mean normalised velocity vectors. The maximum displacement of particles was 9 pixels in the PIV images obtained, which is similar to previous PIV studies. The illuminated particles were between 3 and 5 pixels in the PIV images and the particle density was 15 – 20 per window. With these parameters, the

bias error for window deformation in PIVlab is smaller than 0.005 pixels with the random error below 0.02 pixels.

The post processing of PIV image pairs to obtain velocity has numerous uncertainty parameters associated with the size of seeding particles, overlap of particles in the frames, non-uniform distribution of particles, size of the interrogation window, particle correlations which are unmatched, movement of particles in the z plane (out of laser plane), and noise in optical and electrical measurements (Ozgoren 2006). A detailed account of the effect of the afore mentioned parameters is found in literature such as Westerweel (1993), Keane and Adrian (1990b) and Hart (2000). The effect of these factors have been assessed by Westerweel (1993) and it was shown that velocity measurements from digital PIV are estimated within 2% uncertainty.

2.4 FFT methods

The temporal contribution was identified by calculating the power spectrum using the *pwelch* function in Matlab. A flattop window, with an overlap of 50% was used to output the power spectrum of the streamwise and transverse velocity vectors (u and v respectively). The magnitude at the shedding frequency was then normalised against the square of the freestream velocity, and that resulting in the normalised magnitude of temporal energy at the shedding frequency.

The definition of the energy terms derived for the spatial and temporal analysis of the energy in the wake of the cylinders is given in Equations (1) – (4). The primary shedding frequency was identified for each shape and the corresponding magnitude for that frequency was taken from the power spectrum. Since most of the temporal energy is found at the vortex shedding frequency, the temporal investigation only

includes the normalised energy found at the primary shedding frequency for each bluff body. Contour maps of the resulting magnitudes at their respective locations, were used to observe the trends in temporally occurring energy in the cylinder wake.

Mean Normalised streamwise energy	$E_{\bar{u}} = \bar{u}^2/U_0^2$	(1)
Mean Normalised transverse energy	$E_{\bar{v}} = \bar{v}^2/U_0^2$	(2)
Normalised energy due to fluctuating streamwise component at *fs*	$E_{u'_{fs}} = u_{mag\ ps}/U_0^2$	(3)
Normalised energy due to fluctuating transverse component at *fs*	$E_{v'_{fs}} = v_{mag\ ps}/U_0^2$	(4)

where u = streamwise velocity; v = transverse velocity; $u_{mag\ ps}$ = power spectrum magnitude obtained for the streamwise velocity at the primary shedding frequency, *fs*; $v_{mag\ ps}$ = power spectrum magnitude obtained for the transverse velocity at the primary shedding frequency; U_0 = freestream velocity; and the overbar indicates the mean of the variable (time-averaged quantity). The primary shedding frequency was determined by identifying the peak in the FFT plots for each velocity component. For brevity, the FFT results obtained for the four cross-sections at x/D = 2 and y/D = 0 is plot in Figures 3 (circle and trapezoid) and 4 (semi-circle and convex-edged triangle).

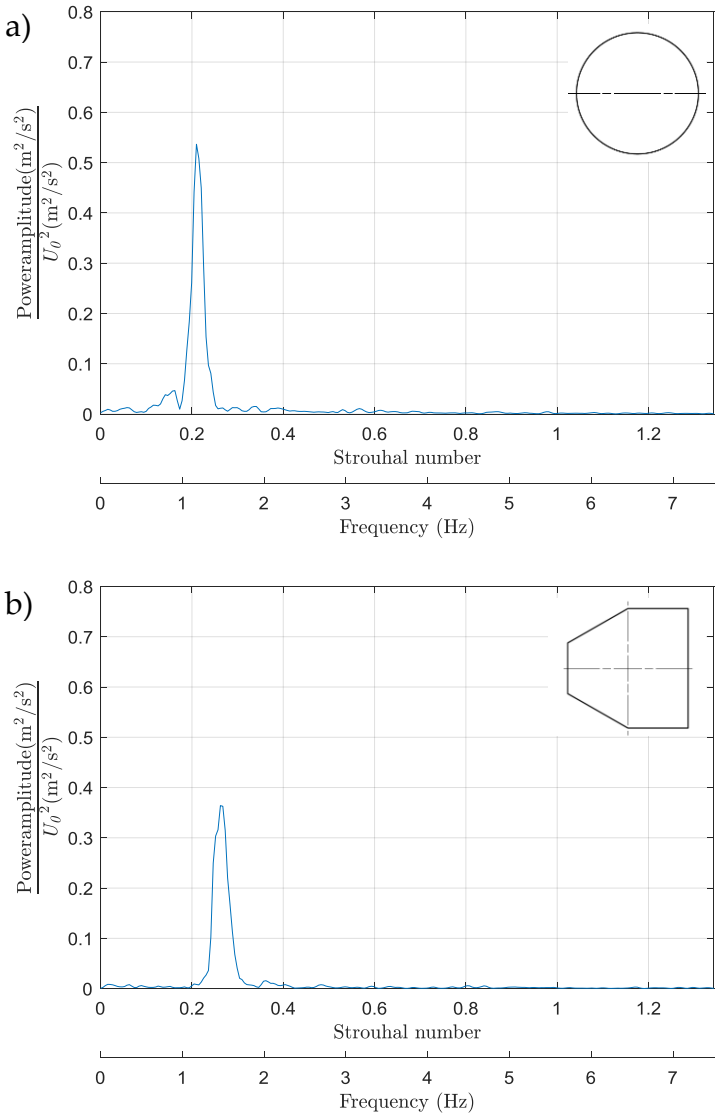

Figure 3 - Power spectrum output for the fluctuating transverse velocity component (v') at x/D = 2 and y/D = 0 for the circular (a) and trapezoidal (b) cylinders.

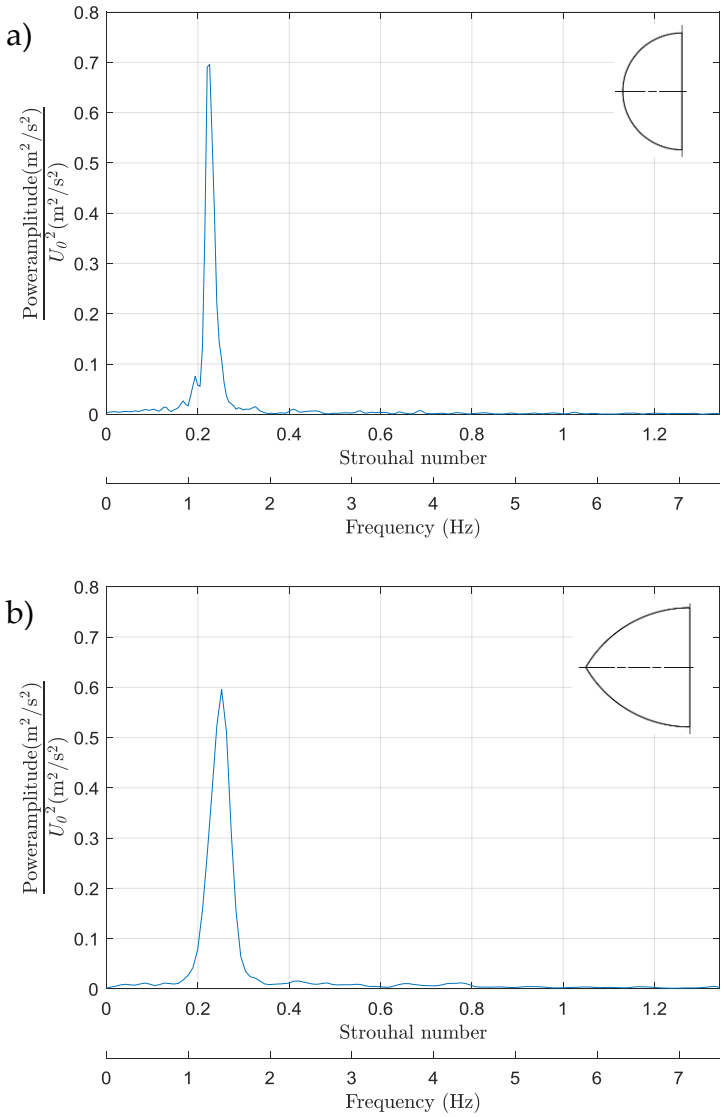

Figure 4 - Power spectrum output for the fluctuating transverse velocity component (v') at x/D = 2 and y/D = 0 for the semi-circular, (a), and convex-edged triangular, (b), cylinders.

2.5 Comparison of circular cylinder data with literature

The data collected for the circular cylinder case has been compared with existing experimental data from Norberg and others (1998) at *Re* = 5,000 and 10,000 to demonstrate experimental data fidelity and accuracy and is presented in this section. Shown in Figure 5 is a comparison of the centreline mean velocities from the current study and the literature. It is clear that the collected data agrees reasonably well with data from

Norberg and others (1998). Also clear, is that both profiles in this work show consistent location of the minimum normalised streamwise velocity and that the recovered velocity downstream of the wake is within a 2% of the published data. The minor differences in the velocity profiles can be attributed to differences in experimental conditions and methods such as the dimensions of the tunnel and cylinder, blockage in the tunnel and turbulence intensity of the upstream flow.

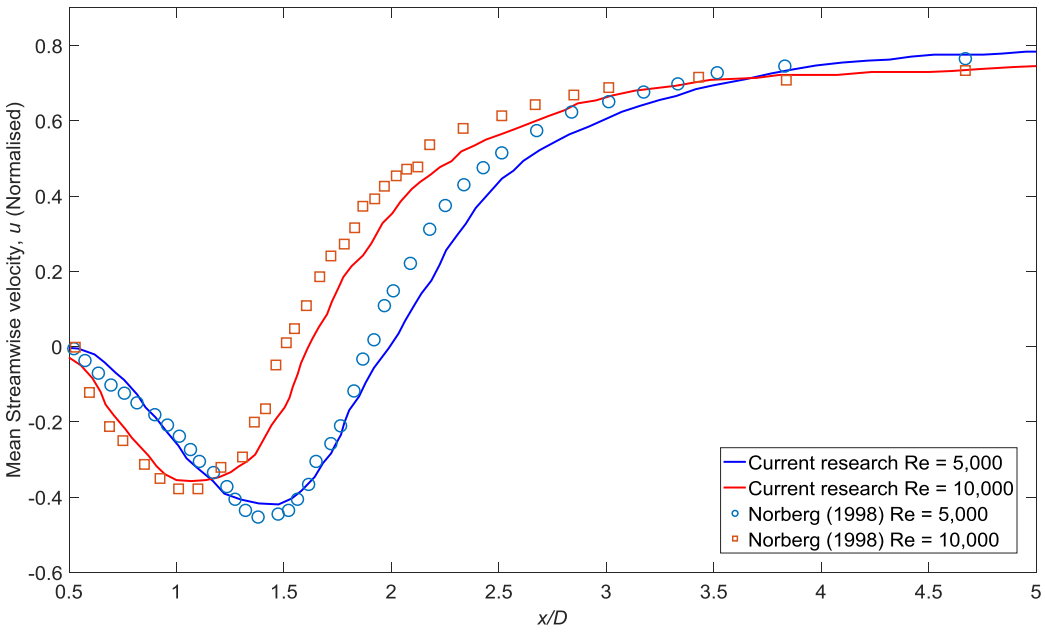

Figure 5 – Normalised mean streamwise velocity, $\overline{u}/U_0$, of the circular cylinder along the centreline (y/D = 0) compared to the published experimental data by Norberg (1998)

The contour plot of mean streamwise velocity ($\bar{u}$) in the wake of the circular cylinder at *Re* = 10,000 is shown in Figure 6 c). Similar PIV and DNS results published by Dong *et al.* (2006) at the same Reynolds number are included in Figure 6 a) and b) for comparison. The lengths of the recirculation bubble obtained from Figure 6 were 0.78*D* for the PIV experiment and 0.82*D* for the DNS simulation. In comparison, a recirculation bubble length of 0.8*D* was obtained in the current study. Hence, it is reasonable to claim that the current experiments and the

methodology provide us with high fidelity data that are consistent with the published results in the literature.

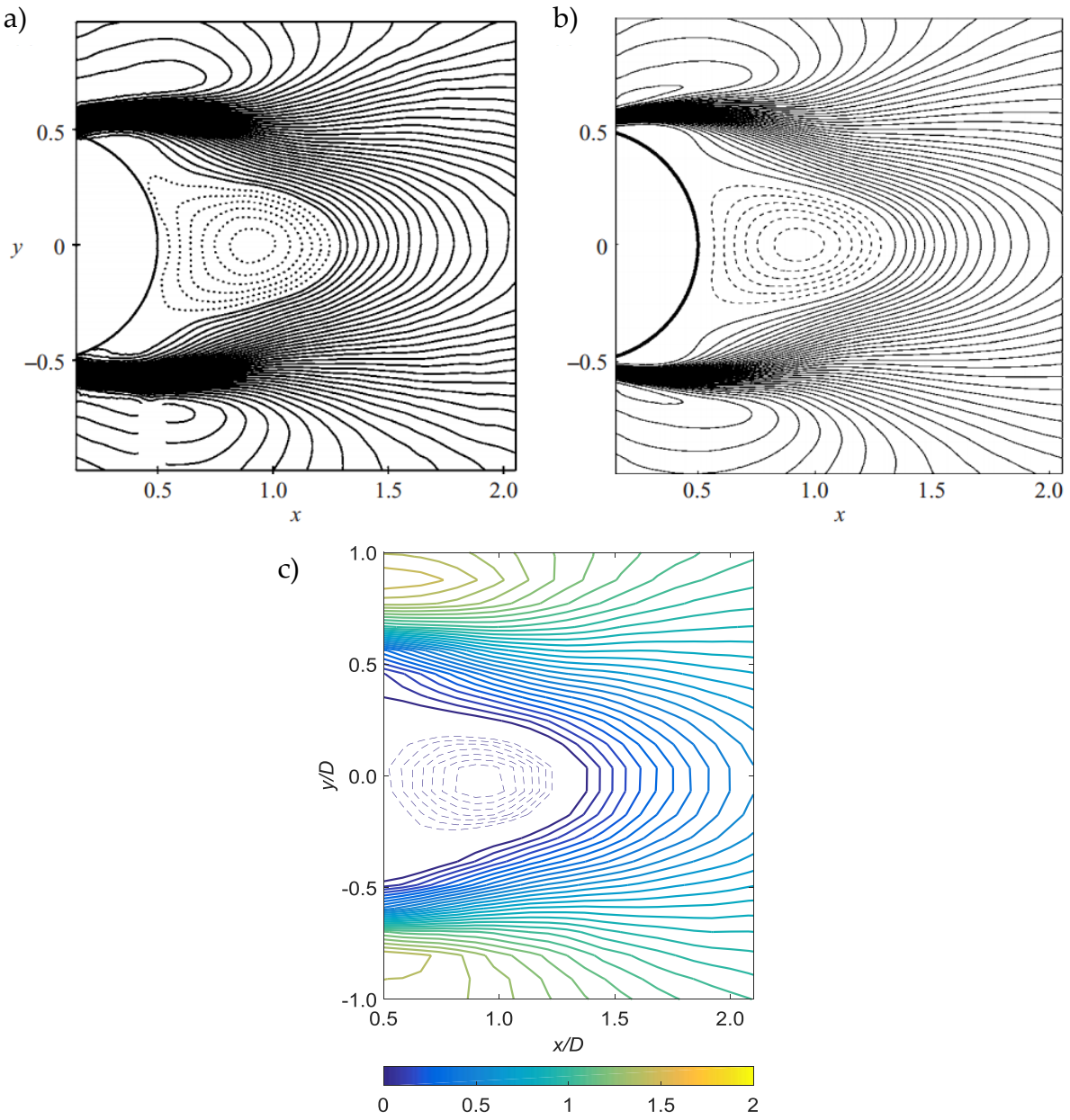

Figure 6 - Normalised streamwise velocity, $\bar{u}/U_0$ in the wake of a circular cylinder at Re = 10,000 from PIV (Dong et al. 2006), a), DNS (Dong et al. 2006), b), current research, c)

3 Results and Discussion

The three shapes, apart from the circular cylinder, investigated in this study have been split in to two categories; shapes with curved fore surfaces and a backward-facing step and the trapezoidal shape, with a flat fore surface. All the results are presented in the following section. The results obtained for the temporal energy in the cylinders' wake are only displayed for the shedding frequency since the magnitudes at higher harmonics were negligible (< 1%).

3.1 Averaged spanwise vorticity and Strouhal number

Figure 7 shows a comparison of the normalised spanwise vorticity $\overline{\omega_z}D/U_0$, where $\overline{\omega_z}$ is the averaged spanwise vorticity. For all the cross-sections investigated, the averaged vorticity layer is longer and thinner at *Re* = 5,000 when compared 10,000. This difference in vortex structure is consistent with previous observations and occurs due to the transition in the shear layer moving closer to the cylinder (Dong *et al.* 2006; Lin *et al.* 1995; Norberg 1998). The length of average spanwise vorticity distribution is similar (= 3*D*) between the semi-circular cylinder and trapezoid at *Re* = 5,000 and is longer than that for the other two sections. The semi-circle also has a longer average vorticity length (2.7*D*) at *Re* = 10,000 compared to the other cross-sections. Hence, the vorticity produced by the semi-circle propagates further downstream compared to the other cross-sections. Since the vorticity *'bubble'* is longer for the semi-circle, the vortices formed by the semi-circle take longer to dissipate than the other shapes.

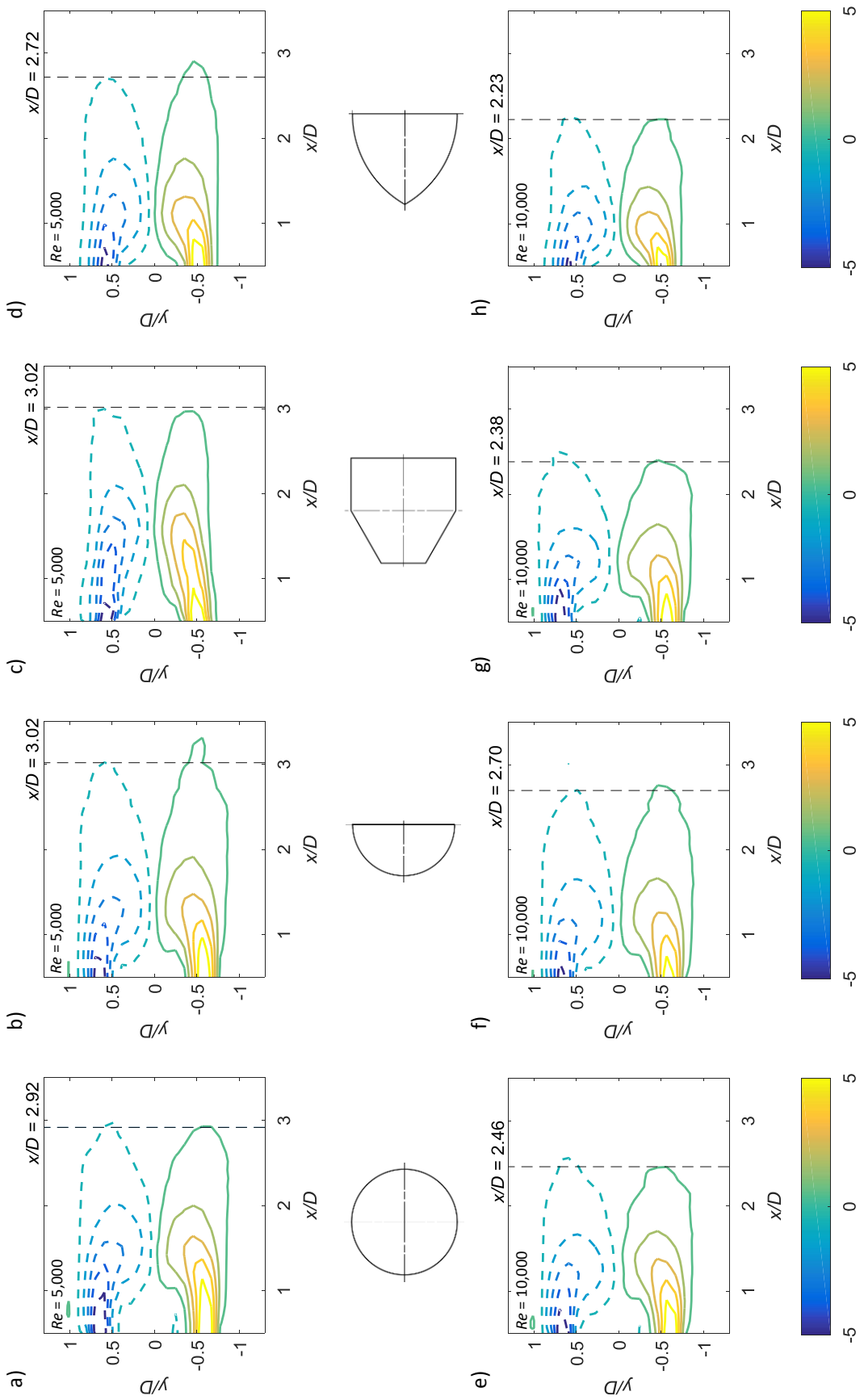

Figure 7 - Mean normalised spanwise vorticity $\overline{\omega_z}D/U_0$ in the wake of the bluff bodies. Top row of images corresponds to Re = 5,000 (a – d) and the bottom row (e –h) to Re = 10,000. Images from left to right – circle (a & e), semi-circle (b & f), trapezoid (c & g) and c-triangle (d & h). All the contours have the same scale.

The trapezoid experiences the largest drop in averaged vortex layer length when the Reynolds number doubles (25%). An interesting observation was that the trapezoid seemed to have a thinner region of mean vorticity at *Re* = 5,000, compared to the other shapes, as seen in Figure 7 c). Hence, the wake bubble encompassing the vorticity at this Reynolds number is diminished for the trapezoid, and the vortex street would also be thinner. This can be attributed to the difference in the upstream face compared to the other shapes, which all have a smooth curved aft-face. The circle and c-triangle have a mean vorticity layer length of 2.9*D* and 2.7*D*, respectively at *Re* = 5,000 and this length reduces by 17% for both, when the *Re* doubles.

The Strouhal number is a non-dimensional parameter associated with the frequency of vortex shedding, which affects the temporal concentration of flow energy. Utilising the Fast Fourier Transform on the signals from zones encompassing peak transverse fluctuations, the Strouhal numbers (*St)* were obtained for the current experiments (Table 1).

Table 1 - Strouhal numbers for the circle, semicircle, trapezoid and c-triangle

	Strouhal Number (*St*)	
	Re = 5,000	*Re* = 10,000
Circle	0.211	0.209
Semi-circle	0.217	0.216
Trapezoid	0.275	0.215
C-triangle	0.244	0.261

Strouhal number of the circle and semi-circle cross-sections show very little sensitivity to the Reynolds number. This is because of the location of the separation point of the shear layers (~ 75 degrees from the

stagnation point) being similar for both cases in this *Re* range. However, the c-triangle experiences an increase in *St* of 7% when the *Re* doubles and has a higher *St* compared to the other shapes. Hence, the frequency of vortex shedding is higher in the c-triangle as well and should be taken in to consideration when designing WIV systems. The Strouhal numbers for the trapezoid were 0.275 and 0.215 at *Re* = 5,000 and 10,000 respectively, meaning the thinner wake at a lower flow speed produces vortices at a higher frequency. This drop in Strouhal number is only observed in the trapezoid and can be attributed to the higher degree of 'bluffness' compared to the other shapes investigated in this research, which affects the properties of the shear layers formed, such as the separation point and the reattachment length.

3.2 Reynolds stresses and turbulent kinetic energy

Figure 8 displays a comparison between the Reynolds stresses $\langle u'v' \rangle / U_0^2$ for each of the cases in the current study. Here, u' and v' are the streamwise and transverse fluctuating velocities, respectively. It is noticeable that all shapes display four distinct regions, comprising of two smaller regions between x/D = 0.5 and 1.0, and two larger regions further downstream. The larger regions extend upstream in a pointy formation which seem to envelope but are not attached to the smaller regions. The elongated 'head' region seen in the Reynolds stresses is indicative of the shear-layer instability and the rolling-up of the shear-layer vortices, which causes an amassing of the Reynolds stresses near the aft region of the bluff body (Dong *et al.* 2006). The dominant regions for the Reynolds stresses are seen at x/D = 2.0 for the circle and trapezoid; whereas the region occurs at x = 1.5D for the c-triangle and x = 1.9D for the semi-circle at *Re* = 5,000.

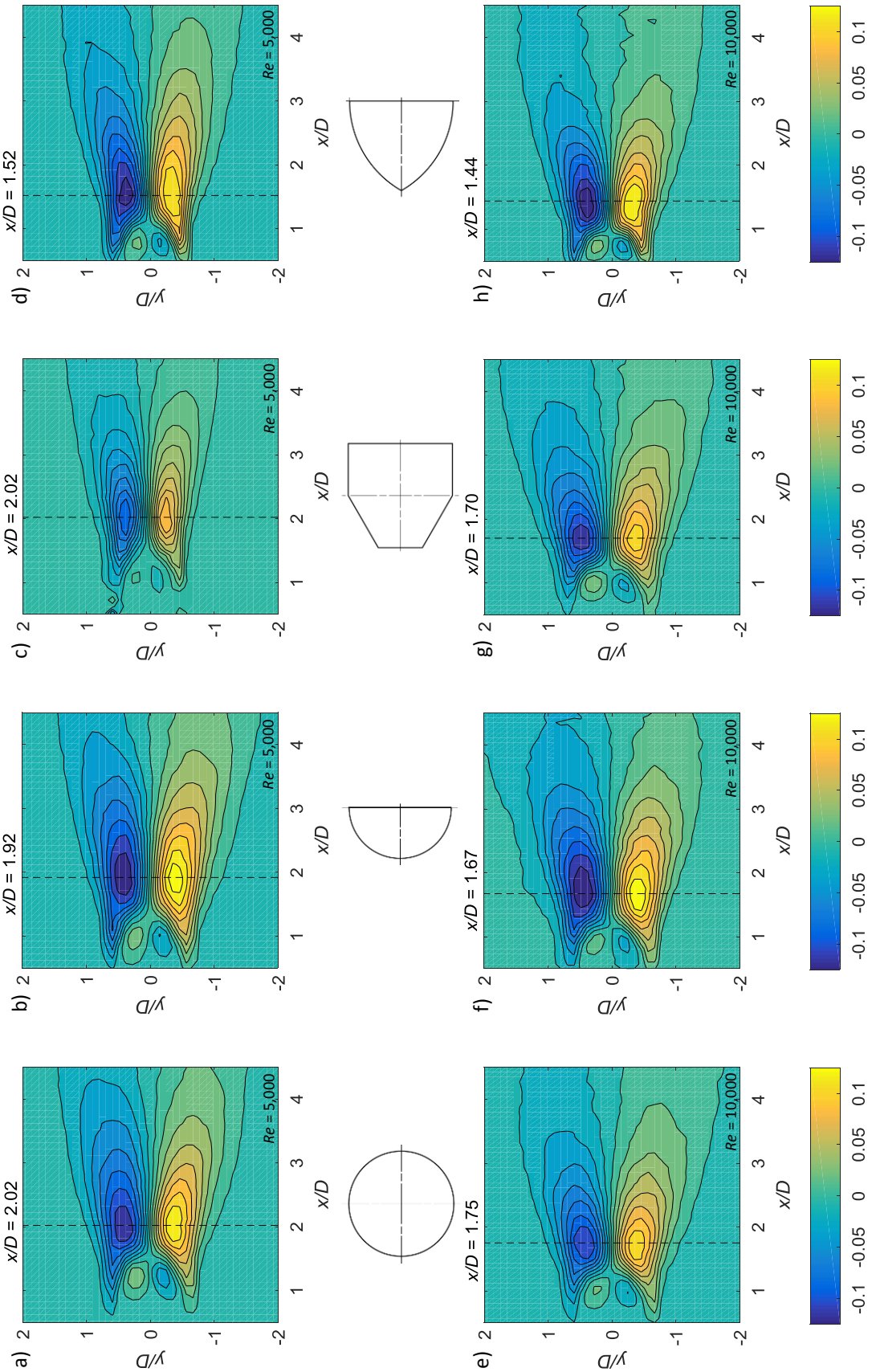

Figure 8 - Reynolds stresses in the current research, $\langle u'v' \rangle / U_0^2$. Order of images same as Figure 7.

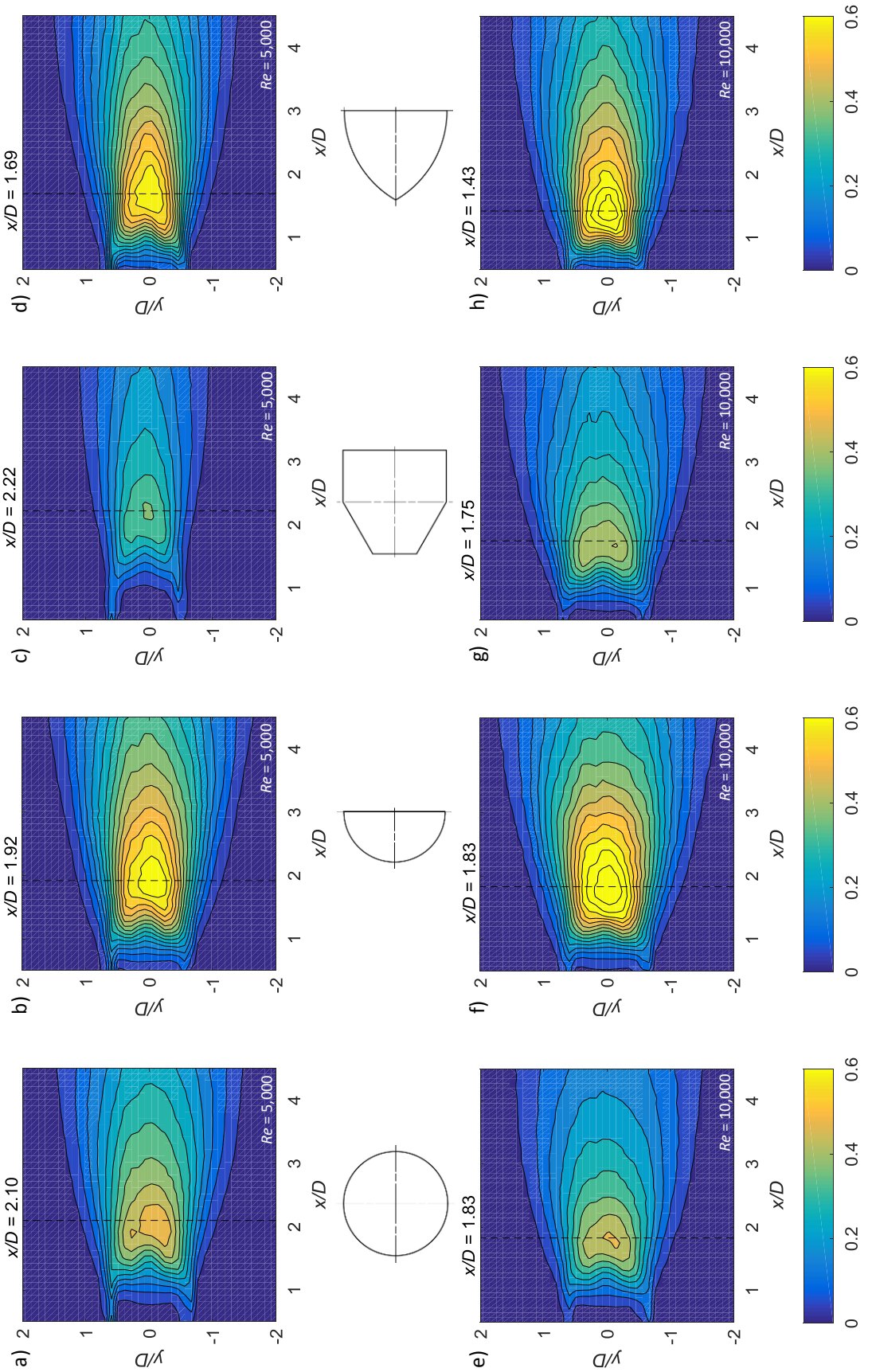

Figure 9 - Turbulent kinetic energy $[\overline{u'^2} + \overline{v'^2}]\,/U_0^2$ *(TKE) in the wake of the investigated bluff bodies Order of images same as Figure 7.*

At *Re* = 10,000, the peak *uv* Reynolds stress zones move closer to the body by 0.3*D* for all the shapes except the c-triangle which only experiences a drop of 0.08*D*. The magnitudes of the peak Reynolds stresses are similar for the semi-circle and c-triangle; however, the region of peak magnitude is larger in the c-triangle and semi-circle (20% higher) compared to the other shapes.

The increased peak magnitude corresponds to a higher level of turbulence (and vorticity), since the stresses are indicative of the fluctuating velocities in the wake, which in turn will lead to more temporal energy being available in the wake. The magnitudes of the peak Reynolds stresses are also lower for the trapezoid (by 10%) compared to the circle at both *Re*, suggesting less turbulence occurring in the wake of the trapezoid.

The normalised Turbulent Kinetic Energy (TKE), $[\overline{u'^2} + \overline{v'^2}]/U_0^2$ distribution in the wake of the bluff bodies is shown in Figure 9. The region of maximum TKE moves upstream when the Reynolds number increases, alike the Reynolds stresses. The circle has a maximum region at x/D = 2.1 for *Re* = 5,000 and x/D = 1.8 for *Re* = 10,000. The max magnitude for the circle is 0.5 and 0.6 for the semicircle, at both Reynolds numbers. The c-triangle has maxima of 0.6 occurring at x/D = 1.7 and 1.4 for Reynolds numbers of 5,000 and 10,000, respectively. The trapezoid has a maximum TKE of 0.32 at x = 2.2*D* for *Re* = 5,000 and a maximum of 0.4 at x = 1.7*D* at *Re* = 10,000, which is lower than the circle by 36% and 24% for the same Reynolds numbers. The trapezoid has lower turbulence and hence lower TKE in the wake compared to the circle and was also the only shape to experience a gain in TKE when the Reynolds number doubled. Comparing the TKE distribution of the cross-sections with the highest TKE magnitudes, the semi-circle has a larger wake

encompassing the TKE compared to the c-triangle. The sizes of the peak regions are similar between both shapes at their respective Reynolds numbers. This increased TKE distribution in the semi-circle and c-triangle suggests a higher level of turbulent fluctuations in the wake of these two shapes and hence the streamwise and transverse energy components were further split up in the proceeding section to analyse the magnitude and frequency of the temporally occurring energy.

3.3 Spatial and Temporal energy components in the wake

The normalised mean streamwise energy in the wake, $E_{\overline{u}}$, is very similar in magnitude between all the cross-sections at both Reynolds numbers and is displayed in Figure 10. The maximum for $E_{\overline{u}}$ occurs near the surface of the bodies due to the jetting effect of the shear layers that form when the bluff body is obstructing the flow (y/D = ± 0.75 – ± 1.5 as shown in Figure 10). This region of high velocity decays past x/D = 1.5 due to the recovery of the wake. Although there is an increase in $E_{\overline{u}}$ on the surface of the cylinder (2 times the freestream energy), this maximum cannot be utilised by WIV technology as the placement of an energy extractor at these locations will disrupt the flow, and hence the vortices that would otherwise be formed.

The mean transverse energy, $E_{\overline{v}}$ has very low magnitudes compared to the streamwise counterpart and is depicted in Figure 11. The flow is mostly streamwise in direction and there is no constant transverse flow displacement to give high transverse mean energies. However, the c-triangle is the most streamlined shape compared to the other bluff bodies investigated and has the highest magnitude of $E_{\overline{v}}$ (magnitude of 0.1 shown in ` 9, d) and h)). These maximum energy regions occur between x/D = 1.0 – 2.0 and y/D = ± 0.5. The mean transverse component

is not very useful for WIV as it is the periodicity of the vortex street that contributes to the fluctuating and desired periodic vibration.

The normalised fluctuating streamwise component, $E_{u'_{fs}}$, shown in Figure 12, is most significant for the circular cylinder (Figure 12 a)) compared to the other bodies at a Reynolds number of 5,000. All cross-sections apart from the trapezoidal cylinder, exhibit higher magnitudes at *Re* = 5,000 compared to *Re* = 10,000. The shed eddies disperse faster when the *Re* increases; hence display lower magnitudes in the direction of the flow. $E_{u'_{fs}}$, alike $E_{\bar{v}}$, isn't of interest in the current research, since most WIV and VIV systems are constrained to vibrate transversely. However, the fluctuating streamwise component should be taken into account for the tandem structures that will be affected by the fluctuating forces.

The contour for normalised fluctuating transverse energy in the wake of the cylinders, $E_{v'_{fs}}$ is shown in Figure 13, and the distribution along the centreline (y = 0) is plotted in Figure 14 for clarity. The fluctuating transverse component is the focus of this research with the aim of enhancing the fluctuations in the wake, and hence intensify the vibrations observed in a WIV system.

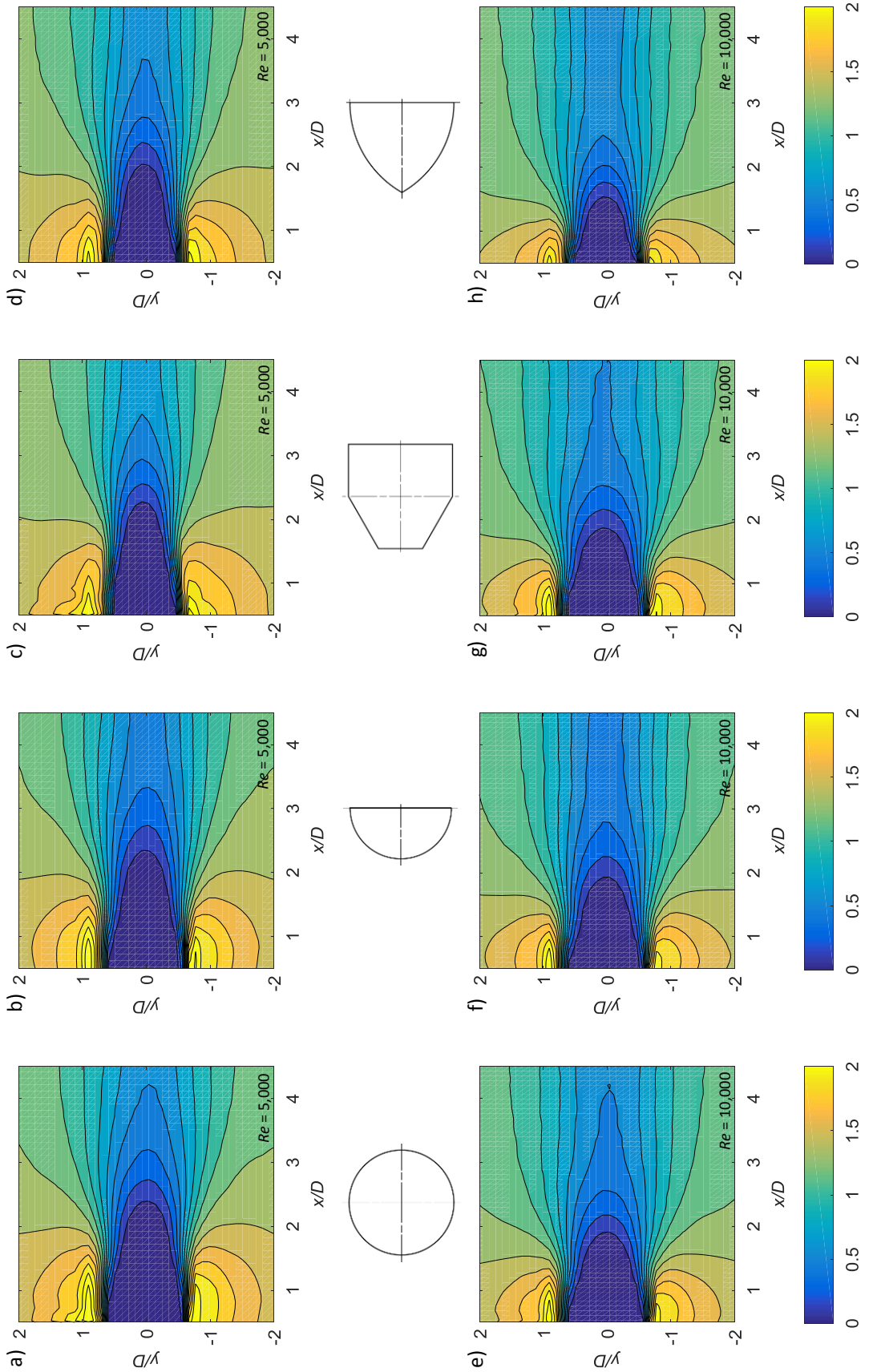

Figure 10 - Normalised energy magnitudes due to the mean streamwise component ($E_{\overline{u}}$). Order of images same as Figure 7

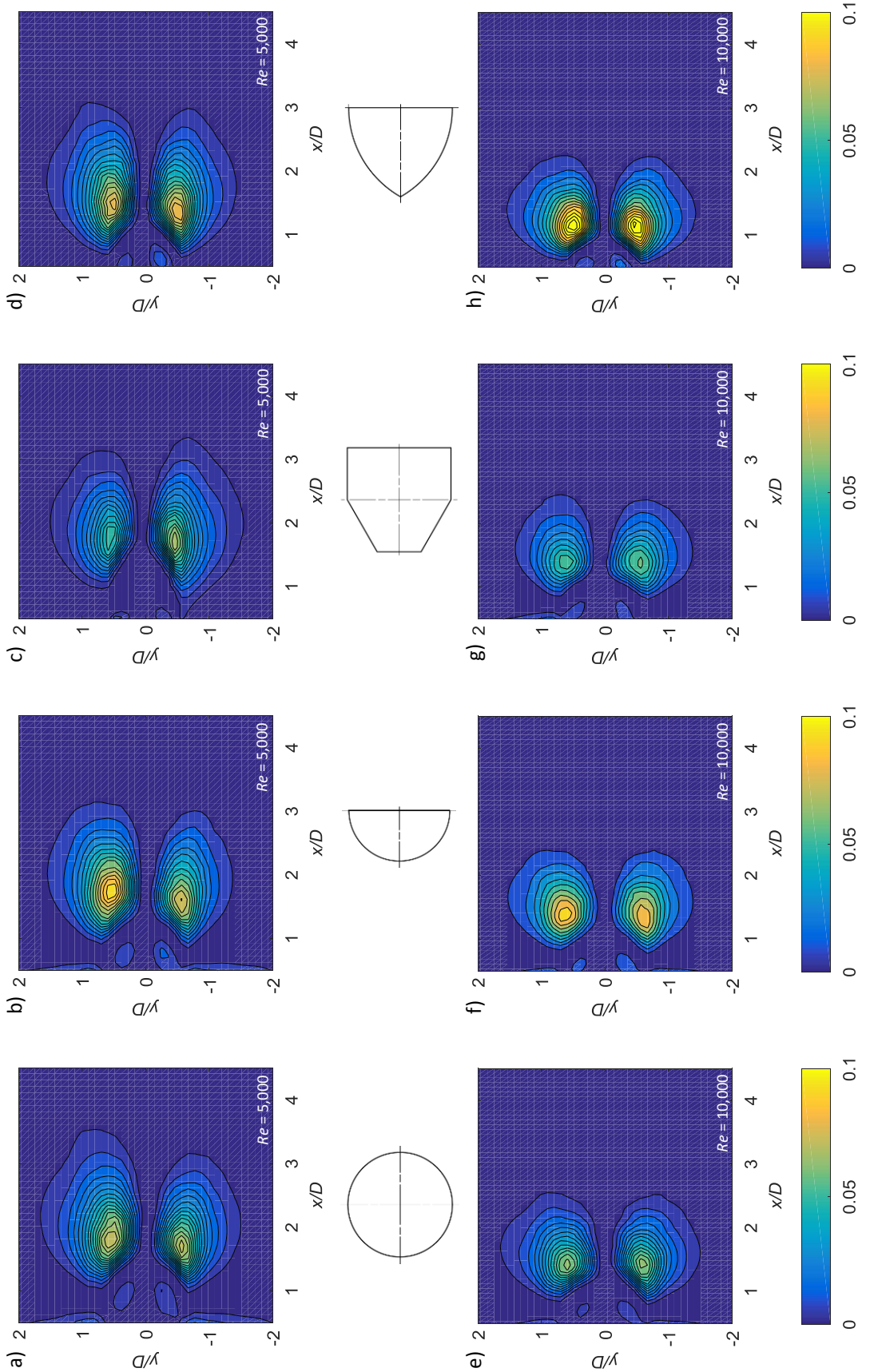

Figure 11- Normalised energy magnitudes due to the mean transverse component ($E_{\bar{v}}$). Order of images same as Figure 7

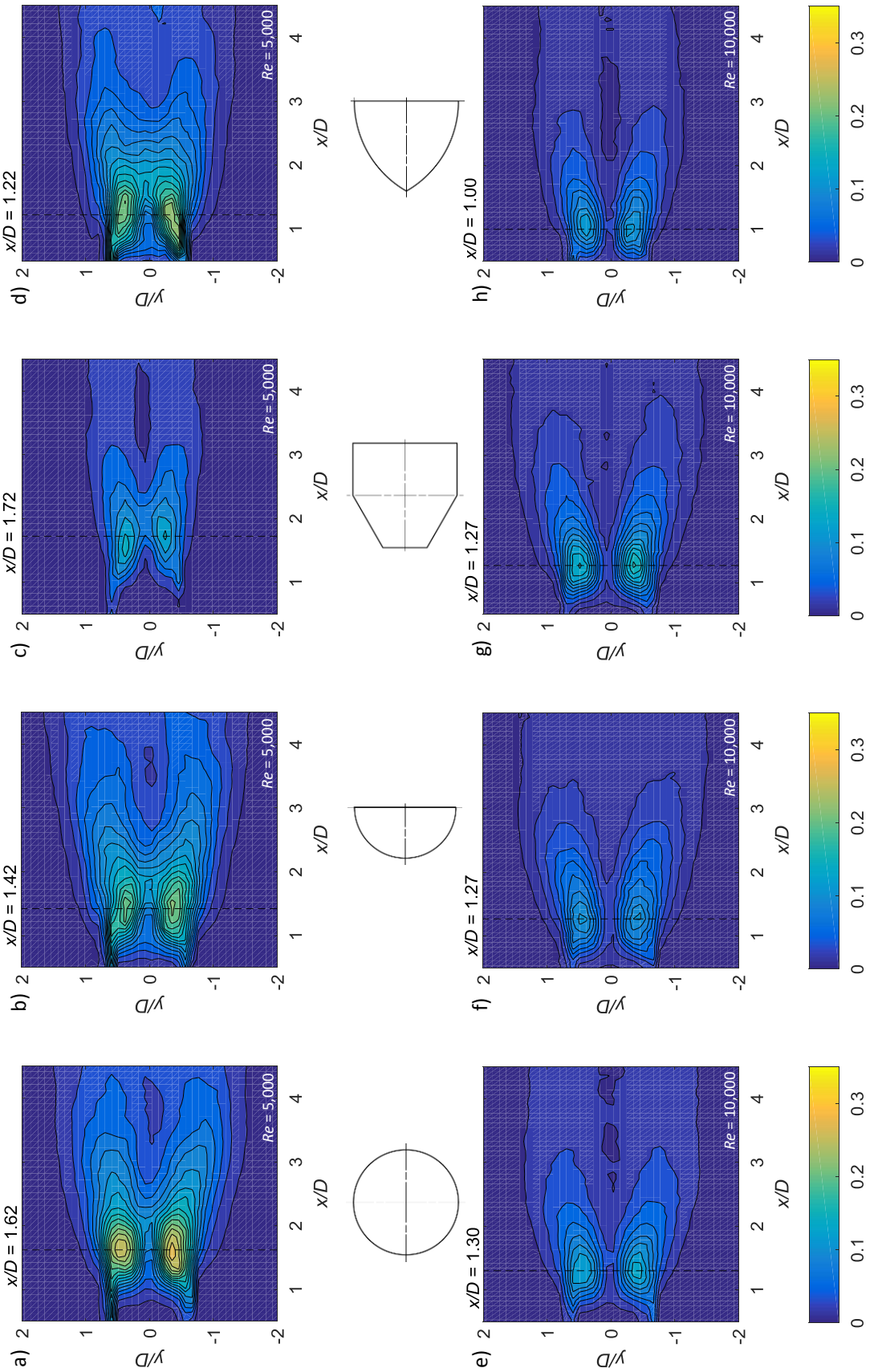

Figure 12 - Normalised energy magnitudes due to the fluctuating streamwise component ($E_{u'_{fs}}$). Order of images same as Figure 7

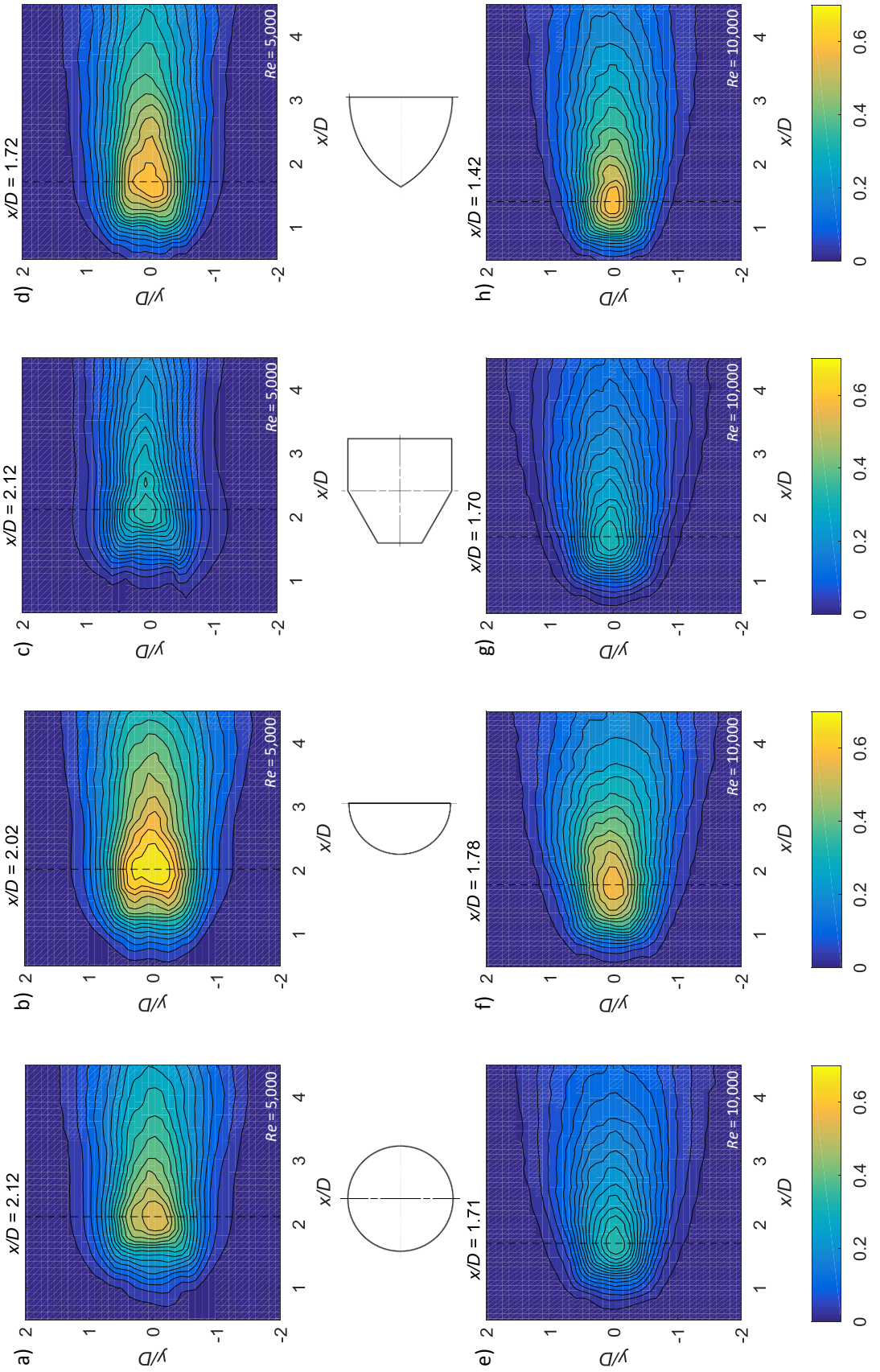

Figure 13 - Normalised energy magnitudes due to the fluctuating transverse component ($E'_{v_{fs}}$). Order of images same as Figure 7

The semi-circular cylinder and the c-triangle are favourable for $E_{v'_{fs}}$ (maximum normalised magnitude = 0.69 and 0.6, respectively) compared to the circular (0.55) cylinder at *Re* = 5,000. This trend is consistent at *Re* = 10,000 where the semi-circle and c-triangle experience a magnitude of 0.48 and 0.35, respectively compared to the circle, which has a magnitude of 0.3. The normalised magnitudes for all the cross-sections are also higher for *Re* = 5,000 compared to a *Re* = 10,000. The zone of maximum $E_{v'_{fs}}$ occurs between x/D = 1.0 – 2.0 for the semi-circle and the c-triangle; and both zones appear at y/D = -0.5 – 0.5. The semi-circle and c-triangle have a sharp change in geometry on the aft part of the cylinder, which contributes to stronger negative base pressure, and hence more pronounced vortices, which contributes to the increase in transverse fluctuation observed. Evidence of stronger back pressure in a semi-circular cylinder compared to a circular cylinder was shown in (Nakamura 1996) where the circular cylinder had a base pressure coefficient ($-C_{pb}$) of 1, whereas the semi-circular cylinder had a larger magnitude of 1.15.

The circular cylinder is favourable for $E_{v'_{fs}}$ (maximum normalised magnitude = 0.55) compared to the trapezoidal prism (0.33). The normalised magnitudes for the trapezoidal cylinder are also slightly higher for *Re* = 5,000 (0.33) compared to a *Re* = 10,000 (0.3) as with the semi-circle and c-triangle, however the max $E_{v'_{fs}}$ at *Re* = 10,000 is the same as the circular cylinder case. The zone of maximum $E_{v'_{fs}}$ occurs at the same locations as that of the circular cylinder; between x/D = 2.0 – 2.5 for *Re* = 5,000 and x/D = 1.5 – 2.0 for *Re* = 10,000, where both zones appear between y/D = -0.5 – 0.5. The beneficial effect of a backward-facing step seen in the semi-circle and c-triangle is not observed in the trapezoid due

to the flat fore face, which causes less energy to be built up in the shear layers.

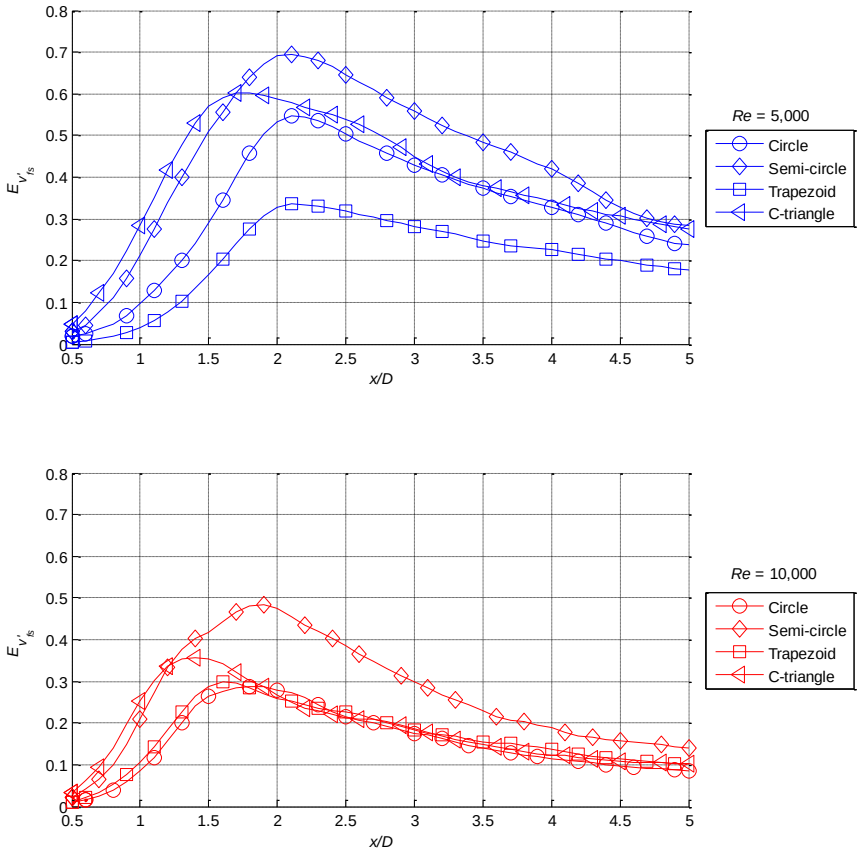

Figure 14 – Normalised transverse fluctuating energy magnitudes along the centreline (y/D = 0) for all the bluff bodies investigated. The top plot is for Re = 5,000 and the bottom plot corresponds to Re = 10,000

3.4 Discussion

A transition from a circle to a flat aft cross-section, at the same Reynolds number, like the semi-circle and c-triangle, increases the frequency of the vortices and the Strouhal number. The semi-circular and c-triangular cylinders also provide a higher magnitude of temporal energy in the wake compared the circular cylinder. At a Reynolds number of 5,000 the semicircle and c-triangle provide more transversely fluctuating energy by 27% and 9%, respectively, compared to the circular cylinder. When the Reynolds number is doubled, the

augmentation of energy increases to 60% and 17%, for the semi-circle and c-triangle respectively, compared to that of the circular cylinder.

Presence of a curved surface in the fore of the cylinder and a flat drop in geometry at the aft of the cylinder results in a higher concentration of temporal fluctuations, supported by an increase in Reynolds stresses, TKE and temporal fluctuations. There isn't a substantial difference seen in the mean energy magnitudes between the cross-sections due to the high magnitude of streamwise energy due to the upstream flow. The curved fore surface in the semi-circle and c-triangle, redirects the flow with minimal energy losses compared to a flat face blockage like the trapezoid. In (Nakamura 1996), the semi-circular cylinder was reported to have a stronger base pressure coefficient compared to a circular cylinder at the same Reynolds number. Hence, it is hypothesised that the stronger base pressure due to the sharp aft surface causes the flow in the shear layers to be sucked back in to the wake sooner than a gradual decline; hence, accumulating a larger concentration of small-scale eddies from the shear layers to provide higher energy large-scale vortices in the wake. An observed difference between the semi-circle and the c-triangle is that the c-triangle has a smaller wake due to its streamlined geometry. This is evidenced in all the figures presented in the preceding sections.

The trapezoid has distinctive characteristics between cases with Re of 5,000 and 10,000, where the wake in the lower Reynolds number is diminished when compared with the higher. This is also accompanied with an increase in the Strouhal number. Owing to the limited amount of research on inverted trapezoidal (shorter of two parallel edges facing the windward side) cylinders in cross flow, the reason for these differences is hypothesised to be the differences in the reattachment

point of the shear layer and transition effects in the shear layer. Since the trapezoid has sharp edges on the leading edge, separation occurs at these edges similar to separation occurring in square and rectangular cylinders (Cimarelli *et al.* 2018). Square cylinders experience an increase in Strouhal number and a diminished wake when separation of shear layers at an upstream sharp edge is accompanied with reattachment on the bluff body (He *et al.* 2014). Similar effects are seen in this study for the trapezoidal shape. An investigation in to the separating and reattaching of shear layers of the inverted trapezoid, as well as the effects of transition in the shear layers is needed to define the effects that were observed in this study but were unfortunately out of the scope of this study.

The trapezoidal shape, with a flat fore surface and a backward-facing step aft surface, also experiences a drop in $E_{v'_{fs}}$ of 36% compared to the circular cylinder at a Re of 5,000. At the higher Reynolds numbers, the peak for $E_{v'_{fs}}$ is similar to the circular cylinder, which is also because of the different wake structures the trapezoid experiences at the two Reynolds numbers investigated. The diminished temporal energy concentration accompanied by the abnormal trend in flow features at the different Reynolds numbers make the trapezoid unsuitable as a replacement to a circular cylinder in WIV technology as the upstream wake energy concentrator at Re = 5,000.

In summary, a WIV system will benefit from the use of an upstream bluff body with a curved upstream face which allows separation of the flow and the formation of the vortex street, and a flat aft surface which increases the pooling of vorticity from the shear layers. Out of all the shapes investigated, the semi-circle would be most suitable as an energy concentrator in a WIV system, as it produces the highest peaks of

temporal fluctuations. The data obtained for temporal energy in the wake of the cylinders provides some insight into the flow structure available to the vibrating body in a WIV system. Utilising this knowledge, further testing would need to be done to identify the system parameters such as position, mass ratio and damping ratio to achieve a phase-locked efficient WIV system.

4 Conclusions

The wake of four different bluff bodies in a flow was analysed to compare trends in the turbulence statistics and the temporal energy. The wake velocity vectors in the streamwise and transverse directions of circular, semi-circular, triangular and trapezoidal cylinders, in a closed-loop water channel at two flow velocities corresponding to Re = 5000 and 10,000 were obtained using PIV. Velocity vectors were further processed to obtain averaged turbulence quantities and Fourier analysis was used to identify the mean energy as well as the temporal energy in the horizontal plane.

Cross-sections with a smooth and convex-curved upstream face combined with a flat downstream face (i.e. semicircular and convex-edged triangular cylinders) are better at temporally concentrating the energy in their wake, compared to a circular cylinder with the same hydraulic diameter. The difference in temporally concentrated energy, compared to the circular cylinder, is higher at higher Reynolds numbers (semicircle = 60%, c-triangle = 17% at *Re* = 10,000) compared to lower Reynolds numbers (semi-circle = 27%, c-triangle = 9% at *Re* = 5,000). It is speculated that these cross-sections with a backward-facing step accumulate more small-scale eddies to form the large-scale coherent

vortices in the near wake, shedding off vortices with a higher level of temporally occurring hydro-kinetic energy.

On the other hand, bluff body cross-sections with a flat upstream face (e.g. trapezoid) are less effective at concentrating energy in the wake temporally when compared to a circular cylinder with the same hydraulic diameter. This difference is more prominent at lower Reynolds numbers (reduction of 36% at Re = 5,000) compared to higher Reynolds numbers (10,000), where there was almost no difference. The wake of the trapezoidal cylinder is also highly dependent on the free stream velocity, where at Re = 5,000 the wake is diminished compared to that at Re = 10,000.

In general, mean flow statistics are not highly affected by the bluff body cross-section because of the high magnitude of mean streamwise energy available in the freestream. Also, most of the temporal energy is concentrated at the shedding frequency (dependent on *Re)* with very low magnitudes (< 1%) present in the harmonics of the shedding frequency.

In conclusion, the peaks for zones of temporally occurring energy are higher in cylinders that have a curved fore surface and a flat aft surface due to a higher accumulation of vorticity before they are shed from the body. Hence these types of cylinders can provide more temporally concentrated energy if placed as the stationary upstream body in a WIV system. Future work will include investigation of a WIV system with a coupled downstream vibrating body to realise a system which is more efficient compared to current standards, as well as to investigate the effect of tandem positioning on the location where temporal energy concentration can occur.

References

Alonso, G & Meseguer, J 2006, 'A parametric study of the galloping stability of two-dimensional triangular cross-section bodies', *Journal of Wind Engineering and Industrial Aerodynamics*, vol. 94, no. 4, pp. 241-53.

Alonso, G, Meseguer, J & Pérez-Grande, I 2005, 'Galloping instabilities of two-dimensional triangular cross-section bodies', *Experiments in fluids*, vol. 38, no. 6, pp. 789-95.

Assi, GRS 2009, 'Mechanisms for flow-induced vibration of interfering bluff bodies', Ph.D thesis, Imperial College London.

NREL 2011, *The VIVACE Convertor - Enhancing Flow Induced Motions to Harness Hydrokinetic Energy in an Environmentally Compatible Way*, by Bernitsas, MM, viewed 29.06.2015, <http://www.nrel.gov/docs/fy12osti/51421-09.pdf>.

Bernitsas, MM, Ben-Simon, Y, Raghavan, K & Garcia, EM 2009, 'The VIVACE converter: model tests at high damping and Reynolds number around 105', *Journal of Offshore Mechanics and Arctic Engineering*, vol. 131, no. 1, pp. 1 - 15.

Bernitsas, MM, Raghavan, K, Ben-Simon, Y & Garcia, EM 2008, 'VIVACE (vortex induced vibration aquatic clean energy): A new concept in generation of clean and renewable energy from fluid flow', *Journal of Offshore Mechanics and Arctic Engineering*, vol. 130, no. 4, pp. 1697–712.

Blevins, RD 1997, *Flow-induced vibration*, Second edn, Van Nostrand Reinhold, New York

Blevins, RD & Coughran, CS 2009, 'Experimental investigation of vortex-induced vibration in one and two dimensions with variable mass, damping, and Reynolds number', *Journal of Fluids Engineering*, vol. 131, no. 10, p. 101202.

Bloor, MS & Gerrard, J 1966, 'Measurements on turbulent vortices in a cylinder wake', *Proc. R. Soc. Lond. A*, vol. 294, no. 1438, pp. 319-42.

Cantwell, B 1975, 'A flying hot wire study of the turbulent near wake of a circular cylinder at Reynolds number of 140,000. Ph. D. Thesis. Progress Report'.

Cantwell, B & Coles, D 1983, 'An experimental study of entrainment and transport in the turbulent near wake of a circular cylinder', *Journal of Fluid Mechanics*, vol. 136, pp. 321-74.

Carmo, BS, Sherwin, SJ, Bearman, PW & Willden, RH 2008, 'Wake transition in the flow around two circular cylinders in staggered arrangements', *Journal of Fluid Mechanics*, vol. 597, pp. 1-29.

Cimarelli, A, Leonforte, A & Angeli, D 2018, 'Direct numerical simulation of the flow around a rectangular cylinder at a moderately high Reynolds number', *Journal of Wind Engineering and Industrial Aerodynamics*, vol. 174, pp. 39-49.

Derakhshandeh, JF, Arjomandi, M, Dally, B & Cazzolato, B 2014a, 'The effect of arrangements of two circular cylinders on the maximum efficiency of vortex-induced vibration power using a scale-adaptive simulation model', *Journal of Fluids and Structures*, vol. 49, pp. 654-66.

Derakhshandeh, JF, Arjomandi, M, Dally, B & Cazzolato, B 2014b, 'Experimental and computational investigation of wake induced vibration', paper presented to 19th Australasian Fluid Mechanics Conference, Melbourne, Australia, 8 - 11 December 2014.

Derakhshandeh, JF, Arjomandi, M, Dally, B & Cazzolato, B 2015a, 'Harnessing Hydro-Kinetic energy from wake induced vibration using virtual mass spring damper system', *Journal of Ocean Engineering*, vol. 108, pp. 115-28.

Derakhshandeh, JF, Arjomandi, M, Dally, B & Cazzolato, B 2015b, 'A study of the Vortex-Induced Vibration mechanism for harnessing hydrokinetic energy of eddies using a single cylinder', *Journal of Applied Mathematical Modelling*.

Derakhshandeh, JF, Arjomandi, M, Dally, B & Cazzolato, B 2016, 'Flow-induced vibration of an elastically mounted airfoil under the influence of the wake of a circular cylinder', *Experimental Thermal and Fluid Science*, vol. 74, pp. 58-72.

Ding, L, Zhang, L, Kim, ES & Bernitsas, MM 2015a, 'URANS vs. experiments of flow induced motions of multiple circular cylinders with passive turbulence control', *Journal of Fluids and Structures*, vol. 54, pp. 612-28.

Ding, L, Zhang, L, Wu, C, Mao, X & Jiang, D 2015b, 'Flow induced motion and energy harvesting of bluff bodies with different cross sections', *Energy Conversion and Management*, vol. 91, pp. 416-26.

Dong, S, Karniadakis, G, Ekmekci, A & Rockwell, D 2006, 'A combined direct numerical simulation–particle image velocimetry study of the turbulent near wake', *Journal of Fluid Mechanics*, vol. 569, pp. 185-207.

Duncan, J, Dabiri, D, Hove, J & Gharib, M 2010, 'Universal outlier detection for particle image velocimetry (PIV) and particle tracking velocimetry (PTV) data', *Measurement Science and Technology*, vol. 21, no. 5, p. 057002.

Gaudin, E, Protas, B, Goujon-Durand, S, Wojciechowski, J & Wesfreid, J 1998, 'Spatial properties of velocity structure functions in turbulent wake flows', *Physical Review E*, vol. 57, no. 1, p. R9.

Hart, DP 2000, 'PIV error correction', *Experiments in fluids*, vol. 29, no. 1, pp. 13-22.

He, GS, Li, N & Wang, JJ 2014, 'Drag reduction of square cylinders with cut-corners at the front edges', *Experiments in fluids*, vol. 55, no. 6, p. 1745.

Hobbs, WB & Hu, DL 2012, 'Tree-inspired piezoelectric energy harvesting', *Journal of Fluids and Structures*, vol. 28, pp. 103-14.

Igarashi, T 1984, 'Characteristics of the flow around two circular cylinders arranged in tandem: 2nd report, unique phenomenon at small spacing', *Bulletin of JSME*, vol. 27, no. 233, pp. 2380-7.

Ji, C, Xu, W, Sun, H, Wang, R, Ma, C & Bernitsas, MM 2018, 'Interactive Flow-Induced Vibrations of Two Staggered, Low Mass-Ratio Cylinders in the TrSL3 Flow Regime (2.5× 104< Re< 1.2× 105): Smooth Cylinders', *Journal of Offshore Mechanics and Arctic Engineering*, vol. 140, no. 4, p. 041801.

Keane, RD & Adrian, RJ 1990a, 'Optimization of particle image velocimeters', in *Orl-DL tentative*, pp. 139-59.

Keane, RD & Adrian, RJ 1990b, 'Optimization of particle image velocimeters', in *ICALEO'89: Optical Methods in Flow and Particle Diagnostics*, vol. 1404, pp. 139-60.

Kinaci, OK, Lakka, S, Sun, H & Bernitsas, MM 2016, 'Effect of tip-flow on vortex induced vibration of circular cylinders for Re< 1.2* 10 5', *Ocean Engineering*, vol. 117, pp. 130-42.

Kourta, A, Boisson, H, Chassaing, P & Minh, HH 1987, 'Nonlinear interaction and the transition to turbulence in the wake of a circular cylinder', *Journal of Fluid Mechanics*, vol. 181, pp. 141-61.

Lan, K, Sun, H & Bernitsas, MM 2018, 'Two Tandem Cylinders With Passive Turbulence Control in Flow-Induced Vibration: Relation of Oscillation Patterns to Frequency Response', *Journal of Offshore Mechanics and Arctic Engineering*, vol. 140, no. 3, p. 031803.

Lin, J-C, Towfighi, J & Rockwell, D 1995, 'Instantaneous structure of the near-wake of a circular cylinder: on the effect of Reynolds number', *Journal of Fluids and Structures*, vol. 9, no. 4, pp. 409-18.

Lourenco, L & Shih, C 1993, 'Characteristics of the plane turbulent near wake of a circular cylinder', *A particle image velocimetry study.(data taken from Beaudan, Moin*.

Ma, C, Sun, H & Bernitsas, MM 2018, 'Nonlinear Piecewise Restoring Force in Hydrokinetic Power Conversion Using Flow-Induced Vibrations of Two Tandem Cylinders', *Journal of Offshore Mechanics and Arctic Engineering*, vol. 140, no. 4, p. 041901.

Manickam Sureshkumar, E, Arjomandi, M, Cazzolato, BS & Dally, BB 2018, 'Spatial and temporal concentration of hydrokinetic energy in the wake of a bluff body', *Ocean Engineering*, vol. 164, pp. 181-98.

Nakamura, Y 1996, 'Vortex shedding from bluff bodies and a universal Strouhal number', *Journal of Fluids and Structures*, vol. 10, no. 2, pp. 159-71.

Norberg, C 1998, 'LDV-measurements in the near wake of a circular cylinder', *ASME Paper No. FEDSM98-521*.

Ong, L & Wallace, J 1996, 'The velocity field of the turbulent very near wake of a circular cylinder', *Experiments in fluids*, vol. 20, no. 6, pp. 441-53.

Ozgoren, M 2006, 'Flow structure in the downstream of square and circular cylinders', *Flow Measurement and Instrumentation*, vol. 17, no. 4, pp. 225-35.

Ozgoren, M, Pinar, E, Sahin, B & Akilli, H 2011, 'Comparison of flow structures in the downstream region of a cylinder and sphere', *International Journal of Heat and Fluid Flow*, vol. 32, no. 6, pp. 1138-46.

Ozkan, GM, Firat, E & Akilli, H 2017, 'Control of Vortex Shedding Using a Screen Attached on the Separation Point of a Circular Cylinder and Its Effect on Drag', *ASME J. Fluids Eng.*, vol. 139, no. 7, p. 071107.

Rajagopalan, S & Antonia, R 2005, 'Flow around a circular cylinder—structure of the near wake shear layer', *Experiments in fluids*, vol. 38, no. 4, pp. 393-402.

Rosetti, GF, Vaz, G & Fujarra, AL 2012, 'URANS calculations for smooth circular cylinder flow in a wide range of Reynolds numbers: solution verification and validation', *ASME J. Fluids Eng.*, vol. 134, no. 12, p. 121103.

Thielicke, W & Stamhuis, E 2014, 'PIVlab–towards user-friendly, affordable and accurate digital particle image velocimetry in MATLAB', *Journal of Open Research Software*, vol. 2, no. 1.

Venugopal, A, Agrawal, A & Prabhu, S 2017, 'Investigations on Bluff Bodies as Improved Vortex Shedders Placed Inside a Circular Pipe', *ASME J. Fluids Eng.*, vol. 139, no. 4, p. 041204.

Wang, D-A & Ko, H-H 2010, 'Piezoelectric energy harvesting from flow-induced vibration', *Journal of Micromechanics and Microengineering*, vol. 20, no. 2, p. 025019.

Wei, ZA & Zheng, ZC 2018, 'Fluid–Structure Interaction Simulation on Energy Harvesting From Vortical Flows by a Passive Heaving Foil', *ASME J. Fluids Eng.*, vol. 140, no. 1, p. 011105.

Weinstein, LA, Cacan, MR, So, PM & Wright, PK 2012, 'Vortex shedding induced energy harvesting from piezoelectric materials in heating, ventilation and air conditioning flows', *Smart Materials and Structures*, vol. 21, no. 4, p. 045003.

Westerweel, J 1993, 'Digital particle image velocimetry: theory and application'.

Westerweel, J & Scarano, F 2005, 'Universal outlier detection for PIV data', *Experiments in fluids*, vol. 39, no. 6, pp. 1096-100.

Xu, W, Ji, C, Sun, H, Ding, W & Bernitsas, MM 2017, 'Flow-Induced Vibration (FIV) and Hydrokinetic Power Conversion of Two Staggered, Low Mass-Ratio Cylinders, With Passive Turbulence Control in the TrSL3 Flow Regime (2.5× 104< Re< 1.2× 105)', in *ASME 2017 36th International Conference on Ocean, Offshore and Arctic Engineering*, pp. V010T09A07-VT09A07.

Zdravkovich, MM 1997, 'Flow around circular cylinders, vol. 1. Fundamentals', *Journal of Fluid Mechanics*, vol. 350, pp. 377-8.

Zdravkovich, MM & Bearman, PW 1998, *Flow Around Circular Cylinders—Volume 1: Fundamentals*, American Society of Mechanical Engineers, 0098-2202.

This page is intentionally left blank

Chapter 5. Effect of upstream geometry on WIV

WIV depends on a variety of factors such as the Reynolds number, mass of the body, stiffness and damping of the system, aspect ratio of the cylinder, shear forces and the turbulence intensity. The circular cylinder has been widely investigated to identify how these factors affect its vibrations. The circular cylinder is also the most common upstream body investigated in two-body WIV systems. However, if the circular cylinder is replaced with other cross sections, there is little known about how the WIV system will react to changes in fluidic parameters that govern the WIV phenomenon and how these parameters can be optimised to provide efficient vibrations capable of harnessing flow energy.

Employing a pair of tandem bodies in a cross flow, vortices shed from the upstream cylinder will not only pass by the downstream cylinder, but also interfere with its own generated vortices. This interference between flow patterns and cylinders will not be a simple VIV and requires more investigation that is affected by the wake coming from the first cylinder.

The previous two chapters have established the concept of temporal and spatial concentration of energy in the wake of cylinders and identified cross-sections that are more efficient than the circular cylinder in temporally concentrating the energy in the wake. In order to assess the applicability of these cross-sections on the energy harnessed by a WIV system, this chapter utilizes different upstream cross-sections in a WIV system. The downstream circular cylinder is attached to a Virtual Mass-Spring-Damper system to maintain the mass and damping ratio, and to record the displacements and force on the cylinder. Different

upstream bluff body cross-sections were investigated for a range of Reynolds numbers and separation gaps between the cylinders. Force and displacement measurements of the downstream cylinder are used to determine the efficiency of the WIV system for the different conditions used. The results indicate that a semi-circular cylinder is a better alternative to the circular cylinder as an upstream body in a WIV system to provide significant vibrations capable of harnessing energy.

This chapter has been submitted for publication as:

Manickam Sureshkumar, E, Arjomandi, M, Dally, B, Cazzolato, B, Ghayesh, M, 'Effect of the upstream bluff body shape on the efficiency of a WIV system', *Journal of Applied Energy* (under review).

Statement of Authorship

Title of Paper	Effect of the upstream bluff body shape on the efficiency of a WIV system
Publication Status	☐ Published ☐ Accepted for Publication ☑ Submitted for Publication ☐ Unpublished and Unsubmitted w ork w ritten in manuscript style
Publication Details	Manickam Sureshkumar, E, Arjomandi, M, Dally, B, Cazzolato, B, Ghayesh, M, 'Effect of the upstream bluff body shape on the efficiency of a WIV system', *Journal of Applied Energy*, (under review)

Principal Author

Name of Principal Author (Candidate)	Eshodarar Manickam Sureshkumar		
Contribution to the Paper	Water channel experiments utilising a stationary upstream cylinder and a transversely vibrating downstream circular cylinder. The upstream cylinder geometry, Reynolds number and separation gap between the cylinders was varied and the efficiency of vibration was computed.		
Overall percentage (%)	85		
Certification:	This paper reports on original research I conducted during the period of my Higher Degree by Research candidature and is not subject to any obligations or contractual agreements with a third party that would constrain its inclusion in this thesis. I am the primary author of this paper.		
Signature		Date	22/06/2018

Co-Author Contributions

By signing the Statement of Authorship, each author certifies that:

i. the candidate's stated contribution to the publication is accurate (as detailed above);
ii. permission is granted for the candidate in include the publication in the thesis; and
iii. the sum of all co-author contributions is equal to 100% less the candidate's stated contribution.

Name of Co-Author	Maziar Arjomandi		
Contribution to the Paper	Supervised the work, assisted in developing ideas and manuscript evaluation		
Signature		Date	22/06/2018
Name of Co-Author	Bassam B. Dally		
Contribution to the Paper	Supervised the work, assisted in developing ideas and manuscript evaluation		
Signature		Date	25/06/2018
Name of Co-Author	Benjamin S. Cazzolato		
Contribution to the Paper	Supervised the work, assisted in developing ideas and manuscript evaluation		
Signature		Date	22/6/18
Name of Co-Author	Mergen H. Ghayesh		
Contribution to the Paper	Supervised the work, assisted in developing ideas and manuscript evaluation		
Signature		Date	22/06/2018

This page is intentionally left blank

Manuscript

Title - Spatial and temporal concentration of hydrokinetic energy in the wake of a bluff body

Authors – Eshodarar Manickam Sureshkumar (Corresponding Author), Maziar Arjomandi, Bassam B. Dally Benjamin S. Cazzolato, Mergen H. Ghayesh

Affiliation – The University of Adelaide

Address – School of Mechanical Engineering, The University of Adelaide, North Terrace, Adelaide, SA, 5005

Abstract

Wake induced vibration (WIV), which is a form of flow induced vibration, has gained recent focus for harnessing hydro-kinetic energy from ocean currents and river flows. This paper reports the experimental results of a circular cylinder undergoing WIV in the wake of four different upstream cross-sections; namely, a circle, a semi-circle, a convex-edged triangle, and a trapezoid. The effects of the upstream bluff body cross-section, Reynolds number and the separation gap between the cylinders were investigated in the current study. The upstream rigid cylinder was kept stationary, whilst the downstream cylinder was constrained to vibrate in the transverse direction. The downstream cylinder was also mounted to a Virtual Mass-Spring-Damper (VMSD) system which maintained the structural parameters such as mass and damping ratio of the WIV system. The Reynolds number was varied from 4,000 to 10,000 and the experiments were performed in a closed-loop water channel at the University of Adelaide. The transverse gap was varied from 0D to 2D and the streamwise gap was varied from 2D to 4D. The results indicated that the semi-circular cylinder increased the WIV energy efficiency of the downstream cylinder compared to the circular cylinder, whereas the other two cross-sections reduced the WIV efficiency. The results also indicated that a staggered arrangement of $y/D = 2$ and $x/D = 4$ gives the highest efficiencies for the WIV system.

1 Introduction

The past few decades have seen increased motivation to develop clean and renewable energy to combat global warming and associated environmental problems that have developed due to the use of fossil fuels to produce majority of the world's energy supply. Hydrokinetic energy which is found in moving water sources such as rivers, ocean currents and water head is a viable source of renewable energy with little environmental impact. Conventional methods of harnessing hydrokinetic energy include the use of potential energy in water head from dams and turbine systems for the conversion of kinetic energy from falling water to useful electrical energy. Recent developments in Flow-Induced Vibration (FIV) for energy has motivated using non-turbine systems to generate hydroelectric energy without modifying the natural environment of the water sources using dams (Khan *et al.* 2009). FIV comprises of Vortex and Wake Induced Vibration (VIV and WIV, respectively) as well as classical galloping. FIV arises due to the interaction of the moving fluid with the structural properties of the bluff body. Due to the applicability of FIV energy harnessing systems in low-speed flows, VIV and WIV can be used to harness energy from ocean currents and river streams (Bernitsas & Raghavan 2004).

The Betz limit (16/27) defines the maximum power coefficient for a turbine based system extracting energy from a moving fluid using a single free blade (Jamieson 2009). However, conventional turbine systems operate at efficiencies of 20% - 55% when electrical and mechanical losses are considered (Vries 1983). Non-turbine systems in their infancy stages have resulted in experimental efficiencies of 22% - 46% and hence, warrant further research to determine their energy

harnessing potential (Bernitsas *et al.* 2009; Derakhshandeh *et al.* 2014; Ding *et al.* 2015).

VIV and WIV have been applied to flow energy technology such as the Vortex Induced Vibration for Aquatic Clean Energy (VIVACE) (Bernitsas *et al.* 2008). Pioneering work by Bernitsas *et al.* (2008), resulted in an early large-scale VIV device, employing a circular cylinder, to produce energy from low speed flows. Small-scale devices, such as those used for remote monitoring in ventilation and air conditioning systems, can use WIV to produce the minuscule amounts of energy needed for them to operate and hence make monitoring easier and viable at remote locations (Hobbs & Hu 2012; Wang & Ko 2010; Weinstein *et al.* 2012).

The main difference between VIV and WIV is that the latter needs a body vibrating in the wake produced from an upstream bluff body, which is usually kept stationary (Assi 2009). The wake produced from the upstream stationary bluff body affects the forces on the downstream vibrating body, causing the WIV response. WIV is of interest for energy production, due to the amplitude response not being limited to a lock-in range of velocities as in VIV (Assi 2009; Derakhshandeh *et al.* 2014) and the efficiency of WIV systems are higher than VIV systems (Derakhshandeh *et al.* 2014; Derakhshandeh *et al.* 2015a). Transverse vibration amplitudes of cylinders undergoing FIV, are about three times greater than the streamwise amplitudes, and hence are of more useful for energy generation (Bernitsas *et al.* 2008; Hobbs & Hu 2012; Wang & Ko 2010).

The circular cylinder has been extensively investigated in published literature due to its axisymmetric cross-section, and hence there is abundant information on VIV arising from a single circular cylinder in cross-flow (Bearman 1984; Bearman *et al.* 1981; Govardhan &

Williamson 2000; Govardhan & Williamson 2004; Sarpkaya 2004; Williamson & Govardhan 2004; Yokuda & Ramaprian 1990; Zdravkovich 1997). Studies on VIV have resulted in documenting the effect of structural parameters such as mass and damping ratio, as well as fluidic parameters such as Reynolds number and reduced velocity on the VIV of a smooth circular cylinder.

WIV or VIV with two cylinders is also dependant on the separation gap between the cylinders, due to the influence of the gap on the vortex streets formed by both cylinders (Igarashi 1981). Brika and Laneville (1999) measured the displacement of an elastically mounted circular cylinder operating in the wake of a stationary circular cylinder for Reynolds numbers (*Re*) between 5,000 and 27,000 at inline separations of 7 – 25 cylinder diameters (*D*), where the smaller separation gaps caused larger displacements in the downstream cylinder. A similar water channel study of WIV conducted by Assi (2009) reported that the amplitude of vibration of the downstream cylinder at low reduced velocities ($U_r \leq 5$) is independent of the streamwise separation gap (4*D* – 20*D*). However, an increase in separation gap from 4*D* to 20*D* at higher reduced velocities ($U_r > 5$) caused a reduced displacement in the vibration response. An investigation of WIV by Derakhshandeh *et al.* (2015a) investigated the effect of staggered arrangements on a system of two circular cylinders for *Re* = 2,000 – 15,000 for streamwise separations of 2.5*D* – 5*D* and transverse gaps of 0*D* – 3*D*, where maximum amplitude vibrations were obtained for a streamwise gap of 3.5*D* – 4.5*D* and a transverse gap of 1*D* – 2*D*. The phase lag between the lift force imposed on the cylinder and the oscillation response is also an important factor to consider in harnessing efficient energy using WIV, as the work done by the cylinder is the

product of the force and displacement of the cylinder (Bernitsas *et al.* 2008).

The vibration response of a cylinder can be modelled as a Mass-Spring-Damper (MSD) system as proposed by Bearman (1984), and the cylinder is usually supported using springs and damper pots. However, force-feedback controllers with computer models have also been used to impose the structural properties on the vibrating cylinder (Derakhshandeh *et al.* 2015a; Hover *et al.* 1997; Lee *et al.* 2011). One of the first Virtual MSD (VMSD) systems was developed by Hover *et al.* (1997), and allowed the authors to change the impedance of the system with ease as compared to using physical damper pots. The viability of the system was proved with many experiments measuring the lift coefficients and amplitudes of oscillation, however a phase lag of 12 degrees was present in the system due to the digital filter used in the computer model. This system also had to account for the gravitational force as the weight and lift force of the cylinder acted in the same direction (transverse to the freestream flow).

Lee *et al.* (2011) developed a similar VMSD using a motor, pulleys and a timing belt, with a horizontally mounted cylinder. Although their system proved to be a significant improvement to that by Hover *et al.* (1997), the cylinder's weight was directly imposed on the motor resulting in significant frictional force in the system. A VMSD system developed by Derakshandeh *et al.* (2015a) utilised a vertically mounted cylinder in cross-flow such that the weight of the cylinder was not directly imposed on the driving motor. This system had advantages of not having the static weight of the cylinder causing friction in the system, as well as a dynamic response that isn't affected by gravity, as

the gravitational force was orthogonal to both the lift and drag forces on the cylinder.

Efficiency studies of WIV and VIV systems have been used to confirm the viability of FIV for energy harnessing. Derakhshandeh *et al.* (2015a, 2015b) showed that a WIV system, consisting of two circular cylinders, had an efficiency of 48.6% (Re = 9000), whereas a VIV system only had a maximum efficiency (η) of 22.2% (Re = 65,000, and η = 10% at *Re* = 6,000) (Derakhshandeh *et al.* 2015a, 2015b). Work by these authors led to realizing that off-centre separations of cylinders in a WIV system are more efficient compared to inline separations for the purpose of energy harvesting. Bernitsas *et al.* (2009) worked out a theoretical efficiency of 37% for a single circular cylinder VIV system, but only obtained η = 22% at *Re* = 100,000. Recent research on single cylinder VIV responses of different bluff body cross-sections, yielded a max efficiency of 45.7% for a trapezoid operating in a Reynolds number range of 10,000 – 130,000 (Ding *et al.* 2015).

WIV for energy is still a relatively novel and new field, which has sparked exciting progression over the last decade with still much improvement possible to increase the energy extraction efficiencies. Focus has been on cross-section and placement of the downstream and vibrating body, as well as system parameters such as mass and damping ratio. However, little work has been accomplished on the effect of varying the cross-section of the upstream stationary body to improve the WIV system.

This paper investigates the WIV response induced in a downstream elastic circular cylinder due to the wake caused by a variety of upstream stationary bluff bodies. The analysis was performed for different Reynolds numbers and a range of streamwise and transverse

distances between cylinders. The WIV amplitudes and lift forces were collected for the downstream cylinder and processed to obtain the amplitude of vibration, lift coefficient, force-displacement phase angle and the WIV power coefficient. These results were used to analyse the effect of the chosen cross-sections and is presented in this paper.

2 Methodology

The experimental apparatus and techniques utilised for the WIV tests are outlined in the following sub-subsections.

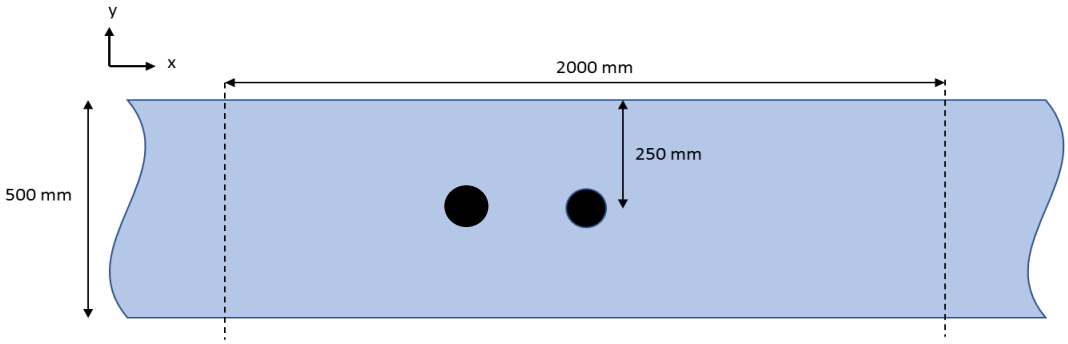

Figure 1 - Cross-sections used as the first body in the WIV system

2.1 Water channel experiments

The experiments were performed in a re-circulating water channel at the University of Adelaide. The test section measured 2000m (length) x 600m (depth) x 500m (width) and its top view is shown in Figure 1. A schematic representation of the WIV system with a stationary upstream cylinder and a 1 degree-of-freedom (DOF) downstream cylinder is depicted in Figure 2. The downstream body is constrained to only be able to move transverse to the freestream flow. Four different bluff body cross-sections with a characteristic diameter of 30mm and a wetted length of 400mm were used as the upstream stationary body in this investigation – circular, semi-circular, convex-edged triangular and trapezoidal cylinders (Figure 3 a) – d),

respectively). These cross-sections were previously investigated for their temporal energy concentration by the authors using Computational Fluid Dynamics, where the semicircular and convex-edged triangular cylinders provided higher temporal energy in the wake compared to the circular cylinder (Manickam Sureshkumar *et al.* [under review]). All the bluff bodies had the same hydraulic diameter of 30mm. Figure 4 displays the 9 different test cases for each cylinder based upon the streamwise and transverse gap between the upstream and downstream cylinders, normalised by the characteristic diameter of the upstream cylinder. The investigated streamwise (x) and transverse (y) separations were based on previous investigations (Derakhshandeh *et al.* 2015a, 2016) and allowed the downstream cylinder to be in the wake interference region of the upstream bluff body. The downstream body oscillated about the centreline of the tunnel test section, whilst the position of the upstream bluff body was varied to test the different separation distances for each of cases specified in Figure 4. The blockage caused by the upstream cylinder was 7% which is alike similar investigations and deemed negligible for the current study (Assi 2009; Derakhshandeh *et al.* 2015a). A maximum velocity of 0.335 m/s was achievable in the water channel, and thus the Reynolds number (Re) was varied between 4,000 and 10,000. The circular cylinder is in the transition-in-shear layer regime (Blevins 1997) which corresponds to a Strouhal number (St) of approximately 0.2.

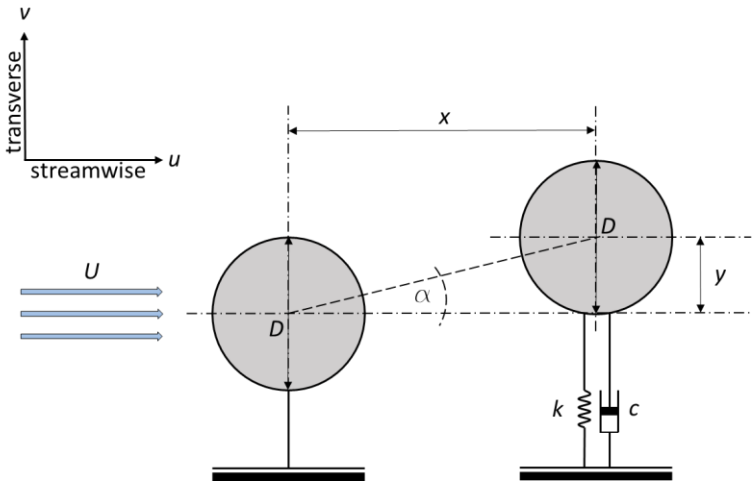

Figure 2 – Schematic representation of the WIV system consisting of a fixed upstream cylinder of diameter D and a transversely vibrating second bluff body. X and y denote the streamwise and transverse separation gap between the cylinders, respectively; k and c are the spring stiffness and damping coefficient, respectively.

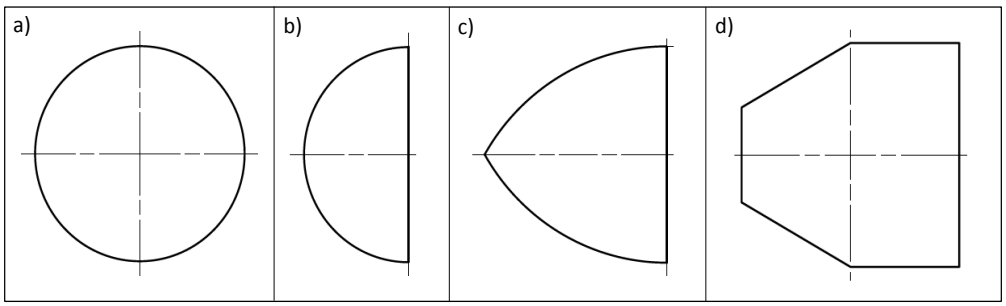

Figure 3 - Cross-sections used as the first bluff body in the WIV system. a), circle; b), semicircle; c), convex-edged triangle (c-triangle); d), trapezoid.

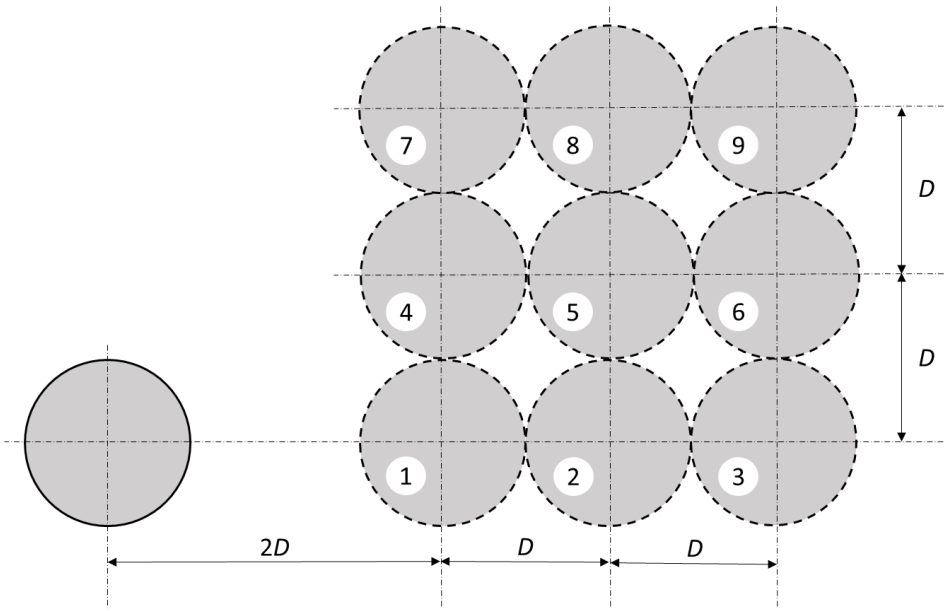

Figure 4 - Schematic representation of the nine different test cases used for each cross-section in this study, where the shaded circle with the solid outline represents the upstream cylinder, and the dashed circles are the nine locations of the downstream cylinder.

2.2 Virtual Mass-Spring-Damper system (VMSD)

The VMSD system imposes virtual mass and damping ratios to the vibrating cylinder to provide the WIV response. This system also accounts for friction hence making it a frictionless system. A photograph of the VMSD system along with a schematic representation is shown in Figure 5. The VMSD system consists of two independent motors – motor 1 provides the required stiffness and damping in the system, and motor 2 varies the angle of attack of the downstream cylinder. To provide the virtual mass and damping ratios in this research, only motor 1 was used. The motors used in this system are Maxon EC-MAX 30 24V servo motors, which are controlled with Maxon ESCON 50/5 servo controllers. The motors have a planetary gearbox with 51:1 ratio, to provide greater movement resolution and torque in the system, as well as an optical encoder to provide position feedback. Motor 1 is connected to the carriage ('Moving assembly' in Figure 5) via a pair of toothed pulleys and a toothed timing belt. One of the toothed pulleys was directly connected to the gearbox output of motor 1, whilst the other acted as an

idler. The moving carriage supported motor 2 as well as the downstream cylinder and ran on a pair of linear bearings. Further details are reported in (Derakhshandeh *et al.* 2015a).

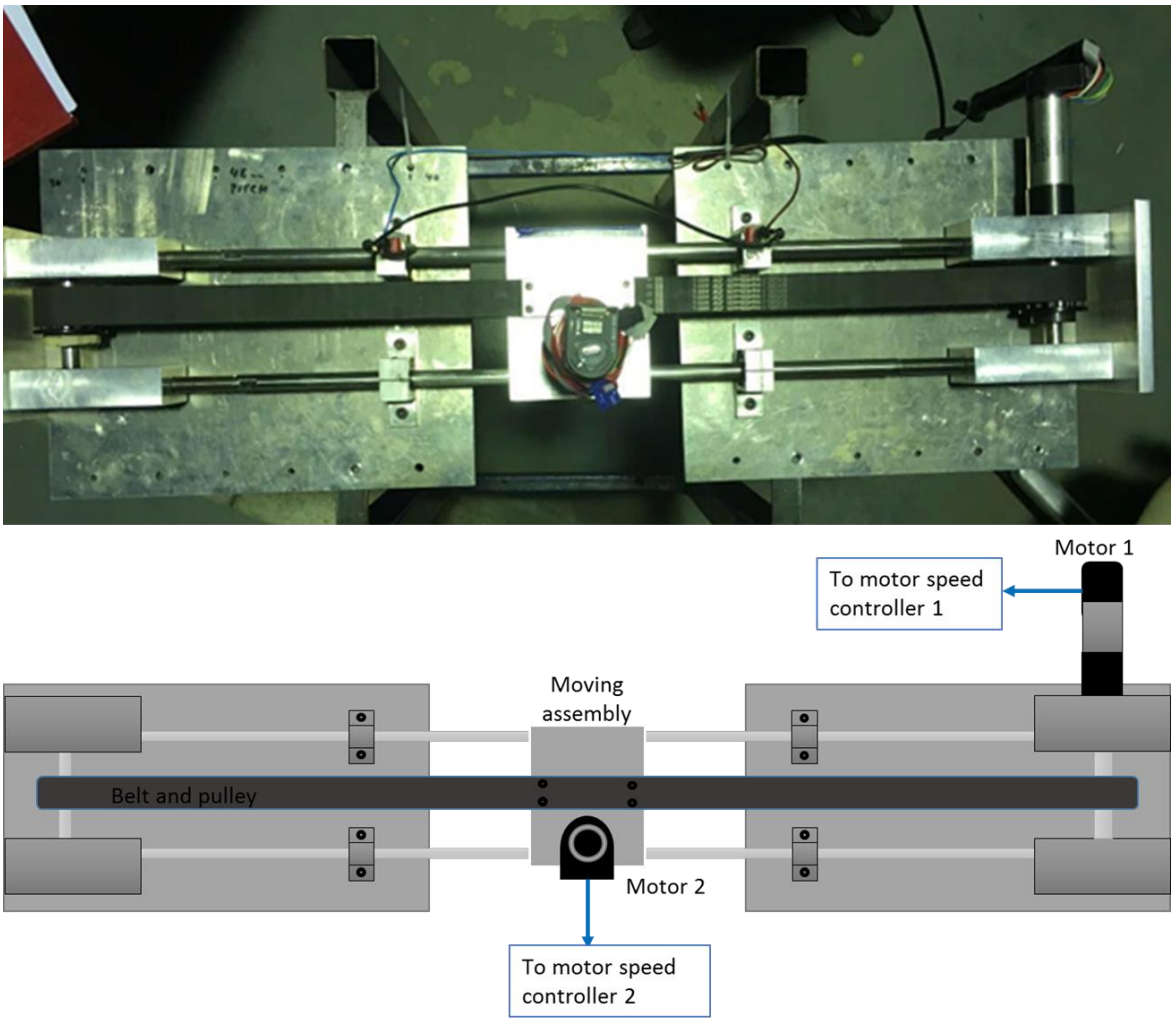

Figure 5 - The Virtual-Mass-Spring-Damper (VMSD) system used in this research

The lift and drag forces on the downstream cylinder, which act in orthogonal directions to the freestream flow, were measured using two pairs of strain gauges positioned in a half-bridge configuration. Using the assumption of 2D flow, the lateral forces on the cylinder were estimated by utilising the moment at the root of the structure supporting the downstream cylinder. The VMSD system was modelled on Simulink in Matlab™. The Simulink control model was then compiled using the Real Time Workshop on to a dSPACE™ environment. A

dSPACE DS1104 rapid prototyping board was used along with the Control Desk software to implement real time control. The input to the system was the analog voltage signal from the half-bridge corresponding to lift force, which was read using a 16-bit analog-to-digital convertor on the dSPACE board. Feedback was achieved by acquiring the position of the motor using the encoder on the motor. The output was an analog voltage sent from the digital-to-analog convertor on the dSPACE board, which controlled the servo controller and motor.

2.3 PID tuning

A PID controller was implemented to achieve accurate positioning of the vibrating cylinder, as governed by the Simulink model. The dedicated encoder input on the dSPACE prototyping board was used to provide feedback on the position of the cylinder for the PID controller. A gain coefficient was calculated using the dimensions of the system, as well as the ratio of the gearbox to convert the rotation of the motor shaft to the vibration of the cylinder, to accurately obtain feedback on the position of the vibrating cylinder from the encoder. An error input to the PID controller was possible using the computed and measured displacements of the downstream cylinder. The PID controller was manually optimised to provide displacement errors less than 0.1 mm which was sufficient for the analysis in this research.

2.4 System parameters

The mass and damping ratios for all the different cross-sections and cases were kept constant to provide meaningful comparisons. Hence, the observed differences in the results are only due to the separation distance and the upstream body cross-section. The parameters given in Table 1 were chosen to aid analyses and

comparisons with previously published results by (Assi 2009; Derakhshandeh *et al.* 2015a)

Table 1 - System parameters used in the experiments

Mass ratio	2.4
Damping ratio	0.07
Reynolds numbers	4,000, 6,000, 8,000 and 10,000
Density of water (20°C)	998.2 kg/m^3

Although the structural parameters (mass and damping ratio) were chosen to be constant for this study, the damping in the system is likely to vary with the test cases due to the varying stiffness caused by the upstream cylinder's wake for the different cases. Therefore, the damping ratio chosen is not optimised for this investigation. However, the chosen damping ratio is consistent with previous investigations to facilitate comparison of results.

2.5 Mathematical modelling

An overview of the mathematical modelling is presented in this section. A detailed description of the model can be found in (Derakhshandeh *et al.* 2015a).

The vibration of a cylinder with a MSD system can be modelled using the following equation (Bearman 1984):

$$m\ddot{y}(t) + c\dot{y}(t) + ky(t) = F_y(t), \quad (1)$$

where, y, $\dot{y}$ and $\ddot{y}$ are the transverse displacement, velocity and acceleration of the cylinder, respectively, c is the damping coefficient, k

is the spring stiffness and m is the mass of the cylinder. $F_y(t)$ is the transverse fluid force exerted on the cylinder and is the sum of viscous and pressure forces on the cylinder.

$$F_y(t) = F_{viscous} + F_{pressure} \quad (2)$$

Table 2 contains the structural parameters that influence the WIV response as well as non-dimensional parameters that govern the vibration response of the cylinder. Here, ρ is the fluid density, U is the freestream velocity, μ is the dynamic viscosity of water, D is the diameter of the downstream cylinder and L is the length of the cylinder.

Table 2 - Non-dimensional parameters.

Mass ratio	m^*	$4m/\rho\pi D^2 L$
Damping ratio	ζ	$c/2\sqrt{km}$
Lift coefficient	C_L	$F_y/0.5\,\rho U^2 DL$
Amplitude ratio	Y^*	y_{max}/D
Frequency ratio	f^*	f/f_n
Reynolds number	Re	$\rho UD/\mu$

Equations (3) and (4) defined the time dependant displacement and lift coefficient of the downstream cylinder, respectively, assuming a harmonic response by the cylinder.

$$y(t) = y_{max}\sin(2\pi f_{osc}t), \quad (3)$$

$$c_L(t) = C_L\sin(2\pi f_{osc}\,t + \Phi), \quad (4)$$

where y_{max} is the displacement amplitude, assuming a harmonic response, and f_{osc} denotes the oscillation frequency in equation (3). In Equation (4), c_L is the temporal lift coefficient, C_L is the magnitude of the lift coefficient and Φ is the phase difference between the driving lift force

and resultant displacement of the cylinder, which affects the efficiency of the WIV response of the cylinder (Bernitsas *et al.* 2008).

The damped natural frequency of the cylinder can be approximated using Equation (5):

$$\omega_{\mathrm{d}} = \frac{2\pi}{T_{\mathrm{d}}} = \omega_{\mathrm{n}}\sqrt{1-\zeta^2} \approx \omega_{\mathrm{n}} = \sqrt{\frac{k}{m_{\mathrm{eff}}}} \tag{5}$$

where, T_{d} represents the damped period of oscillation.

The rotation of the shaft in the servo motor of the VMSD system is converted to the linear vibration of the downstream cylinder using the connected gearbox, pulleys and timing belt. Feedback to this system is via the angle measurements from the encoder connected to the motor. The lift force on the cylinder is measured using the strain gauges attached to the cylinder. The force measurements are used to calculate the vibration response which is imposed on the cylinder using the torque created by the servo motor, whilst maintaining the desired spring stiffness and damping constant. The torque produced by the motor controls the velocity of the cylinder, whilst the forces caused by shed vortices are exerted on the cylinder. Thus, the work generated by the cylinder during one cycle of oscillation (T) can be calculated by integrating the inner product of the force and the instantaneous velocity of the cylinder, as per Equation (6) below:

$$W_{\mathrm{WIV}} = \int_0^T F_y \dot{y} dt. \tag{6}$$

The average power is then given by

$$P_{\mathrm{WIV}} = \frac{W_{\mathrm{WIV}}}{T}. \tag{7}$$

The fluid power given by $P_{\text{fluid}} = FU = (½)\rho U^3 D_2 L$ (Bernitsas & Raghavan 2004), can be used to evaluate the power coefficient of the downstream cylinder.

$$\eta_{\text{WIV}} = \frac{P_{\text{WIV}}}{P_{\text{fluid}}}. \tag{8}$$

Utilising the equations above the power coefficient for WIV of the cylinder can be represented by the following equation;

$$\eta_{\text{WIV}} = \frac{\pi C_{\text{L}} f_{\text{osc}} y_{\max} \sin(\Phi)}{U}. \tag{9}$$

Further details of the mathematical derivation is found in Derakhshandeh *et al.* (2015a).

2.6 Validation of the VMSD system

The VMSD system was developed and validated by Derakhshandeh *et al.* (2015). This section presents some of the results from the present system and the comparisons with similar studies by Derakhshandeh *et al.* (2015) and Assi (2009) to prove the validity of the current system for the VIV and WIV experimental analysis presented in this paper.

Figure 6 displays the amplitude of vibration and lift coefficient due to VIV of a single elastically mounted cylinder at upper (*Re* = 6,000) and lower (*Re* = 10,000) branches of oscillation. I can be noted that the deviation of peak amplitude with respect to the amplitude of the cylinder is insignificant. Additionally, the lift force on the cylinder and the displacement of the cylinder are in phase at the upper branch of oscillation (*Re* = 6,000, Figure 6 a)). Hence, the maximum amplitude of vibration for a single elastically mounted cylinder occurs at this Reynolds number. Increasing the Reynolds number to 10,000 results in a phase shift between the lift force acting on the cylinder and the

displacement of the cylinder, which results in a drop in the peak amplitude of vibration. At the lower branch of oscillation, the lift force-displacement phase angle shows approximately a 180° phase shift (*Re* = 10,000, Figure 6 b)).

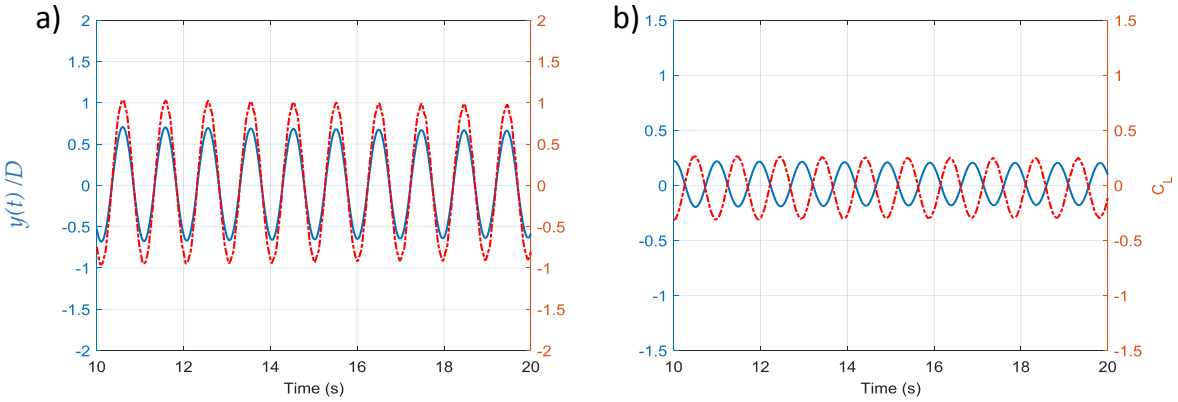

Figure 6 - Typical time series of the lift coefficient (dotted line) , c_L, and the dimensionless displacement (solid line), y(t) /D, of a single circular cylinder undergoing VIV at a) Re = 6,000 and b) Re = 10,000. (mass ratio = 2.4, damping ratio = 0.01)

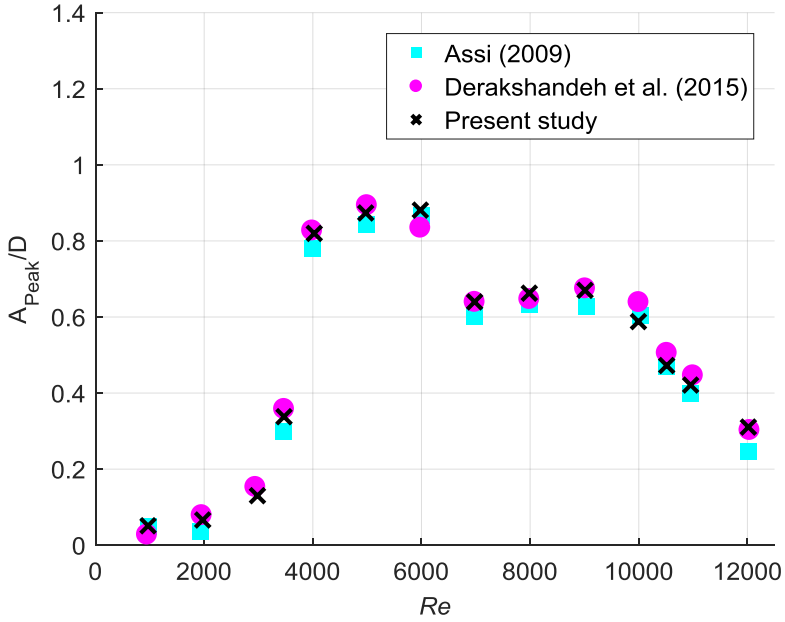

Figure 7 - Results of the peak dimensionless displacement vs Reynolds number for a single cylinder undergoing VIV using the VMSD system. The results are compared with published experimental results (Assi 2009; Derakhshandeh et al. *2015) with the same structural properties (m*= 2.4 and ζ = 0.01).*

The amplitude of oscillation of the cylinder was compared against published experimental results (Assi 2009; Derakhshandeh *et al.* 2015), obtained under the same fluidic (*Re* = 4,000 and 8,000) and

structural properties (m^*= 2.4 and ζ = 0.01). Figure 7 depicts the non-dimensional peak amplitude of VIV (A_{Peak}) for a single cylinder as a function of the Reynolds number. The experimental results of the VMSD are compared with a real MSD mechanism, presented by Assi (2009) and previous results for the VMSD system published by Derakhshandeh *et al.* (2015). It is evident that the results are very similar and the VMSD system can produce the correct VIV response of a single circular cylinder

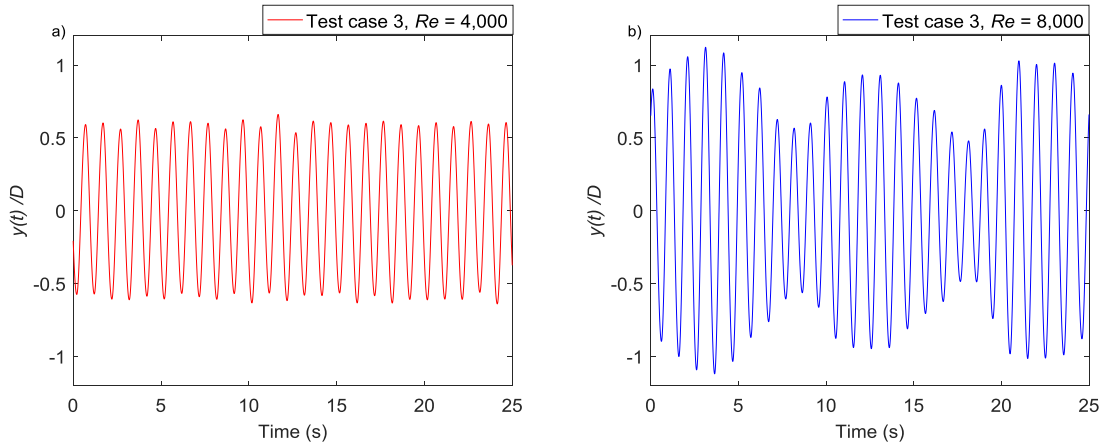

Figure 8 - Measured time history of displacement for Test Case 3 (x/D = 4, y/D = 0) at Re = 4,000, a), and 8,000, b) for a two-cylinder WIV system.

The non-dimensional oscillation amplitude ($y(t)/D$) for Test case 3 ($x/D = 4$, $y/D = 0$) is plot in Figure 8 for Re = 4,000 (Figure 8 a)) and 8,000 (Figure 8 b)). It can be seen that the displacement of the downstream cylinder becomes irregular with increasing Reynolds number (or reduced velocity); however, the displacement amplitude of the cylinder increases at higher Reynolds number and plays an important role in increasing the power coefficient of the WIV mechanism. The dimensionless displacement amplitudes are in a good quantitative agreement with the ones produced by Assi (2009), which were 0.6 and 0.9, respectively.

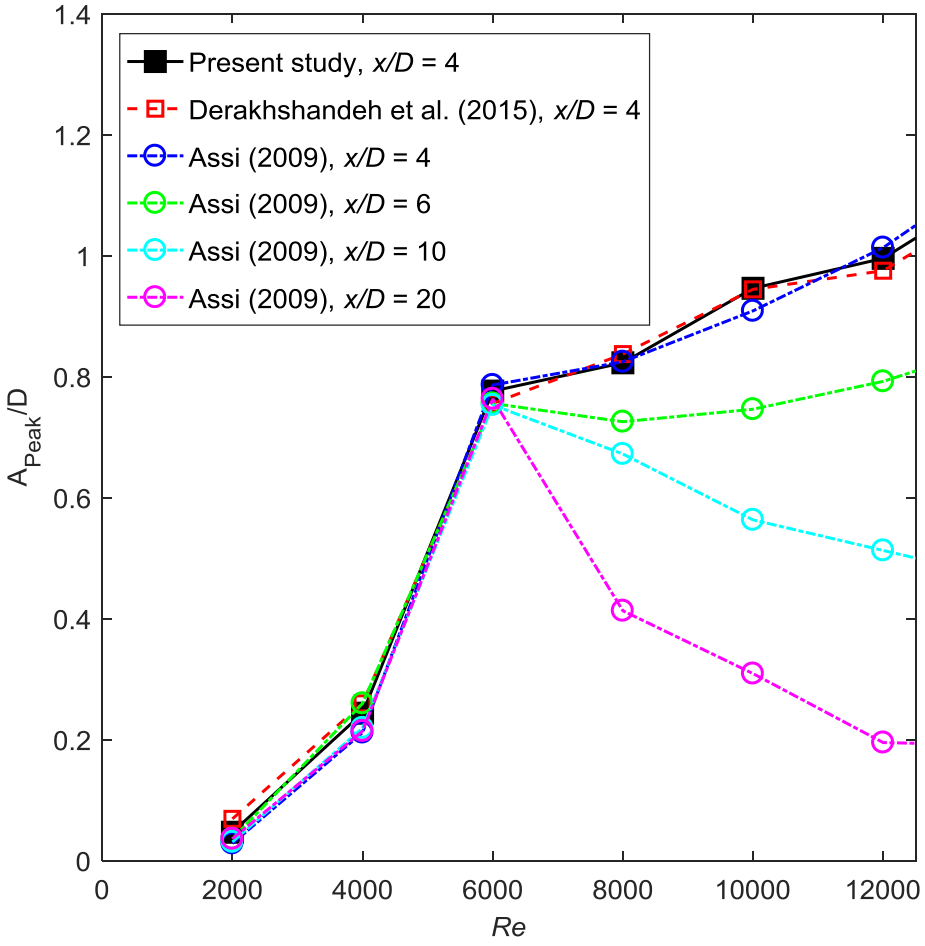

Figure 9 - WIV response of the downstream cylinder as a function of the Reynolds number and a comparison of the data for x_0/D = 4 with previous work (Assi 2009) (Test Case 3).

The non-dimensional amplitude of vibration for a range of Reynolds numbers of a two-cylinder WIV system was compared with experimental works (Assi 2009; Derakhshandeh *et al.* 2015) with similar properties (m^*= 2.4 and ζ = 0.01; x/D = 4, y/D = 0) in Figure 9. From Figure 9 it can be seen that the displacement of the cylinder for Test case 3 is in good agreement with published experimental data at the same separation gap and structural properties. The results vary by less than 8%, between this study and the previous work. The small discrepancy between the data is likely due to different experimental methods and is within acceptable bounds for experimental reproducibility.

Additionally, results from Assi (2009) also confirm that there is no benefit to increasing the longitudinal separation beyond 4D ($x/D > 4$); as there is a reduction of amplitude at high Reynolds numbers ($Re > 6{,}000$) for $x/D > 4$.

3 Results and Discussion

The vibration amplitudes and lift forces collected from the VMSD rig and control system were processed to obtain the amplitude of vibration, lift coefficient, force-displacement phase angle and the WIV power coefficient. These results are presented and discussed in this section.

3.1 Amplitude of vibration

Figures 10 to 13 display the effect of streamwise and transverse separation on the amplitudes of vibration observed for the circular, semi-circular, trapezoidal and convex-edged triangular cylinders, respectively. The peak amplitude was obtained by multiplying the root mean square (r.m.s.) of the displacement output, from Control desk, by the square root of 2. The normalised peak amplitudes for the 9 test cases, for each upstream cross-section, are displayed as scatter points for their respective Reynolds numbers. Also displayed in this graph are line plots for the minimum (case 1) and maximum (case 9) amplitude responses (blue and red, respectively). It is clear from these figures that increasing the Reynolds number increases the vibration amplitude of the downstream cylinder, independent of the upstream bluff body cross-section and position of the downstream cylinder. This can be observed in Figures 10 - 13 where all the test cases have a positive slope, which is a characteristic of WIV and reflects previous findings by Derakhshandeh *et al.* (2015a) and Assi (2009).

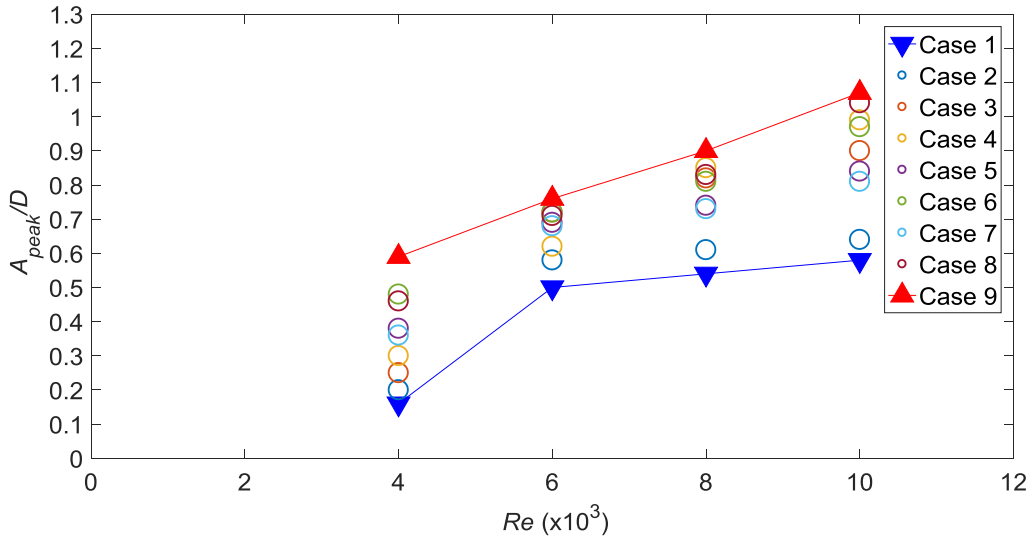

Figure 10 - Amplitude response for the circular cylinder

Examining the effect of streamwise and transverse spacing, the highest vibration amplitude for all the different upstream bluff bodies was observed for case 9, whilst the lowest amplitude occurs for case 1. All the other cases are bounded by the maximum and minimum values recorded for case 9 and case 1, respectively.

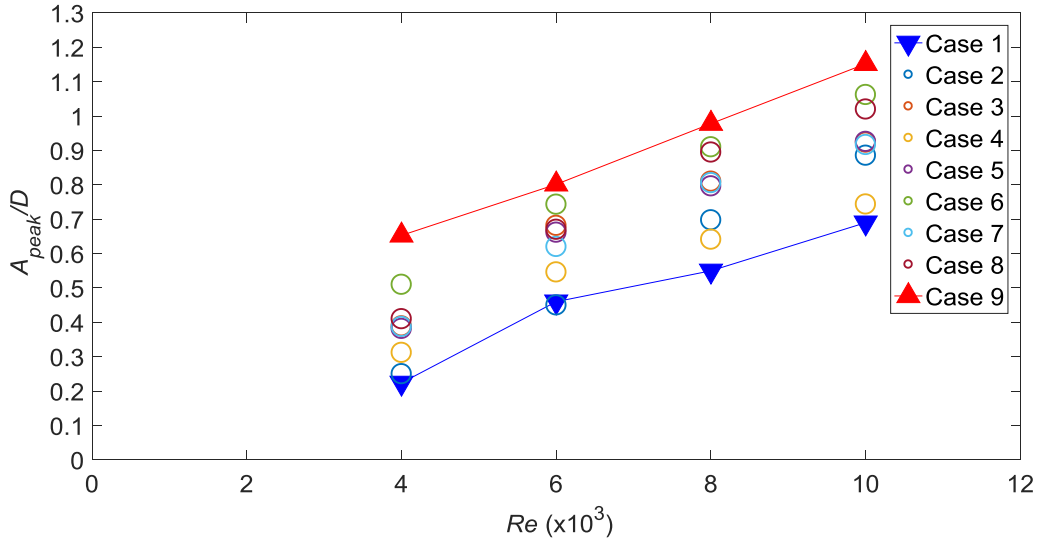

Figure 11 - Amplitude response for the semi-circular cylinder

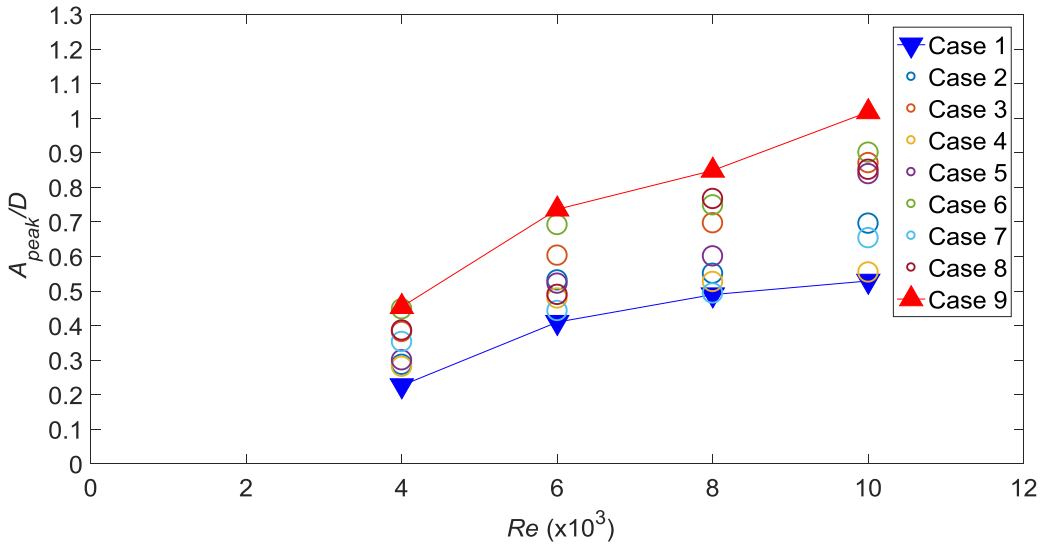

Figure 12 - Amplitude response for the trapezoidal cylinder

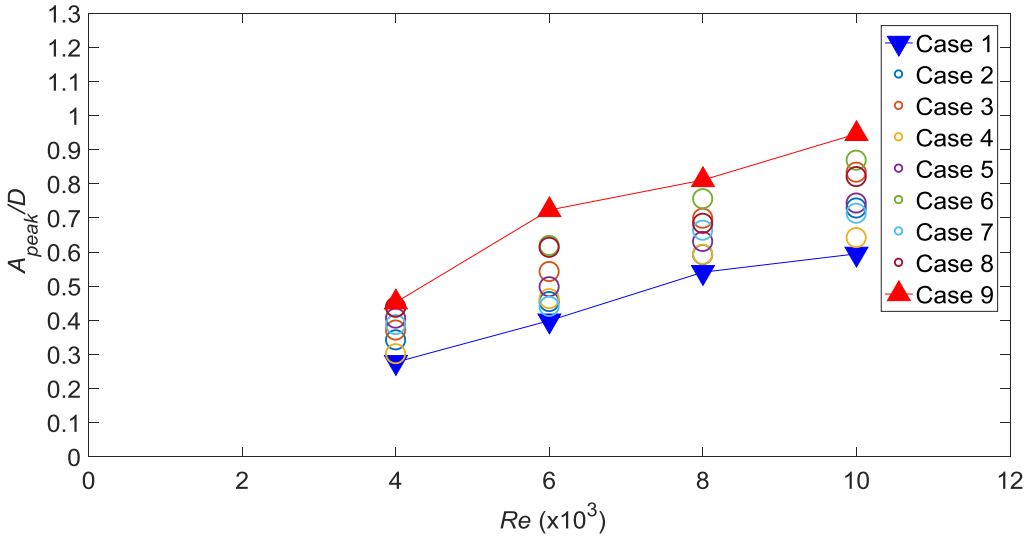

Figure 13 - Amplitude response for the c-triangular cylinder

Another trend observed is that the vibration amplitude increases when the streamwise gap increases from 2*D* to 4*D* whilst the transverse gap is kept the same (case 7 vs case 9). The vibration amplitude also increases as the transverse gap increases from 0*D* to 2*D*, whilst the streamwise gap is kept the same (case 1 vs case 7). These trends were reported previously by Derakhshandeh *et al.* (2015a) and remained evident for the different cross-sections used in this study, as depicted in Figures 10 – 13.

The vibration amplitudes among the different test cases for each cross-section are much closer together at *Re* = 6,000 compared to the other Reynold numbers investigated. At *Re* = 6,000 the downstream cylinder is in the upper branch of the VIV regime (where there is frequency matching between the vortex shedding frequency and the natural frequency of the cylinder) and hence, undergoes high amplitude resonance and the separation gap seemed to have less of an effect at this regime than at other Reynolds numbers. Compared to the distinct three-branch response of a cylinder undergoing only VIV, the WIV response has increasing amplitudes when the 'lock-in' range of Reynolds numbers is surpassed. Hence, the maximum amplitude response is not limited to system properties such as stiffness, mass and damping which are known to contribute to the natural frequency of the downstream cylinder.

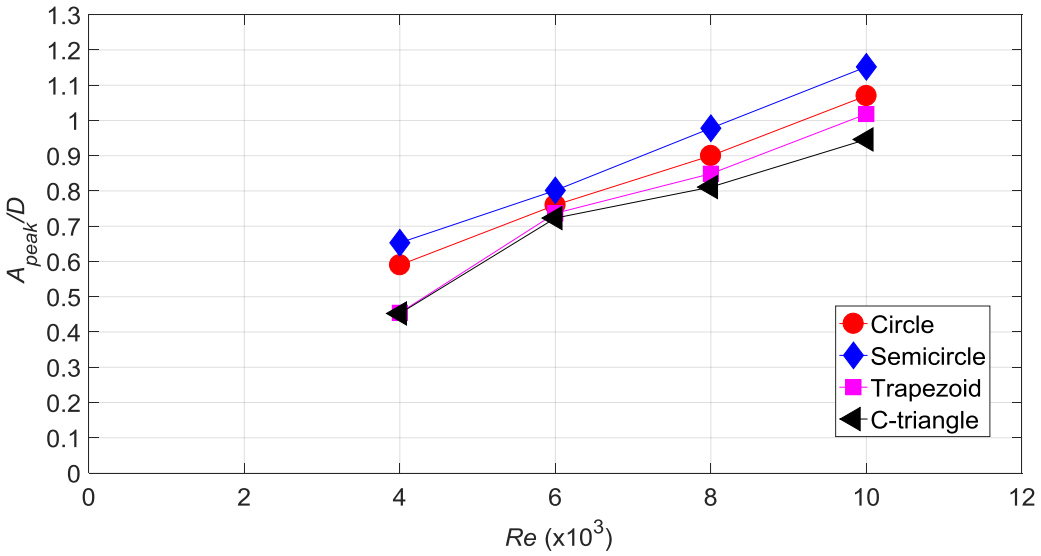

Figure 14 - Amplitude comparison for case 9 (x/D = 4, y/D = 2) for all the test cases

Out of the four cross-sections investigated in this project, the semi-circular cylinder provided the highest amplitudes for $x/D = 4$ and $y/D = 2$ at *Re* = 10,000 compared to the circle, whilst the trapezoid and convex-edged triangular had lower amplitudes than the circle (Figure

14). The semicircular cylinder produced a maximum amplitude in the downstream cylinder of 1.15*D*, which was 7.5% higher than the circular cylinder, whilst the trapezoidal and convex-edged triangular cylinders had a loss in amplitude of 5% and 12%, respectively, compared to the circular cylinder.

3.2 Lift coefficient

The calculated lift coefficients (equation in Table 2) were very similar across the different test cases for each individual Reynolds number and upstream cross-section investigated. Hence, the lift coefficient was less dependent on the separation gap between the cylinders and a mutual relationship between the lift coefficient and the Reynolds number was observed for all the test cases. The averaged lift coefficient for each cross-section and Reynolds number is plotted on the bar charts in Figure 15. The bars on this chart also have the standard deviation across the different test cases.

The largest increase in lift coefficient occurs when *Re* increases from 4,000 to 6,000. The large lift coefficient occurs due to a maximised lift force as well as a beneficial phase angle between the lift force and the velocity of the cylinder. The lift force on the cylinder is comprised of the potential lift force and the vortex lift force (Williamson & Govardhan 2004). The potential lift force arises due to the inertial force on the cylinder due to its acceleration and hence, is proportional to the added mass (mass of fluid) of the cylinder multiplied by its acceleration. On the contrary, the vortex force is a product of the vortex street produced by the cylinder and depends on the dynamics of the shed vortices. Hence, a maximum for the lift coefficient is obtained when both the vortex and potential lift forces are at a maximum and the force and velocity of the cylinder are in-phase. The potential and vortex lift forces are very similar

and the force-velocity phase angle is close to zero at a reduced velocity of 4.4 (Assi 2009). Therefore, the maximum lift coefficient is obtained in this study at *Re* = 6,000 where the reduced velocity is 4.2.

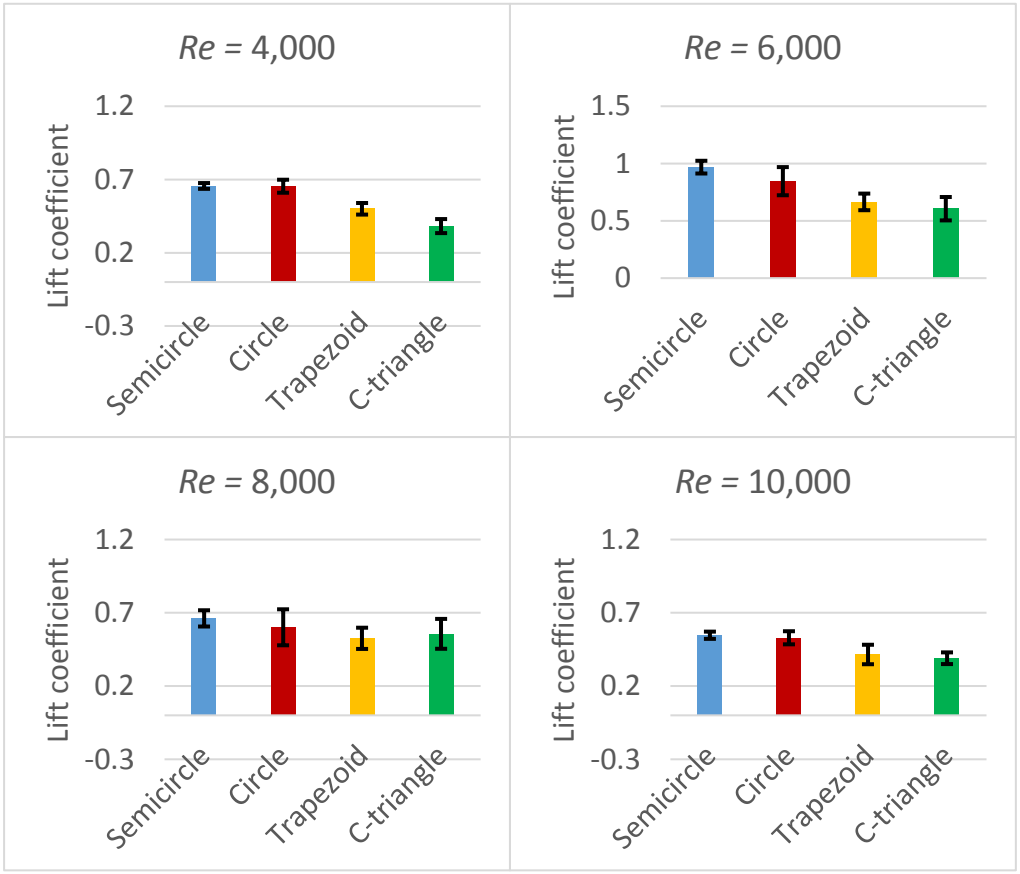

Figure 15 - Comparison of the average lift coefficient across all tests cases for each Reynolds number and upstream cross-section investigated. The corresponding Reynolds numbers are given in the title of each subplot. The error bars indicate the standard deviation of the lift coefficient across the 9 test cases for each bar on the plots.

Apart from the trapezoid, the lift coefficient for *Re* = 4,000 is higher than that for *Re* = 10,000. The lift coefficient is normalised using the free stream fluid velocity. The reduction in lift coefficient can be attributed to the increased fluid velocity at higher Reynolds numbers.

The semicircular cylinder has the highest lift coefficients compared to the other cross-sections at all the Reynolds numbers, which contributes to the higher vibration amplitudes observed. The semi-circular cylinder also had a lower standard deviation compared to the

other cross-sections for the Reynolds numbers, and hence, there is greater correlation of the lift coefficient between the test cases.

3.3 Force-displacement phase angle

The energy harnessing efficiency of WIV is heavily dependent on the force-displacement phase difference of the cylinder (Derakhshandeh *et al.* 2015a, 2015b, 2016). The phase angle between force and displacement signals in this study was evaluated using the Transfer Function Estimate in Matlab, with a sampling time of 0.001s using a 8192-point FFT and a flat-top window. The contour plots of the phase results as a function of streamwise and transverse spacing shows that the trends observed are similar between the circular and trapezoidal cylinders, as well as the semi-circular and convex-edged triangular cylinders. Hence, the phase contour plots for only the circular and semi-circular cylinders are presented in Figures 16 and 17, along with a comparative bar plot of the average phase angles in Figure 18.

The general trend among the cross-sections is that increasing Reynolds number from 4,000 to 6,000 causes an increase in the force-displacement phase angle as shown in Figure 18. Increasing the Reynolds number further, from 6,000 to 10,000 then causes a decrease in the phase angle.

The largest force-displacement phase angle (closest to 90 degrees) for all cross-sections occurs at Re = 6,000 and at a location of $3 \leq x/D \leq 4$ and $1 \leq y/D \leq 2$ for all the cross-sections. Since an efficient linearly vibrating system has a force-displacement angle of 90 degrees, a Reynolds number of 6,000 provides the most efficient vibrations, due to the system being in its VIV 'lock-in' range.

For the circular (Figure 16 d)) and trapezoidal cylinders at *Re* = 10,000, the phase angle is more sensitive to the location of the downstream cylinder than at other Reynolds numbers for the circular and trapezoidal cylinders. This causes a larger deviation of the phase angle between the different cases. However, the semi-circular (Figure 17 d)) and convex-edged triangular cylinders seem to reduce the sensitivity of the phase angle to the downstream cylinder location.

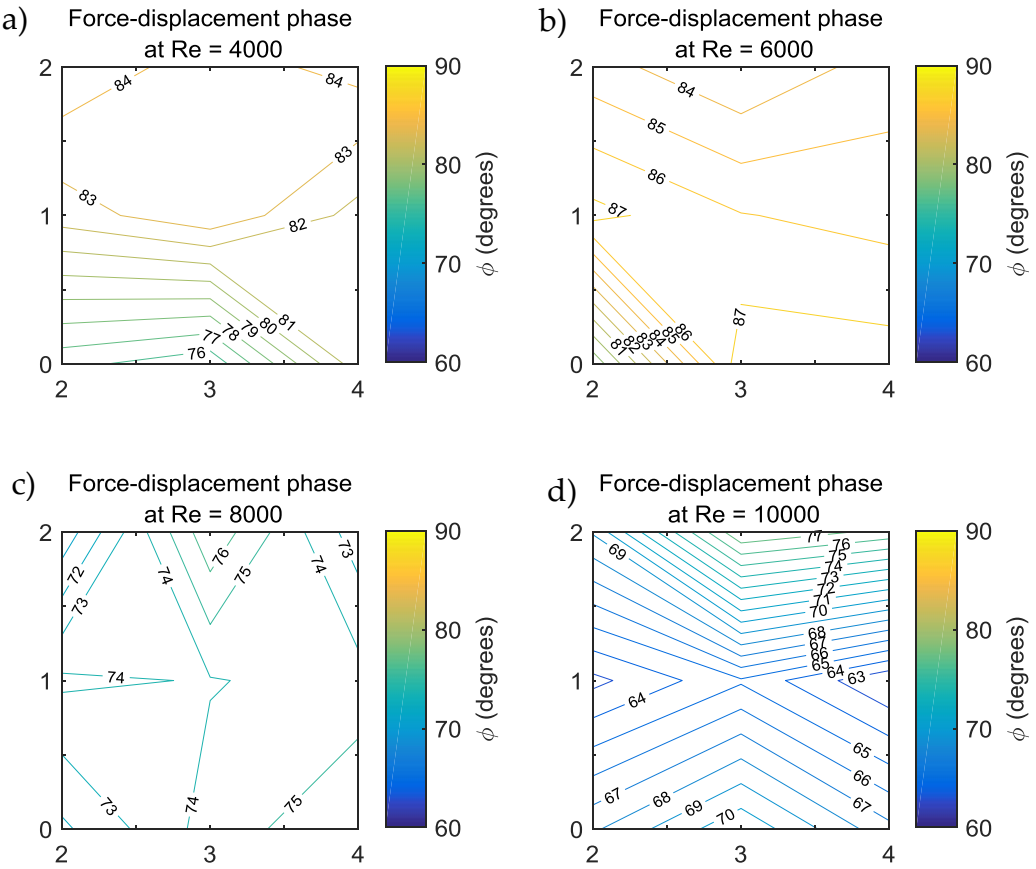

Figure 16 - Force-displacement phase angle distribution for the circular cylinder

A comparison of the average phase angles showed that the phase angle has a higher dependency on the Reynolds number as compared to

the cross-section of the upstream cylinder, since the phase angles at each Reynolds number differed by less than 5% (Figure 18).

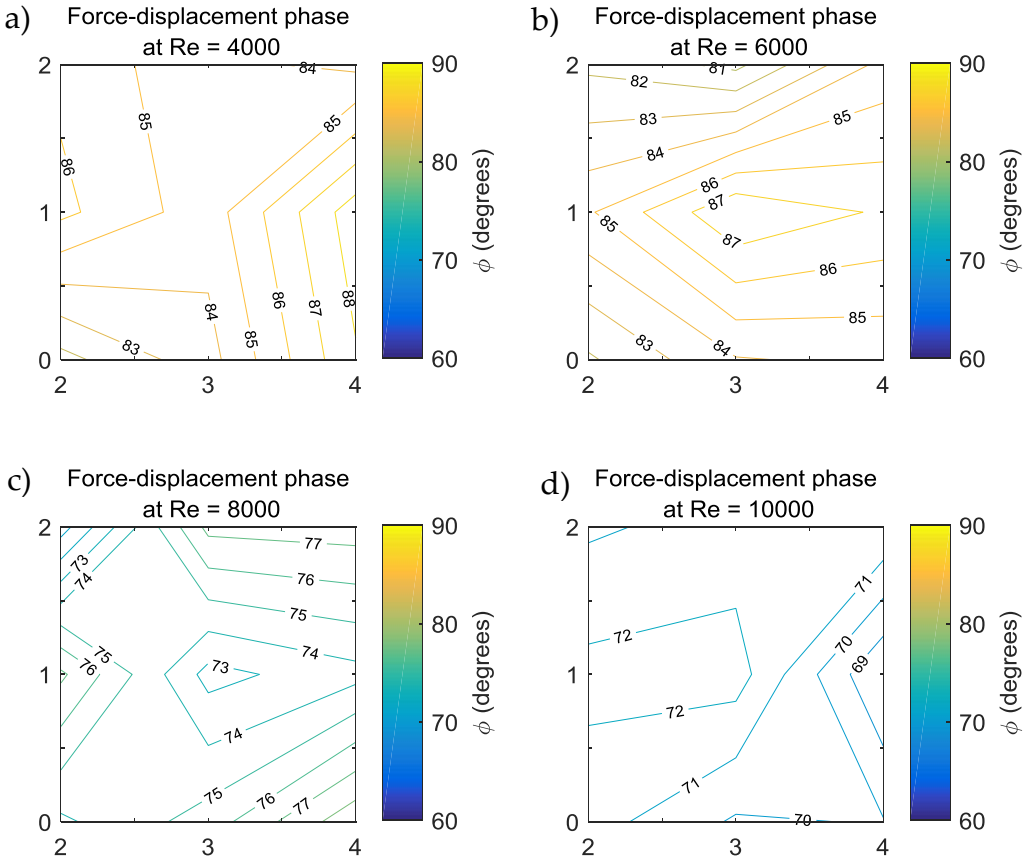

Figure 17 - Force-displacement phase angle distribution for the semi-circular cylinder

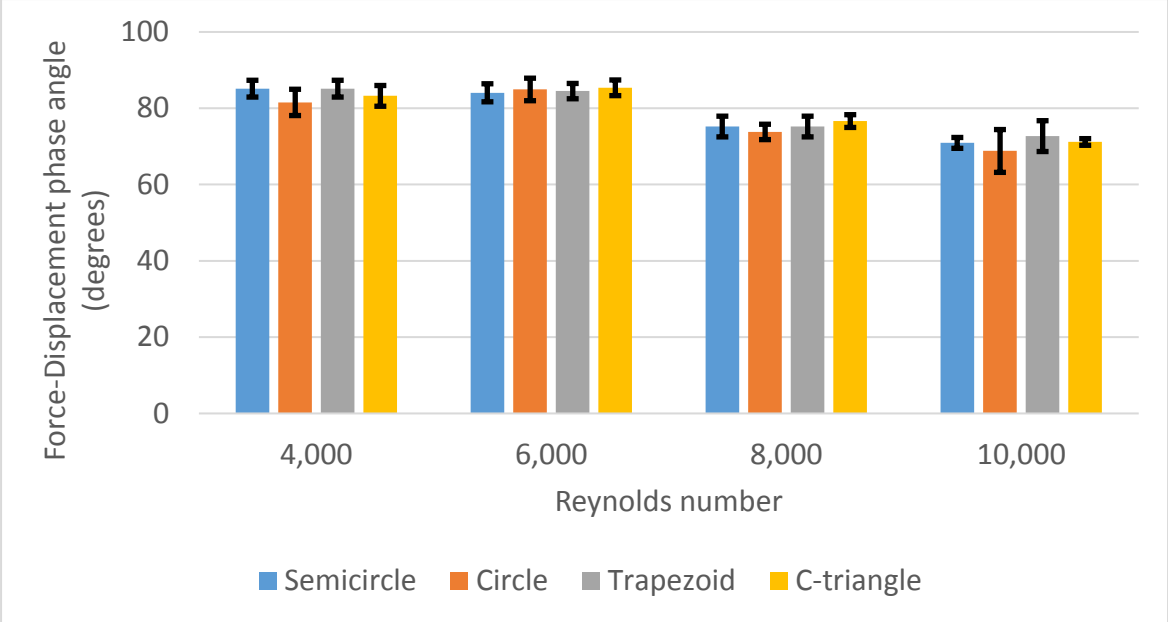

Figure 18 - Correlation of the average force-displacement phase angles and Reynolds number for the different upstream cross-sections used in this project. The standard deviation between the tests cases for each cross-section and Reynolds number is indicated by the error bars.

3.4 WIV power coefficient

The WIV power coefficient was calculated using Equation (9) and the results for each cross-section are shown in Figures 19 – 22 for the circular, semicircular, trapezoidal and c-triangular cylinders. The contours represent the variation of the power coefficient with varying streamwise (x/D) and transverse (y/D) separation from the upstream cylinder, which corresponds to the different test cases. Each individual plot also has subplots corresponding to the Reynolds number.

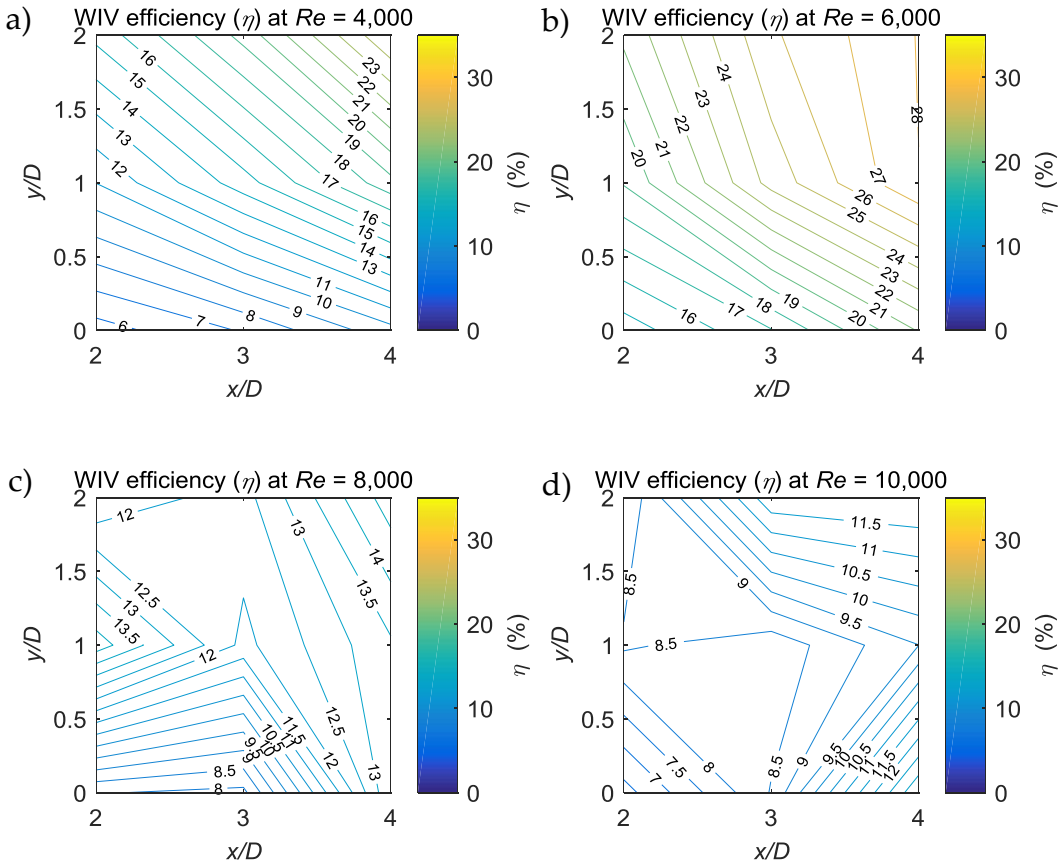

Figure 19 - Power coefficient distribution for the circular cylinder

From Figures 19 - 22, it is observed that the power coefficient increases with increasing streamwise and transverse separations. The maximum power coefficients occur at a Reynolds number of 6,000 and when the downstream cylinder is placed between $3 \leq x/D \leq 4$ and $1 \leq y/D \leq 2$ in the wake of the upstream cylinder. This arrangement gives the highest force-displacement phase angles (closest to 90 degrees) and hence the highest power coefficient calculated using Equation (9).

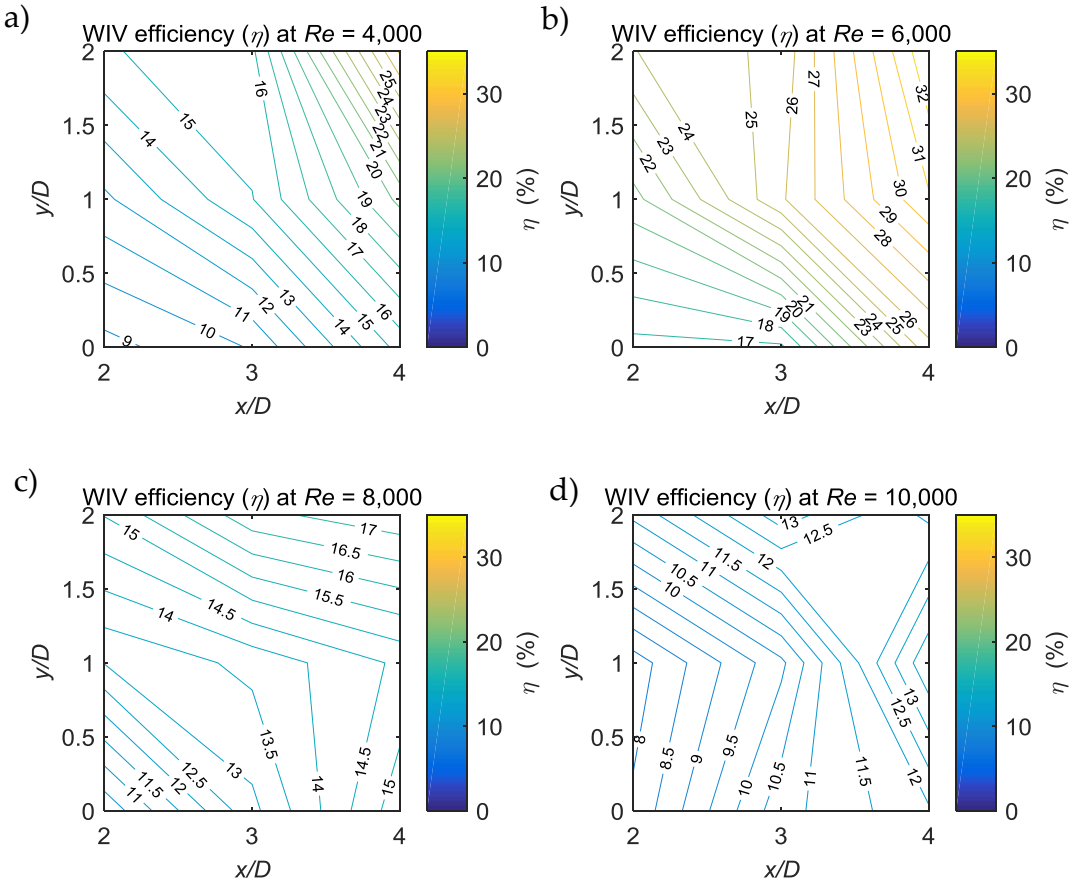

Figure 20 - Power coefficient distribution for the semi-circular cylinder

A comparison of the highest power coefficients occurring for each cross-section is depicted in Figure 23. All the cross-sections have the maximum occurring at Re = 6,000. The bar chart in Figure 23 also has the case number which corresponds to the maximum power coefficient. All cross-sections have a maximum power coefficient for case 9 (x/D = 4, y/D = 2). The magnitude of the maximum power coefficient for the semicircular cylinder was 33%, which was 5% higher than the circular cylinder, and the maximum for the trapezoidal and convex-edged triangular cylinders was 6 % lower than the circular cylinder.

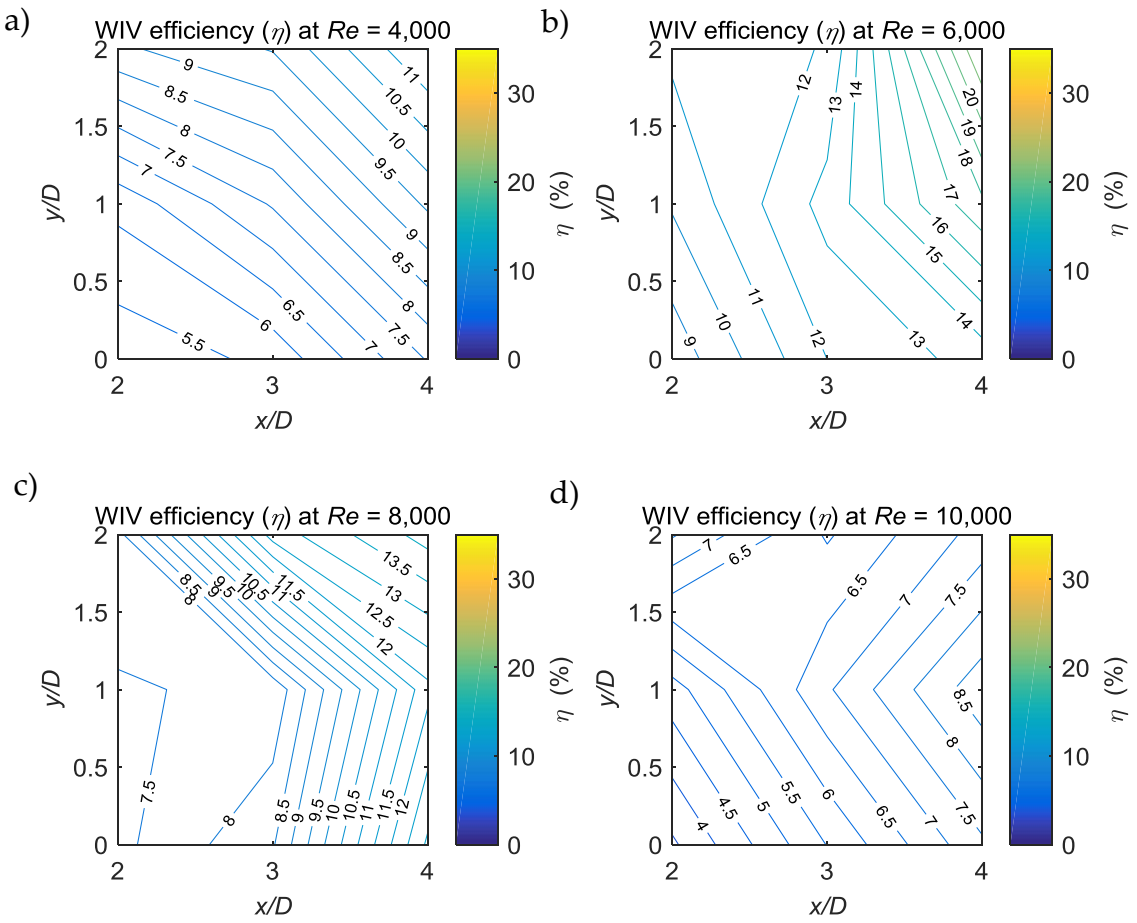

Figure 21 - Power coefficient distribution for the trapezoidal cylinder

The variation of the power coefficient is highly dependent on the force-displacement phase angles. The phase angle between the force and displacement influences the fluid force transfer during the cycle of oscillation and small changes in the phase attribute to significant changes in the power coefficient.

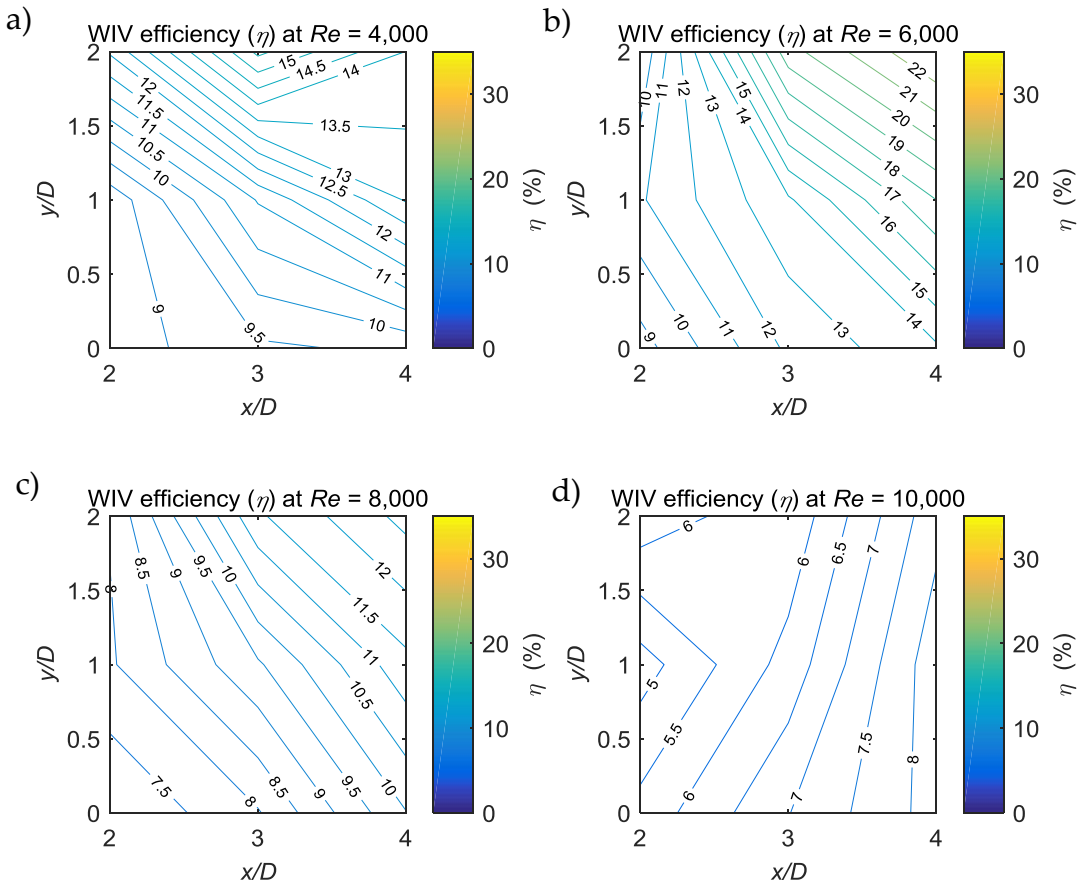

Figure 22 - Power coefficient distribution for the c-triangular cylinder

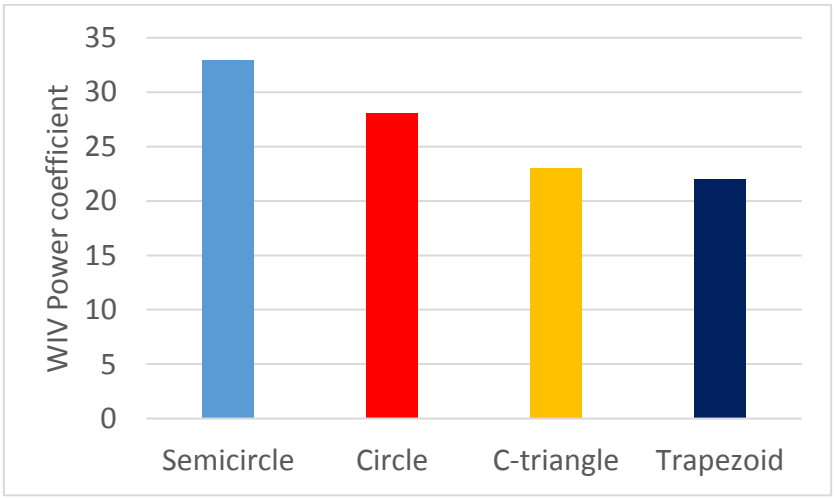

Figure 23 - Comparison of the maximum WIV power coefficient obtained for the upstream bluff body cross-sections at Re = 6,000. The maximum efficiencies occur for case 9, where x/D = 4 and y/D = 2.

3.5 Discussion

The highest amplitudes of vibration, lift coefficient, phase angle and power coefficient for all investigated cross-sections occurred at *Re* = 6,000. This was attributed to the fact that this is the lock-in range for VIV for the downstream cylinder and hence there is a combined upper branch VIV and WIV response. Hence the high amplitude vibration response of VIV is further augmented by the wake from the upstream cylinder.

The semicircular cylinder provided higher fluid forces in the wake, and hence more temporal energy to the downstream cylinder. This resulted in higher amplitudes of vibration as well as a higher power coefficient for the WIV system compared to the other cross-sections investigated. The phase angles at *Re* = 6,000 are very similar for the circular and semi-circular cylinders (less than 2% difference), as shown in Figure 18. However, the semicircular cylinder has higher phase angles than the circular cylinder for the other Reynolds numbers investigated, which results in higher power coefficient. Hence, the semi-circular cylinder would be an improvement to the circular cylinder for use in a WIV system as the upstream body.

A previous investigation by the authors resulted in identifying the semicircular and convex-edged triangular cylinders as higher temporal wake energy concentrators compared to the circular cylinder (Manickam Sureshkumar *et al.* [under review]). However, despite the energy concentration what can be achieved with some cross-sections, in the current study only the semicircular cylinder caused augmentation of the power coefficient. The difference in vibration responses observed was attributed to the frequency matching between the upstream and downstream cylinders. The semicircular cylinder has shedding

frequencies which are similar the circular cylinder, due to the separation points being comparable for the transition in shear layer regime. Hence the larger concentration of temporal energy is properly utilised by the WIV system. The c-triangular cylinder has shedding frequencies that are higher than the circle and hence would need the structural parameters to be tuned to the frequencies observed in the wake to obtain higher efficiencies. Since this study aimed to compare the shapes whilst keeping all other system parameters identical, the c-triangular cylinder did not improve the chosen WIV system. However, this finding suggests that frequency matching is an important factor to consider in WIV systems such that the upstream and downstream cylinder produce vortex streets at similar frequencies, to facilitate efficient energy transfer from the wake of the upstream body to the vortex street of the downstream body.

4 Conclusions

The effects of upstream bluff body cross section on a WIV system was investigated in this study. Four cross-sections of the upstream cylinder were investigated for different staggered arrangements of the cylinders and for a range of Reynolds numbers, and the power coefficient of WIV is reported along with associated parameters of the WIV response. The four bluff body cross-sections used were: circle, semicircle, trapezoid and convex-edged triangular of the same characteristic diameter. A Virtual Mass-Spring-Damper (VMSD) system controlled using a real-time control system was utilised to model the WIV response of the cylinder. The water channel experiments resulted in measurements of the lift force and cylinder position (vibration displacement), which were analysed to develop the following outcomes:

1. A semicircular cross-section cylinder placed as the first body in a WIV system provides a higher power coefficient (33%) compared to the circular cylinder (28%) at a Reynolds number of 6,000. Both the circular and semi-circular cylinder produce are most efficient as upstream bodies when the downstream circular cylinder is at a staggered arrangement of $x/D = 4$ and $y/D = 2$. A semi-circular cylinder provides increased temporal energy at a similar frequency to the shedding frequency of the circular cylinder and hence provides a more efficient WIV system. The flat aft-face of the semi-circular cylinder forms vortices with more circulation than the circular cylinder and hence carry more temporal energy into the wake to be used by the downstream cylinder;
2. Temporal concentration of energy is the same for the semi-circular and convex-edged triangular cylinders. However, for the geometries considered the convex-edged triangular does not provide an increased WIV response alike the semicircle due to the difference in frequency of the shed vortices, which are not tuned to the natural frequencies of the WIV system. Hence, frequency matching in the WIV system is important in order to make use of increased temporal energy by the upstream body;
3. The lift coefficient is mostly dependant on the Reynolds number and less dependent on the position of the downstream vibrating bluff body, as it is mostly influenced by the freestream velocity;
4. A higher Reynolds number causes a greater range of phase angles in test cases for the circular and trapezoidal cylinders compared to lower Reynolds numbers. This effect was absent in the semicircular and c-triangular cylinders due to their flat aft faces. Hence a larger back pressure on the upstream cylinder can reduce

the variation of the phase angles imposed on the downstream cylinder;

5. The maximum efficiency for all upstream cross-sections occurs at a Reynolds number of 6,000 due to the system operating at its natural frequency, and hence a combination of VIV and WIV response occurs at this Reynolds number;
6. The vibration amplitude continues to increase with increasing Reynolds number for all the cross-sections and cases considered, which is definitive of the WIV response;
7. The location of the maximum efficiency is similar between all the shapes and occurs between $x/D = 3 – 4$ and $y/D = 1 – 2$ (staggered arrangement). The phase angle between the lift force and vibration is also closest to 90 degrees for this location, which results in more efficient transfer of force to displacement.

References

Assi, GRS 2009, 'Mechanisms for flow-induced vibration of interfering bluff bodies', Ph.D thesis, Imperial College London.

Bearman, PW 1984, 'Vortex shedding from oscillating bluff bodies', *Annual Review of Fluid Mechanics*, vol. 16, no. 1, pp. 195-222.

Bearman, PW, Graham, J, Naylor, P & Obasaju, E 1981, 'The role of vortices in oscillatory flow about bluff cylinders', in *International Symposium on Hydrodynamics in Ocean Engineering*, pp. 621-35.

Bernitsas, MM, Ben-Simon, Y, Raghavan, K & Garcia, EM 2009, 'The VIVACE converter: model tests at high damping and Reynolds number around 105', *Journal of Offshore Mechanics and Arctic Engineering*, vol. 131, no. 1, pp. 1 - 15.

Bernitsas, MM & Raghavan, K 2004, 'Converter of current/tide/wave energy', *Provisional Patent Application, US Patent and Trademark Office Serial*, no. 60/628,252.

Bernitsas, MM, Raghavan, K, Ben-Simon, Y & Garcia, EM 2008, 'VIVACE (vortex induced vibration aquatic clean energy): A new concept in generation of clean and renewable energy from fluid flow', *Journal of Offshore Mechanics and Arctic Engineering*, vol. 130, no. 4, pp. 1697–712.

Blevins, RD 1997, *Flow-induced vibration*, Second edn, Van Nostrand Reinhold, New York

Brika, D & Laneville, A 1999, 'The flow interaction between a stationary cylinder and a downstream flexible cylinder', *Journal of Fluids and Structures*, vol. 13, no. 5, pp. 579-606.

Derakhshandeh, JF, Arjomandi, M, Cazzolato, B & Dally, B 2014, 'Experimental and computational investigation of wake induced

vibration', paper presented to 19th Australasian Fluid Mechanics Conference, Melbourne, Australia, 8 - 11 December 2014.

Derakhshandeh, JF, Arjomandi, M, Dally, B & Cazzolato, B 2015a, 'Harnessing Hydro-Kinetic energy from wake induced vibration using virtual mass spring damper system', *Journal of Ocean Engineering*, vol. 108, pp. 115-28.

Derakhshandeh, JF, Arjomandi, M, Dally, B & Cazzolato, B 2015b, 'A study of the Vortex-Induced Vibration mechanism for harnessing hydrokinetic energy of eddies using a single cylinder', *Journal of Applied Mathematical Modelling*.

Derakhshandeh, JF, Arjomandi, M, Dally, B & Cazzolato, B 2016, 'Flow-induced vibration of an elastically mounted airfoil under the influence of the wake of a circular cylinder', *Experimental thermal and fluid science*, vol. 74, pp. 58-72.

Ding, L, Zhang, L, Wu, C, Mao, X & Jiang, D 2015, 'Flow induced motion and energy harvesting of bluff bodies with different cross sections', *Energy Conversion and Management*, vol. 91, pp. 416-26.

Govardhan, R & Williamson, CHK 2000, 'Modes of vortex formation and frequency response of a freely vibrating cylinder', *Journal of Fluid Mechanics*, vol. 420, pp. 85-130.

Govardhan, R & Williamson, CHK 2004, 'Critical mass in vortex-induced vibration of a cylinder', *European Journal of Mechanics-B/Fluids*, vol. 23, no. 1, pp. 17-27.

Hobbs, WB & Hu, DL 2012, 'Tree-inspired piezoelectric energy harvesting', *Journal of Fluids and Structures*, vol. 28, pp. 103-14.

Hover, F, Miller, S & Triantafyllou, M 1997, 'Vortex-induced vibration of marine cables: experiments using force feedback', *Journal of Fluids and Structures*, vol. 11, no. 3, pp. 307-26.

Igarashi, T 1981, 'Characteristics of the flow around two circular cylinders arranged in tandem: 1st report', *Bulletin of JSME*, vol. 24, no. 188, pp. 323-31.

Jamieson, PM 2009, 'Beating Betz: Energy Extraction Limits in a Constrained Flow Field', *Journal of Solar Energy Engineering*, vol. 131, no. 3, p. 031008.

Khan, M, Bhuyan, G, Iqbal, M & Quaicoe, J 2009, 'Hydrokinetic energy conversion systems and assessment of horizontal and vertical axis turbines for river and tidal applications: A technology status review', *Applied Energy*, vol. 86, no. 10, pp. 1823-35.

Lee, J, Xiros, N & Bernitsas, M 2011, 'Virtual damper–spring system for VIV experiments and hydrokinetic energy conversion', *Ocean Engineering*, vol. 38, no. 5-6, pp. 732-47.

Manickam Sureshkumar, E, Arjomandi, M, Cazzolato, B & Dally, B [under review], 'Spatial and temporal concentration of hydrokinetic energy in the wake of a bluff body', *Ocean Engineering*.

Sarpkaya, T 2004, 'A critical review of the intrinsic nature of vortex-induced vibrations', *Journal of Fluids and Structures*, vol. 19, no. 4, pp. 389-447.

Vries, O 1983, 'On the theory of the horizontal-axis wind turbine', *Annual Review of Fluid Mechanics*, vol. 15, no. 1, pp. 77-96.

Wang, D-A & Ko, H-H 2010, 'Piezoelectric energy harvesting from flow-induced vibration', *Journal of Micromechanics and Microengineering*, vol. 20, no. 2, p. 025019.

Weinstein, LA, Cacan, MR, So, PM & Wright, PK 2012, 'Vortex shedding induced energy harvesting from piezoelectric materials in heating, ventilation and air conditioning flows', *Smart Materials and Structures*, vol. 21, no. 4, p. 045003.

Williamson, CHK & Govardhan, R 2004, 'Vortex-induced vibrations', *Annual Review of Fluid Mechanics*, vol. 36, pp. 413-55.

Yokuda, S & Ramaprian, B 1990, 'The dynamics of flow around a cylinder at subcritical Reynolds numbers', *Physics of Fluids A: Fluid Dynamics (1989-1993)*, vol. 2, no. 5, pp. 784-91.

Zdravkovich, MM 1997, 'Flow around circular cylinders, vol. 1. Fundamentals', *Journal of Fluid Mechanics*, vol. 350, pp. 377-8.

Chapter 6. Effect of mass and damping ratio

The complex phenomenon of WIV is not only affected by fluidic parameters, but also by structural parameters such as mass and damping ratio. The fluidic parameters were investigated in Chapter 5 to realise that a semi-circular cylinder as the upstream and stationary body in a staggered arrangement provides efficient vibrations in a WIV system. The structural parameters define the impedance of the system and hence are important when considering the efficiency of WIV energy technology.

This chapter investigates the effect of the mass and damping ratio (structural parameters) on the efficiency of vibration of a downstream circular cylinder. The mass and damping ratios are effortlessly varied using the VMSD system, which controls the movement of the downstream cylinder. The experiments were performed in a water channel and results such as the lift force and displacement of the cylinder were recorded and analysed to identify the optimum impedances for such a system. The results from this chapter are beneficial to identifying the effect of impedance on the chosen WIV system. A lower damping ratio was found to be beneficial to WIV whilst a mass ratio between 2 and 3 can result in efficient vibrations.

This chapter has been submitted for publication as:

Manickam Sureshkumar, E, Arjomandi, M, Dally, B.B, Cazzolato, B.S, Ghayesh, M.H, 'Effect of mass and damping ratio on a circular cylinder vibrating in the wake of a semi-circular cylinder', (under review).

Statement of Authorship

Title of Paper	Effect of mass and damping ratio on a circular cylinder vibrating in the wake of a semi-circular cylinder
Publication Status	☐ Published ☐ Accepted for Publication ☑ Submitted for Publication ☐ Unpublished and Unsubmitted w ork w ritten in manuscript style
Publication Details	Manickam Sureshkumar, E, Arjomandi, M, Dally, B, Cazzolato, B, Ghayesh, M, 'Effect of mass and damping ratio on a circular cylinder vibrating in the wake of a semi-circular cylinder', *Journal of Fluids and Structures*, (under review)

Principal Author

Name of Principal Author (Candidate)	Eshodarar Manickam Sureshkumar		
Contribution to the Paper	Water channel experiments utilising a stationary upstream cylinder and a transversely vibrating downstream circular cylinder. The upstream cylinder geometry, Reynolds number and separation gap between the cylinders was varied and the efficiency of vibration was computed.		
Overall percentage (%)	85		
Certification:	This paper reports on original research I conducted during the period of my Higher Degree by Research candidature and is not subject to any obligations or contractual agreements with a third party that would constrain its inclusion in this thesis. I am the primary author of this paper.		
Signature		Date	22/06/2018

Co-Author Contributions

By signing the Statement of Authorship, each author certifies that:

i. the candidate's stated contribution to the publication is accurate (as detailed above);
ii. permission is granted for the candidate in include the publication in the thesis; and
iii. the sum of all co-author contributions is equal to 100% less the candidate's stated contribution.

Name of Co-Author	Maziar Arjomandi		
Contribution to the Paper	Supervised the work, assisted in developing ideas and manuscript evaluation		
Signature		Date	22/06/2018
Name of Co-Author	Bassam B. Dally		
Contribution to the Paper	Supervised the work, assisted in developing ideas and manuscript evaluation		
Signature		Date	25/06/2018
Name of Co-Author	Benjamin S. Cazzolato		
Contribution to the Paper	Supervised the work, assisted in developing ideas and manuscript evaluation		
Signature		Date	22/6/18
Name of Co-Author	Mergen H. Ghayesh		
Contribution to the Paper	Supervised the work, assisted in developing ideas and manuscript evaluation		
Signature		Date	22/06/2018

Manuscript

Title - Effect of mass and damping ratio on a circular cylinder vibrating in the wake of a semi-circular cylinder

Authors – Eshodarar Manickam Sureshkumar (Corresponding Author), Maziar Arjomandi, Bassam B. Dally, Benjamin S. Cazzolato, Mergen H. Ghayesh

Affiliation – The University of Adelaide

Address – School of Mechanical Engineering, The University of Adelaide, North Terrace, Adelaide, SA, 5005

Abstract

This paper investigates the wake induced vibration of a circular cylinder constrained to vibrate transversely in the wake of a semicircular cylinder. Structural parameters such as mass and damping ratio affect the impedance of the WIV system and hence the vibration response. To achieve maximum efficiency in harvesting vibration energy the separation gap is maintained constant at a streamwise separation of 4 diameters ($x = 4D$) and a transverse separation of $2D$. The investigations were performed for Reynolds numbers of 4,000, 6,000 and 8,000 in a closed loop water channel for mass ratios varied between 2 and 5 and damping ratios varied between 0.001 and 0.1. The mass and damping ratio of the vibrating cylinder were varied using a Virtual Mass-Spring-Damper (VMSD) system connected to the vibrating downstream cylinder. The results indicate that a smaller damping ratio, $O(0.001)$, increases the amplitude and efficiency of vibration, whilst a mass ratio between 2 and 3 gives high efficiencies of WIV for all the damping ratios used.

Highlights: WIV, Fluid structure interaction, mass and damping ratio, renewable energy technology, hydrokinetic energy, efficiency of vibration

1 Introduction

Wake induced vibration (WIV) is a form of flow induced vibration (FIV) of bodies, which is capable of harnessing clean renewable hydrokinetic flow energy. Arising from research on vortex-induced vibration (VIV) for energy harnessing, recent focus has been put on WIV energy harnessing due to higher system efficiencies observed in WIV when compared to VIV under the same flow and structural conditions.

The mechanism behind WIV is not the same as for VIV. The VIV response of bluff bodies occurs only for a specific range of frequencies, where the frequency of shed vortices is similar to the natural frequency of the supporting structure. Contrastingly, two cylinders in tandem produce a WIV response, which is a result of the unsteady vortex-structure interactions between the downstream cylinder and the wake of the upstream cylinder.

Both VIV and WIV responses of a cylinder are governed by several structural and fluidic parameters such as the Reynolds number, Strouhal number, reduced velocity, mass ratio and damping ratio, which are defined in Table 1.

Table 1 – Non-dimensional structural and fluidic parameters that govern VIV and WIV

Reynolds number	Re	$\rho UD/\mu$
Strouhal number	St	fD/u
Reduced velocity	V_r	u/fD
Mass ratio	m^*	$4m/\rho\pi D^2 L$
Damping ratio	ζ	$c/2\sqrt{km}$

In Table 1, D is the hydrodynamic diameter of the cylinder, m is the mass of the vibrating cylinder, ρ is the density of the fluid, U is the freestream

velocity, f is the frequency of vortex shedding, L is the length of the cylinder, k is the spring constant and c is the damping constant.

VIV and WIV have been applied to harness flow energy by using technology such as the Vortex Induced Vibration for Aquatic Clean Energy (VIVACE) project (Bernitsas *et al.* 2008). Pioneering work by Bernitsas *et al.* (2008), resulted in an early large-scale VIV device, employing a circular cylinder, to produce energy from low speed flows. Small-scale devices, such as those used for remote monitoring in ventilation and air conditioning systems, can use WIV to produce the minuscule amounts of energy needed for them to operate and hence make monitoring easier and viable at remote locations (Hobbs & Hu 2012; Wang & Ko 2010; Weinstein *et al.* 2012).

The main difference between VIV and WIV is that the latter needs a body vibrating in the wake produced from an upstream bluff body, which is usually kept stationary (Assi 2009). The wake produced from the upstream stationary bluff body affects the forces on the downstream vibrating body, causing the WIV response. WIV is of interest for energy production, due to the amplitude response not being limited to a lock-in range of velocities as in VIV (Assi 2009; Derakhshandeh, Arjomandi, Cazzolato, *et al.* 2014) and the efficiency of WIV systems are higher than VIV systems (Derakhshandeh, Arjomandi, Cazzolato, *et al.* 2014; Derakhshandeh *et al.* 2015a). Transverse vibration amplitudes of cylinders undergoing FIV, are about three times greater than the streamwise amplitudes, and hence are of more useful for energy generation (Bernitsas *et al.* 2008; Hobbs & Hu 2012; Wang & Ko 2010).

A multitude of research exists on the effect of Reynolds number and reduced velocity on VIV and WIV (Anagnostopoulos & Bearman 1992; Assi 2009; Assi *et al.* 2006; Bearman 2011; Carmo *et al.* 2011;

Derakhshandeh, Arjomandi, Cazzolato, *et al.* 2014; Derakhshandeh, Arjomandi, Dally, *et al.* 2014; Derakhshandeh *et al.* 2015b; Ding *et al.* 2015; Sarpkaya 1979; Sarpkaya 2004; Williamson & Govardhan 2004b; Zdravkovich & Bearman 1998). The effect of structural parameters such as the mass and damping ratio have also been investigated for VIV in past studies, but very little investigation has been performed on the effect of mass and damping ratio on WIV.

WIV or VIV with two cylinders is also dependent on the separation gap between the cylinders, which affects the vortex streets formed by both cylinders (Igarashi 1981). Brika and Laneville (1999) measured the displacement of an elastically mounted circular cylinder operating in the wake of a stationary circular cylinder for Reynolds numbers (Re) between 5,000 and 27,000 at inline separations of 7 to 25 cylinder diameters (D), where the smaller separation gaps caused larger displacements in the downstream cylinder. A similar water channel study of WIV conducted by Assi (2009) reported that the amplitude of vibration of the downstream cylinder at low reduced velocities ($U_r \leq 5$) is independent of the streamwise separation gap ($4D$ to $20D$). However, an increase in separation gap from $4D$ to $20D$ at higher reduced velocities ($U_r > 5$) caused a reduced displacement in the vibration response. In an investigation of WIV Derakhshandeh *et al.* (2015a) showed the effect of staggered arrangements on a system of two circular cylinders for Re = 2,000 to 15,000 for streamwise separations of $2.5D$ to $5D$ and transverse gaps of $0D$ to $3D$, where maximum amplitude vibrations were obtained for a streamwise gap of $3.5D$ to $4.5D$ and a transverse gap of $1D$ to $2D$. This recommendation for a staggered arrangement of cylinders was utilized in this study to attain significant vibrations. The phase lag between the lift force imposed on the cylinder

and the oscillation response is also an important factor to consider in harnessing efficient energy using WIV, as the work done by the cylinder is the product of the force and displacement of the cylinder (Bernitsas *et al.* 2008) and needs to be investigated in WIV efficiency studies (Derakhshandeh *et al.* 2015a).

The product of the mass and damping ratio ($m^*\zeta$) is inversely proportional to the amplitude response of a cylinder undergoing VIV (Bearman 1984). The acceleration of the cylinder in the fluid is governed by the mass of the cylinder and mass of the fluid which is displaced. Hence the mass ratio ($m*$) affects the frequency of oscillation of the cylinder, as evidenced by the differences in oscillation frequencies for VIV of a cylinder vibrating in air and water, due to the different densities of the fluids. Hence, most research on VIV and WIV is focused on low mass and damping ratios to attain large displacements.

A water channel investigation of both the mass (m^*) and damping ratio (ζ) for VIV was conducted by Khalak and Williamson (1997). The product of mass and damping ratios ($m^*\zeta$) was varied from 0.006 to 0.030, whilst individual mass ratios used were m^* = 2.4, 10.3 and 20.6. The amplitude of vibration was reported to increase with reducing mass ratios. A numerical investigation by Bahmani and Akbari (2010) at low Reynolds numbers (80 to 160) in the laminar flow regime further confirmed an increase in oscillation amplitude, as well as the synchronization range for the upper and lower branches of VIV, when either the mass or the damping ratio of the system was reduced. However, the authors reported that the mass ratio had a more profound effect on the vibration response compared to the damping ratio.

Investigations by Govardhan and Williamson (2000) regarding VIV of a circular cylinder confirmed the inversely proportional

relationship between $m^*\zeta$ and the vibration amplitude of the cylinder. Accompanying this finding, Govardhan and Williamson (2000) also concluded that the synchronization band of Reynolds numbers or reduced velocity was primarily dependent on the mass ratio, where lower m^* results in a larger band of synchronisation when the product $m^*\zeta$ was constant (Figure 1). They also reported the existence of the 'upper branch' of VIV with high amplitude vibrations existing for low $m^*\zeta$ (order of 1), whilst higher mass damping ratios only had the 'initial' branch and 'lower' branch of VIV.

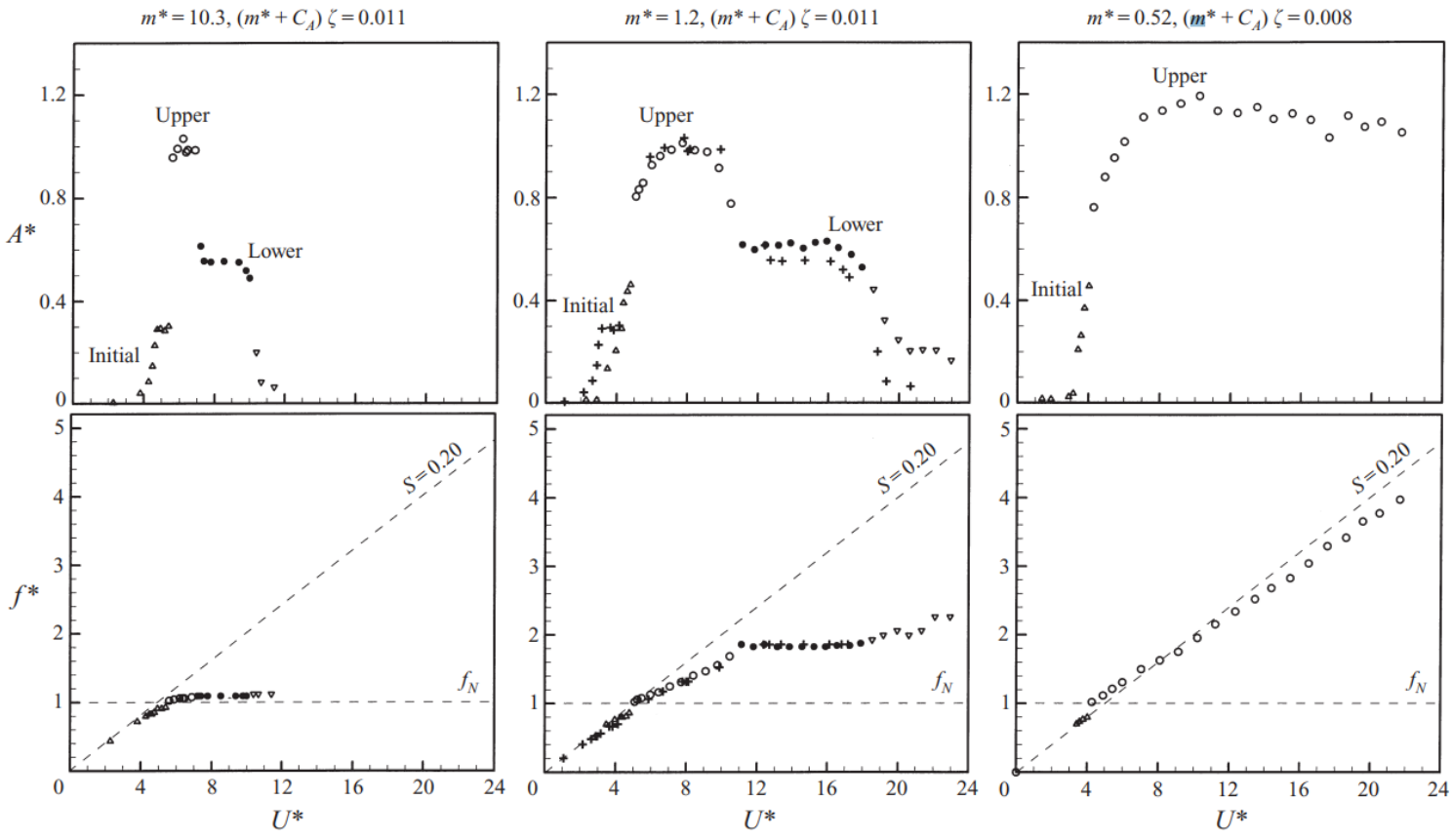

Figure 1 - Pairs of amplitude-frequency plots of a single cylinder VIV system for decreasing mass ratio (m) plot to the same scale (Govardhan & Williamson 2000)*

The oscillation frequency for single cylinder VIV is primarily dependent on the mass ratio. At large mass ratios (order of 100), the vibration frequency for synchronization lies close to the natural

frequency, whilst lower mass ratios (order of 1) can result in vibration frequencies that are higher than the natural frequency (Figure 1). The highest mass ratio at which this high frequency vibration occurs is defined as the critical mass ratio. Williamson and Govardhan (2004a) performed a study on the effect of mass ratio on VIV and reported a critical mass ratio of 0.54 below which large amplitude vibrations occur at high frequencies (higher harmonics of the natural frequency). Amplitudes of 0.8D were reported at mass ratios (0.45) below the critical mass ratio when no springs were attached to the cylinder (i.e. no structurally restoring force). However, such conditions are not feasible in real life situations where a power-take-off unit is connected to the cylinder for energy extraction. Additionally, high frequency vibrations can be chaotic in nature and need to be investigated further for their feasibility in energy harnessing.

Blevins and Coughran (2009) reported a precise relationship between the VIV response and changes of parameters such as mass ratio, damping coefficient and Reynolds number. Their tests were performed for mass ratios of 1.77 to 19.30, damping ratios of 0.002 to 0.4, and Reynolds numbers of 170 to 15,000 which corresponded to a reduced velocity of 2 to 12. For transversely limited vibration, increasing the damping ratio from 0.002 to 0.02 decreased the amplitude of vibration by 15% whereas further increase in damping ratio by a factor of 10 (0.02 to 0.2) decreased the amplitude by 90%. The maximum vibration amplitude was nearly identical when the mass and damping ratios were individually varied, but the product of mass and damping was maintained constant. Hence, damping ratios less than $O(0.01)$ are of more use in VIV for energy harnessing.

Lee and Bernitsas (2011) investigated the effect of the damping ratio on the VIVACE convertor. Water channel tests were performed at high Reynolds numbers between 40,000 and 120,000, where the damping ratio was varied between 0 and 0.16. The authors reported that increasing damping ratio reduced the amplitude response of the cylinder as well as the synchronization range for VIV. However, the authors' primary focus was on sustaining high amplitude vibration at high damping ratios, since a power-take-off (PTO) unit in real world scenarios is likely to have high damping. The authors performed the tests at a range of high spring stiffness (400 to 1,800N/m) and found that at a high damping ratio, high amplitude vibrations can be sustained so long as the system has a high spring stiffness as well.

It has been established that WIV of a body is defined by the structural and fluidic parameters imposed on it. There is abundant research on the fluidic parameters and as such, this paper aims to progress the current state-of-art by investigating the effect of the mass ratio and damping ratio on the body operating in a WIV system. Investigations on the mass and damping ratio have been primarily focused for single cylinder VIV systems and little attention has been given to two-cylinder systems, particularly systems with a stationary upstream cylinder and a downstream cylinder free to move in a single degree of freedom. This study focuses on the effect of mass and damping ratio on a staggered two-cylinder WIV system with a circular downstream cylinder which is separated from a semi-circular upstream cylinder by a streamwise gap of 4D and a transverse gap of 1D. This geometry arrangement was chosen as it proved to be the more efficient compared to a circular-circular cylinder WIV system in a previous investigation by the authors (Manickam Sureshkumar *et al.* 2). The mass and damping ratio are

varied according to values obtained from literature to observe the effects on the vibration of the downstream cylinder, particularly on the displacement and the lift forces. The data obtained from the tests were processed to obtain the vibration characteristics and vibration efficiencies which are reported in this paper for three Reynolds numbers of 4,000, 6,000 and 8,000.

2 Methodology

The experimental apparatus and techniques utilized for the WIV tests are outlined in the following sub-subsections.

2.1 Water channel experiments

The experiments were performed in a re-circulating water channel at the University of Adelaide. The test section measured 2000 mm (length) x 600 mm (depth) x 500 mm (width) and had a water depth of 500 mm. A schematic representation of the WIV system with a stationary semi-circular upstream cylinder and a single degree-of-freedom (DOF) downstream circular cylinder is depicted in Figure 2. The downstream body is constrained to only be able to move transversely to the oncoming flow. Both the upstream and downstream cylinders have a hydraulic diameter of 30mm and a wetted length of 400mm. The investigated streamwise (x) and transverse (y) separation was based on the most efficient wake position identified in previous WIV energy harnessing investigations (Derakhshandeh *et al.* 2015a, 2016) and allowed the downstream cylinder to be in the wake interference region of the upstream bluff body. The blockage caused by the upstream cylinder was 7% which is similar to previous investigations and deemed negligible for the current study (Assi 2009; Derakhshandeh *et al.* 2015a). A maximum velocity of 0.335 m/s was

achievable in the water channel, and thus the Reynolds number (*Re*) was varied between 4,000 and 8,000. In these conditions the circular cylinder was in the transition-in-shear layer regime (Blevins 1997) which corresponds to a Strouhal number (*St*) of approximately 0.2. The natural frequency of the structure was matched to the shedding frequency at *Re* = 6,000 (*f* = 1.22 Hz) and this frequency was kept constant for all tests. Hence, the spring stiffness and damping coefficients were calculated using the fixed shedding frequency and the chosen mass and damping ratios.

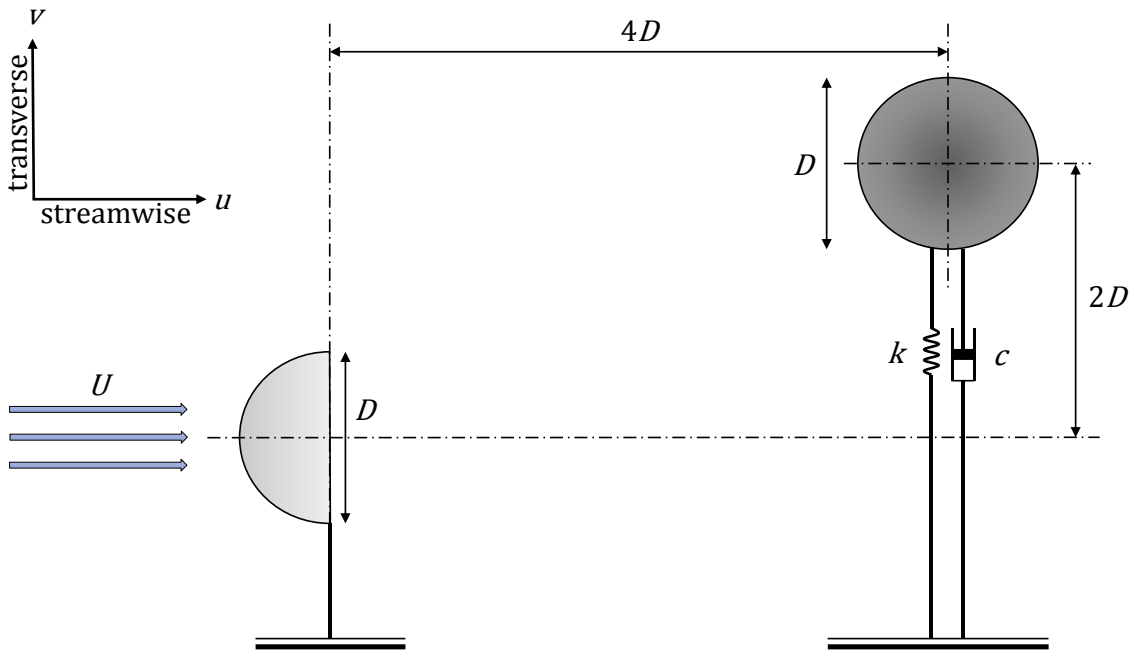

Figure 2 – Schematic representation of the WIV system consisting of a fixed upstream semicircular cylinder of diameter D and a transversely vibrating downstream circular cylinder of diameter D. k and c are the spring stiffness and damping coefficient, respectively and the downstream cylinder has a separation of 4D and 2D streamwise and transverse from the upstream cylinder, respectively.

2.2 Virtual Mass-Spring-Damper system (VMSD)

A VMSD system was used to impose virtual mass and damping ratios on the vibrating cylinder to provide the WIV response. This system was adjusted such to account for friction hence effectively

making it a frictionless system. A photograph of the VMSD system along with a schematic representation is shown in Figure 3. The VMSD system consists of two independent motors: motor 1 provides the required stiffness and damping in the system, and motor 2 varies the angle of attack of the downstream cylinder. However, only motor 1 was used in this investigation. The motors used in this system are Maxon EC-MAX 30 24V servo motors, which are controlled with Maxon ESCON 50/5 servo controllers. The motors have a planetary gearbox with 51:1 ratio, to provide greater movement resolution and torque in the system. An integral optical encoder is used to provide position feedback. Motor 1 is connected to the carriage ('Moving assembly' in Figure 3) via a pair of toothed pulleys and a toothed timing belt. One of the toothed pulleys is directly connected to the gearbox output of motor 1, whilst the other acts as an idler. The moving carriage supports motor 2 as well as the downstream cylinder and run on a pair of linear bearings. Further details are reported in (Derakhshandeh *et al.* 2015a).

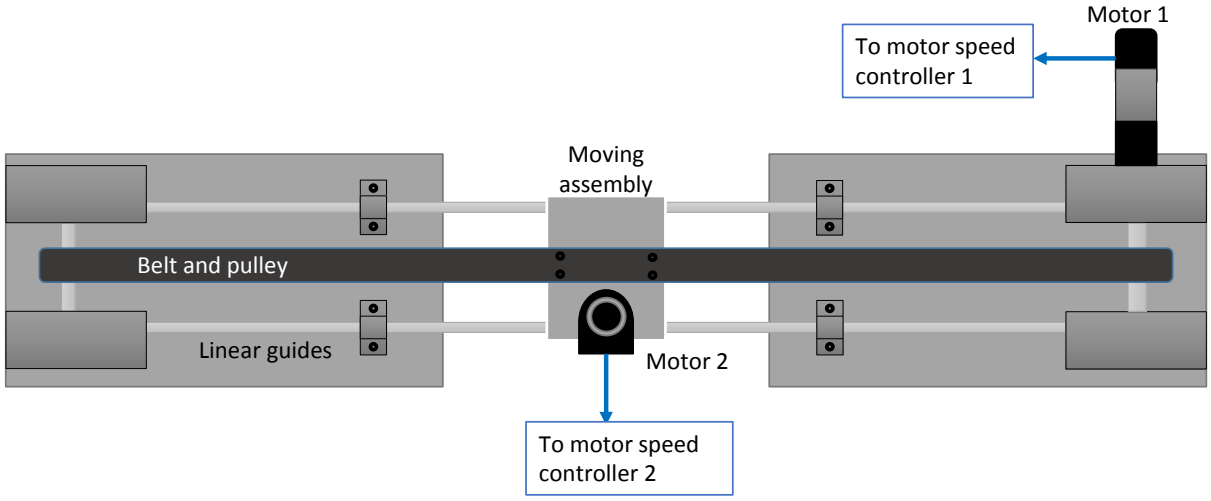

Figure 3 - The Virtual-Mass-Spring-Damper (VMSD) system used in this research

The lift and drag forces on the downstream cylinder, which act in orthogonal directions to the freestream flow, are measured using two pairs of strain gauges positioned in a half-bridge configuration. Using

the assumption of 2D flow, the lateral forces on the cylinder can be estimated by utilizing the moment at the root of the structure supporting the downstream cylinder.

The VMSD system was modelled in Simulink Matlab™. The Simulink control model was then compiled using the Real Time Workshop on to a dSPACE™ environment. A dSPACE DS1104 rapid prototyping board was used along with the Control Desk software to implement real time control. The input to the system was the analog voltage signal from the half-bridge corresponding to lift force, which was read using a 16-bit analog-to-digital convertor on the dSPACE board. Feedback was achieved by acquiring the position of the motor using the encoder on the motor. The output was an analog voltage sent from the digital-to-analog convertor on the dSPACE board, which controlled the servo controller and motor.

2.3 PID tuning

A PID controller was implemented to achieve accurate positioning of the vibrating cylinder, as governed by the Simulink model. The dedicated encoder input on the dSPACE prototyping board was used to provide feedback on the position of the cylinder for the PID controller. A gain coefficient was calculated using the dimensions of the system, as well as the ratio of the gearbox to convert the rotation of the motor shaft to the vibration of the cylinder, to accurately obtain feedback on the position of the vibrating cylinder from the encoder. An error input to the PID controller was possible using the computed and measured displacements of the downstream cylinder. The PID controller was manually optimized to provide displacement errors of less than 0.1 mm which was sufficient for the analysis in this research.

2.4 Variation of mass and damping ratios

The mass and damping ratio were varied in this study to observe the effect on the efficiency of WIV for the circular cylinder operating at a staggered arrangement behind a semicircular cylinder. The mass and damping ratios are virtually enforced on the system using the VMSD rig. The VMSD rig could only emulate mass ratios of higher than 2 as lower mass ratios resulted in vibrations that exceeded the amplitude and frequency restrictions of the VMSD system (Figure 4). Hence, the mass ratio was varied from 2 to 5 and the damping ratio was varied from 0.001 to 0.100. The effect of a broad range of damping ratios (0.001 to 0.1) was initially tested for two distinct mass ratios of 2.5 and 5.0 in Test 1. Following on from the initial tests on the effect of damping ratio, a finer assessment was performed using mass ratios between 2.0 and 4.0 and damping ratios between 0.005 and 0.025 to investigate the effect mass ratios on WIV. The details of the ratios used for each test are given in Table 2. For all the mass and damping ratios used, the natural frequency was maintained constant at 1.22 Hz and the required mass, spring stiffness and damping constants were calculated accordingly.

Table 2 – Mass and damping ratios used for experiments

	Mass ratios	Damping ratios
Test 1	2.5, 5.0	0.001, 0.005, 0.010, 0.050, 0.100
Test 2	2.0, 2.5, 3.0, 3.5, 4.0	0.005, 0.010, 0.015, 0.020, 0.025

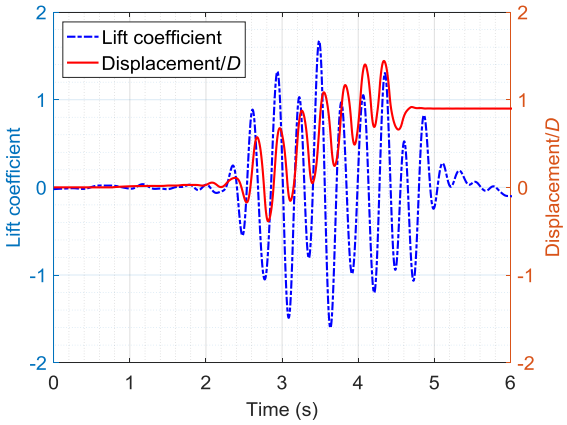

Figure 4 – Lift coefficient and normalised displacement for the downstream cylinder for a mass ratio of 1 and damping ratio of 0.01 using the VMSD system which exceeds the capabilities of the VMSD rig.

2.5 Mathematical modelling

An overview of the mathematical modelling is presented in this section. A detailed description of the model can be found in (Derakhshandeh *et al.* 2015a).

The vibration of a cylinder with a MSD system can be modelled using the following equation (Bearman 1984):

$$m\ddot{y}(t) + c\dot{y}(t) + ky(t) = F_y(t), \qquad (1)$$

where, y, $\dot{y}$ and $\ddot{y}$ are the transverse displacement, velocity and acceleration of the cylinder, respectively, c is the damping coefficient, k is the spring stiffness and m is the mass of the cylinder. $F_y(t)$ is the transverse fluid force exerted on the cylinder and is the sum of viscous and pressure forces on the cylinder.

$$F_y(t) = F_{viscous} + F_{pressure} \qquad (2)$$

Table 3 contains the non-dimensional parameters that govern the vibration response of the cylinder used in the experiments. Here, ρ is the fluid density, U is the freestream velocity, μ is the dynamic viscosity of water, D is the diameter of the downstream cylinder and L is the length of the cylinder.

Table 3 - Non-dimensional parameters.

Lift coefficient	C_{L}	$F_y/0.5\,\rho U^2 DL$
Amplitude ratio	Y^*	$y_{\max}/D$
Frequency ratio	f^*	f/f_n

Equations (3) and (4) define the time dependent displacement and lift coefficient of the downstream cylinder, respectively, assuming a harmonic response by the cylinder,

$$y(t) = y_{\max}\sin(2\pi f_{\mathrm{osc}}t), \tag{3}$$

$$c_{\mathrm{L}}(t) = C_{\mathrm{L}}\sin(2\pi f_{\mathrm{osc}}\,t + \Phi), \tag{4}$$

where $y_{\max}$ is the maximum displacement amplitude, assuming a harmonic response, and f_{osc} denotes the oscillation frequency in Equation (3). In Equation (4), c_{L} is the temporal lift coefficient, C_{L} is the magnitude of the lift coefficient and Φ is the phase difference between the driving lift force and resultant displacement of the cylinder, which affects the efficiency of the WIV response of the cylinder (Bernitsas *et al.* 2008).

The damped natural frequency, ω_{d}, of the cylinder can be approximated using Equation (5):

$$\omega_{\mathrm{d}} = \frac{2\pi}{T_{\mathrm{d}}} = \omega_{\mathrm{n}}\sqrt{1-\zeta^2} \approx \omega_{\mathrm{n}} = \sqrt{\frac{k}{m}} \tag{5}$$

where, T_{d} represents the damped period of oscillation.

The rotation of the shaft in the servo motor of the VMSD system is converted to the linear vibration of the downstream cylinder using the connected gearbox, pulleys and timing belt. Feedback to this system is via the angle measurements from the encoder connected to the motor.

The lift force on the cylinder is measured using the strain gauges attached to the cylinder. The force measurements are used to calculate the vibration response which is imposed on the cylinder using the torque created by the servo motor, whilst maintaining the desired spring stiffness and damping constant. The torque produced by the motor controls the velocity of the cylinder, whilst the forces caused by shed vortices are exerted on the cylinder. Thus, the work generated by the cylinder during one cycle of oscillation (T) can be calculated by integrating the inner product of the force and the instantaneous velocity of the cylinder, given by:

$$W_{\mathrm{WIV}} = \int_0^T F_y \dot{y} dt. \tag{6}$$

The average power is then given by

$$P_{\mathrm{WIV}} = \frac{W_{\mathrm{WIV}}}{T}. \tag{7}$$

The fluid power given by $P_{\mathrm{fluid}} = FU = (½)\rho U^3 DL$ (Bernitsas & Raghavan 2004), can be used to evaluate the power coefficient of the downstream cylinder.

$$\eta_{\mathrm{WIV}} = \frac{P_{\mathrm{WIV}}}{P_{\mathrm{fluid}}}. \tag{8}$$

Utilizing the equations above the power coefficient for WIV of the cylinder can be represented by the following:

$$\eta_{\mathrm{WIV}} = \frac{\pi C_{\mathrm{L}} f_{\mathrm{osc}} y_{\mathrm{max}} \sin(\Phi)}{U}. \tag{9}$$

3 Results and discussion

The collected force and displacement measurements were processed to evaluate the WIV response in terms of the normalized oscillation amplitude (normalized using the cylinder diameter), lift coefficient,

force-displacement phase angle and the WIV power coefficient. These results are reported and discussed below.

3.1 Variation of damping ratio from 0.001 to 0.100

The first tests were performed to investigate the effect of varying the damping ratio over two orders of magnitude. Tests performed for two mass ratios of 2.5 and 5.0 and the processed results are reported in Figures 4 to 6. An increase in damping ratio was accompanied by a reduction in the oscillation amplitude for both mass ratios tested and is depicted in Figure 5. This trend was reflected across all three Reynolds numbers, but the peak amplitude for any given mass and damping ratio increased with increasing Reynolds number, which is a characteristic of the WIV amplitude response. A larger damping ratio means that the cylinder loses more energy to move the same distance when compared to a case with a lower damping ratio. Since the damping ratio is a measure of the decay of the oscillations in a system, a higher damping ratio causes a larger rate of decay which reduces the overall amplitude attained by the cylinder.

The mass ratio of 2.5 provided higher amplitude vibrations when compared to a mass ratio of 5.0, confirming an inverse relationship between the mass ratio and the vibration amplitude for the WIV response. There was a higher reduction in amplitude when the damping ratio increased from 0.010 to 0.100 (~90% for $m^* = 2.5$) than when it increased from 0.001 to 0.010 (~20% for $m^* = 2.5$) with amplitudes beyond a damping ratio of 0.05 being very low ($< 0.3D$). It was decided that high damping ratios are not very useful for energy harnessing applications and hence Test 2 was only performed for damping ratios less than 0.025. A lower mass ratio corresponds to a lower mass of the oscillating body compared to the mass of fluid displaced by the cylinder. Hence, a lower

mass ratio results in larger displacements, as the force from the fluid can move the lighter masses a larger distance as compared to a higher mass ratio.

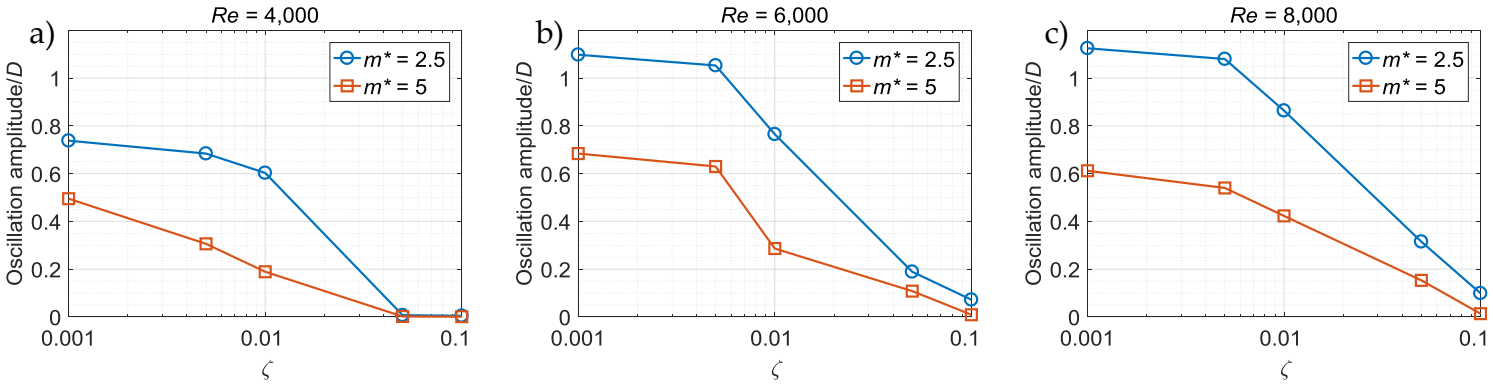

Figure 5 - Normalised oscillation peak amplitude vs damping ratio for mass ratios of 2.5 and 5.0 for the vibrating downstream cylinder in a staggered semicircular - circular cylinder WIV system

The lift coefficient also showed a similar relationship to that of the amplitude response, where the lift coefficient was inversely proportional to both the mass ratio and the damping ratio (Figure 6). However, the lift coefficient was highest for a Reynolds number of 6,000 (Figure 5 b) as the frequency of vortex shedding was closest to the natural frequency of the cylinder which aids in efficient transfer of force from the fluid to the cylinder.

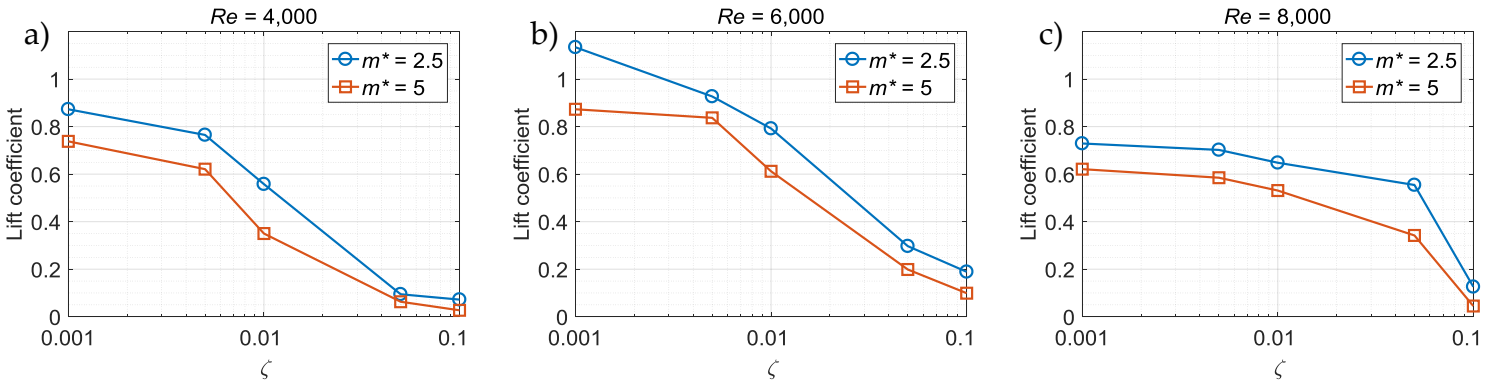

Figure 6 - Lift coefficient vs damping ratio for mass ratios of 2.5 and 5.0 for the vibrating downstream cylinder in a staggered semicircular - circular cylinder WIV system.

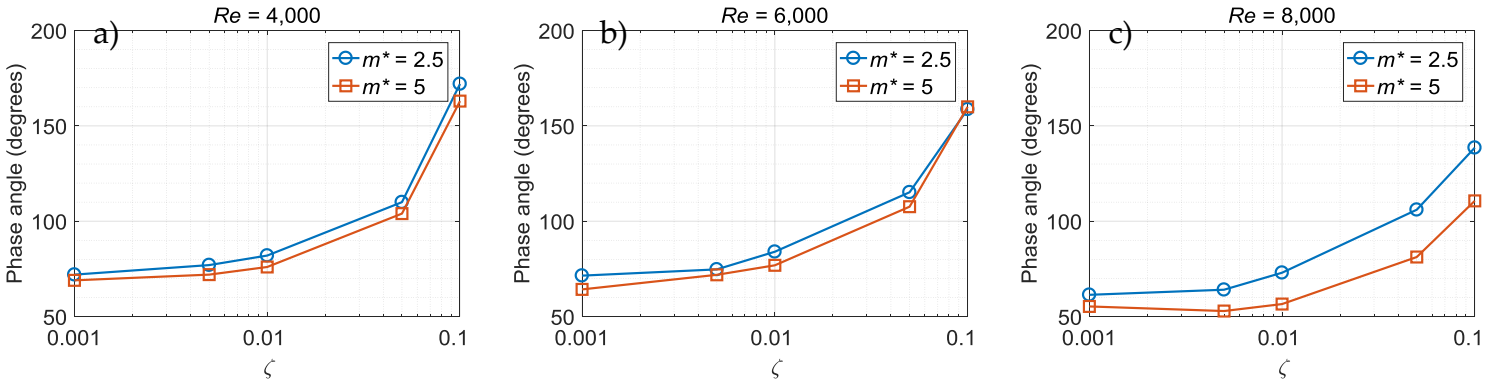

Figure 7 - Force-velocity phase difference vs damping ratio for mass ratios of 2.5 and 5.0 for the vibrating downstream cylinder in a staggered semicircular - circular cylinder WIV system.

The relationship between the force-displacement phase angle and damping ratio for the two mass ratios tested is plotted in Figure 7. The phase angle increased with increasing damping ratio. There was a slight reduction of the phase angle for the lower mass ratio of 2.5 (4 to 10 degrees) at Reynolds numbers lower than 6,000 (Figure 7 a and b), but a larger difference was observed at the higher Reynolds number (10 to 30 degrees) of 8,000 (Figure 7 c). It is also interesting to note that the phase angle was very similar for a damping ratio of 0.1 and a Reynolds number of 6,000 for both mass ratios (Figure 7 b), suggesting an independence of the phase angle to mass ratio at high damping ratios within the lock-in region. The largest difference in phase angle (40 degrees) between the two mass ratios was observed at a Reynolds number of 8,000 and a damping ratio of 0.1. Hence, a high damping ratio accompanied by fast flow speeds causes a delayed vibration response compared to the fluctuating lift force, making high damping ratios unsuitable for WIV energy harnessing.

3.2 Test 2 – Finer variation of mass ratio and damping ratio

Proceeding from Test 1, the damping ratios were limited between 0.005 and 0.025 as damping ratios higher than 0.025 provided very low amplitude vibrations for the chosen test parameters. The mass ratios

were varied from 2.0 to 4.0 to observe the effect of varying the mass ratio within the capabilities of the VMSD system. The processed results are given in Figures 8 to 11, and discussed in the following section.

The trends observed in Test 1 for the effect of damping ratio were also observed in Test 2. Increasing damping ratio reduced the displacement response (Figure 8) and lift coefficient (Figure 9) of the cylinder but increased the phase angle (Figure 10) between the lift force and displacement. The highest lift coefficients occurred for a Reynolds number of 6,000 and a mass ratio of 3.0 (Figure 9 b) for all damping ratios tested. Also, for each unique mass and damping ratio, the phase angle increased from Re = 4,000 to 6,000 and then reduced when Re was further increased to 8,000.

The effect of mass ratio was more complex than the damping ratio for the range of mass ratios tested (2.0 to 4.0). Increasing the mass ratio from 2.0 to 2.5 resulted in a reduction of the amplitude and lift coefficient, with a further increase of mass ratio to 3.0 leading to an increase in lift coefficient and displacement of the cylinder. It is interesting to note that the largest oscillatory response was recorded for a mass ratio of 3.0 at all three Reynolds numbers. Increasing the mass ratio beyond 3.0 followed the same trend as Test 1 with reduced vibration amplitudes and lift coefficients across all damping ratios and Reynolds numbers. The phase angle continued to decrease gradually with increasing mass ratio at any given damping ratio, however, the decrease was more pronounced at higher damping ratios (e.g. damping ratio = 0.025 in Figure 9). Utilizing these parameters for WIV, the WIV power coefficient (Equation 9) was calculated and is displayed in Figure 11. The results in Figure 11 indicate that lower mass ratios generally provide more efficient vibrations for energy harnessing compared to

higher mass ratios, apart from a mass ratio of 3.0, which has efficiencies comparable to a mass ratio of 2.0. The maximum at $m^* = 3.0$ is due to a maximum observed for the lift coefficient, which comprises of the vortex lift and the potential lift. Since the potential lift is proportional to the added mass of the cylinder, it is believed that the vortex lift due to the shed vortices is at a maximum at $m^* = 3.0$ in the range of mass ratios tested.

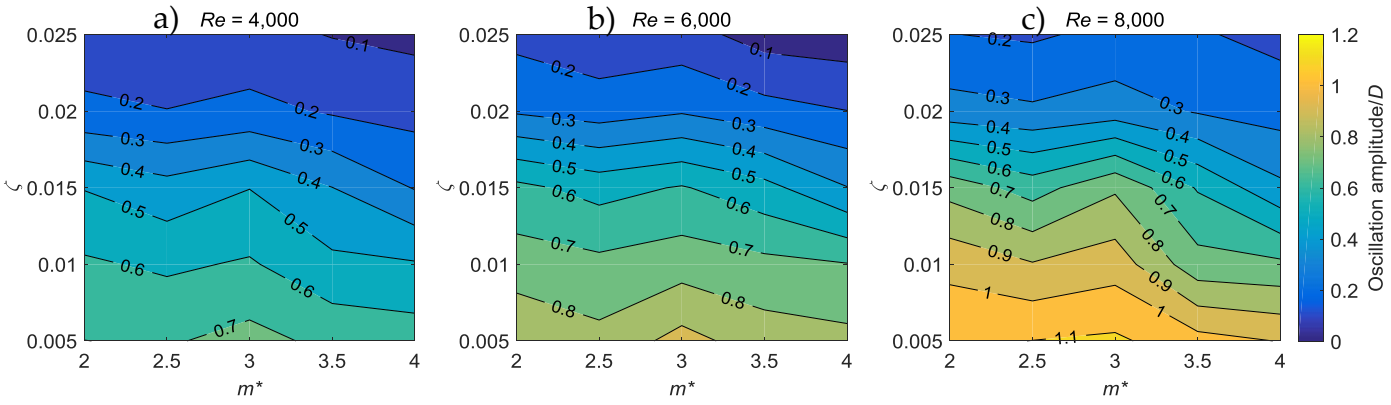

Figure 8 - Normalised oscillation peak amplitude (Y) obtained for the range of damping and mass ratios of the vibrating downstream cylinder in a staggered semicircular - circular cylinder WIV system.*

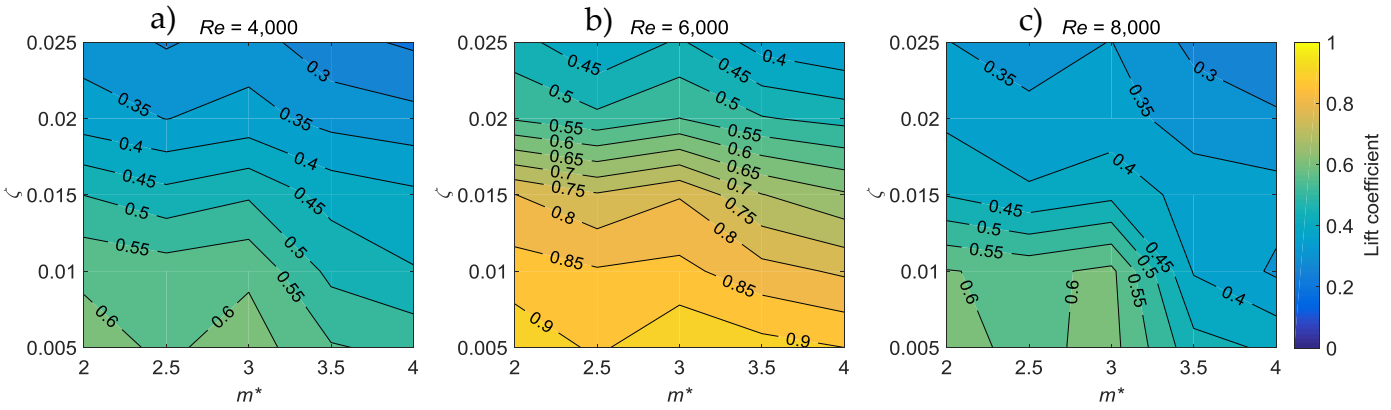

Figure 9 – Lift coefficient obtained for the range of damping and mass ratios of the vibrating downstream cylinder in a staggered semicircular - circular cylinder WIV system.

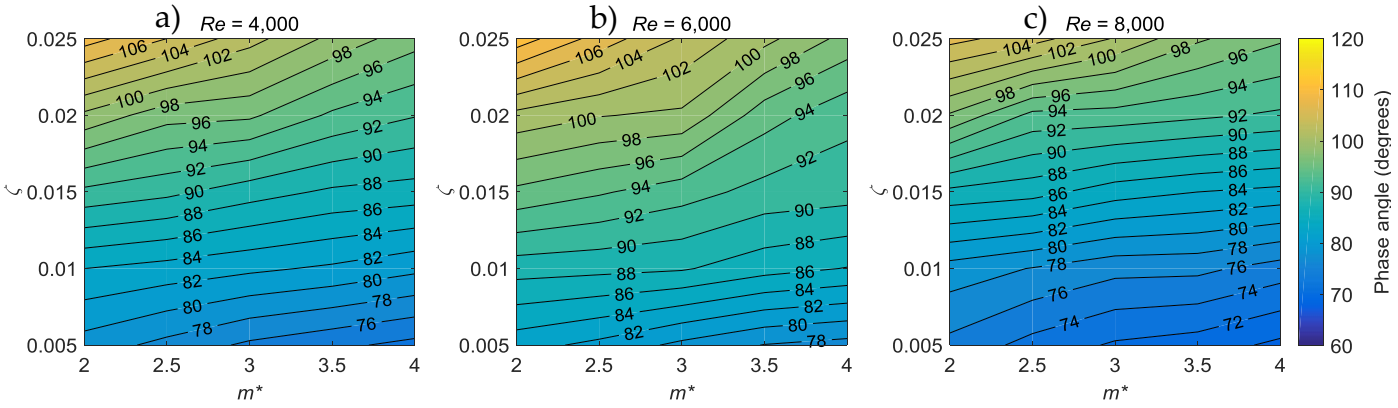

Figure 10 – Force-displacement phase angle obtained for the range of damping and mass ratios of the vibrating downstream cylinder in a staggered semicircular - circular cylinder WIV system.

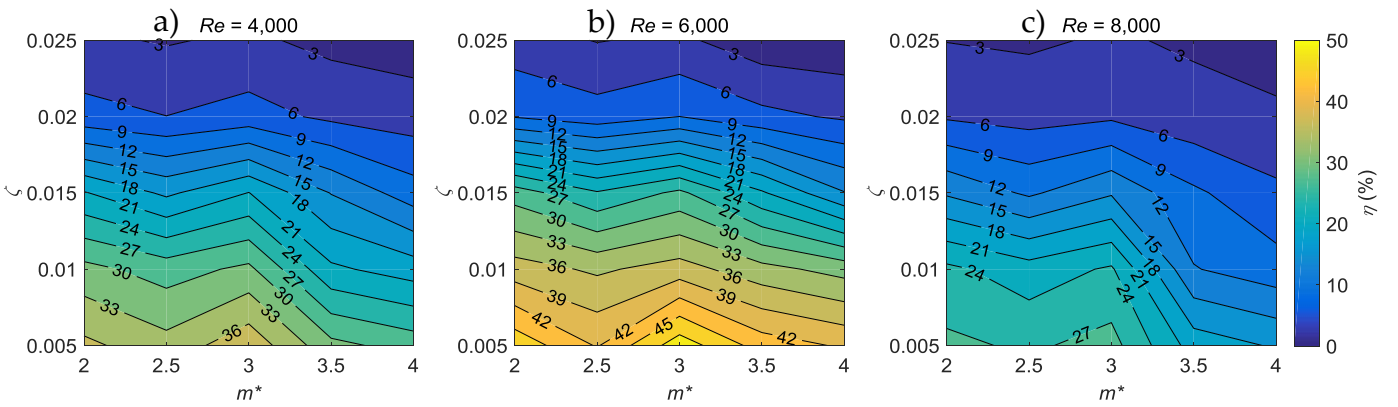

Figure 11 – WIV power coefficient (efficiency) obtained for the range of damping and mass ratios of the vibrating downstream cylinder in a staggered semicircular - circular cylinder WIV system.

The highest efficiencies occurred at a Reynolds number of 6,000 (Figure 11 b) due to high lift coefficients and favorable force-displacement phase angles occurring at this flow velocity. A Reynolds number of 6,000 corresponds to a reduced velocity of 5 and is within the lock-in region for VIV, which aids in efficient transfer of fluid force to the vibrations of the cylinder. The highest WIV power coefficient obtained in this test was 49% for a mass ratio of 3.0 and a damping ratio of 0.005 at *Re* = 6,000. Hence staggered WIV systems with a stationary upstream cylinder have great potential to provide high energy extraction efficiencies even at very low flow speeds (*U* = 0.201 m/s at *Re* = 6,000).

As mentioned earlier, mass ratios lower than 2.0 were not tested with the current system due to the chaotic vibrations exceeding the limitations of the VMSD system, however future work should examine the efficiencies of operating a WIV system at lower mass ratios ($m^* < 1$). Additionally, the results indicate that a range of mass ratios between 2.0 and 3.0 provide more efficient vibrations. This can be explained due to the lower mass of the cylinder which aids in higher acceleration due to the forces imparted by the fluid. The trends suggest that a mass ratio less than 2 should provide comparable efficiencies if not higher than that observed in this study. However, mass ratios close to and less than 1.0 approach the critical mass ratio ($m^* = 0.54$) and result in vibrations that are chaotic in nature and at higher harmonics of the natural frequency. Hence, any investigation in to lower mass ratios will need to be designed to extract energy at the higher frequencies observed. However, the tested range in this study provides stable vibrations that are suitable for energy extraction via WIV.

3.3 The combined effect of mass and damping ratio

It has been long argued that the VIV response of a cylinder can be characterized by just using the combined mass and damping parameter, $m^*\zeta$. Skop and Griffin (1973) introduced the Skop-Griffin number, S_G and proposed that the maximum amplitude of oscillation at all reduced frequencies is a function of this parameter only. The Skop-Griffin number was defined as

$$S_G = 2\pi^3 (St)^2 (m^*\zeta) \qquad (10)$$

In Equation (10), St is the Strouhal number of a stationary cylinder. In a later investigation, Griffin (1980) used a log-log plot of the maximum amplitude of vibration versus the Skop-Griffin number, which later

became known as the Griffin plot. Khalak and Williamson (1999) modified the Griffin plot and plotted the maximum amplitude versus $(m^* + C_A)\zeta$, where C_A is the potential added mass coefficient. Contrastingly, other researchers (Sarpkaya 1978; Sarpkaya 1995) hold a firm stance that the response is governed independently and not by the combined mass-damping parameter.

To investigate the effect of combined mass and damping on WIV, the maximum normalized amplitudes for cases with the same combined mass-damping parameter is plotted in Figure 12. In this figure, the plots each have a combined mass-damping from 0.02 to 0.05. Although the maximum amplitude does reduce when the combined parameter is reduced, a combined mass-damping parameter cannot be used to describe the amplitude of the WIV response. Referring to Figure 12 c) there is a significant difference in amplitude between the cases of the same mass-damping factor. It can also be observed that for damping ratio < 0.02, there are large amplitude vibrations (Figure 12 a) and b)) and a further increase in damping ratio drastically reduces the amplitude. Another interesting observation is that amplitudes of vibration are also small when the mass-damping ratio exceeds 0.04 (Figure 12 d)). Hence, a combined mass-damping less than 0.04 is ideal for WIV energy applications.

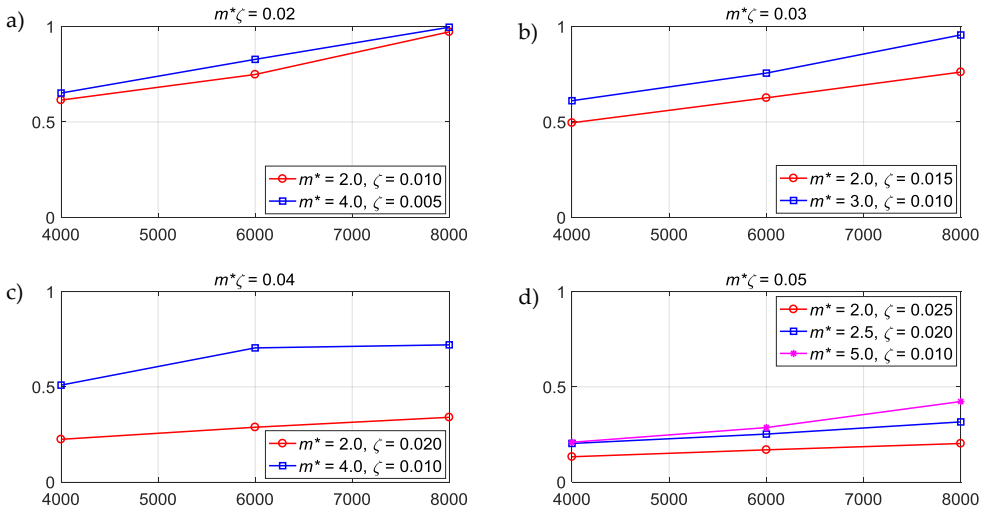

Figure 12 - Plots of normalised displacement amplitude (Y) versus Reynolds number for combined mass-damping of 0.02, a), 0.03, b), 0.04, c), and 0.05 d). The individual values of mass ratio and damping ratio are given in the legend for each subplot.*

4 Conclusion

The effect of mass and damping ratio on a WIV system consisting of a stationary upstream semicircular cylinder and a transversely vibrating downstream circular cylinder in a staggered arrangement (x = 4*D*, y = 2*D*) was experimentally investigated in the current study. The frequency of vibration was maintained constant and the mass and damping ratio were imposed on the system using the VMSD system at three Reynolds numbers. The oscillatory response was recorded and analyzed to result in the following outcomes:

i) A lower damping ratio provides large oscillation amplitudes and high vibration efficiencies due to lower resistance during oscillations. However, very low damping ratios are not always feasible in real world scenarios where the impedance (resistance) of the energy extractor is present.

ii) Generally, a lower mass ratio provides large oscillation amplitudes due to high accelerations imposed on the cylinder. However, a high oscillatory response, lift coefficient and

power coefficient were also identified for a mass ratio of 3.0 which is suitable for WIV energy technology involving staggered arrangements. Hence, a range of m^* = 2.0 to 3.0 is suggested as a choice for efficient wake induced vibrations out of the mass ratios that were tested (2.0 to 5.0).

iii) Mass ratios lower than 1.0 resulted in chaotic vibrations with high frequencies and amplitudes as the critical mass ratio was approached. The limitations of the VMSD rig did not allow for investigation at very low mass ratios, but should be further investigated for their applicability to WIV energy technology.

iv) The most efficient transfer of fluid force to cylinder displacement occurs within the lock-in range of VIV for the cylinder (i.e., Re = 6,000 in this case) and results in the highest efficiencies observed (η = 49% for m^* = 3 and ζ = 0.005).

v) WIV can be used to efficiently harness energy even at very low flow velocities by using a well-tuned system. An efficiency of 49% was experimentally demonstrated even at a low flow speed of 0.201 m/s.

vi) The phase angle between force and displacement is increases with increasing damping ratio but decreases with increasing mass ratio. Hence, efficient vibrations can be attained by tuning the WIV system to appropriate system parameters as the phase angle directly influences the efficiency of the vibration.

References

Anagnostopoulos, P & Bearman, P 1992, 'Response characteristics of a vortex-excited cylinder at low Reynolds numbers', *Journal of Fluids and Structures*, vol. 6, no. 1, pp. 39-50.

Assi, GRS 2009, 'Mechanisms for flow-induced vibration of interfering bluff bodies', Ph.D thesis, Imperial College London.

Assi, GRS, Meneghini, JR, Aranha, JAP, Bearman, PW & Casaprima, E 2006, 'Experimental investigation of flow-induced vibration interference between two circular cylinders', *Journal of Fluids and Structures*, vol. 22, no. 6, pp. 819-27.

Bahmani, M & Akbari, M 2010, 'Effects of mass and damping ratios on VIV of a circular cylinder', *Ocean Engineering*, vol. 37, no. 5, pp. 511-9.

Bearman, PW 1984, 'Vortex shedding from oscillating bluff bodies', *Annual Review of Fluid Mechanics*, vol. 16, no. 1, pp. 195-222.

Bearman, PW 2011, 'Circular cylinder wakes and vortex-induced vibrations', *Journal of Fluids and Structures*, vol. 27, no. 5, pp. 648-58.

Bernitsas, MM & Raghavan, K 2004, 'Converter of current/tide/wave energy', *Provisional Patent Application, US Patent and Trademark Office Serial*, no. 60/628,252.

Bernitsas, MM, Raghavan, K, Ben-Simon, Y & Garcia, EM 2008, 'VIVACE (vortex induced vibration aquatic clean energy): A new concept in generation of clean and renewable energy from fluid flow', *Journal of Offshore Mechanics and Arctic Engineering*, vol. 130, no. 4, pp. 1697–712.

Blevins, RD 1997, *Flow-induced vibration*, Second edn, Van Nostrand Reinhold, New York

Blevins, RD & Coughran, CS 2009, 'Experimental investigation of vortex-induced vibration in one and two dimensions with variable mass,

damping, and Reynolds number', *ASME J. Fluids Eng.*, vol. 131, no. 10, p. 101202.

Brika, D & Laneville, A 1999, 'The flow interaction between a stationary cylinder and a downstream flexible cylinder', *Journal of Fluids and Structures*, vol. 13, no. 5, pp. 579-606.

Carmo, BS, Sherwin, SJ, Bearman, PW & Willden, RHJ 2011, 'Flow-induced vibration of a circular cylinder subjected to wake interference at low Reynolds number', *Journal of Fluids and Structures*, vol. 27, no. 4, pp. 503-22.

Derakhshandeh, JF, Arjomandi, M, Cazzolato, B & Dally, B 2014, 'Experimental and computational investigation of wake induced vibration', paper presented to 19th Australasian Fluid Mechanics Conference, Melbourne, Australia, 8 - 11 December 2014.

Derakhshandeh, JF, Arjomandi, M, Dally, B & Cazzolato, B 2014, 'The effect of arrangements of two circular cylinders on the maximum efficiency of vortex-induced vibration power using a scale-adaptive simulation model', *Journal of Fluids and Structures*, vol. 49, pp. 654-66.

Derakhshandeh, JF, Arjomandi, M, Dally, B & Cazzolato, B 2015a, 'Harnessing Hydro-Kinetic energy from wake induced vibration using virtual mass spring damper system', *Journal of Ocean Engineering*, vol. 108, pp. 115-28.

Derakhshandeh, JF, Arjomandi, M, Dally, B & Cazzolato, B 2015b, 'A study of the Vortex-Induced Vibration mechanism for harnessing hydrokinetic energy of eddies using a single cylinder', *Journal of Applied Mathematical Modelling*.

Derakhshandeh, JF, Arjomandi, M, Dally, B & Cazzolato, B 2016, 'Flow-induced vibration of an elastically mounted airfoil under the influence of the wake of a circular cylinder', *Experimental thermal and fluid science*, vol. 74, pp. 58-72.

Ding, L, Zhang, L, Wu, C, Mao, X & Jiang, D 2015, 'Flow induced motion and energy harvesting of bluff bodies with different cross sections', *Energy Conversion and Management*, vol. 91, pp. 416-26.

Govardhan, R & Williamson, CHK 2000, 'Modes of vortex formation and frequency response of a freely vibrating cylinder', *Journal of Fluid Mechanics*, vol. 420, pp. 85-130.

Griffin, O 1980, 'Vortex-excited cross-flow vibrations of a single cylindrical tube', *Journal of Pressure Vessel Technology*, vol. 102, no. 2, pp. 158-66.

Hobbs, WB & Hu, DL 2012, 'Tree-inspired piezoelectric energy harvesting', *Journal of Fluids and Structures*, vol. 28, pp. 103-14.

Igarashi, T 1981, 'Characteristics of the flow around two circular cylinders arranged in tandem: 1st report', *Bulletin of JSME*, vol. 24, no. 188, pp. 323-31.

Khalak, A & Williamson, CH 1999, 'Motions, forces and mode transitions in vortex-induced vibrations at low mass-damping', *Journal of Fluids and Structures*, vol. 13, no. 7-8, pp. 813-51.

Khalak, A & Williamson, CHK 1997, 'Investigation of relative effects of mass and damping in vortex-induced vibration of a circular cylinder', *Journal of Wind Engineering and Industrial Aerodynamics*, vol. 69, pp. 341-50.

Lee, J & Bernitsas, M 2011, 'High-damping, high-Reynolds VIV tests for energy harnessing using the VIVACE converter', *Ocean Engineering*, vol. 38, no. 16, pp. 1697-712.

Manickam Sureshkumar, E, Arjomandi, M, Cazzolato, B & Dally, B 2, *Spatial and temporal concentration of hydrokinetic energy in the wake of a bluff body*.

Sarpkaya, T 1978, 'Fluid forces on oscillating cylinders', *NASA STI/Recon Technical Report A*, vol. 78, pp. 275-90.

Sarpkaya, T 1979, 'Vortex-induced oscillations: A selective review', *Journal of applied mechanics*, vol. 46, no. 2, pp. 241-58.

Sarpkaya, T 1995, 'Hydrodynamic damping, flow-induced oscillations, and biharmonic response', *Journal of Offshore Mechanics and Arctic Engineering*, vol. 117, no. 4, pp. 232-8.

Sarpkaya, T 2004, 'A critical review of the intrinsic nature of vortex-induced vibrations', *Journal of Fluids and Structures*, vol. 19, no. 4, pp. 389-447.

Skop, R & Griffin, O 1973, 'A model for the vortex-excited resonant response of bluff cylinders', *Journal of Sound and Vibration*, vol. 27, no. 2, pp. 225-33.

Wang, D-A & Ko, H-H 2010, 'Piezoelectric energy harvesting from flow-induced vibration', *Journal of Micromechanics and Microengineering*, vol. 20, no. 2, p. 025019.

Weinstein, LA, Cacan, MR, So, PM & Wright, PK 2012, 'Vortex shedding induced energy harvesting from piezoelectric materials in heating, ventilation and air conditioning flows', *Smart Materials and Structures*, vol. 21, no. 4, p. 045003.

Williamson, CHK & Govardhan, R 2004a, 'Critical mass in vortex-induced vibrations of a cylinder', *European Journal of Mechanics-B/Fluids*, vol. 23, pp. 17-27.

Williamson, CHK & Govardhan, R 2004b, 'Vortex-induced vibrations', *Annual Review of Fluid Mechanics*, vol. 36, pp. 413-55.

Zdravkovich, MM & Bearman, PW 1998, *Flow Around Circular Cylinders—Volume 1: Fundamentals*, American Society of Mechanical Engineers, 0098-2202.

This page is intentionally left blank

Chapter 7. Summary, conclusions and future work

7.1 Summary and conclusions

This thesis was concerned with the efficient harnessing of hydrokinetic energy using Wake Induced Vibration (WIV) of bluff bodies. Hydro-kinetic energy is a widely available resource that has the potential to provide clean and renewable energy using WIV. Feasibility of VIV and WIV technology has been established in recent research; hence, this study strived to increase the efficiency of present day WIV energy technology.

First, the spatial and temporal energy of flow around a circular cylinder was categorised. Following this, properties of temporally concentrated energy in the wake of different bluff bodies was compared to identify a prismatic bluff body cross-section that performs better than the circular cylinder. These bluff body cross-sections were also used as the upstream stationary body in a WIV system with a downstream and vibrating (1DOF) circular cylinder, to identify an efficient upstream flow energy concentrator. Finally, the effect of mass and damping ratios on WIV of a circular cylinder operating in the wake of a semi-circular cylinder were analysed and reported. In the following pages a summary of the work, and the conclusions and outcomes are presented.

7.1.1 Spatial and temporal concentration of flow energy by bluff bodies

The concept of spatial and temporal energy concentration by a bluff body was investigated and the data was presented in Chapter 3. The wake produced by a stationary circular cylinder was studied numerically to identify the form and frequency of the hydro-kinetic energy. A circular cylinder was chosen for the investigation due to the

abundant information on the flow properties and vibration response of the circular cylinder. Following this, a comparison between the wake energy of different bluff bodies was investigated.

The energy in the wake of a cylinder was found to be concentrated spatially (due to the mean velocity components) and temporally (due to the fluctuating velocity components). Significant spatial concentration of the mean streamwise energy component of the flow around the cylinder occurred near the top and bottom surfaces of the cylinder ($0 < x/D < 0.5$), due to the blockage caused by the cylinder. The mean transverse component of energy in the wake of the cylinder does not display any significant augmentation of energy in the wake as there is not net mean movement of the flow in the transverse direction. Hence, the mean velocity components produced due to the upstream cylinder are not very useful to enhance the vibrations of a downstream body.

The fluctuating components of velocity were found to contribute to the temporal concentration of energy in the wake of the cylinder, at different harmonics of the vortex shedding frequency. Most of the temporal concentration occurs at the shedding frequency due to the large scale von Karman vortices shed from the body and the maximum concentration of fluctuating energy occurs at $1< x/D < 3$ and $0 < |y/D| < 1$. Higher harmonics of the shedding frequency were found to have negligible energy due to the fluctuating components. Hence a the power take-off unit (downstream cylinder) needs to operate at the shedding frequency of the upstream body to harness the temporally concentrated energy in the wake of the upstream cylinder.

The maximum amount of streamwise and transverse energy that could be captured by an ideal wake energy extractor (WEE), assuming that the WEE could capture high energy density regions in a single cycle

of vortex shedding was also computed. A maximum of 3.25 times the available upstream energy can be harnessed at a streamwise distance of x = 1*D* if both the temporally and spatially concentrated energy is harnessed.

The effect of varying the cross-section of the cylinder was briefly investigated using shapes such as the semi-circle, straight-edged triangle, concave-edged triangle and convex-edged triangle. The spatial concentration of energy in the wake the bodies varied very little from that of the circular cylinder. However, there was a significant increase (approximately twice that of the circular cylinder) in the temporal concentration of flow energy in the wake of the convex-edged triangular and the semi-circular cylinder. It is believed that a larger base pressure accompanied by a stronger vortex-street leads to the higher concentration of temporally occurring energy in the wake of the aforementioned cylinders. Hence, these bodies would be ideal for use as upstream and stationary bodies in WIV systems, where they can provide a large amount of concentrated energy in the form of transverse fluctuations in the wake.

7.1.2 Effect of bluff body cross-section on temporal flow energy concentration in the wake

The wake of four different bluff bodies in a flow was experimentally analysed to compare trends in the turbulence statistics and the temporally concentrated energy in the wake of the cylinders. This section aimed at experimentally identifying upstream cross-sections that can provide a high concentration of energy in the cylinder wake due to the fluctuating components. The experiments were conducted in a water channel with Particle Image Velocimetry (PIV) to obtain the velocity field in the wake of stationary cylinders. The velocity vectors were

processed to report and analyse the energy density and turbulence statistics in the wake of the different bluff body cross-sections to identify possible cross-sections that can increase the efficiency of a WIV system.

Cross-sections with a smooth and convex-curved upstream face combined with a flat downstream face (i.e. semi-circular and convex-edged triangular cylinders) are better at concentrating the temporally occurring energy in the cylinder wake compared to a circular cylinder with the same hydraulic diameter. The percentage increase in temporally concentrated energy in the wake, compared to the circular cylinder, is higher at higher Reynolds numbers (semicircle = 60% higher, convex-edged triangle (c-triangle) = 17% higher at Re = 10,000) compared to lower Reynolds numbers (semi-circle = 27% higher, c-triangle = 9% higher at Re = 5,000). These cross-sections with a backward-facing step accumulate larger number of small-scale eddies to form the large-scale coherent vortices in the near wake, shedding off vortices with a higher level of temporal energy.

On the other hand, bluff body cross-sections with a flat upstream face (e.g. trapezoid) are less effective at concentrating temporal wake energy when compared to a circular cylinder with the same hydraulic diameter. This difference is more prominent at lower Reynolds numbers (reduction of 36% at Re = 5,000) compared to higher Reynolds numbers (Re = 10,000), where there was almost no difference. The wake of the trapezoidal cylinder is also highly dependent on the free stream velocity, where at Re = 5,000 the wake is diminished compared to that at Re = 10,000.

The semi-circular cylinder also has a longer average vorticity length (2.7D) at Re = 10,000 compared to the other cross-sections. Hence, the vorticity produced by the semi-circle propagates further downstream

compared to the other cross-sections. Since the vorticity *'bubble'* is longer for the semi-circle, the vortices formed by the semi-circle take longer to dissipate than the other shapes. Strouhal number of the circle and semi-circle cross-sections show very little sensitivity to the Reynolds number. This is because of the location of the separation point of the shear layers (~ 75 degrees from the stagnation point) being similar for both cases in this *Re* range which would allow for easy frequency matching between the upstream semi-circular cylinder and downstream circular cylinder in a WIV system.

The dominant regions for the Reynolds stresses are seen at x/D = 2.0 for the circle and trapezoid; whereas the region occurs at x = 1.5D for the c-triangle and x = 1.9D for the semi-circle at *Re* = 5,000. At *Re* = 10,000, the peak *uv* Reynolds stress zones move closer to the body by 0.3D for all the shapes except the c-triangle which only experiences a drop of 0.08D. The magnitudes of the peak Reynolds stresses are similar for the semi-circle and c-triangle; however, the region of peak magnitude is larger in the c-triangle and semi-circle (20% higher) compared to the other shapes. The increased peak magnitude corresponds to a higher level of turbulence (and vorticity), since the stresses are indicative of the fluctuating velocities in the wake, which in turn will lead to more temporal energy being available in the wake. The magnitudes of the peak Reynolds stresses are also lower for the trapezoid (by 10%) compared to the circle at both *Re*, suggesting less turbulence occurring in the wake of the trapezoid.

The normalised Turbulent Kinetic Energy (TKE), $[\overline{u'^2} + \overline{v'^2}]/U_0^2$ distribution in the wake of the bluff bodies was also investigated. The region of maximum TKE moves upstream when the Reynolds number increases, similar to the Reynolds stresses. Comparing the TKE

distribution of the cross-sections with the highest TKE magnitudes, the semi-circle has a larger wake encompassing the TKE compared to the c-triangle. The sizes of the peak regions are similar between both shapes at their respective Reynolds numbers. This increased TKE distribution in the semi-circle and c-triangle suggests a higher level of turbulent fluctuations in the wake of these two shapes and hence the streamwise and transverse energy components were further split up in the proceeding section to analyse the magnitude and frequency of the temporally occurring energy. The trapezoid has lower turbulence and hence lower TKE in the wake compared to the circle and was also the only shape to experience a gain in TKE when the Reynolds number doubled due to the complex separation and reattachment of shear layers which is observed in bodies with sharp windward edges.

In general, mean flow statistics are not highly affected by the bluff body cross-section because of the high magnitude of mean streamwise energy available in the freestream. Also, most of the temporal energy is concentrated at the shedding frequency (dependent on *Re)* with very low magnitudes (< 1%) present in the harmonics of the shedding frequency.

Thus, it is hypothesized that the peaks for zones of temporally occurring transverse flow energy in the wake of the cylinders, are higher in cylinders that have a curved fore surface and a flat aft surface due to a higher accumulation of vorticity before coherent vortices are shed from the body. Hence these types of cylinders can enhance temporal concentration of energy when used as the stationary upstream body in a WIV system.

7.1.3 Effect of upstream geometry on a WIV system

Following on from the previous two objectives, four cross-sections of the upstream cylinder were investigated for different staggered arrangements of the cylinders and for a range of Reynolds numbers (Re = 4,000 to 8,000). This objective was aimed at comparing the vibration statistics and efficiency of changing the geometry of the upstream cylinder. The experiments were performed in a recirculating water channel and the downstream cylinder was mounted to the Virtual Mass-Spring-Damper (VMSD) system which maintained the system parameters (mass and damping ratio) for all the tests. The water channel experiments resulted in measurements of the lift force and cylinder position (vibration displacement), which were analysed to develop the following outcomes.

A semi-circular cross-section cylinder placed as the first body in a WIV system provides a higher power coefficient (33%) compared to the circular cylinder (28%) at a Reynolds number of 6,000. The WIV system is most efficient when the downstream circular cylinder is at a staggered arrangement of x/D = 4 and y/D = 2. A semi-circular cylinder provides increased temporal energy at a similar frequency to the shedding frequency of the circular cylinder and hence creates a more efficient WIV system. The flat aft-face of the semi-circular cylinder forms vortices with more circulation than the circular cylinder and hence carry more temporal energy into the wake to be utilised by the downstream cylinder.

Temporal concentration of energy is the same for the semi-circular and convex-edged triangular cylinders. However, for the geometries considered, an upstream convex-edged triangular cylinder does not

provide an increased WIV response of a downstream circular cylinder which occurs when the semi-circular cylinder is used as the upstream body. This is due to the difference in frequency of the shed vortices, which are not tuned to the natural frequencies of the WIV system. Hence, frequency matching in the WIV system is important in order to make use of increased temporal energy by the upstream body. The lift coefficient is mostly dependant on the Reynolds number and less dependent on the position of the downstream vibrating bluff body, as it is mostly influenced by the freestream velocity.

A higher Reynolds number flow causes a greater range of phase angles in test cases for the circular and trapezoidal cylinders compared with lower Reynolds number flows. This effect was absent in the semi-circular and c-triangular cylinders due to their flat aft-faces. Hence, a larger base pressure on the upstream cylinder can reduce the variation of the phase angles imposed on the downstream cylinder.

The maximum efficiency for all upstream cross-sections occurs at a Reynolds number of 6,000 due to the system operating at its natural frequency, and hence a combination of VIV and WIV response occurs at this Reynolds number. Frequency matching between the vortex generator (upstream body) and the vibrating structure (downstream cylinder) provides the greatest efficiencies due to a combined VIV and WIV response. Design of WIV systems with adequate frequency matching is necessary to result in an efficient flow energy harnessing system. The vibration amplitude also continues to increase with increasing Reynolds number for all the cross-sections and cases considered, which is characteristic of the WIV response.

The location of the maximum efficiency is similar between all the shapes and occurs between x/D = 3 – 4 and y/D = 1 – 2 (staggered arrangement). The phase angle between the lift force and vibration is also closest to 90 degrees for this location, which results in more efficient transfer of force to displacement.

Hence, this study identified the semi-circular cylinder as a more efficient alternative to the circular cylinder as the stationary and upstream body in a WIV system. The harnessed efficiency of WIV is also benefited by employing frequency matching to result in a combined VIV and WIV response, as well as utilising a staggered arrangement of the cylinders.

7.1.4 Effect of mass and damping ratio on the WIV system

Although the effect of mass and damping ratio are well documented for VIV of a circular cylinder, there is a lack of research on the effect of these structural parameters on the WIV response of a system. In particular, this section was focused on investigating the effect of the parameters on the efficiency of a staggered cylinder system employing a non-traditional upstream body (semi-circular cylinder). An upstream semi-circular and a staggered downstream circular cylinder system, identified in the previous objective, was used to investigate the effect of mass and damping ratio on a WIV system. A staggered arrangement of $x = 4D$ and $y = 2D$ was used as it provided the highest power coefficients for WIV in Chapter 5. The frequency of vibration was maintained constant and different mass and damping ratios were imposed on the system using the VMSD system at three Reynolds numbers of 4,000, 6,000 and 8,000.

A lower damping ratio provides large oscillation amplitudes and high vibration efficiencies due to less resistance during oscillations.

However, very low damping ratios are not always feasible in real world scenarios where the impedance of the energy extractor is present. Generally, a lower mass ratio provides large oscillation amplitudes due to a high acceleration imposed on the cylinder. However, a high oscillatory response, lift coefficient and power coefficient were also identified for a mass ratio of 3.0, which is suitable for WIV energy technology involving staggered arrangements. Hence, a range of m^* = 2.0 – 3.0 is suggested as a choice for efficient wake induced vibrations out of the mass ratios that were tested (2.0 -5.0).

Mass ratios lower than 1.0 resulted in chaotic vibrations with high frequencies and amplitudes as the critical mass ratio was approached. The limitations of the VMSD rig did not allow for investigation at very low mass ratios, but should be further investigated in future studies for their applicability to WIV energy technology. The phase angle between force and displacement was found to increase with increasing damping ratio but reduce with increasing mass ratio. Hence, efficient vibrations can be attained by tuning the WIV system to appropriate system parameters as the phase angle directly influences the efficiency of the vibration.

The most efficient transfer of fluid force to cylinder displacement occurs within the lock-in range of VIV for the cylinder (i.e., Re = 6,000 in this case) and results in the highest efficiencies observed (η = 49% for m^* = 3 and ζ = 0.005). Hence, high efficiencies are realisable when the system is frequency matched to result in a combined VIV and WIV response. It is shown that WIV can be used to efficiently harness energy even at very low flow velocities by using a well-tuned system. An efficiency of 49% was experimentally demonstrated even at a low flow speed of 0.201 m/s. Hence the feasibility of a high efficiency, small-scale WIV system was

demonstrated in this section. Due to the increased energy in the flow with increasing flow velocity, large-scale WIV systems following the recommendations in this section can result is significant power harnessed from currents in rivers and oceans.

7.2 Significance of the present work

The most common cylinder used in VIV and WIV systems is the circular cylinder. Past studies have analysed and demonstrated that such systems are able to harness energy from low-speed flows. This study investigated the energy components in the wake of a circular cylinder to provide insight in to the form and frequency of the energy in the wake of the cylinder. It is found that the shedding frequency contains most of the energy due to the fluctuating components. Frequency matching between the upstream and downstream body was found to be an important factor to realise efficient WIV systems. The semi-circular cylinder was identified as a strong vortex generator that is able to enhance the vibrations in a downstream cylinder. Staggered arrangements of cylinders are also recommended to increase the vibration efficiency of the downstream cylinder. Furthermore, a mass ratio envelope between 2.0 and 3.0 has been identified to provide periodic, high amplitude vibrations in the downstream structure. As expected, a lower damping ratio is beneficial to obtain high amplitude vibrations and an efficient transfer of force in the moving fluid to lift force of the cylinder. Utilising this knowledge, an optimised WIV system with a staggered arrangement of an upstream semi-circular cylinder and a downstream circular cylinder was tested to provide an energy harnessing efficiency of 49% at a low flow speed of 0.201 m/s, which is a significant improvement to vibration efficiencies seen in similar small-scale and low flow speed systems.

7.3 Recommendations for future work

As a consequence of this research, several recommendations for future investigations are presented in this section.

7.3.1 Effect of very low mass ratios, $O(1)$

The VMSD rig was incapable of handling the vibrations below a mass ratio of unity. Previous VIV studies have shown that mass ratios close to the critical mass ratio (0.45) result in VIV vibrations at a high frequency, which is usually a harmonic of the natural frequency (Williamson & Govardhan 2004). Hence further investigation in to the effect of low order mass ratios ($m^* < 1$) on the WIV response is warranted in order to deduce the feasibility of low mass ratios for energy harnessing using WIV.

7.3.2 Effect of high Reynolds numbers on the system

This study has been performed at relatively low Reynolds numbers in the Transition in Shear-Layers (TrSL) regime. The WIV response is not limited to a synchronisation band like VIV and has increasing amplitudes with increasing Reynolds number. Higher Reynolds number flows also contain more flow energy, and hence future investigations are required to observe the efficiencies at larger Reynolds numbers ($Re > 20{,}000$).

7.3.3 Effect of spring stiffness

High damping and high stiffness have been shown to produce efficient vibrations for energy harnessing in a multiple cylinder VIV system (Bernitsas *et al.* 2009). Although the current study investigated the effect of mass and damping ratio, the effect of spring stiffness on a WIV system has not been investigated. Future investigation in to the relationship between spring stiffness, damping and WIV efficiency will

be useful in designing WIV energy technology that can handle the impedances that are caused due to the Power Take-Off (PTO) system.

7.3.4 Implementation of a real PTO system

All experiments were conducted using a servo-motor driven virtual power take-off in the VMSD system. Utilising a linear motor with low resistance and friction (impedance), the real power harnessed should be investigated by generating power into load bank.

References for Chapter 7

Bernitsas, MM, Ben-Simon, Y, Raghavan, K & Garcia, EM 2009, 'The VIVACE converter: model tests at high damping and Reynolds number around 105', *Journal of Offshore Mechanics and Arctic Engineering*, vol. 131, no. 1, pp. 1 - 15.

Williamson, C & Govardhan, R 2004, 'Critical mass in vortex-induced vibrations of a cylinder', *European Journal of Mechanics-B/Fluids*, vol. 23, pp. 17-27.